THE PETROLOGY AND GEOCHEMISTRY OF THE LOWER PYROXENITE SUCCESSION OF THE GREAT DYKE IN THE MUTORASHANGA AREA

THESIS
Submitted in partial fulfillment of the requirements for the
Degree of MASTER OF SCIENCE (ECONOMIC GEOLOGY)
in the Department of Geology, Rhodes University, Grahamstown

by

ALEXANDER DYMOKE MASON-APPS

February 1998

ABSTRACT

This thesis focuses on the petrology and geochemistry of the lower Pyroxenite Succession of the Great Dyke of Zimbabwe in an area to the south of Mutorashanga. Particular emphasis is placed upon the economically important chromitite C5, and on the pervasive serpentinization of olivine-rich rocks. An overview of the Great Dyke, including the Satellite Dykes, the structure and stratigraphy of the Great Dyke, the economic resources of the Great Dyke, and the evolution of the Great Dyke magma, is given. A review of the geodynamic history of the Zimbabwe Archaean craton, which culminated in widespread cratonisation and emplacement of the Great Dyke is also provided.

The silicate rocks of the lower Pyroxenite Succession are highly adcumulate dunites and orthopyroxenites, with well-developed granular textures and a restricted mineral assemblage of olivine and pyroxene, with very minor plagioclase and clinopyroxene. Within cyclic units, the silicate rocks commonly display a textural and modal progression from granular dunite through poikilitic harzburgite, granular harzburgite, and olivine orthopyroxenite, to granular orthopyroxenite. Chromitites commonly occur at the base of each cyclic unit, these are thin, massive, coarse-grained layers, and are shown to be modified, texturally and compositionally, by postcumulus annealing processes.

The olivine-rich rocks are pervasively serpentinized to a depth of over 300 metres. The serpentites typically display well-developed pseudomorphic mesh textures, with a slight overprint of non-pseudomorphic interpenetrating textures and late-stage cross-cutting veins. X-Ray diffraction studies indicate that chrysotile is the dominant serpentine mineral, and also reveal the presence of a nickeliferous magnesium hydroxide, occurring as an intimate admixture with serpentine, and believed to be a nickel-bearing analogue of brucite.

Mineral and whole rock compositions of chromitite and silicate rocks highlight the strongly magnesian nature of the Ultramafic Sequence. Studies of the footwall chromites below chromitite C5 are consistant with a model of replenishment of primitive magma into the Great Dyke magma chamber, at the base of each cyclic unit. The magma injection and subsequent mixing with the evolved resident magma gives rise to chromitite formation, and a causes a reversal of the fractionation trend, resulting in a return to more primitive compositions in the silicate rocks. The silicates display an overall fractionation trend that reflects the evolving composition of the parental magma.

CONTENTS

LIST OF FIGURES

LIST OF TABLES

LIST OF PLATES

ACKNOWLEDGEMENTS

I should like to thank all the staff at the Department of Geology, Rhodes University, for their assistance and patience throughout the course of this thesis. In particular, I would like to thank Prof. John Moore, Dr Eric Ferre, and John Hepple. Fellow student Harilaos Tsikos is thanked for his invaluable help, discussions, and encouragement throughout my time at Rhodes.

Charlie Murahwi and all those at Prospecting Ventures in Harare are thanked for their advice and support during the course of the field research in Zimbabwe. My thanks also to Dr Rob Harris of Geodatec for his continued assistance with the MIPS and NTN software.

My thanks to family and friends for their constant support and encouragement. Particular thanks to Pippa Russell for her patience and understanding during the writing-up stage of this thesis.

Finally, I would like to dedicate this thesis to the memory of my late grandmother, Mrs Juliet de Schanschieff, whose unwavering optimism and incredible support throughout my life, and particularly during the course of my time at Rhodes has been inestimable and inspirational.

DECLARATION

All work in this thesis is the original work of the author, except where specific acknowledgement is made of the work of others. This thesis has not been submitted for a degree at any other institution.

Signed: ____________

A.D. MASON-APPS

1998

CHAPTER 1 : INTRODUCTION

1.1 : THE GREAT DYKE

The Great Dyke of Zimbabwe is one of the world's most remarkable geological features, forming a major linear NNE-trending feature 550 km long, and an average of 8 km wide, along the central axis of Zimbabwe (see figure 1.1). The Great Dyke is flanked by Archaean granitoids for 90% of its length, the remainder being rocks of Archaean greenstone belts, as shown in figure 1.1, and holds significant world-class deposits of chromite and platinum. The earliest identification of the Great Dyke as a geological entity was made by the geologist explorer Carl Mauch, probably in 1868 , on the first of two journeys into the Southern African interior (Harger, 1934). The intrusion was first named the 'Great Dyke' by Zealley (1912), who quotes an earlier description of the Great Dyke as "the great mass of coarsely crystalline picrite extending for nearly the whole distance across Rhodesia from north to south" by F.P. Mennell in 1910.

The Great Dyke is one of several major layered intrusions, including the Bushveld, Stillwater, and Munni Munni complexes, emplaced during the late Archaean - early Proterozoic into stable cratonic environments. These stratiform complexes are particularly important in respect of their considerable chromite and platinum mineralization. The emplacement of the Great Dyke has been variously described as the final defining event of the Archaean or as the first major event of the Proterozoic. Nisbet (1982) suggested that the "time of cooling of the Hartley Complex of the Great Dyke of Zimbabwe" should be used as the defining lithological division of the Archaean-Proterozoic boundary, arguing that the continual refinement of dating techniques rendered a formal age boundary problematic. The most accurate published age for the Great Dyke by Hamilton (1977) is an Rb:Sr age of 2460 ± 16 Ma (recalculated, Cahen and Snelling, 1984), although an unpublished U-Pb age of 2584 ± 16 Ma was recently determined by A.H.Wilson (pers.comm).

The Great Dyke essentially represents the remains of two major, initially composite, magma chambers, both with a high length: width ratio (Prendergast, 1988). In addition to these two chambers, known as the North and South Chambers, the north-easternmost segment of the intrusion, first mentioned as an outlying body of the Great Dyke by Lightfoot (1940), is now considered to be a third chamber, named the Mvuradona Chamber (Wilson and Prendergast, 1989). The major subdivisions of the Great Dyke according to the current nomenclature are given in table 1.1:

Table 1.1 : Subdivisions of the Great Dyke, including lengths and sequence thicknesses. Modified after Wilson and Prendergast (1989).

Chamber	**Subchamber**	**Length** (km)	Max. thicknesses (m)	
			Mafic	**Ultramafic**
Mvuradona		43	300	2160
North	Musengezi			
	Darwendale	321	1150	2200
	Sebakwe			
South	Selukwe	96	270	1600
	Wedza	80	420	1500

The first major geological investigations of the Great Dyke were carried out by Lightfoot (1927, 1940), and Hess (1950). It was only with the work of Worst (1958, 1960), however, that a fully comprehensive account of the Great Dyke was published. In the course of several years of research, B.G.Worst mapped almost the entire length of the Great Dyke, a monumental achievement given the scale of the intrusion. Subsequent to Worst's publications, a number of researchers have contributed to the current understanding of the Great Dyke, including Hughes (1970, 1976), Bichan (1969, 1970), Hamilton (1977), Wilson (1982), and Podmore and Wilson (1987). A growing interest in the vast platinum resources of the Great Dyke has contributed to the considerable increase in publications during the last 10 years (e.g. Wilson et al., 1989; Wilson and Prendergast, 1989; Prendergast and Keays, 1989; Prendergast, 1989, 1990, 1991; Wilson, 1992, 1996; Coghill and Wilson, 1993).

1.2 : OBJECTIVES OF THE CURRENT STUDY

The main thrust of the current study focuses on the geology of the Great Dyke in an area 30 km south of Mutorashanga near the Sutton, Great Dyke II, and Caesar mining areas. The study area comprises ultramafic rocks of the lower Pyroxenite and upper Dunite Successions within the northern part of the Darwendale Subchamber. A geochemical and petrographical investigation of samples from borehole core and surface samples from the research area was undertaken. The main objectives of the current study are outlined below:

1. A comprehensive review of the current level of understanding of the Great Dyke, including its tectonic and geologic setting, internal structure, emplacement, stratigraphy, and mineralization.

2. A detailed study of the stratigraphy, petrography, and geochemistry of the Great Dyke rocks in study area.

3. A detailed study of chromitite C5, with an aim to providing further evidence of the genetic history of the chromitite.

4. A descriptive and interpretive analysis of the serpentinization of the Great Dyke rocks in the study area.

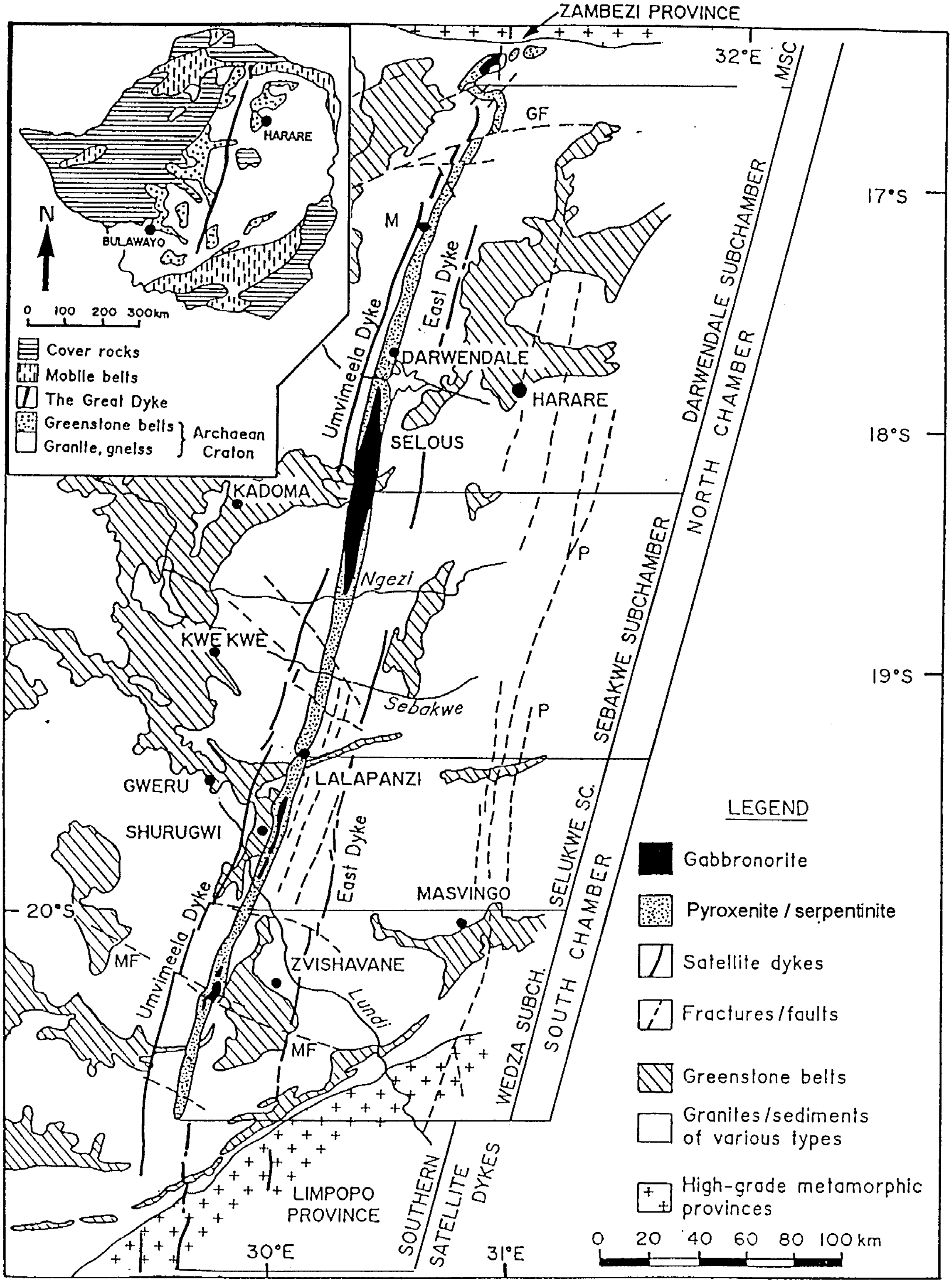

Figure 1.1 : Geological map of the Zimbabwe craton in the area of the Great Dyke, its satellites, and associated fractures. Divisions into chambers and subchambers are indicated on right. Abbreviations: MSC, Mvuradona Subchamber; P, Popoteke fault set; Gurungwe fault; MF, Mchingwe fault; M, Mutorashanga. Inset shows locality of the Great Dyke in relation to the cover rocks and basement in Zimbabwe. (Modified after Wilson, 1996)

CHAPTER 2 : THE ARCHAEAN ZIMBABWE CRATON

2.1 : INTRODUCTION

The Zimbabwean craton is one of five structural provinces in southern and central Africa. The cratonic regions are separated from each other by mobile belts, which are now characterised by high-grade metamorphism. The Zimbabwean craton is bounded on at least three sides by mobile belts: to the north and northwest by the Zambezi belt, to the east by the Moçambique belt, and to the south by the Limpopo belt. The western limits of the craton are obscured by undeformed cover rocks of Karoo age and younger. The major features of the Archaean Basement Complex are shown in figure 2.1.

2.2 : GRANITE-GREENSTONE TERRAINS

The development of the Archaean Zimbabwe Craton was essentially restricted to two major "accretionary super-events" (Wilson, 1990). The first of these periods of volcanism, crustal growth, and orogeny occurred during the early Archaean and essentially involved the Tokwe Segment, a broadly triangular protocraton (see figure 2.2a). The second period of major tectonism was much more widespread and took place in the late Archaean between *c.*2900 and *c.*2600 Ma. This period is characterised by a number of magmatic cycles, each of which involved initial mafic volcanism, followed by a period of felsic-intermediate volcanism culminating in related granitoid plutonism.

2.2.1 : Greenstone Belts

Within the Tokwe Segment are preserved the remnants of the oldest of Zimbabwe's greenstone belt material (figure 2.3a), the *c.*3.6 Ga Sebakwian Group (Wilson et al.,1995). The existence of an early ensialic basement is indicated by the presence of granitic boulders within Sebakwian conglomerates, and the high initial Sr-ratios (0.7107) of the *c.*3.3 Ga Mont d'Or granite that intrudes the Sebakwian Group in the Shurugwe area (Cahen and Snelling, 1984).

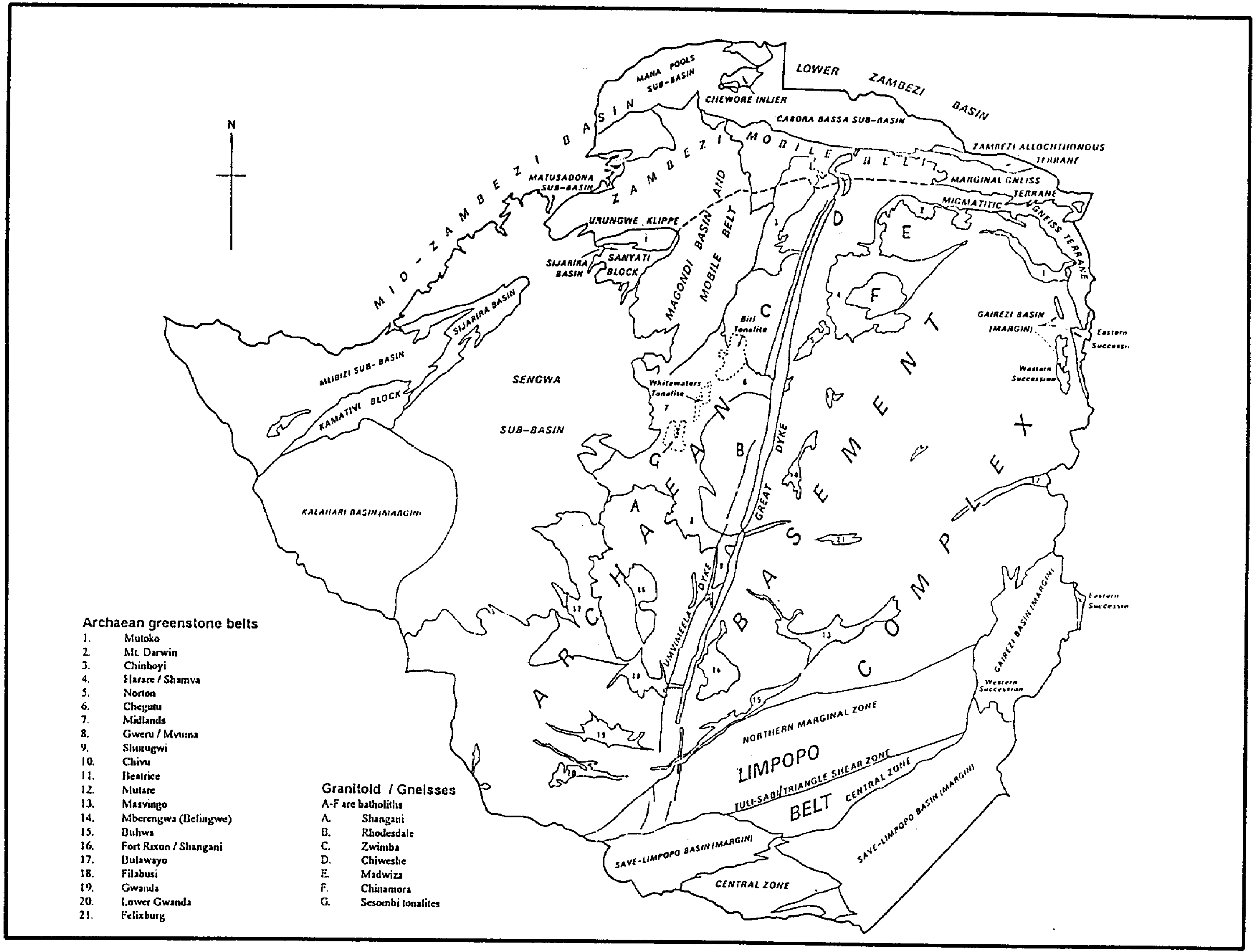

Figure 2.1 : Tectonic map of Zimbabwe showing outlines of major terranes and the locations of the main Archaean greenstone belts and granite-gneiss suites. (Modified after Campbell et al., 1992)

The Belingwean, Bulawayan and Shamvaian Supergroups represent greenstone belt material of the second Archaean 'super event'. Table 2.1 is a summary of the current stratigraphic nomenclature, geochronology, and lithological features of all the greenstone belts. Above U3, the Upper Bulawayan is differentially developed to the east and west within the craton (U4E and U4W in table 2.1). U4W may pass laterally and upwards into the U5 unit, which is only developed within the western succession. Stratigraphic and geochronologic relations indicate that two similar, but not contemporaneous greenstone sequences were developed within the Upper Bulawayan (figure 2.3d): one in the south-central region at *c.*2700 Ma, and one in the northern region, named the Harare sequence, at *c.*2650 Ma (Wilson et al., 1995).

Table 2.1 : Stratigraphy of the greenstone belts of the Zimbabwean craton. Heavy lines represent major unconformities. Stratigraphic nomenclature and U-Pb zircon ages (where given) after Wilson et al. (1995).

Stratigraphic Division		**Unit**	**Description**
Shamvaian Supergroup		U6	Predominantly sedimentary sequence of poorly sorted clastics derived from volcanic and granitic terrains, some local felsic volcanics. Upper succession is markedly ferruginous within the Masvingo belt.
Bulawayan Supergroup	Upper Bulawayan *c.***2700 Ma**	U5	Calc-alkaline suite of basalt, andesite, and dacite flows and pyroclasts
		U4 W	Bimodal volcanic suite of pillowed and massive basalt flows alternating with dacitic flows and volcaniclastics. Local intercalations of clastic and chemical metasediments showing evidence of significant shallow-water reworking.
		U4E	Sequence of fine-grained clastics with BIF (Banded Iron Formation) and localized stromatolites occurrences, passing upwards into, and partly interbedded with, tholeiitic (and some Mg-rich) basalt pillowed and massive flows
		U3	4-6 km of massive and pillowed tholeiitic basalt lava flows
		U2	High Mg- basalt and komatiite succession of massive and pillowed lava flows
		U1	Clastic and chemical sediments with BIF common and local stromatolite development.
	Lower Bulawayan **2800 - 2830 Ma**	L4	Felsic volcanic sequence, with no apparent mafic volcanism, and generally fine-grained metasediments. Conglomerates locally developed, particularly in the Belingwe belt.
Belingwean Supergroup *c.***2900 Ma**	Upper Belingwean	L3	Mafic-ultramafic volcanic sequence with BIF interlayering
	Lower Belingwean	L2	Bimodal felsic/mafic volcanic succession, also contains minor BIF
		L1	Dominantly mafic volcanics.
Sebakwian Group			Altered mafic-ultramafic volcanics rocks with various supracrustal metasediments, including conglomerates, quartzites, metapelites and Banded Iron Formations (BIF).

2.2.2 : Granitoids

The late Archaean granitoids are the result of major crustal-forming events, culminating in the final stabilization of the Zimbabwe craton with the intrusion of the *c.*2600 Ma Chilimanzi Suite. The distribution of these granitoids is shown in figure 2.2. The Chingezi, Wedza, and Sesombi Suites are broadly contemporaneous with felsic-intermediate volcanism of Belingwean - Bulawayan Supergroups, and are interpreted as plutonic equivalents of these volcanic episodes (Wilson et al., 1995). Table 2.2 summarises these suites and the related volcanic events preserved in the greenstone belts.

Table 2.2 : Description, approximate age of intrusion, and correlation with volcanic events of pre-Chilimanzi granitoids of the Archaean Zimbabwean craton (compiled from Wilson et al., 1995, and others).

Granitoid Suite	**Age (Ma)**	**Description**	**Correlation**
Chingezi Suite	2900-2700	Tonalites and granodiorites with lesser diorites and monzogranites	Belingwean felsic volcanism: the *c.*2830 Ma event in response to Chingezi plutonism, while the *c.*2800 Ma volcanism may be an expression of later, post-tectonic Chingezi intrusions
Sesombi Suite	2700	Tonalitic-granodioritic granitoids	U4W and U5 Bulawayan volcanism; of similar age (*c.*2600 Ma) and initial Sr-ratio as calc-alkaline volcanics of the Maliyami Formation (U5)
Wedza Suite	2700	Complex suite of granitoids, essentially tonalitic-granodioritic.	Correlated to volcanism of the *c.*2650 Ma Harare sequence.

The *c.*2600 Ma Chilimanzi Suite represents a major, craton-wide, post-Shamvaian event (Wilson et al., 1995). Overall initial Sr-ratios of the granitoids are indicative of large-scale melting of lower sialic crust. The suite consists mainly of adamellites, with some granodiorites, many of which are intruded as sill-like bodies (Treloar and Blenkinsop, 1995).

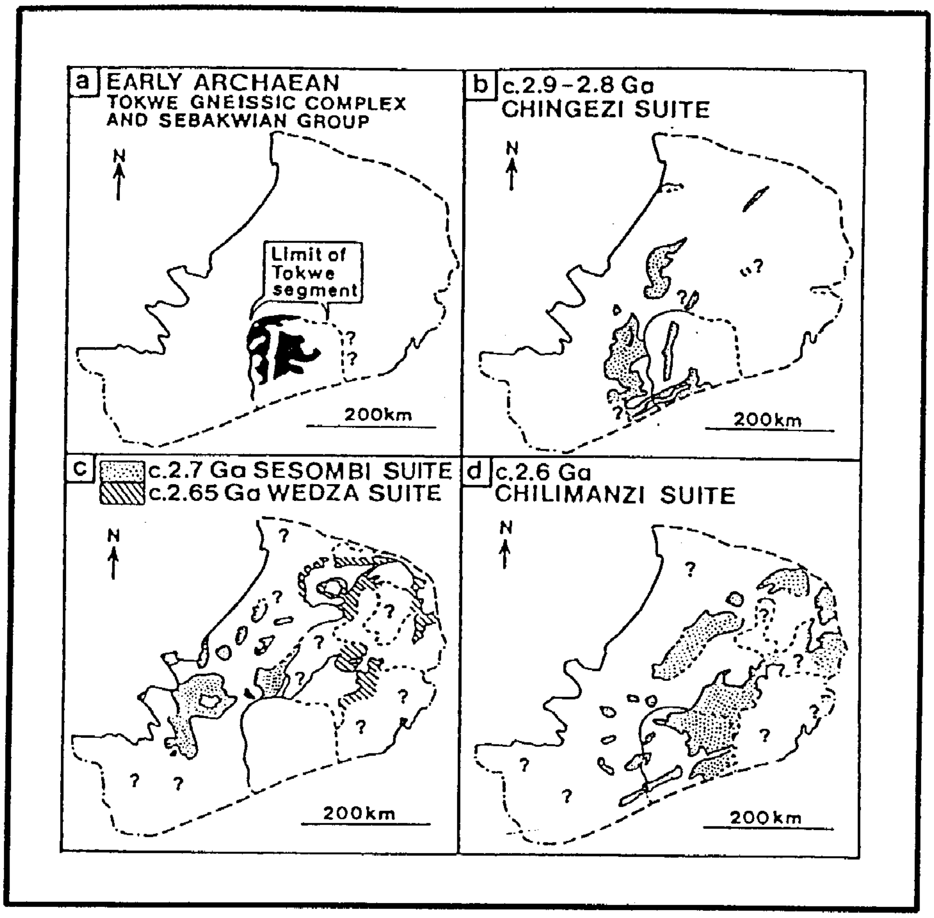

Figure 2.2 : The approximate areal distribution of the major Archaean granitoid suites according to age. Areas containing question marks are not comprehensively mapped and probably contain extensive areas of Chilimanzi Suite granitoids (after Wilson et al., 1995).

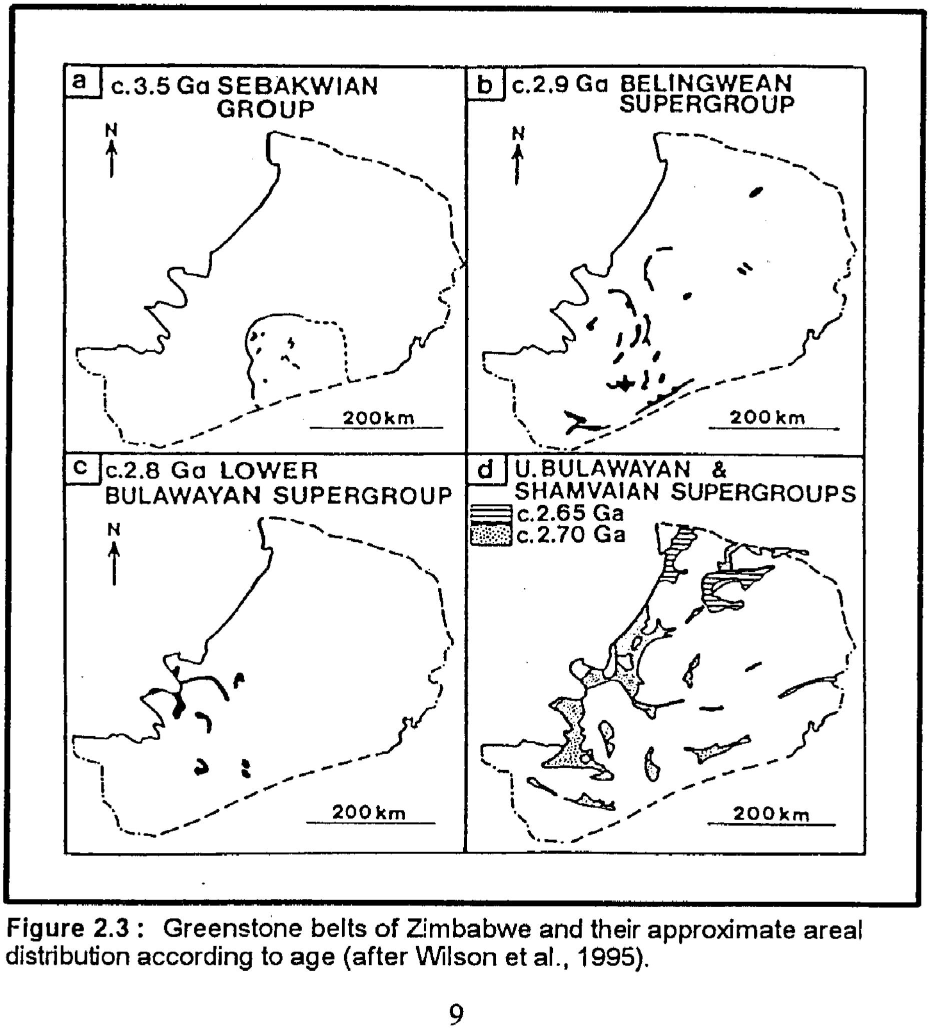

Figure 2.3 : Greenstone belts of Zimbabwe and their approximate areal distribution according to age (after Wilson et al., 1995).

2.3 : MINERALIZATION ASSOCIATED WITH THE ZIMBABWE CRATON

Zimbabwe is an important world producer of gold, chrome, asbestos, lithium, and is soon to be a major platinum producer. The most consistently valuable mineral products of the country in modern times have been gold and asbestos (Bartholomew, 1990). Most of the economic mineral deposits occur within the Archaean Basement Complex (see figure 2.1), particularly in association with greenstone belt terrains.

Although gold mineralization in the Archaean craton occurs within rocks of wide-ranging ages, most of the mineralization is related to Upper Bulawayan tectonic and magmatic activity. There are two main associations of the gold mineralization (Wilson and Nutt, 1990): non-stratabound vein and shear-zone related deposits, and stratabound deposits, particularly BIF-associated. The major controls on economic gold concentrations are considered to be late-stage Upper Bulawayan shear zone development and Sesombi Suite intrusion (Wilson and Nutt, op.cit.).

Zimbabwe's most important chrysotile asbestos deposits are at Zvishavane and Mashava, where they are hosted by peridotitic sills of the Mashaba Igneous Complex, part of the Mashaba Ultramafic Suite which also includes the Mashaba-Shabani intrusions. The Complex occurs at the western end of the Masvingo belt where it intrudes the >3500 Ma granite-gneiss terrain and Sebakwian Group remnants. The development of the chrysotile asbestos deposits is the result of major faulting of the Complex associated with a D_2 deformation event (Wilson et al., 1995). The sills of the Mashaba Ultramafic suite and Mafic dykes of the Mashaba-Chibi dyke swarm are interpreted as representing a part of the feeder system to Upper Bulawayan tholeiitic / high Mg-basaltic volcanism (Wilson et al., op cit.).

Economically important podiform chromite deposits are mainly associated with Sebakwian Group greenstones at Shurugwi, where they occur in the heavily altered peridotitic Selukwe Ultramafic Complex. The chromite bodies are hosted within altered dunites, and are believed to be highly deformed stratiform chromitite layers (Wilson and Nutt, 1990). Other podiform chromite deposits include a chromite-bearing serpentinite occurring above the main sill of the Mashaba Igneous Complex, and has previously been interpreted as a part of the complex but is now understood to be a part of the Sebakwian Group remnants (Wilson et al., 1995).

Nickel deposits in Zimbabwe are all related to Upper Bulawayan mafic-ultramafic magmatism, with the exception of Madziwa Mine which occurs in a mafic intrusion related to the Proterozoic Mashonaland Igneous Event (see chapter 3.1). Of the main nickel producing mines, the Shangani and Epoch deposits are associated with Mashaba Ultramafic Suite intrusions, the Trojan Mine deposit is associated with komatiitic flows, and the Empress Mine deposit occurs in a differentiated mafic sill (Wilson and Nutt, 1990).

Pegmatites are an important source of numerous industrial minerals in Zimbabwe. Numerous pegmatites across the craton are considered as late stage products of the Chilimanzi Suite magmatic event, and constitute a major source of lithium, particularly the Bikita pegmatite at the eastern end of the Masvingo greenstone belt, which is one of the world's largest lithium deposits (Bartholomew, 1990).

2.4 : METAMORPHISM AND DEFORMATION

2.4.1 : Metamorphism

Sebakwian group rocks generally exhibit regional metamorphism up to amphibolite facies, although this may locally be up to granulite facies. The main greenstone belts show an approximate regional metamorphic zonation, in which grades increase from zeolite-lower greenschist facies in the central area, through lower and upper greenschist facies, to amphibolite facies at the southern and northern cratonic margins. Wilson (1981) suggests that this zonation is most likely to be related to thermal highs developed along the Limpopo and Zambezi belts.

2.4.2 : Deformation

The greenstone belts generally have a characteristic arcuate and sigmoidal outline (as defined by Upper Bulawayan rocks) and internal foliation. The late Archaean main deformation events, which largely controlled structure and distribution patterns of the greenstone belts, can be broadly divided into two major overlapping and diachronous stages (Wilson et al., 1995). The first stage involved initial doming, related to the intrusion of the Sesombi and Wedza suites. A later shear zone stage, involving zones of intense flattening and strike-slip movements resulting from a NNW-SSE directed regional compressive stress, then came into effect. This stage is associated with a main cleavage-forming event (S2, F2), which has been interpreted as consisting of regional ENE-trending sinistral strike-slip shear zones that curve westwards into NNW-trending shears (Coward & Daly, 1984; Treloar et al. 1992). Subsequent work by Campbell et al. (1992) and Treloar & Blenkinsop (1995) indicates that there is little evidence for the regional sinistral strike-slip shear zones previously described. Treloar & Blenkinsop (1995)identify a major regional distribution of conjugate sets of dextral ESE- and sinistral NNE- trending shears, shown in figure 2.4, which are suggested as significant features of the geodynamic evolution of the craton. .

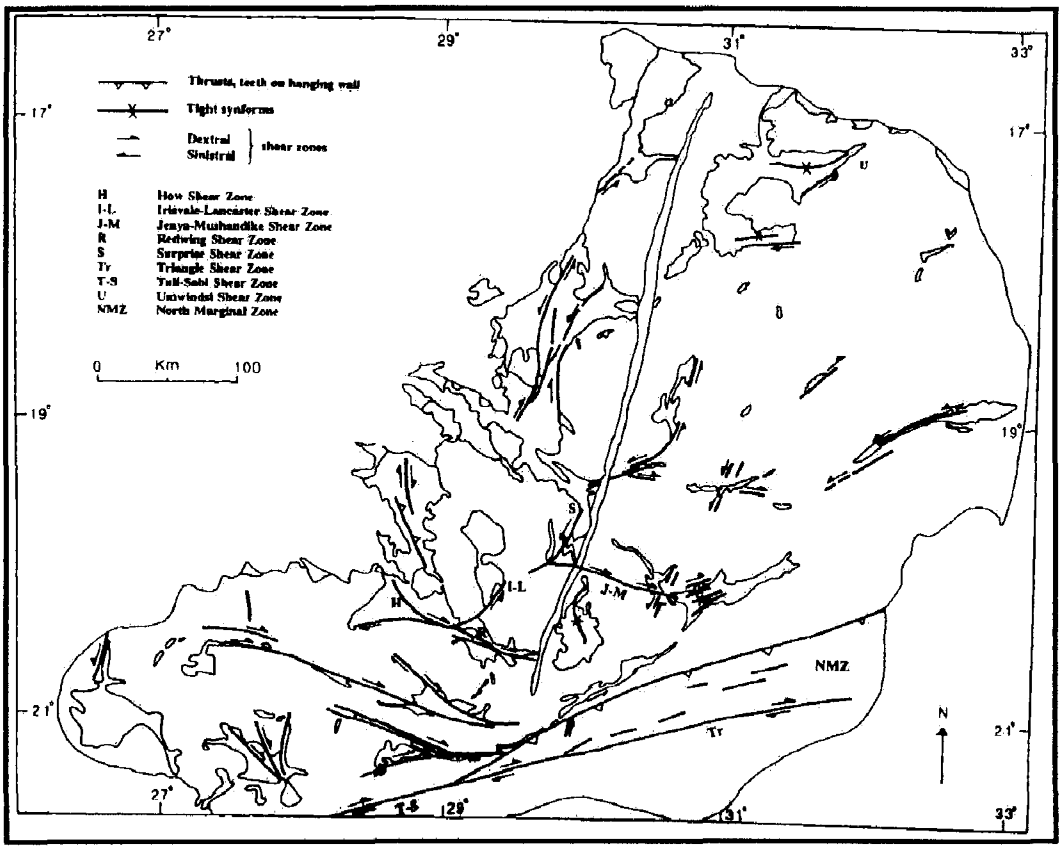

Figure 2.4 : Revised structural map of the Zimbabwe craton showing, in particular, the conjugate ESE-striking dextral and NNE-striking sinistral conjugate shear zones (after Treloar and Blenkinsop, 1995).

2.5 : EVOLUTION OF THE ARCHAEAN ZIMBABWE CRATON

2.5.1 : Craton Formation and Growth

Wilson et al. (1995) found that the occurrence of the oldest (*c.*3.6 Ga) xenocrystic zircons are restricted to the area of the Tokwe segment, suggesting that the protocraton was limited to a small area of southern Zimbabwe. Oceanic crust is therefore likely to have underlain the majority of what is now the Zimbabwe craton during the Early Archaean. There is no evidence of oceanic crust having formed during the Upper Bulawayan greenstone cycles, which have a proven ensialic origin and are probably the finest example of greenstone belts produced entirely on a basement of earlier granite-greenstone terrains. Wilson et al. (op.cit.) suggest that the Upper Bulawayan greenstones were deposited in an intracratonic setting under conditions of extension and rifting, perhaps in response to mantle plume activity. The origin of the Belingwean greenstone cycles is less well established and it is entirely possible that the L1 unit has an oceanic crustal origin.

The diachronous stabilization of the Zimbabwe craton by westward growth of the craton outwards from the Tokwe segment is indicated by progressively younger granitoid plutonism, from the *c.*3500 Ma Tokwe gneisses westwards through the *c.*2800-2900 Ma Chingezi suite to the *c.*2700 Ma Sesombi suite (Wilson et al., 1995). Outward crustal growth from the Tokwe Segment may also have occurred northwards and eastwards.

2.5.2 : Geodynamic evolution of the Limpopo Belt

An understanding of the geodynamic evolution of the Limpopo Belt is essential due to the fundamental role it has played in the tectonic evolution of the Zimbabwe Archaean craton, and in the emplacement of the Great Dyke itself. The Limpopo Belt is a high-grade polymetamorphic and polymetallic terrain extending east-northeast for ~680 km and separating the Kaapvaal and Zimbabwe cratons by over 260 km (Robertson and du Toit, 1981). The belt is divided into three main structural domains: the northern marginal zone (NMZ), the central zone (CZ), and the southern marginal zone (SMZ). In the absence of well defined structural breaks along most of the margins, the northern and southern limits of the belt are delineated by the orthopyroxene isograd, although tectonic and metamorphic elements of the NMZ and SMZ continue well beyond this limit. The eastern extent of the belt is uncertain due to blanketing by Mesozoic rocks, the western extent is thought to die out at about longitude 27°E (Hunter and Pretorius, 1991).

The tectonic history of the CZ extends over most of the Archaean, from *c.*3.8 Ga to *c.*2.6 Ga, and is clearly exotic to the Kaapvaal and Zimbabwe cratons, apparently having been displaced to the SSW with respect to the NMZ and SMZ along the Triangle and Tuli-Sabi shear zones to the north and the Palala-Sunnyside shear zones to the south (Treloar and Blenkinsop, 1995). Remnants of greenstone belt material occur in the NMZ, suggesting a possible correlation with the southern Zimbabwe craton, comparable to the SMZ which is clearly a deformed equivalent of the Kaapvaal craton (Treloar and Blenkinsop, 1995).

The Limpopo Belt has had a long ensialic history culminating in at least one major late-Archaean event. The main phase of orogenic deformation, metamorphism, and granitic magmatism took place between 2700 Ma and 2650 Ma (Rollinson and Blenkinsop, 1995), and involved the convergence of the CZ terrain onto the northern margin of the Kaapvaal craton, shown diagrammatically in figure 2.5a. Main thrusting of the SMZ, which resulted from this collision, shows lineations consistent with SW- or WSW- directed displacement. The timing of deformation and metamorphism is not synchronous across the belt: convergence of the Zimbabwe craton with the Kaapvaal-CZ cratonic pair, and associated NMZ thrusting, is estimated to have taken place *c.*2580 Ma (figure 2.5b), and therefore post-dates the main phase of the Limpopo orogeny by approximately 70 My (Treloar and Blenkinsop, 1995). Evidence of the uplift of NMZ rocks over the craton is observed at the transition between the NMZ and the Zimbabwe craton, best seen in the discrete shear zones occurring in the east. Shear sense criteria in mylonites of a shear zone south of Masvingo show that NMZ granulites were thrust NNW over the craton, with the NMZ estimated to have been horizontally displaced by 27 km and vertically displaced by 25 km (Coward et al., 1976).

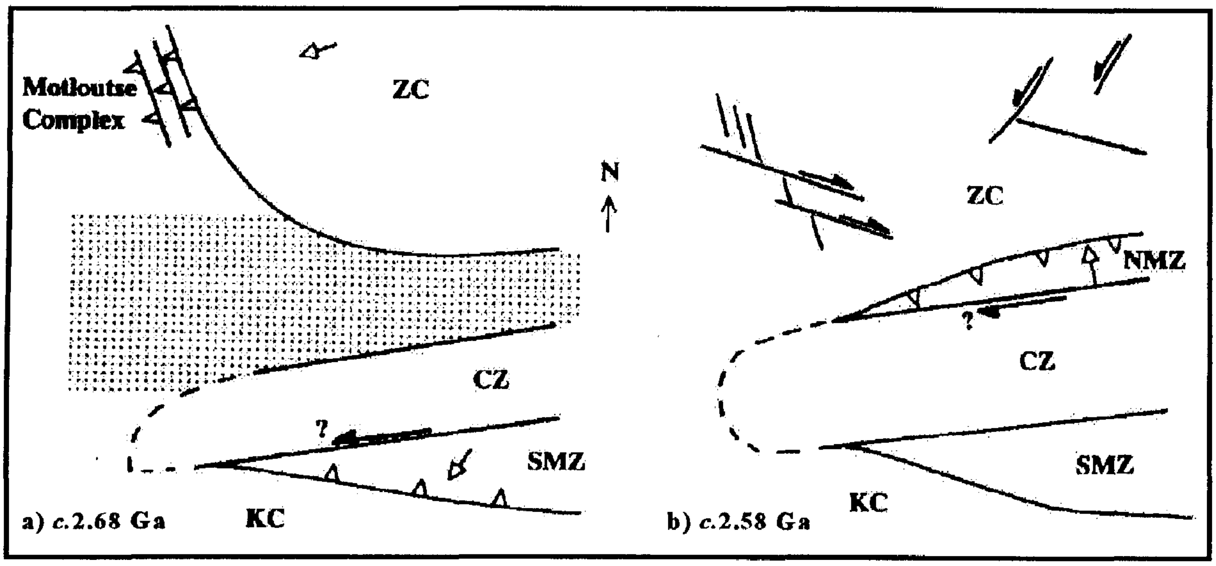

Figure 2.5 : Evolution of the Limpopo Belt. Question marks refer to the uncertainty of timing of the major shearing in the CZ (probably at c.2000 Ma). The shaded areas indicate crust of unknown type which disappeared during convergence at c.2580 Ma. (Modified after Treloar and Blenkinsop, 1995).

2.5.3 : Geodynamic evolution of the Zimbabwe Craton

There have been a number of models of Archaean tectonics in Zimbabwe proposed to explain the observed deformation and structure of the craton. McGregor's (1951) famous 'Gregarious batholith' model was based on the presence of the many ovoidal batholiths in certain areas of the craton and the observed deformation in the intervening greenstone belts. In this model the deformation of the greenstone belts was through density-controlled sagging between domes of granite and granite-gneiss that were emplaced as batholithic diapirs. The model has been largely discredited due to the geographical limitations of the ovoidal batholiths with respect to the greenstone belts, and the complex composite nature of the granite batholiths. There has also been general criticism of diapirism as a significant mechanism of granitoid emplacement, in which thermal modelling predicts that the rising diapirs would suffer a 'thermal death' and lock-up within the middle crust. Some workers have suggested that, although batholithic diapirism is no longer valid, individual pluton diapirism may occur: Snowden (1984) proposed a model for the Chinamora Batholith, whereby pluton diapirism, followed by regional deformation, leads to the formation of a "structural batholith". It is currently favoured that the granitoids of the Zimbabwe craton were generally emplaced by fault-controlled mechanisms (Treloar and Blenkinsop, 1995), although a degree of "balloon diapirism" at emplacement depth may occur, giving rise to the observed 'ovoid' geometry.

A more currently acceptable model is that of intracratonic tectonics, dominated by horizontal displacements (Coward and Daly, 1984). This model was based on the observation of the regional sinistral ENE-trending shears and southwestern NNW structural grain within the craton (see figure 2. 4). It was proposed that the granite-gneiss terrain of the east midlands was displaced to the west-southwest along the ENE shears, with the block bounded to the southwest by the NNW-trending grain which supposedly marked the frontal ramp of a thrust system. Developed as a refinement and extension of this model was the 'Tibetan analogy' model of Treloar et al. (1992). In this model collision between the Kaapvaal-CZ cratonic pair and the Zimbabwe craton the overall NNW-SSE shortening was accommodated by initial crustal thickening followed by the lateral extrusion of blocks of thickened crust along the ENE shear zones, as shown in figure 2.6. The main problem with both of these models is that, as discussed in chapter 2.3, there has been a re-evaluation of the regional importance and validity of the ENE shear zones, the results of which prove that the structural framework on which these models are based is invalid.

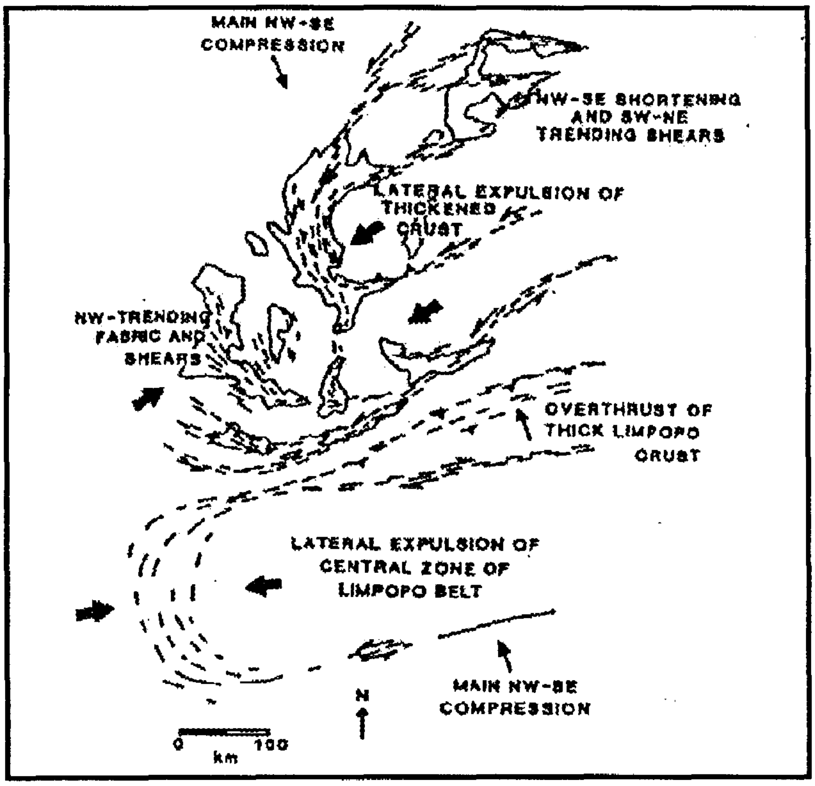

Figure 2.6 : Structural map of the Zimbabwe Archaean craton showing the 'Tibetan Analogy' model for the lateral extrusion of blocks of thickened crust (modified after Treloar and Blenkinsop, 1995).

The revised structural framework by Treloar and Blenkinsop (1995) emphasises the importance of the conjugate dextral ESE- and sinistral NNE- trending shears in the geodynamic evolution of the craton. The development of these shears, and the NNW-shortening fabrics, is inferred to be related to the main deformation event resulting from the *c.*2580 Ma collision with the CZ-Kaapvaal pair, and the major NNW shortening caused by the thrusting of the NMZ onto the southern margin (figure 2. 5b). The earlier collision, at *c.*2680 Ma, of the main Zimbabwe craton and the Motloutse Complex of the Matsitama fragment caused a shortening across the south-western part of the craton, producing the steep NNW-trending fabrics of this region (figure 2.5a). The conjugate shears are suggested by Treloar and Blenkinsop (op.cit) to provide a mechanism for billiard ball tectonics", where rotations and displacements of small crustal blocks and granite bodies take place, relative to each other, in response to regional displacements. It is also suggested that the conjugate shears could be near-surface representations of deep-crustal structures, and that the shears were the locations of granite transport to higher crustal levels. Treloar and Blenkinsop (1995) therefore envisage the late Archaean craton to have consisted of a number of small crustal blocks geometrically defined by the conjugate shears, which also provided a mechanism of granite emplacement. Deformation along the margins of the greenstone belts and adjacent granites were controlled by movements along the conjugate shears . The overall effect of the deformation was one of crustal shortening and thickening, this contributed to the cratonization process that was finalized by Chilimanzi Suite emplacement.

2.6 : PROTEROZOIC COVER SEQUENCES

Proterozoic cover sequences to the Archaean granite-greenstone terrains, post-dating Great Dyke emplacement, are preserved along the eastern margin (Umkondo Group) and north-western margins (Piriwiri, Deweras, and Lomagundi Groups). Deposition of these sequences is likely to have been in response to subsidence along the margins of the craton in the Early Proterozoic, the sediments probably being deposited in marine environments (Cahen and Snelling, 1984). The north-western sequences were involved in the Pan-African thermal event (Hunter and Pretorius, 1981). South of 17° there is little evidence of involvement in Pan-African events. However, discordant results from zircon dating of south-central greenstone material, with low intercepts at 600-500 Ma and 800-900 Ma, may represent Pan-African influence (Wilson et al., 1995).

CHAPTER 3 : OVERVIEW OF THE GREAT DYKE OF ZIMBABWE

3.1 : EMPLACEMENT AND TECTONIC SETTING

3.1.1 : Introduction

The highly elongate nature of the Great Dyke has presented problems to many workers on the Great Dyke. Lightfoot (1927) was the first to suggest the possibility that the dyke was supplied by "several feeders spread along its course". Keep (1930) proposed that the Great Dyke formed within a rift environment, "it (the Great Dyke) owes its present size and shape to a zone of weakness similar to those which determined the courses of the Great Rift Valleys of Central Africa". The correlation of the Great Dyke with a craton-wide fracture-forming event (see chapter 3.2) requires models of dyke emplacement that also account for the fracture pattern and related movements within these fractures.

3.1.2 : Emplacement Models

Whilst it is generally acknowledged that the Great Dyke was emplaced during a period of crustal extension, there have been numerous models proposed to explain the mechanisms involved. These can be broadly divided into those invoking vertical tectonics and those where horizontal tectonics were the principle mechanisms.

3.1.2.1 : *Vertical tectonic models*

The models of Worst (1958) and Bichan (1970) are essentially ones of intracratonic rifting as a result of vertical tectonics. Worst (op. cit.) proposed that the upwelling of underlying magma, along the line of what is now the Great Dyke, resulted in the formation of a "line of weakness". Continued pressure from the magma resulting in the creation of at least four fissures along which the Great Dyke was intruded. Bichan (1970) proposed a four-step model for the formation of the Great Dyke and Outer Satellites. The initial stage was the establishment of a large-scale convection cell beneath the Zimbabwe craton, with upward heat flow towards the Great Dyke region, and downward heat flow along the craton margins. This heat flow, combined with the diapiric emplacement of McGregor's (1951) "gregarious batholiths", resulted in an extensional regime that caused the complete fracturing of the craton along the line of the Great Dyke and two subsidiary fractures, equivalent to the Outer Satellite Dykes. A third stage of magma intrusion into these fractures followed. These events were envisaged to be accompanied by deformation in the orogenic zones of the Limpopo belt and the proto-Zambezi and proto-Moçambique belts. During the fourth stage, a waning of the convection system was followed by graben development and slumping, as suggested by Worst (1958).

Podmore and Wilson (1987) noted the marked lack of symmetry of the craton to the east and west of the Great Dyke, and suggested that a monoclinal flexure about a NNE-trend may have been a feature throughout the cratonic history of Zimbabwe, continuing well into the Phanerozoic. The late Archaean granite-greenstone terrains show distinctly different development from east-west: in the differential development of the Upper Bulawayan and overall greenstone belt distribution (see figure 2.3d) and in the late granites, which are sheet-like in the east. There is also a general absence of Proterozoic and Phanerozoic basins in the east; the overall indications are that in the east of the craton there was greater erosion and uplift.

Hunter and Reid (1987) suggested that many of the Archaean and Proterozoic dyke swarms of South Africa were emplaced along hinge zones of antiformal or monoclinal flexures which may have developed in response to collision and overthrusting of crustal blocks. Podmore and Wilson (1987) proposed that such a flexure in Zimbabwe may have been a major feature in the emplacement of the Great Dyke, and would also provide a mechanism for the dyke to sill transition suggested by the dyke geometry and chemical fractionation of the mafic rocks. However, Hunter and Reid (op.cit.) specifically related the Great Dyke to the *c*.2.8 Ga Usushwana Intrusive Suite as examples of dykes formed in a rifting environment, and suggest that the trumpet-shape of the dykes may have been a consequence of the proximity to a boundary between basement granitic terrain and overlying supracrustal material. Although no supracrustal rocks are preserved in proximity to the Great Dyke, they may well have been developed and subsequently removed by erosion. The concept of a major flexure in Zimbabwe has been questioned by E.R.Morrison (in Lister, 1987) in the light of extensive fieldwork by Lister (op.cit.), which indicated that the high central axis, and differential development to east and west, was mainly due to the relative effects of the Zambezi and Limpopo catchments.

3.1.2.2 : *Horizontal Tectonics*

Barton and Key (1984) suggested that convergence of the Zimbabwe and Kaapvaal cratons across the eastern end of the Limpopo belt, dying out towards the west-southwest, indicates the occurrence of a 15° clockwise rotation of the cratons, relative to each other. They suggest that the Great Dyke fracture was developed as a rift, either in response to, or alternatively causing, this rotation. Katz (1976) also related Great Dyke emplacement to a rotation: in this model, the rotation occurred in reaction to dextral transcurrent movement of the Limpopo Belt, resulting in the emplacement of the Great Dyke under simple shear conditions of orthogonal tension with limited rifting.

Katz's (1976) model was based on the formation of the greenstone belts of the Kaapvaal and Zimbabwe cratons in response to initiation of the Limpopo Belt as a transform zone. Wilson (1981) noted that the NNE trend shown by the Great Dyke has been a feature throughout the Archaean in the Zimbabwe craton, and is particularly evident in the western succession of the Upper Bulawayan Group greenstones. Invoking a similar mechanism to Katz (op.cit.), greenstone belt development was considered a result of intracontinental rifting induced by transcurrent movements along the Limpopo and proto-Zambezi belts. The Great Dyke fracture pattern was described by Wilson (1981) as the result of a final attempt at greenstone belt production, the stabilization of the craton at this stage inhibiting successful greenstone belt formation.

Stowe (1980) identified eight systems of faulting and shear zone development in the Zimbabwe craton during the late Archaean and Proterozoic. Systems A-C are represented by a series of shear zones across the craton in response to overall compression. System D produced dextral wrench faulting in response to conditions of transcurrent shear . Systems A-D, mainly controlled by the Limpopo Belt orogeny, show an overall rotation of the surface maximum compressive stress (σ_1) by 140° during a short time-span between late granite intrusion and formation of the Great Dyke fracture pattern. Stowe (1980) suggests that this rotation of σ_1 is the result of changing external stresses, as opposed to the alternative of clockwise rotation of the craton; this indicates that lateral stresses during the late Archaean were short-lived. Rotation of σ_1 from System D (N75W) back to N14°E, perhaps in response to relaxation of the dextral shear couple in the Limpopo Belt, resulted in overall crustal tension and development of the Great Dyke fracture pattern, essentially consisting of normal faults, although many have a small sinistral component. Wilson (1990) considered many features of Stowe's (op.cit.) rationalization of wrench tectonics in the Zimbabwe craton to be both speculative and unsubstantiated.

Robertson and van Breemen (1970) proposed two potential models for the formation of the Great Dyke fracture system and subsequent dyke emplacement, based on 2-D strike analysis of the Great Dyke and Southern Satellite Dykes. The two models were designed to explain the development of both the NNE Great Dyke pattern and the NNW-trending, which are now correlated with the post-Great Dyke Mashonaland Igneous Event. The models were based on the principles of pure and simple shear (figure 3.1). Bliss and Stidolph (1969) considered that the

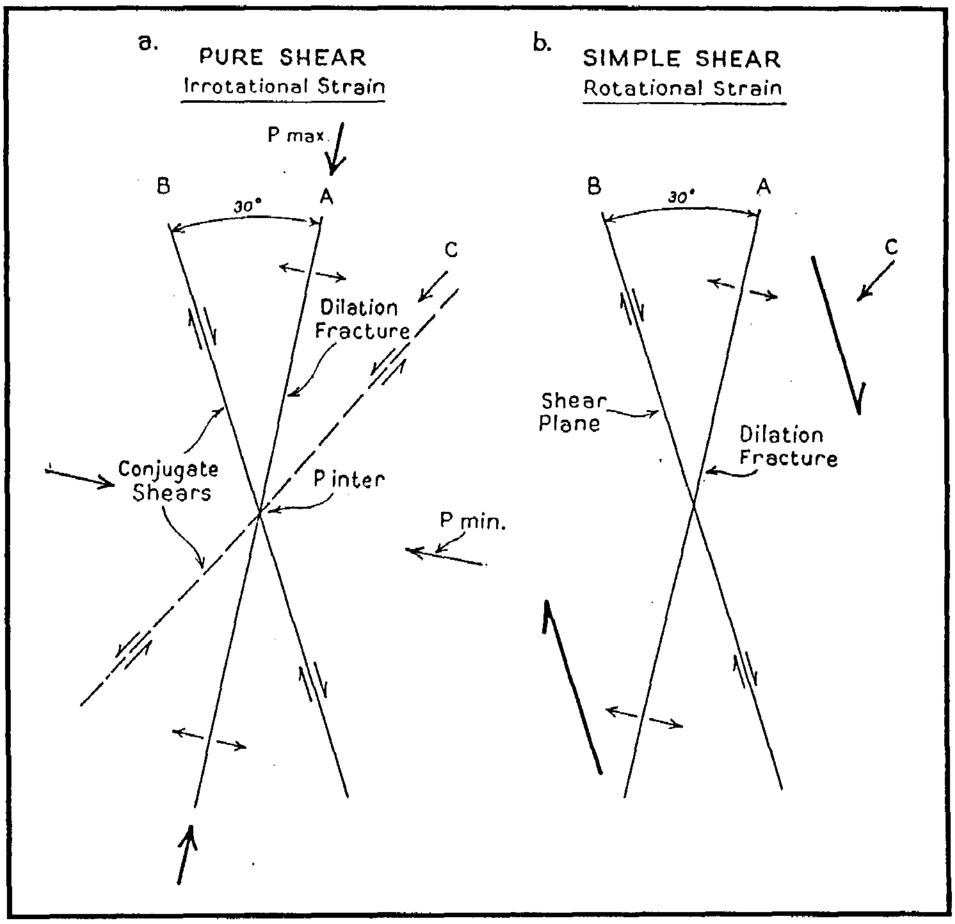

Figure 3.1 : Interpretations of the Southern Satellite fracture pattern as the product of: (a) pure shear, or (b) simple shear. (After Robertson and van Breemen, 1970)

Great Dyke is most likely to occupy a dilation fracture, which Robertson (1973) suggested would explain the overall sigmoidal surface form of the Great Dyke. The simple shear model involved a rotational strain, in which a dilation fracture was developed at a 30° angle to the shear plane (figure 3.1b). In the pure shear model σ_1 was orientated NNE and produced a dilation fracture, with the associated development of a set of conjugate shears (figure 3.1a). Bliss and Stidolph (op.cit.) and Robertson and van Breemen (op.cit.) preferred the simple shear model, as only one shear plane, occupied by the Crystal Springs and Bubi swarms, was developed.

3.1.2.3 : *Simple Shear Model*

The most recent model, developed by Wilson and Prendergast (1989) and Wilson (1990), is based on a pure shear model, similar to that of Robertson and van Breemen (1970), but with several stages of rotation of the stress field. A diagrammatic outline of the model is shown in figure 3.2. The sinistral strike-slip faults of the Great Dyke fracture pattern, including the Popoteke Fault set, were developed in response to NNW-directed maximum compressive stress resulting from the NMZ main deformation event (chapter 2.4). Wilson (1990) attributed the lack of NNE-trending fracture development west of the Umvimeela Dyke to westward decreasing stress. This is supported by the restricted development of discrete shear zones to the east, such as the SE-dipping belt of mylonitic rocks at the NMZ-craton transition to the south of Masvingo (Coward et al., 1976). The Mchingwe Fault set generally follows the WNW direction of D_1 (figure 3.2a) and is thought to have originally developed as sinistral conjugate shears to the Great Dyke fracture pattern.

Subsequent to the initial stage of fault generation, the stress field was rotated with σ_1 parallel to the Great Dyke, creating extension along the NNE Great Dyke fractures (figure 3.2b). Wilson (1990) estimated the overall extension during this stage did not exceed 2 km. This stage resulted in limited rifting and emplacement of the Great Dyke magma, quartz gabbros of the Outer Satellites, and some Popoteke dykes into the dilated fracture system.

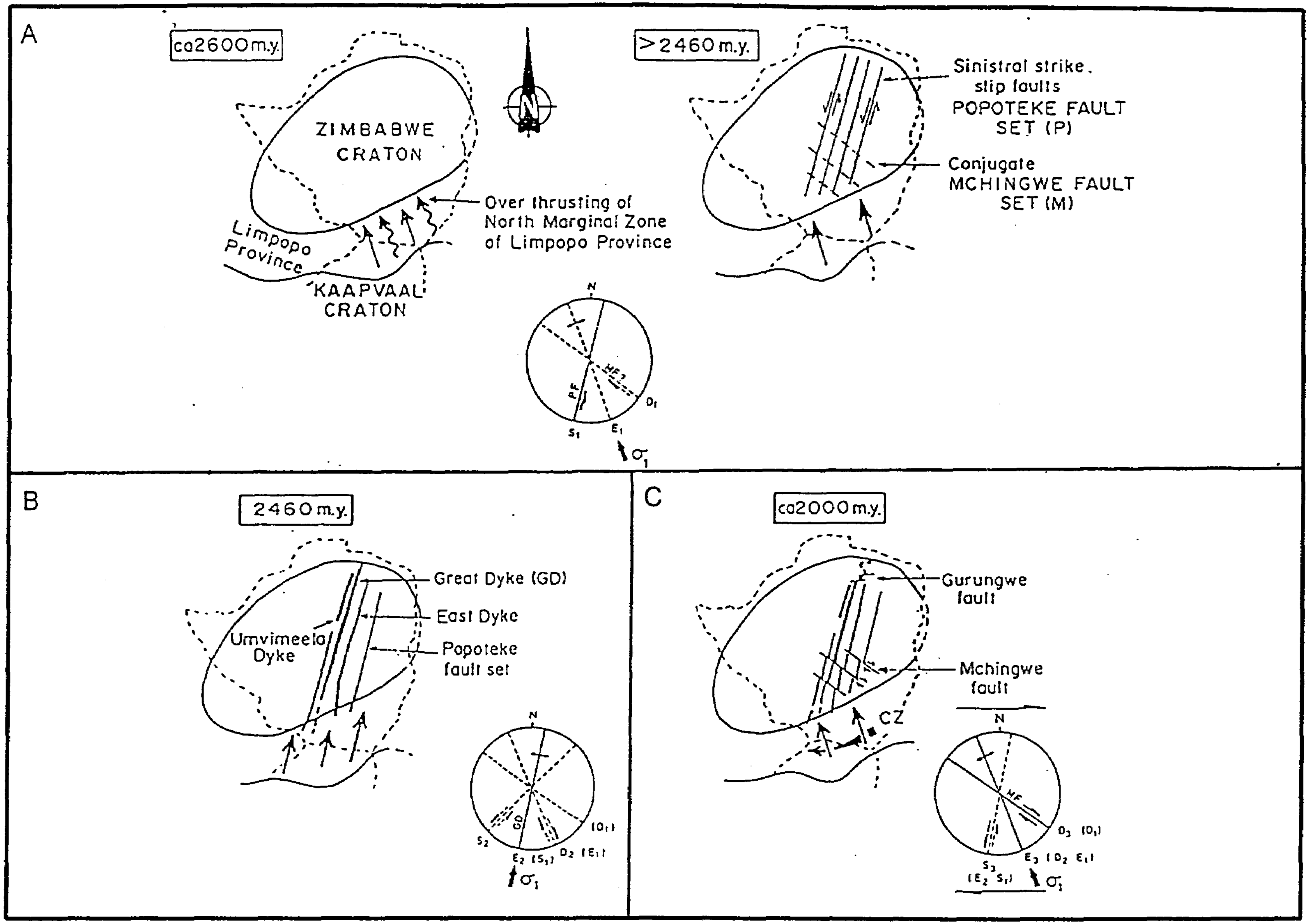

Figure 3.2 : Schematic representation of events leading to emplacement of the Great Dyke: A) Collision of Zimbabwe and Kaapvaal cratons and northward overthrusting of the Northern Marginal Zone of the Limpopo Belt and subsequent development of sinistral strike-slip faults of the Popoteke fault set (P) together with the conjugate Mchingwe fault set (MF); B) rotation of maximum compressive stress causing extensional conditions and emplacenent of Great Dyke and satellites; C) post-Great Dyke reactivation of Mchingwe fault set resulting in dextral movement. (Modified after Wilson and Prendergast, 1989; and Wilson, 1990)

3.1.3. : Post-emplacement Tectonism

3.1.3.1 : *Early brittle deformation*

Prior to the re-activation of the Mchingwe Fault set (see below), small-scale block faulting occurred along the Great Dyke. These are common features along the dyke and occur in an approximate ENE-direction, transverse to the wall-rock contacts. Wilson and Prendergast (1987) note that these are dominantly normal faults, downthrown away from the direction of plunge of the dyke rocks, and suggest that the faulting is probably the result of post-emplacement isostatic adjustments.

3.1.3.2 : *Mashonaland Igneous Event*

A major Proterozoic event at c.2000 Ma, probably related to crustal thickening (Treloar and Blenkinsop, 1995) caused amphibolite-granulite facies metamorphism in the CZ and NMZ of the Limpopo Belt, also causing re-activation of the Tuli-Sabi - Triangle shear zone, resulting in high temperature and pressure conditions associated with dextral strike-slip movements (Kamber at al, 1995). The Mashonaland Igneous Event on the Zimbabwe craton coincides with, and was probably caused by, this event.

The craton-wide Mashonaland Igneous Event involved the emplacement of numerous dolerite sills and dykes. Stress field conditions by this time had rotated back to the NNW-direction σ_1 (figure 3.2c), producing a trend of NNW-trending dyke swarms that generally fill dilation fractures (E_3 in figure 3.2c) with no indication of strike-slip displacement; the exceptions to this are the Crystal and Bubi dyke swarms, which fill strike-slip faults (Wilson, 1990). Palaeomagnetic studies by Jones et al. (1975) showed that the southern half of the Southern Satellite Dykes have undergone complete re-magnetisation in response to a major thermal event. The re-setting shows a swing of palaeomagnetic direction towards Mashonaland dyke directions, and the re-magnetisation is therefore concluded to be in response to the Mashonaland event.

The Great Dyke fracture pattern was affected by the Mashonaland Igneous Event in two ways: the Popoteke Fault set suffered limited sinistral strike-slip displacement in response to the S_3 shear (figure 3.2c); and re-activation of the Mchingwe Fault set, caused by the dextral component of the conjugate shears, D_3, resulted in major dextral displacements of up to 6 km (Gurungwe Fault). The Mchingwe Fault forms a 2 km wide graben in which the Great Dyke is displaced by several hundred metres. Tension gashes, infilled by Mashonaland dolerites, occur along the Mchingwe Fault, and within western branches of the fault, supporting the correlation of the fault set with the Mashonaland Igneous Event (Wilson and Prendergast, 1987).

3.1.3.3 : *Pan-African Deformation*

South of the Zambezi Belt the Great Dyke is relatively undeformed, the most significant brittle deformation being related to the conjugate faults. However, within the belt, the Musengezi Complex has been extensively deformed, giving this region of the dyke it's distinctive 'Snakes Head" morphology (figure 1.1). The Great Dyke in this region is highly faulted, and interdigitates with rocks of the Zambezi Belt. The Outer Satellite Dykes are also deformed in this region: the Umvimeela Dyke is highly faulted, with sheared margins, and has been displaced by approximately 10 km to the east.

A magnetic Mesozoic overprint has been detected in the Umvimeela Dyke that is correlated with the onset of Pan African activity at 1100 Ma (Mushayendebvu *et al.*, 1994). This overprint is best developed towards the Zambezi and Limpopo belts. An additional magnetic overprint introduced at *c.*650 Ma is restricted to the northern deformed section of the dyke within the Zambezi Belt. All available evidence indicates that the major re-orientation of the Musengezi Complex is mainly due to the major E-W dextral movement of the Zambezi Belt during the Pan-African Orogeny, with the major deformation occurring during the later stages, *c.*650 Ma.

3.2 : THE SATELLITE DYKES OF THE GREAT DYKE

3.2.1 : Introduction

Associated with the Great Dyke are a craton-wide set of major faults and dykes that comprise the Great Dyke fracture pattern, all of which trend broadly parallel to the Great Dyke (see figure 1.1). These include the Popoteke fault set, the Outer Satellite Dykes, and the Southern Satellite Dykes.

The Popoteke fault set, which are in places filled with quartz gabbro similar to that of the Outer Satellite Dykes, occur 90 to 100 km to the east of the Great Dyke. The correlation of the Outer Satellite Dykes with the Great Dyke on the basis of structural and petrological relations by Worst (1960) is supported by the palaeomagnetic evidence of Jones et al. (1975) and Mushayendebvu et al. (1994), who identified a primary thermoremanent magnetization direction of approximately 220° for the Great Dyke, Outer Satellite Dykes, and Popoteke gabbro.

3.2.2 : Southern Satellite Dykes

The Southern Satellite Dykes were subdivided by Robertson and van Breemen (1970) into the Outer and Inner Satellite Dykes, the dykes extend over 80 km south of the Great Dyke and cut into rocks of the NMZ in the Limpopo Belt. The Outer Satellite Dykes are the southern extensions of the Umvimeela and East Dykes. The Inner Satellite Dykes were originally taken to comprise the 'Main Swarm', and the Bubi and Crystal Springs dyke swarms were collectively referred to as the 'Narrow Swarms' (Robertson, 1973). However, on the basis of palaeomagnetic and tectonic affinities, the 'Narrow Swarms' are now considered to be a part of the Mashonaland Igneous Event, dated at 1830 Ma (Jones et al., 1976; Wilson et al., 1987).

The Main Satellite *(see footnote overleaf)* comprises 13 sections of varying length, from 100 m to 26 km, which together represent a single discontinuous dyke (Wilson et al., 1987). The dyke was first described by Lightfoot (1927), who reported the occurrence of a 'harzburgite dyke' running parallel and to the south of the Great Dyke. Robertson and Van Breemen (1970) obtained an Rb-Sr age of 2533 ±54 Ma (re-calculated by Cahen and Snelling, 1984) for the Main Satellite which agrees well with that calculated for the Great Dyke (see chapter 1). This age also places a constraint on the main metamorphic event of the NMZ, as the dykes cut the NMZ granulites and are relatively undeformed.

The rock types of the Main Satellite are dark green, poikilitic melanorites and discontinuous layers of olivine websterites with minor plagioclase oikocrysts. The petrology of the Main Satellite rocks correlate well with the more evolved rocks of the ultramafic sequence of the Great Dyke: Wilson (1982) noted the similarity of the discontinuous peridotitic rocks to those found in marginal facies of Cyclic Unit 1 in the Great Dyke.

Contacts of the Main Satellite with the country rock are rarely exposed, although Worst (1956) reports observing a contact on the eastern margin at an inclination of 75°W. The margins of the dyke are often mylonitized and showing near-vertical shearing that is also occasionally developed in the surrounding granites (Worst, 1960). Layering is not common, but where present is sub-vertical and parallel to the dyke margins.

The Main Satellite, at least the Msiningira section, is generally considered to represent a feeder system to a Great Dyke - related body that has since been totally removed by erosion (Lightfoot, 1927; Robertson and Van Breemen, 1970; Wilson, 1996). Robertson and Van Breemen (op.cit.) consider that the lack of a border series in the Main Satellite is evidence of a high flow rate within the dyke, which was supplying magma to the overlying chamber. Wilson and Prendergast (1989) suggest that harzburgite and orthopyroxenite xenoliths found within the dyke represent remnants of earlier layers that were subsequently removed by additional magma input.

A note on Satellite Dyke terminology:
Wilson et al. (1987) suggest that the 'Main Swarm' be re-named the "Main Satellite", thereby inferring (although this is not specified) a new subdivision of the Southern Satellite Dykes into the Main Satellite Dyke and the East and Umvimeela dyke extensions. Robertson and van Breemen's (1970) nomenclature for the Main Swarm is retained in this thesis, but refers to sections, not dykes. The term 'Outer Satellite Dykes', although formally referring only to the southern extensions (Robertson and van Breemen, op.cit.), is coming into usage as a general term for the East and Umvimeela Dykes (Wilson and Prendergast, 1989). The proposed terminology that will be used in this thesis is summarised in the table below:

SOUTHERN SATELLITE DYKES		*OUTER SATELLITE DYKES*	
Main Satellite	*Msiningira, Masase, Dwala, Mkashi, Manyoli, and Sitauzi sections.*	*East Dyke*	*East Dyke*
			East Dyke Extension
Southern Outer Satellites	*East Dyke Extension*	*Umvimeela Dyke*	*Umvimeela Dyke*
	Umvimeela Dyke Extension		*Umvimeela Dyke Extension*

3.2.3 : Outer Satellite Dykes

The Outer Satellite Dykes parallel the Great Dyke for the majority of it's length, and their southern extensions continue south of the dyke into the NMZ of the Limpopo Belt. The Umvimeela Dyke is situated 1-18 km to the west, and the East Dyke 10-24 km to the east, of the Great Dyke. Although generally both the Outer Satellites increase their distance from the Great Dyke towards the south, the East Dyke shows a marked divergence from the Great Dyke trend south of Lalapanzi (figure 1.1): this is described by Wilson and Prendergast (1989) as a feature of the competency contrast of the surrounding rocks with the ancient Tokwe Segment (see chapter 2.2).

Limited outcrop and poorly exposed dyke margins, particularly in the East Dyke, necessitate general information on dyke orientation and thickness to be established by aeromagnetic modelling. Both dykes are revealed by aeromagnetic surveys and space shuttle imagery to be persistent features (Wilson, 1996). Mushayendebvu (1995) reports varying thicknesses for the dykes, with an average of 200 m for the Umvimeela and 100 m for the East Dyke. North of latitude 20.5°S, the Umvimeela Dyke dips towards the Great Dyke at a mean of 84°, whereas the East Dyke dips away from the Great Dyke at a mean of 89°. South of 20.5°S, there is a distinct shallowing in the mean dips of the Outer Satellite Dykes, which is interpreted to represent a 10° vertical tilting of the craton adjacent to the Limpopo Belt (Mushayendebvu, op.cit.). This tilting occurs over 100 km width, with the axis of the rotation parallel to the Limpopo Belt. The northern extent may be limited by the Mchingwe Fault set. These findings have yet to be correlated with any observed features in the region, but the tilting is most likely to be related to the *c.*2000 Ma Limpopo event (see chapter 2.5). The Outer Satellite Dykes are relatively undeformed to the south of the Gurungwe Fault, although they are affected by cross-cutting faults. Within the Zambezi belt, however, where the dykes parallel the southern part of the Musengezi Complex, the dykes are highly faulted and sheared.

The rocks of the Outer Satellite Dykes are essentially quartz gabbros and gabbronorites exhibiting varying degrees of hydrothermal alteration; intergrowths of K-feldspar and quartz occur, and plagioclase and pyroxene grains are commonly zoned (Wilson and Prendergast, 1989). The increasing degree of alteration towards the margins (Worst, 1958), and the textural features and variable compositions of the rocks are indicative of extensive localized contamination by the granitic wall rocks. The effects of contact metamorphism extend about 10 m into the country-rock granites (Wilson, 1968). Robertson (1973) reported that the Southern Outer Satellites are less altered than the main dykes, and relates this feature to their intrusion into relatively water-poor granulite facies rocks. In the deformed northern end of the Umvimeela Dyke the gabbros are locally extensively altered, with pervasive uralitization and saussuritization (Mushayendebvu et al., 1994).

An offshoot of the East Dyke, northwest of Masvingo, discovered by Wilson (1968) and described as an 'intrusion breccia" containing fragments of quartz and granite, has a fine-grained matrix that is considered to be a chill phase. The matrix is an olivine basalt, consisting of microphenocrysts of high-Mg olivine and orthopyroxene, set in a groundmass of plagioclase laths enclosed by clinopyroxene oikocrysts. This is considered to be the most likely representative of the primary magma of the Great Dyke suite and is discussed in chapter 8.

3.3 : INTERNAL STRUCTURE

3.3.1 : Introduction

Early workers were of divided opinion about the structure of the Great Dyke, it being variously described as a dyke, a gently dipping sheet, and an elongated laccolith (Lightfoot, 1926). However, Lightfoot (1927) stated that whilst "geologists in this country have accepted a dyke origin...it can by no means be conclusively proved to the satisfaction of others". Hess (1950) proposed that the mafic portion of the Great Dyke may have extended as a large sill-like body "perhaps 3000 feet thick for sixty miles or more on either side of the present dyke". Figure 3.3 shows Hess' (op.cit.) suggestion for the transverse structure of the dyke and the subsequent erosion of the mafic portion, with down-warping of the dyke in response to isostatic adjustment. Worst (1960) considered that the Great Dyke was not a true dyke and rather occupied four elongate laccoliths, each with a 'boat-like' longitudinal structure. The transverse section of the Great Dyke was seen as a circular synclinal structure, with dyke-like feeders restricted to the central regions of the four complexes (see figure 3.8).

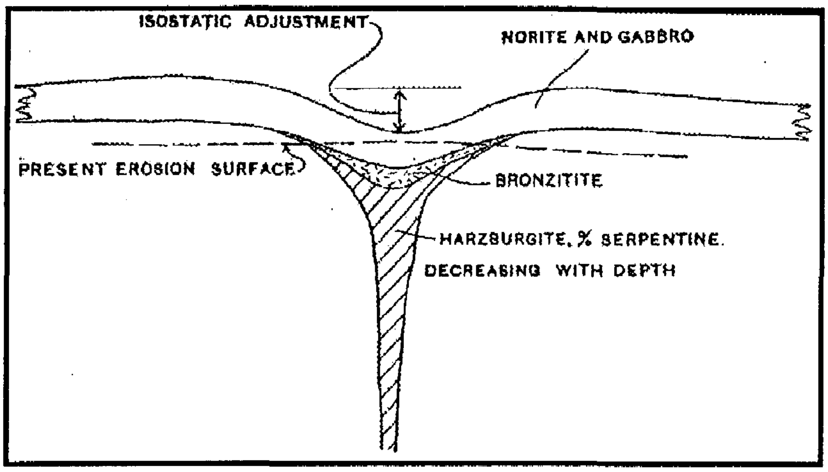

Figure 3.3 : Transverse section showing the initial form of the Great Dyke as proposed by Hess (1950). Synclinal attitude of the layering is attributed mainly to post-emplacement isostatic adjustment. Note the sill-like extensions of the Mafic Sequence. (After Hess, 1950)

3.3.2 : Structure of the Great Dyke

The bulk of information on the transverse structure of the Great Dyke comes from gravity surveys, which have been carried out by Weiss (1940), Podmore (1970), and Podmore and Wilson (1987). The main feature of the gravity profiles is a characteristic bell-shaped Bouger anomaly across the width of the dyke. The most recent data, reported in Podmore and Wilson (op.cit.), was the product of 18 traverses across the Great Dyke, covering most of the dyke's length south of the Musengezi Complex. A selection of the traverses are shown in figure 3.4: traverses 2 and 5 are from the South Chamber, and traverses 10, 11, 16, 17, and 19 are from the North Chamber. The study identified several major features:

1) A 1 km wide dyke-like structure exists at depths of between 3 and 10 km along most of the Great Dyke (figure 3.4, traverse 16) The axial feeder may have been wider in the centres of the Selukwe and Wedza Subchambers, presumably representing area where the volume of magma discharge was highest. The existence of a deep structure beneath the Great Dyke was identified by Weiss (1940), who suggested that the Great Dyke would be better

termed the "Great Abyssolith".

2) The cross section of the Great Dyke suggests a V or Y-shaped chamber, with fairly shallow dipping walls that steepen at depth, becoming sub-vertical in the feeder zone. The inward dip of the dyke walls at the present erosion level agrees well with the dips suggested by gravimetric modelling: the wall rocks of the dyke at surface generally dip towards the dyke axis at 20-35° although steeper dips have been reported, such as an inward-dipping contact at 45° in the Shurugwi area reported by Murahwi (1995).

3) The greatest magnitude of the Great Dyke is in the central regions of the North and South Chambers, where mafic remnants are preserved. An important observation is that these areas coincide with the few regions where the dyke in close proximity to, or intrusive into, greenstone belts: this suggests a potential correlation of contrasting country rock competency with the greater transverse development of the Great Dyke in these regions. It seems probable that greater extension of the initial dilation fracture and/or greater ease of magma emplacement occurred in areas of greenstone belt development.

4) There is a marked asymmetry of many profiles, such as shown in figure 3.4 (traverse 17), which may be explained by a tilting of the Great Dyke. The apparent tilting to the west in the North Chamber would be important to the evolution of the Chamber, and lends support to the theory of uplift of the craton to the east (see chapter 3.1).

5) The presence of a lower chamber to the Great Dyke is suggested at ~5 km depth by at least four of the profiles (see figure 3.4, traverse 19): this chamber is up to 2.5 km wide and is parallel to the dyke.

6) The profile at Lalapanzi is much shallower than anywhere else in the Great Dyke (figure 3.4, traverse 9), and is suggestive of a major structural break in the dyke; this is supported by stratigraphic evidence and is the basis of the subdivision by Wilson and Prendergast (1989) of the Great Dyke into North and South Chambers.

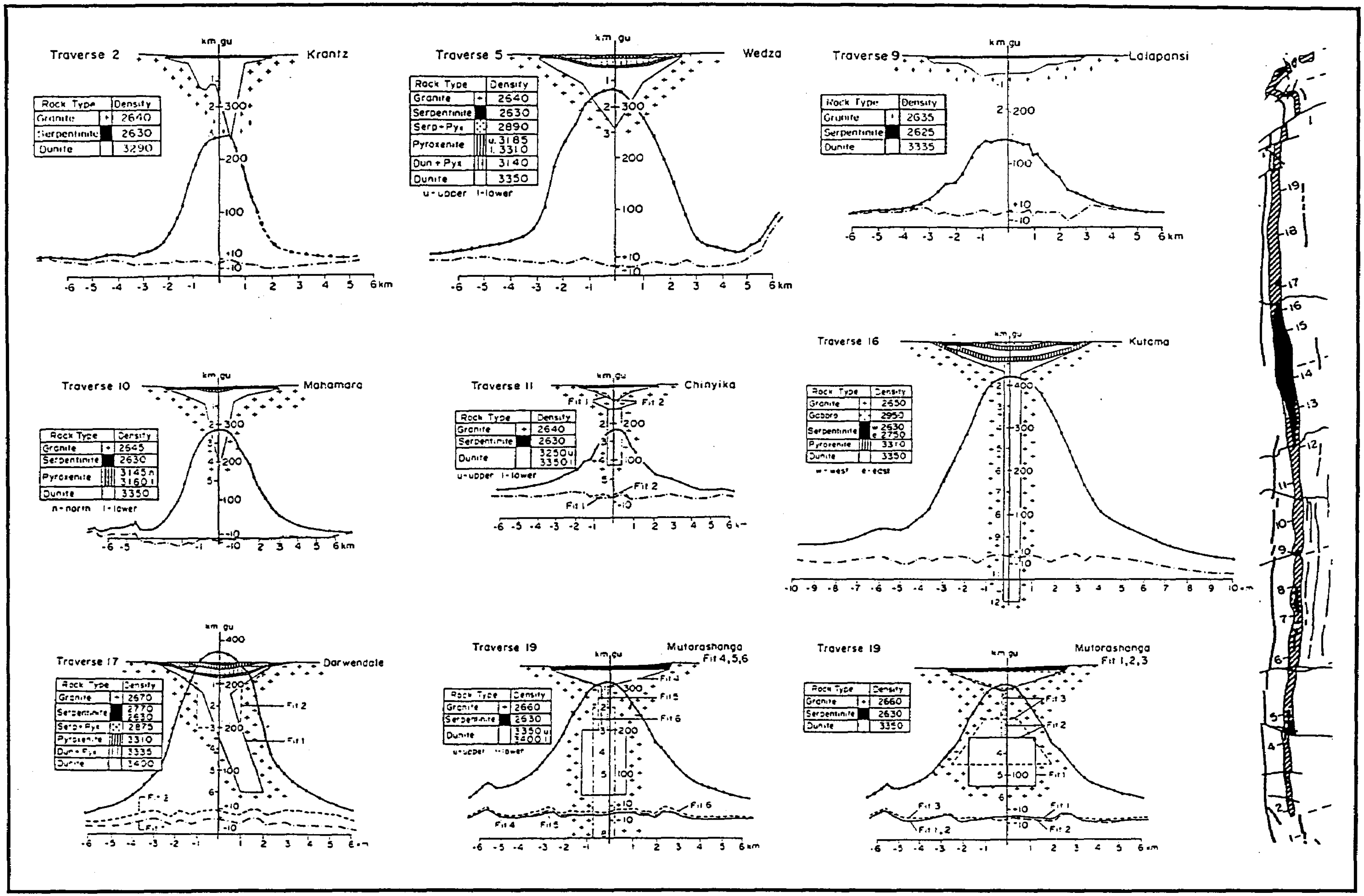

Figure 3.4 : Bouguer gravity anomalies (heavy line) and modelled profiles of selected traverses along the Great Dyke. Rock densities (kg/m^3) used in the modelling are given for each profile. The residual background is shown by a broken line relative to the **0** gu line for each profile. Where appropriate, several possible fits are given. Locations of traverses are given in the Great Dyke map on the right. (Modified after Podmore and Wilson, 1987)

7) The subdivision of the Hartley Complex into Sebakwe and Darwendale Subchambers was proposed by Podmore and Wilson (1987) due to the overall shallower profiles in the Sebakwe area (figure 3.4, traverses 10-11). This is supported by stratigraphic differences below Cyclic Unit 2 (see chapter 3.4) and the more evolved orthopyroxene compositions in the Sebakwe area.

The overall structure of the Great Dyke indicates that whilst the upper portions have a broadly 'lopolithic' structure, similar to that described by Worst (1960), the layered sequence is likely to pass into a true dyke at depth. Wilson and Prendergast (1989) constructed figure 3.5 using the gravity traverses of Podmore and Wilson (1987) to show the relative volumes of the Great Dyke chambers: it is clear that the North Chamber, particularly in the Darwendale Subchamber, is of significantly greater volume than the South Chamber. This suggests a north to south increase in magma input, and opens the possibility that the dyke-like feeders themselves were fed mainly from the north. It should also be noted that the positions of mafic remnants are correlated with the maximum transverse area within in the chambers.

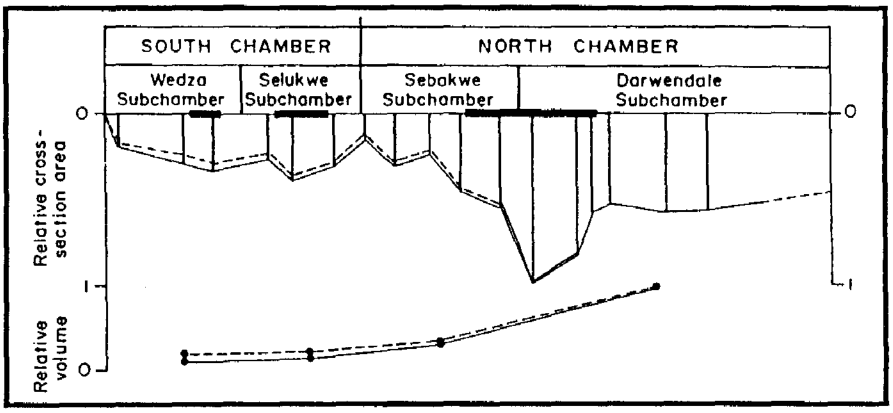

Figure 3.5 : Relative cross-sectional area for eighteen gravity traverses (positions identified by vertical lines) across the Great Dyke relative to the section with the greatest area (southern Darwendale Subchamber). The relative volumes for each of the subchambers are shown in the lower part of the diagram; solid lines represent volumes calculated to account for elevation differences in the depth of erosion between the north and south ends of the Great Dyke, dashed lines show uncorrected variations. (After Wilson, 1996)

Extraction modelling based on pyroxene geochemistry by Podmore and Wilson (1987) indicates the original transverse shape of the magma chamber at upper levels to be sill-like, extending up to 10 km across either side of the dyke. Figure 3.6 shows the results of these studies: whilst the shape of the Lower Mafic Unit was considered realistic, extending upwards and outwards from the"trumpet shape" of the Great Dyke at its current erosion level, the predicted shapes of the Middle and Upper Mafic units are unlikely to be representative, due to the uncertainties associated with emplacement and subsequent mixing of a new magma input at the level of the Middle Mafic Unit (see chapter 8).

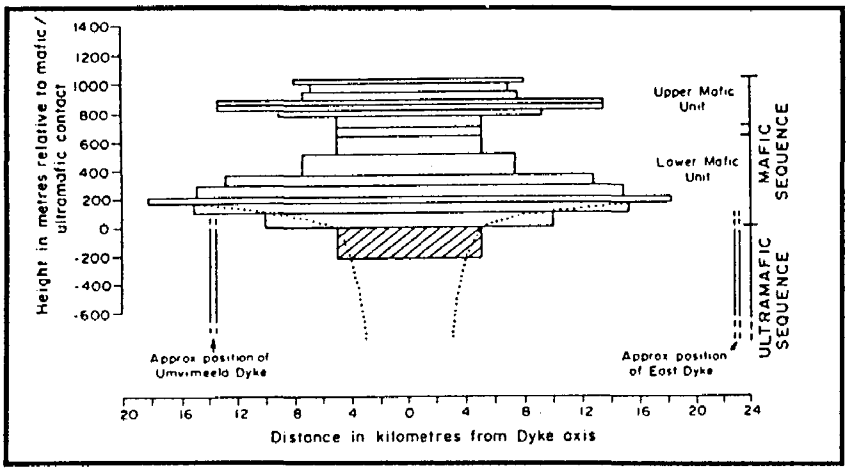

Figure 3.6 : Block diagrams for incremental 10% (volume) extractions showing relative height-width for the mafic sequence. The irregular upper modelled shape for the Middle and Upper Mafic Units is probably not a correct representation (see text for discussion). The shaded block represents Unit 1 of the Ultramafic Sequence. There is a 10-fold vertical exaggeration. (After Podmore and Wilson, 1987)

3.3.3 : Layering features

Wilson (1996) reported that layering is essentially planar with a constant dip inwards towards the axis, where there is a general flattening of the layers (see figure 3.7). Towards the margins there is a small decrease in dip and thinning of individual layers, and the layering is thought to lie at a progressively lower height above the inward sloping walls of the Great Dyke, finally merging with the steep Border Group layers.

The boat-like structure of the layering is attributed to varying combinations of primary and secondary features. Layering plunges slightly unevenly at 3-5° from the ends of the chambers: the southward plunge in the Darwendale Subchamber and the northward plunge in the Sebakwe Subchamber has lead to the preservation of the mafic sequence to the south of Darwendale Dam. The boat-like structure of the subchambers is suggested by Worst (1960) to be the result of subsidence of the floor of the chambers, which lead to the development of a complex graben. Subsidence was centred on the areas of greatest volume near the proposed feeder sites. The primary layering was considered the to have been sub-horizontal, with deformation related to subsequent down-faulting within the graben.

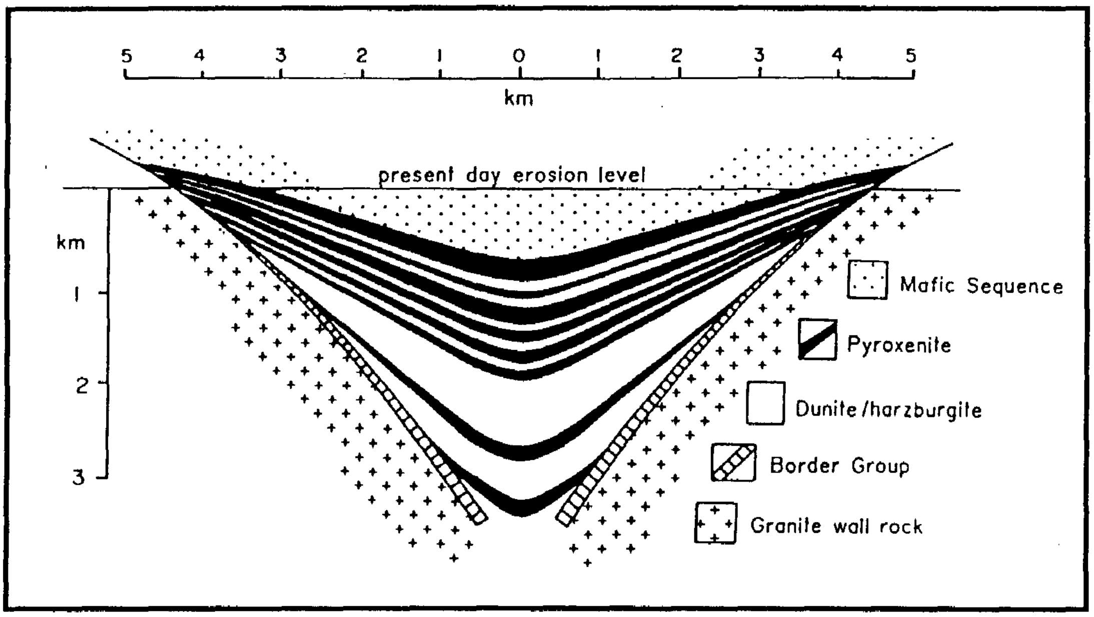

Figure 3.7 : Transverse section of the layered sequence of the Great Dyke in the Darwendale Subchamber. Note the small angular decrease and progressive thinning towards the margins. (After Wilson, 1996)

Podmore and Wilson (1987) noted that the positive anomaly of the Great Dyke is situated within a wider area of a shallow gravity low, and suggested that this may be the result of depression of the relatively lighter, more rigid granite country rocks in response to crustal loading by the overlying (and now eroded) upper portions of the Great Dyke magma chamber. Prendergast (1988) proposed that syn-depositional compaction of the axial cumulus layers would have contributed to development of the boat-like structure. It is currently accepted that the transverse shape is essentially primary, but may have been exaggerated by later subsidence (Prendergast, 1991; Wilson, 1992). The thinning of layers towards the marginal regions is suggested by Wilson (1996) to be the result of crystallization from a relatively smaller vertical column of magma with a higher cooling rate caused by proximity to the country rocks.

3.4 : STRATIGRAPHY

The major stratigraphic division of the Great Dyke is into the Ultramafic Sequence and the overlying Mafic Sequence. Wilson and Prendergast (1989) suggested the subdivision of the Ultramafic Sequence into an upper Bronzitite Succession (re-named Pyroxenite Succession - Wilson, 1996) and a lower Dunite Succession, based on the dominant lithologies within the cyclic units. There are broad stratigraphic similarities between the individual Subchambers of the Great Dyke that permit the development of a unitary stratigraphic framework; however, several fundamental differences in the extent and style of lithological development exist, which require an element of flexibility in the stratigraphic system.

Several attempts have been made to establish a systematic stratigraphy of the Great Dyke. Worst (1958) proposed that pyroxenite and chromitite layers be independently numbered downwards from the top of the Ultramafic Sequence. Hughes (1970) recognised that the stratigraphy should reflect the cyclicity of the lithologies and the order of crystallization, and proposed a similar system to Jackson (1970), where the stratigraphy is divided into cyclic units numbered from the base upwards. This numbering system is not well-suited to the Great Dyke stratigraphy, as only the uppermost Ultramafic Sequence and the mafic rocks are continuous along the length of the dyke. In this system cyclic units would therefore be assigned a different number within each of the subchambers. The limited exposure of basal lithologies in most regions of the dyke would also be problematic. Bichan (1969) suggested that the cyclic units should be numbered downwards from the Mafic Sequence: this is not easily applicable, since the mafic rocks are only well-developed along a relatively small portion of the dyke's length, and the designation of the entire Mafic Sequence to Unit 1 is an over-simplification.

The modern stratigraphic framework of the Great Dyke was largely developed by Wilson (1982) and Wilson and Prendergast (1989) and allows for considerable refinement as new stratigraphic detail is acquired. Essential elements of the stratigraphic framework can be seen in figure 3.8, and are described on the following page:

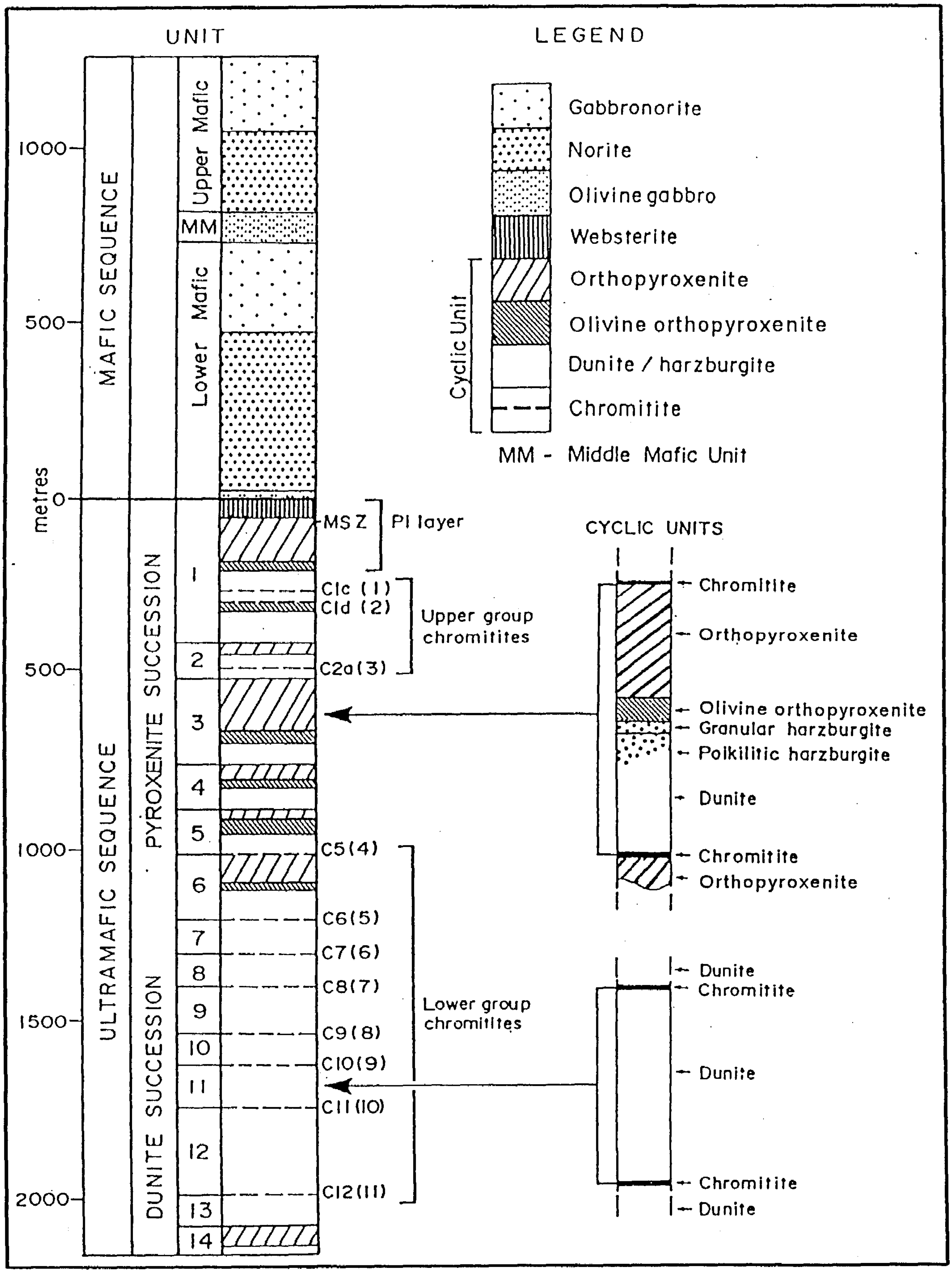

Figure 3.8 : Major stratigraphic subdivision of the Mafic and Ultramafic Sequence of the Great Dyke in the Darwendale Subchamber. Detail of ideal cyclic units of the Pyroxenite and Dunite Successions is shown. (Modified after Prendergast and Wilson, 1989; and Wilson and Tredoux, 1990)

a) Cyclic units of the Ultramafic Sequence are numbered from the Mafic-Ultramafic contact downwards, which allows for the differing stratigraphy between subchambers.

b) Each cyclic unit is subdividable into subunits, labelled alphabetically in lower case (e.g. CU1b). Subunit nomenclature is applied to individual layers, such as chromitite layers C1a to C1e.

c) Individually mappable layers are labelled according to the cyclic unit number, for example P3 is the pyroxenite layer from CU3, and C5 is the main chromitite seam from CU5. Within the current study, the use of the informal S designation is applied to serpentinized dunite layers, e.g. S3 layer (from CU3).

d) An informal further subdivision of mappable layers can be made, as in the case of the P1 layer (see *Cyclic Unit 1*, this chapter) into subunits (e.g.SU1) and sublayers (e.g.SL1b).

3.4.1 : Ultramafic Sequence

Although each of the subchambers differs in detailed stratigraphy, there is a broad similarity of lithotypes and textural characteristics within the Great Dyke. The sequence as a whole consists essentially of dunites, orthopyroxenites, and peridotites intermediate between the two extremes. Texturally, the lower layers of the Ultramafic sequence are generally coarse-grained adcumulates, whereas in the upper parts of the sequence, and in the smaller subchambers, the rocks tend to be finer-grained and of a more orthocumulate nature. The ideal cyclic unit in the Ultramafic Sequence consists of a basal chromitite overlain by dunite, which grades through harzburgite and olivine pyroxenite into an uppermost orthopyroxenite; however, as shown in figure 3.8, the cyclic units show differential development in the Pyroxenite and Dunite successions.

The cyclic units of the Dunite Succession generally consist of a basal chromitite overlain by dunite, with no upper pyroxenite layer, although poikilitic harzburgite is locally developed in some units. The exception to this in the Darwendale Subchamber is the lowermost CU14 which consists of a dunite-harzburgite that grades into a orthopyroxenite layer. At the base of CU14 is the Basal Unit, a 2-5 m thick norite, in which orthopyroxene laths are subpoikilitically enclosed by plagioclase (Wilson, 1982).

The cyclic units of the Pyroxenite Succession are generally well-developed, although there is usually some deviation from the ideal sequence. Major basal chromitites are not always present in all the cyclic units, in which case the base of the unit is defined by dunite. Although the division of the Pyroxenite Succession into cyclic units is made on the basis of mappable lithological change, the chemical base of the cyclic units is shown by geochemical reversals to be within the pyroxenite of the underlying cyclic unit (Wilson, 1982). The basal chromitite of cyclic units within the Dunite Succession is broadly equivalent to the location of the chemical boundary.

3.4.1.1 : *Chromitite stratigraphy*

The chromitites of the Great Dyke are informally divided into the Upper Group Chromitites (UGC) and the Lower Group Chromitites (LGC) (Prendergast and Wilson, 1989). The LGC occur within the Dunite Succession, with the exception of chromitite C5 which is the only well-developed and continuous chromitite layer in the lower Pyroxenite Succession. The LGC are generally more poorly developed and less numerous in the smaller subchambers. The group is best developed in the Darwendale Subchamber where the LGC comprise 8 main chromitite layers, generally consisting of thin layers (<20 cm) of massive coarse-grained chromite. There are numerous additional minor chromitites and chromite concentrations, often occurring 1 to 1.5 m above the main chromitite (Wilson, 1996).

Located within the upper part of the Pyroxenite Succession, the 6 UGC layers are, at 1-2 m thick, considerably thicker and more disseminated than the LGC, generally occurring as composite layers of thin chromitites separated by harzburgite. The UGC contain up to 20% post-cumulus phases, relatively high compared to the less than 5% generally present within the LGC (Wilson, 1982). Nodular textures are characteristic of the UGC, the 1-3 cm wide nodules being the weathered expression of reaction orthopyroxene poikilitically enclosing fine-grained chromite. Nodular chromitite is interlayered with massive chromitite on a centimetre scale. Unlike the LGC, the main chromitites of the UGC, C1c and C1d, can be correlated between all subchambers. Thin chromitite lenses occur at the level of the mafic-ultramafic contact in the South Chamber, representing the highest stratigraphic occurrence of chromitites in the Great Dyke.

3.4.1.2 : *Cyclic Unit 1*

The best example of a cyclic unit in the Ultramafic Sequence is CU1. This is the most lithologically complete and complex cyclic unit, and is also the most intensely studied and well-understood, partly due to its good outcrop in many areas, but mainly due to the presence of economic PGE-mineralization in the upper P1 layer. Within the Darwendale Subchamber, pyroxenites of varying modal, textural, and mineralogical characteristics dominate the ~420 m thick unit. The pyroxenites are much finer-grained than the very coarse varieties found lower in the succession and are less adcumulate, with up to 15% post-cumulus phases.

CU1 is subdivided into 6 sublayers, CU1a-f, on the basis of lithological variation and chromitite occurrences. Figure 3.9B shows the ideal development of CU1 in the Darwendale Subchamber. The lowermost silicate lithology of each sublayer, excluding CU1a, is a poikilitic harzburgite that grades upwards into granular harzburgite. CU1b and CU1e grade upwards from the granular harzburgite into olivine pyroxenite, whereas CU1c, d, and f show a reversal back to poikilitic harzburgite (Wilson and Prendergast, 1989). CU1b contains 150 m of orthopyroxenite, the upper limit of which is marked by a reversal to olivine pyroxenite, representing the basal layer of CU1a. The uppermost layer of CU1a is the Main Websterite, which marks the introduction of clinopyroxene into the cumulus assemblage. The highly continuous nature of the stratigraphy along the Great Dyke at this level is seen in chromitite C1e. This is a 2-3 cm thick chromite concentration that is persistent over a distance of at least 185 km within the North Chamber (Prendergast and Wilson, 1989)

Between the basal olivine pyroxenite and the Main Websterite layer is an orthopyroxenite, which, combined with that of CU1b, forms the P1 layer. The P1 is host to the PGE-mineralization in the Great Dyke, which is largely contained within two sulphide-rich zones (see figure 3.9): the sub-economic Lower Sulphide Zone (LSZ), and the economically important Main Sulphide Zone (MSZ). The MSZ is generally situated 10-35 m below the Main Websterite layer, and the LSZ occurs 35-60 metres below the Main Websterite (Wilson and Prendergast, 1989). A characteristic lithological variety within the P1 layer is the so-called "Potato Reef": a nodular orthopyroxenite that weathers to form rounded cobbles. There is a sharp contact of the Ultramafic Sequence with the Mafic Sequence. A semi-discordant pegmatoid, containing blebs of non - PGE-bearing sulphides, is commonly developed above the Main Websterite layer at this contact.

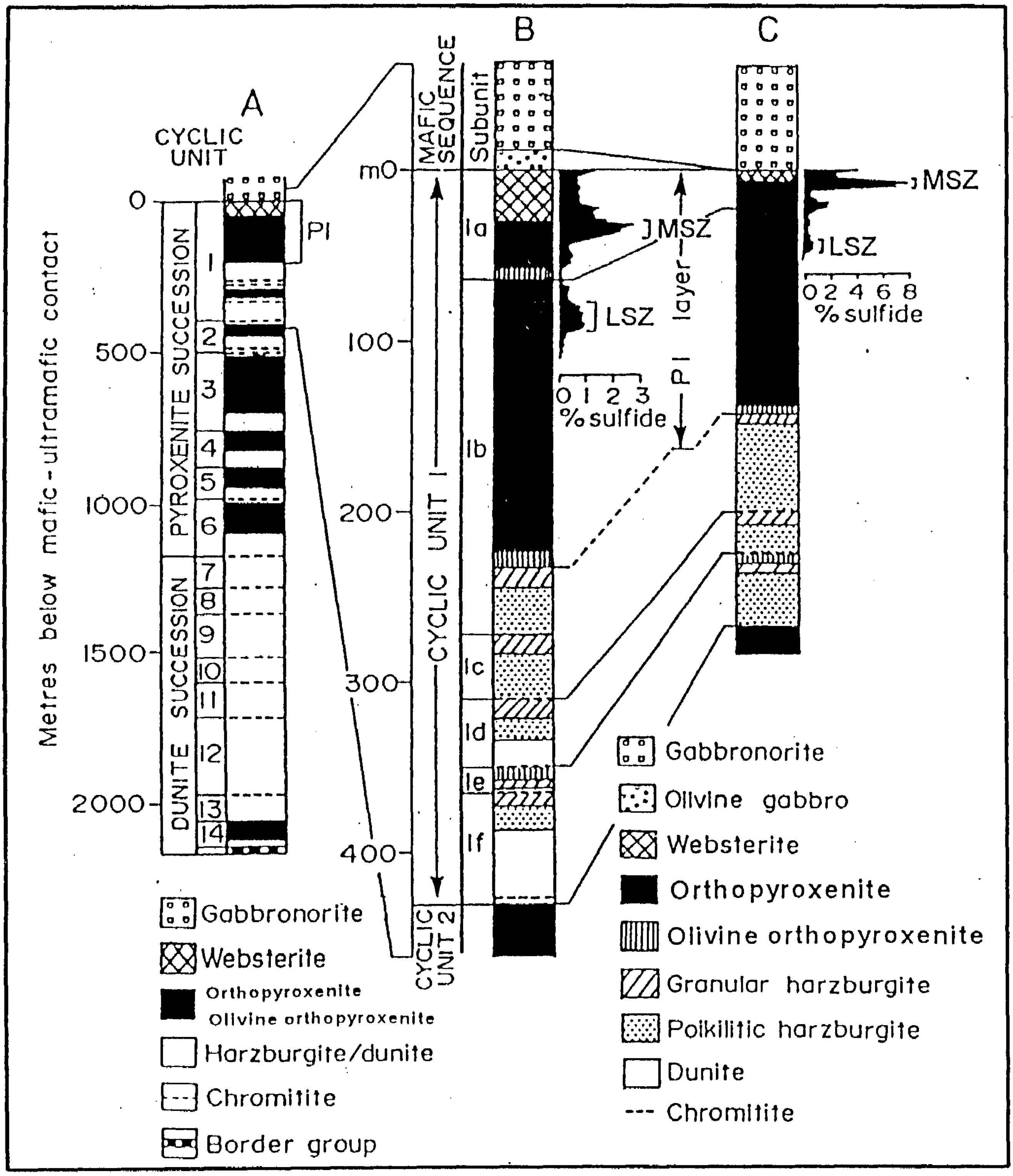

Figure 3.9 : Stratigraphic subdivision and correlation of axial (B) and marginal (C) facies of Cyclic Unit 1 of the Ultramafic Sequence in the Darwendale Subchamber. Note the overall thinning of the P1 layer and the increased sulphide concentration of the MSZ in the marginal facies. (Modified after Wilson and Tredoux, 1990)

The P1 layer exhibits a high degree of vertical and lateral variability in the Wedza Subchamber. In this subchamber, the P1 layer is subdivided into 3 subunits (SU#), on the basis of pyroxene compositions, mineralogical and textural variation, bulk sulphide content, and precious and base metal contents (Prendergast, 1990). The top subunit, SU1, is divided into two sublayers: SL1b is at the base, and includes the MSZ; SL1a contains the Main Websterite layer, often with lenses of mafic lithologies.

3.4.2 : Stratigraphic variation between Chambers

Above CU2, the North and South Chambers are very similarly developed, with strong continuity of individual layers along the length of the dyke. This supports geophysical evidence that a structural break at Lalapanzi separated the North and South Chambers, and the proposal that the dyke formed one continuous chamber from CU1 crystallization onwards. Minor differences between subchambers above CU2 are largely related to differences arising from the size and shape of the subchambers. Below CU1, however, the Ultramafic Sequence in the South Chamber differs from the north in several fundamental ways:

1) The Pyroxenite Succession is much thicker in the North Chamber, and consists of a few thick cyclic units, as opposed to the numerous thin cyclic units in the South Chamber, shown in figure 3.10.

2) Within the Pyroxenite Succession of the South Chamber, the base of each cyclic unit is generally represented by poikilitic harzburgite, whereas dunites are the common basal lithology in the North.

3) In the South Chamber, olivine orthopyroxenite is commonly the most evolved lithology in the Pyroxenite Succession.

4) The Dunite succession is not well-known from the south, although deep boreholes indicate development at depth (Wilson, 1996).

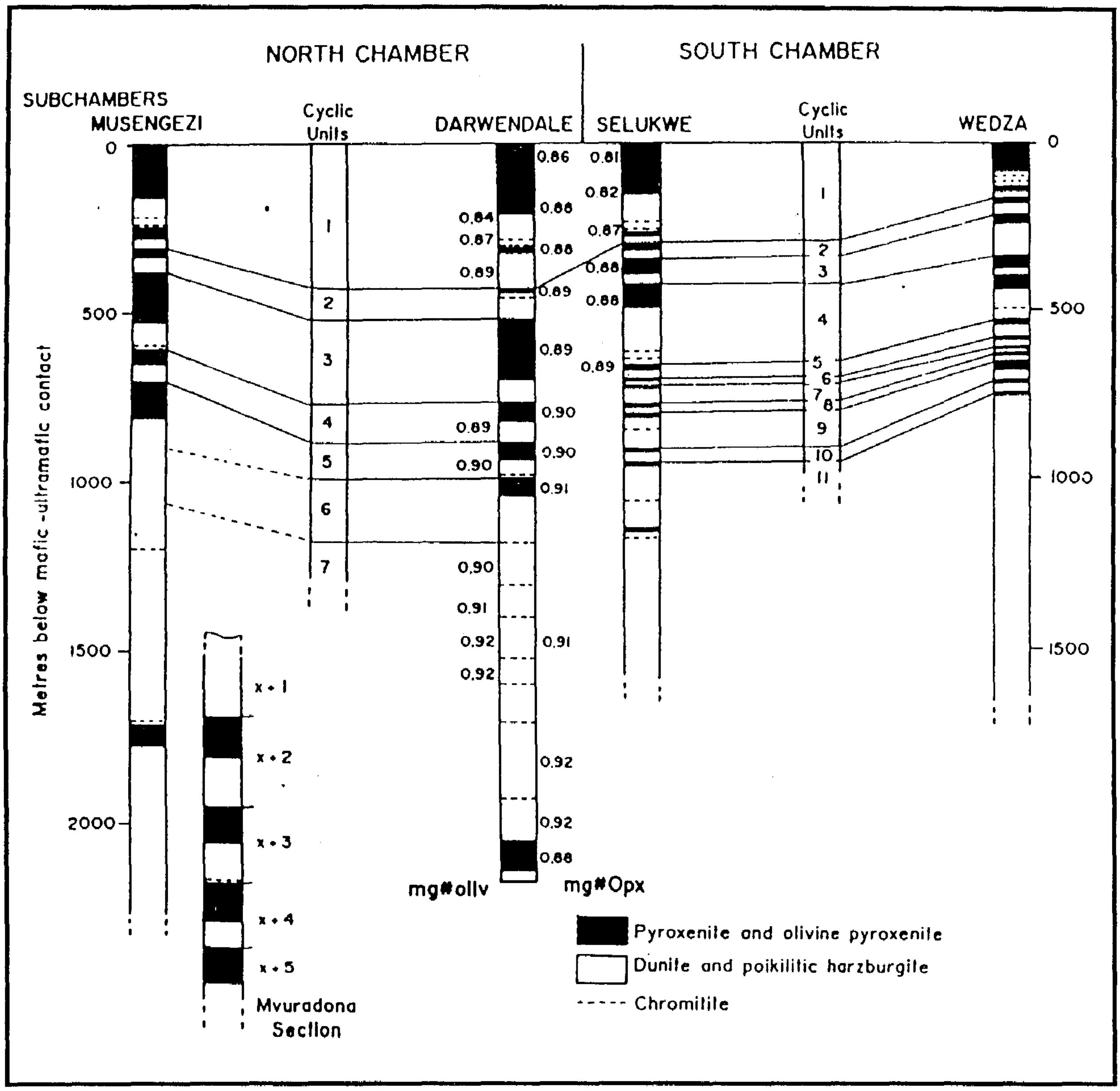

Figure 3.10 : Lithostratigraphic correlation of the Ultramafic Sequence between, and within, the North and South Chambers (after Wilson, 1996).

The Sebakwe Subchamber shares many similarities with those of the South Chamber, being a condensed sequence with relatively thin pyroxenite layers: this is essentially a feature of its smaller size compared with the Darwendale and Musengezi Subchambers. The western part of the Musengezi complex has a similar stratigraphy to the Darwendale Subchamber, shown in figure 3.10, and is considered to be an extension of the North Chamber. The isolated eastern segment of the Musengezi complex has significantly different stratigraphical characteristics, however, and was proposed by Wilson and Prendergast (1989) to represent a separate northern chamber, named the Mvuradona Chamber.

3.4.3 : Mafic Sequence

The Mafic Sequence consists of plagioclase cumulates, essentially gabbros and gabbronorites. The sequence is preserved to differing degrees in all subchambers, with only the lower 250-450 m of the Lower Mafic Unit found within the Musengezi, Selukwe and Wedza Subchambers. The Mafic Sequence is best developed in the core of the canoe-like structure of the Darwendale and Sebakwe Subchambers, where over 1000 m is preserved.

The base of the Mafic Sequence occurs immediately above the Main Websterite layer, and is defined by the introduction of plagioclase as a cumulus phase. The Mafic Sequence has a broad three-fold division into Upper, Middle, and Lower Mafic Units (figure 3.8). The subdivision is based upon the field relationships of the mappable units, and textural characteristics (Wilson and Wilson, 1981); the main features of the units are outlined below:

1) Lower Mafic Unit (LMU): A distinctive 10 m thick olivine gabbro - olivine gabbronorite occurs near the base of the LMU, marking the re-appearance of olivine in the stratigraphy. The remainder of the LMU is a ~700 m thick succession of relatively monotonous gabbronorites, with fairly consistent proportions of cumulus and postcumulus orthopyroxene, clinopyroxene, and plagioclase. There is a general transition of orthopyroxene from a cumulus phase at the base, through to a post-cumulus iron-rich variety in the upper parts (Wilson and Prendergast, 1989). Minor leucogranites occur as

discontinuous layers in the lower LMU. Post-cumulus phases within the gabbronorites generally comprise less than 2% of the rock, and include hornblende, phlogopite, and opaque oxides. The proportion of post-cumulus minerals exhibits a general increase with stratigraphic height, with a marked increase to ~8% modal proportion towards the top of the LMU (Wilson and Chaumba, 1997).

2) Middle Mafic Unit (MMU):A 30-150 m thick gabbroic sequence exhibiting greater variation than the LMU. The MMU is dominated by orthopyroxene and clinopyroxene cumulates, with plagioclase generally a postcumulus phase. Olivine re-appears as a minor, but ubiquitous, cumulus phase (Wilson and Prendergast, 1987). Minor lithologies of the MMU include websterite and feldspathic pyroxenite.

3) Upper Mafic Unit (UMU): A 300 m thick norite succession, consisting of cumulus iron-rich orthopyroxene and clinopyroxene, plagioclase, and magnetite-ilmenite. The dominant phase of the norites is pigeonite, now inverted to orthopyroxene. Modal layering of alternating pyroxenes and plagioclase is moderately developed. Quartz is an interstitial component, and olivine is absent. The absence of olivine is suggested by Wilson and Prendergast (1989) to be a reflection of the high degree of roof-rock contamination in the UMU. The roof zone of the Mafic sequence is not preserved.

Podmore and Wilson (1987) used comparative geochemistry of Great Dyke pyroxenes with those of the mafic portions of the Bushveld, Dufek and Skaergaard intrusions to calculate the portion of the mafic sequence that has been subsequently removed by erosion. Their results indicate that an additional 2-300 m of gabbroic rocks were originally present. Wilson and Prendergast (1989) postulate that the uppermost rocks were olivine-bearing ferrogabbros that were prone to erosion.

Within the Mchingwe Fault zone at Wedza, the presence of a thick quartz gabbro, which had previously been identified as a late-stage evolved product of the Great Dyke magma by Worst (1960), is now recognised as the product of extreme country rock contamination (Wilson and Prendergast, 1987, 1989; Chaumba, 1995). The extensive partial melting of the roof-rock granite mixed with the evolved Great Dyke magma to form a hybrid magma from which the quartz gabbro crystallized. A similar mechanism for the development of Great Dyke quartz gabbros was suggested by Hess (1950), who also erroneously described dolerites of Mashonaland age as a chilled roof zone of the Great Dyke. Wall-rock contamination is not restricted to the Mafic Sequence: along the eastern margin of the Selukwe Subchamber for example, hybrid rocks, such as biotite diorite, provide strong evidence of contamination affecting the marginal facies of the Ultramafic sequence. At the western margin of the subchamber, small pods of chromite, believed to be derived from the Shurugwe podiform chromitites, are found within Great Dyke rocks (Murahwi, 1995).

Xenoliths are a common feature of the upper part of the Mafic Sequence and within marginal zones of the Great Dyke. Xenoliths in the UMU of the North Chamber include granitoids and greenstone belt material. Partial melting of some xenolithic material is extensive, resulting in pegmatitic quartz gabbro; other xenoliths, such as quartzites and ultramafic rocks, are relatively resistant to alteration (Wilson and Prendergast, 1989).

3.4.4 : Border Group

This is a rarely exposed succession of relatively evolved pyroxenites and norites. The Border Group is not well understood due to a general lack of exposure. Wilson (1996) reports that field evidence indicates that the Border Group is not always present, but where developed the group ranges from fine-grained and massive, to complex and steeply-dipping layered rocks with distinctive textures. In the Mchingwe Fault zone, a well-developed Border Group occurs, which Wilson and Prendergast (1987) divided into two zones: a 5-10 m thick hybrid zone of feldspathic pyroxenites and norite/gabbronorite, marginal to the wall-rock contact; and a ~50 m thick pyroxenitic inner zone, which includes a peculiar feldspathic orthopyroxenite with elongated orthopyroxenes aligned perpendicular to the wall-rock. Autoliths of the Border Group within the layered sequence are especially common in the Selukwe Subchamber.

3.4.5 : Stratigraphic and Petrological Lateral Variation

Within the Ultramafic sequence, layers exhibit a general tendency to become thinner, finer-grained and more orthocumulate towards the margins of the Great Dyke. The dunites of the Ultramafic Sequence are remarkably adcumulate in the axial regions of the dyke, but show an increase in the proportions of intercumulus orthopyroxene, grading into harzburgite towards the margins.

CU1 shows very well-developed lateral variations, shown in figure 3.9. The cyclic unit as a whole, and the individual sub-units, thin towards the margin: in the Darwendale Subchamber, P1 shows a marked lateral decrease in thickness from 220 m in the axis, to around 150 m at the margins (Wilson, 1996). In the Wedza Subchamber, there is less overall thinning of the layers towards the margins although there are marked lateral variations in layering, mineralogy, and textures. Harzburgite lithologies of CU1 generally show an increase in plagioclase towards the margins, becoming feldspathic harzburgites; these contain phlogopite, with a high K_2O content suggestive of contamination by the granitic wall-rocks (Wilson and Prendergast, 1989). Towards the margin, orthopyroxenites interdigitate with websterites, and in SU3 the orthopyroxenite grades into a massive websterite layer at the margin. At the upper boundary of CU1, the Main Websterite is interlayered with gabbros and norites towards the margins, and erosional channels filled with fine-grained mafic rocks cut into the P1; in some areas, the websterite has been completely removed, and the mafic sequence rests directly on the orthopyroxenite.

Chromitites of the Great Dyke also show marked lateral variation. The LGC are characteristically massive chromitites in the axis of the dyke, but grade into disseminated olivine chromitite at the margins. Chromitites of the UGC exhibit significant lateral and longitudinal variation, exemplified by C1d which shows systematic textural and modal variation, diagrammatically summarised in figure 3.11. Within the marginal regions C1d occurs as a massive chromitite consisting of either two closely spaced layers, or a single layer. Towards the axis, C1d thickens and forms two highly disseminated chromitites, separated by a thick harzburgite: the lower layer consists of an unlayered olivine chromitite, whereas the upper layer is a well-layered harzburgitic chromitite with a distinctive 'nodular' appearance (Prendergast and Wilson, 1989).

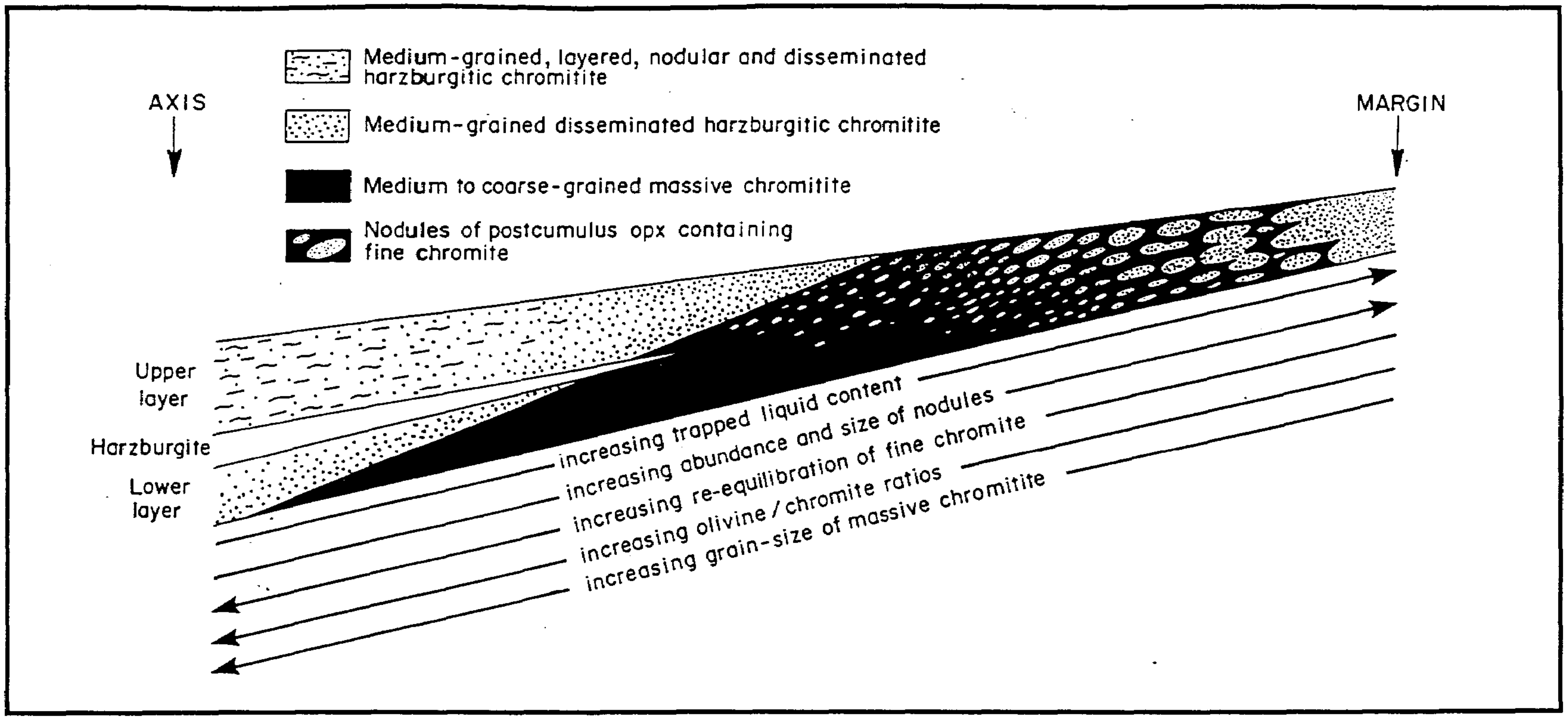

Figure 3.11 : Chromitite C1d: graphical summary of transverse variations across the magma chamber (not to scale). Note the progressive trend from thick, finely layered, disseminated olivine chromitite in axis through coarse-grained massive chromitite and then nodular chromitite to fine-grained pyroxene-rich chromitite at margin. Note apparent discordant layering relationships with modal layering dipping inwards at a steeper angle than major phase layering. (After Prendergast and Wilson, 1989)

3.5 : MINERALIZATION IN THE GREAT DYKE

> "While the rifting of any great land is not a pleasing prospect, in the case of Rhodesia it has been very fortunate in that it has led to those important economic deposits of chromite, and eventually platinum"
>
> A.L. du Toit, 18th March, 1940.

3.5.1 : Introduction

Zimbabwe is rich in mineral resources and has an active mining industry which contributes 7% of Zimbabwe's GDP. Some 40% of the country's foreign exchange earnings are derived from the export of metals and minerals. The Great Dyke is widely acknowledged as one of the world's largest resources of high-chromium ores, and contains the second largest resource of platinum group elements (PGE) in the world.

The potential economic importance of the Great Dyke as a source of both chromium and platinum has long been appreciated. Subsequent to the discovery of extensive chrome seams in the Umvukwe Range (northern Darwendale Subchamber), Maufe (1921) commented that the Great Dyke's chrome ore resources "must amount to many millions of tons". After the initial discovery of platinum in the dyke, Lightfoot (1926) perceptively concluded that "there is an enormous tonnage of this ore in Rhodesia...the future establishment of a mining industry depends entirely on whether the metallurgical difficulties of extracting low values of such a chemically inactive metal..can be surmounted".

The following sections on chromium and PGE mineralization outline the mining history of these resources in the Great Dyke and a brief assessment of the current mining situation is provided. Additionally, a brief overview of the PGE-ore zones is given, chromitite stratigraphy and detailed descriptions of lower group chromitites, particularly the economically important C5 chromitite, being discussed earlier in this chapter and in chapters 4,5,and 6. A brief description of eluvial chromite, nickel laterite, and chrysotile asbestos deposits is also provided.

3.5.2 : PGE mineralization

Platinum is one of the key minerals produced by the African mining industry. Africa has 85% of the world's platinum reserves, and produces 70% of the world's platinum. Production is dominated by South Africa which supplies 90% of the market (2,75 million ounces in 1992). Platinum is predominantly used in the manufacture of catalytic converters for automobiles and jewellery, but has a number of other uses, including medical applications and as a catalyst in the chemical and petrochemical industries.

The potential for platinum mineralization in the Great Dyke was predicted early this century, although concerted exploration for platinum in Zimbabwe only took place from 1925 onwards. This was in direct response to the discovery of platinum the Bushveld Complex at Mooihoek and Onverwacht, as reported by Wagner (1925a). The subsequent discovery of platinum in several localities of the dyke was made by late 1925 (Lightfoot, 1926), prompting Wagner (1925b) to suggest that this was "additional testimony that the huge intrusion is an offshoot from the Bushveld Complex". The Grainger Brothers' Wedza Mine operated from 1926 to 1928, exploiting the oxidized surface portion of the MSZ. The main platinum-carrier in the oxidized MSZ ore was sperrylite, which is markedly resistant to weathering. Poor recovery resulted in the early closure of the mine; Wilson and Prendergast (1987) suggested that current metallurgical technology would allow for potentially economic exploitation of the oxidized portion of the MSZ.

Renewed interest in the PGE of the Great Dyke began in 1960 with the publications of Worst (1958, 1960), and continued into the early 1980's with Anglo American, Union Carbide (now owned by Zimasco), and Rio Tinto the major companies involved. Major PGE targets on the Great Dyke were the Wedza-Mimosa (Wedza Subcomplex), Middleridge (Selukwe Subchamber), Zinca (Sebakwe Subchamber), and Selous (Darwendale Subchamber). Although significant potential ore reserves were identified, and the technical feasibility of mining the MSZ was proven, depressed metal markets, and continued problems with economic extraction were prohibitive to full-scale production.

In 1986 Delta Gold NL acquired the Hartley property and in 1990 signed a Joint Venture Agreement with Broken Hill Proprietary Company Limited (BHP). The Hartley Platinum Mine will account for approximately 3.5 per cent of the world's current annual platinum production, making Zimbabwe the second largest producer of platinum in the world after South Africa. Mining operations commenced in 1995 and, after a series of delays, the first shipment of platinum group metals (PGM) from the Hartley Platinum Mine was announced on 22 October 1997. At full production, the operation will mine 2.16 million tonnes of ore per-annum, producing 150 000 oz of platinum and 110 000 oz of palladium, with rhodium, gold, nickel, and copper as bi-products (Hartley Platinum data sourced from BHP at http://www.bhp.com.au/ on the world-wide web).

In addition, Zimasco is already mining at Wedza-Mimosa, and pre-feasibility studies at Unki (Anglo-American, Middleridge claims) and the Ngezi Platinum project (Delta Gold) were completed in 1997. The Ngezi Platinum project could potentially mine 3 million tons a year, with full production achievable by 2002. Coghill and Wilson (1993) estimated that total potential ore reserves of the dyke are in excess of 2.5 * 10^9 tons, making the MSZ a potential rival to the Merensky Reef in the Bushveld Complex..

The renewed industrial interest in the PGE-deposits of the Great Dyke has lead to increased geological research, and a number of recent publications have concentrated on the P1 layer and associated PGE-mineralization (Wilson et al., 1989; Prendergast and Keays, 1989; Prendergast, 1990; Wilson and Tredoux, 1990; Prendergast, 1991; Coghill and Wilson, 1993).

The PGE mineralization is hosted by orthopyroxenite with variable proportions (2-30%) of postcumulus minerals, including plagioclase, clinopyroxene, quartz, biotite, and sulphides. The PGE are closely associated with base metal sulphide (BMS), and occur in a broad, weakly disseminated zone in the LSZ, and as a narrow concentration in the MSZ. The MSZ is subdivided into a lower PGE-enriched subzone, and an upper BMS-enriched subzone. Wilson (1996) described the MSZ as essentially a six-metal ore body of Pt, Pd, Rh, Au, Cu and Ni. Platinum and palladium principally occur as arsenides and bismutho-tellurides, and pyrrhotite is the main BMS, with minor pentlandite, chalcopyrite and pyrite. Primary sulphides occur as very small interstitial and anhedral grains where sparse, but have a poikilitic net-textured appearance where abundant (Coghill and Wilson, 1993).

Although sulphide concentrations are restricted to the LSZ and MSZ, sulphides are distributed throughout the P1 layer and are broadly correlated with the proportion of postcumulus phases; sulphides also form a significant matrix component in the Potato Reef. Hydrosilicate alteration of primary phases is broadly correlated with sulphide mineralization and is conspicuous within the MSZ. Post-cumulus replacement of orthopyroxene, and less commonly clinopyroxene and plagioclase, has resulted in alteration to an assemblage that includes hornblende, talc, tremolite, biotite, chlorite, and secondary magnetite (Prendergast, 1990). Hydrosilicate alteration also occurs as small hydrothermal bodies throughout the upper parts of P1, consisting of quartz, potassic feldspar, carbonate, minor plagioclase and clinopyroxene .

Although the vertical distribution of PGE is similar throughout the Great Dyke, significant lateral variation has been observed: in the Darwendale Subchamber the thickness of PGE increases from 1.5 m at the margins to >12 m at the axis (Lee, 1996). Additionally, the concentrations of PGE and BMS decrease from the margins to the axis. This combination of a condensed MSZ with increased sulphide proportions away from the axis, as shown in figure 3.9, is advantageous to mining operations in the marginal regions of the dyke.

A major difficulty in the exploitation of the PGE is the lack of visual indications of the PGE-rich zone, although sulphide concentrations are used as a rough guide to the high-grade ore. The Potato Reef also forms a useful marker horizon at the hanging wall of the PGE-mineralization in the MSZ. At the Unki deposit in the Selukwe Subchamber, Murahwi (1995) noted the occurrence of a footwall shear at, or close to, the base of the MSZ. The basal shear is not, however, known from other localities, and at Unki would become a hindrance to mining at certain cut-off grades.

3.5.4 : Chromium

Chromium, from the Greek word *chroma*, was discovered in 1797 by Louis-Nicholas Vauquelin. 55% of total chromium consumption is used in stainless steel production (Mutemererwa, 1996), with numerous other uses, including: in steel and non-ferrous alloy production; in the refractory industry as chromite bricks; in the chemical industry, particularly in pigments; in the leather industry; and as chromium plating.

The estimated world output of chromium ore in 1991 was 13.25 million tons, of which African countries produced 5.76 million tons, making Africa the leading producer of chromium ore. About 70% of the world's known reserves of chromium ore are found in South Africa and 10% in Zimbabwe (information sourced from MBendi at http://mbendi.co.za/ on the world-wide web). Chromium ore in Zimbabwe is sourced from the stratiform deposits of the Great Dyke, and from a number of podiform deposits, the most important of these being at Shurugwi to the west of the central Selukwe Subchamber. The main chromite mining centres on the Great Dyke are at Lalapanzi, Darwendale, and Mutorashanga.

In 1912, A. E. V. Zealley reported finding chromite pebbles which, although not *in situ*, he believed to be derived from the Great Dyke. Maufe et al. (1919) later noted that chromite was "a common constituent of the olivine rocks, and in places is abundant; it even becomes the sole constituent of certain seams ". The first pegged chromite claims in the Mutorashanga region were 'Peake's Umvukwe Chrome' in December 1919; a decade later, Keep (1930) reported that the majority of the mapped chromitite outcrops in the Umvukwe Range had been opened up by claim holders. Chromite mining along the Great Dyke has been continuous since these times, although the high unit mining costs of the Great Dyke chrome ore and the friability of many of the chromitite layers has resulted in the considerable chromite resources of the Great Dyke (total resource 10000 million tons) being under-utilized. 50% of Zimbabwe's chrome ore is currently sourced from the less substantial, but more economically viable, podiform chromite deposits.

The main producers of ferrochrome in Zimbabwe are the Zimbabwe Mining and Smelting

Company (Zimasco), and Zimbabwe Alloys Limited (a subsidiary of Anglo-American). Mining operations at Zimbabwe Alloys' Great Dyke II Mine have been intermittent in recent years in response to economic factors, mainly the importation of low carbon ferrochrome from China and the former Soviet Union, coupled with escalating power tariffs, and high inflation with an overvalued Zimbabwe dollar.

Early mining of chrome seams was by "pig rooting' in near-surface pits. Current mining operations fall into two broad categories: small-scale surface / near surface mining, and underground mining operations via inclined shafts, essentially the domain of larger companies such as Zimasco and Zimbabwe Alloys. Surface trenching is also being re-evaluated on the eastern margins near the Sutton - Great Dyke mines in the Muturoshanga area. Low-cost small-scale mining has become increasingly common in recent years, in response to the high costs for large-scale company production (Prendergast and Wilson, 1989). Both Zimbabwe Alloys and Zimasco operate ferrochrome smelters within Zimbabwe, and small-scale miners sell directly to these companies, co-operative miners selling through the Zimbabwe Mining Development Corporation (Mutemererwa, 1996).

The chromitites of the Great Dyke have distinctly different metallurgical properties, summarised in table 3.1. The Lower Group Chromitites, with relatively high bulk Cr_2O_3 wt.%, and Cr/Fe ratios, form metallurgical grade ores although the friability of C6 to C12 is problematic. The friability of chromite ore is defined as 'its tendency to break down into smaller fragments and particles under applied and abrasive loads' (Smith and Slatter, 1978). In the Great Dyke, the friability is commonly due to the separation of chromite grains from the soft serpentinite matrix. 'Hard and Lumpy' metallurgical-grade chromitite is the most desirable for low-carbon ferrochromium production, and chromitite C5 is mined extensively in the Mutorashanga area for these qualities. The Upper Group Chromitites, with lower bulk Cr_2O_3 wt.%, and Cr/Fe ratios, form chemical grade ore; these chromitites are mainly exploited from shallow workings in the Lalapanzi and Darwendale areas.

Table 3.1 : Summary of mining and metallurgical properties of chromitites in Darwendale and Sebakwe Subchambers (modified after Prendergast and Wilson, 1989).

	Upper Group Chromitites	Lower Group Chromitites
Bulk %Cr_2O_3	36 - 49	43 - 54
Bulk refractory ratio	2.8 - 3.2	3.9 - 4.4
Chromite Cr/Fe ratio	2.0 - 2.7	2.7 - 3.9
Friability at present mining depths	Ore lumpy to semi-friable	Chromitite C5 ± lumpy throughout. Chromitites C6 - C12 highly friable with some lumpy ore
Form/thickness	Composite layers (up to 400 cm +) comprising one or more massive to disseminated layers, each 5-100 cm thick	Single massive layers 10 to 15 cm thick
Wallrocks/Mining conditions	Harzburgite wallrocks (except footwall pyroxenite of chromitite C1d). Serpentinized form relatively hard; good ground conditions, but jackhammers required	Dunite wallrock (except for footwall pyroxenite of chromitite C5). Serpentinized form very soft; poor ground conditions, but suitable for electric coal drills. Chromitite C5 requires jackhammers and special extraction techniques

Bulk refractory ratio : (Cr_2O_3 + MgO + Al_2O_3) / (total Fe as FeO + SiO_2)

3.5.5 : Eluvial chromite and nickel laterite deposits

In the elevated northern regions of the Great Dyke, chromite-bearing eluvial soils are relatively common, and are particularly concentrated within wide valleys: Wilson and Prendergast (1989) considered the mature African erosion surface (see chapter 4) to have been a fundamental factor in the formation of these deposits. The long-lasting weathering associated with the African erosion surface also resulted in the concentrations of up to 2% nickel within a 1 metre thick zone of weathered serpentinite, the nickel being present as a garnieritic hydrated magnesium silicate (Slatter, 1979). Individually, the eluvial chromite and nickel laterite deposits are considered sub-economic, but smelting of the eluvial chromite and underlying laterite together to produce ferrochromium nickel alloys has been proven to be technically feasible and may become an economically viable proposition in the future.

3.5.6 : Chrysotile Asbestos

In the Great Dyke, chrysotile asbestos occurs in small quantities associated with major lateral faults. The only area where chrysotile asbestos has been commercially mined was at the Ethel Mine, between 1920 and 1966. The deposit, containing chrysotile asbestos fibres 1 to 25 mm long, occurs on the southern side of a major dextral shear with significant displacement, as seen in figure 3.12. No asbestos is developed in the fault plane itself, and the deposits are restricted to three parallel, east-west trending zones, separated by areas of relatively barren serpentinite (Annheusser, 1986). To the north of the Ethel Mine, small quantities of Mtoralite, a chrome-rich variety of chalcedony, have been mined from highly sheared and altered Great Dyke rocks close to the granite wallrocks (Wilson and Prendergast, 1989).

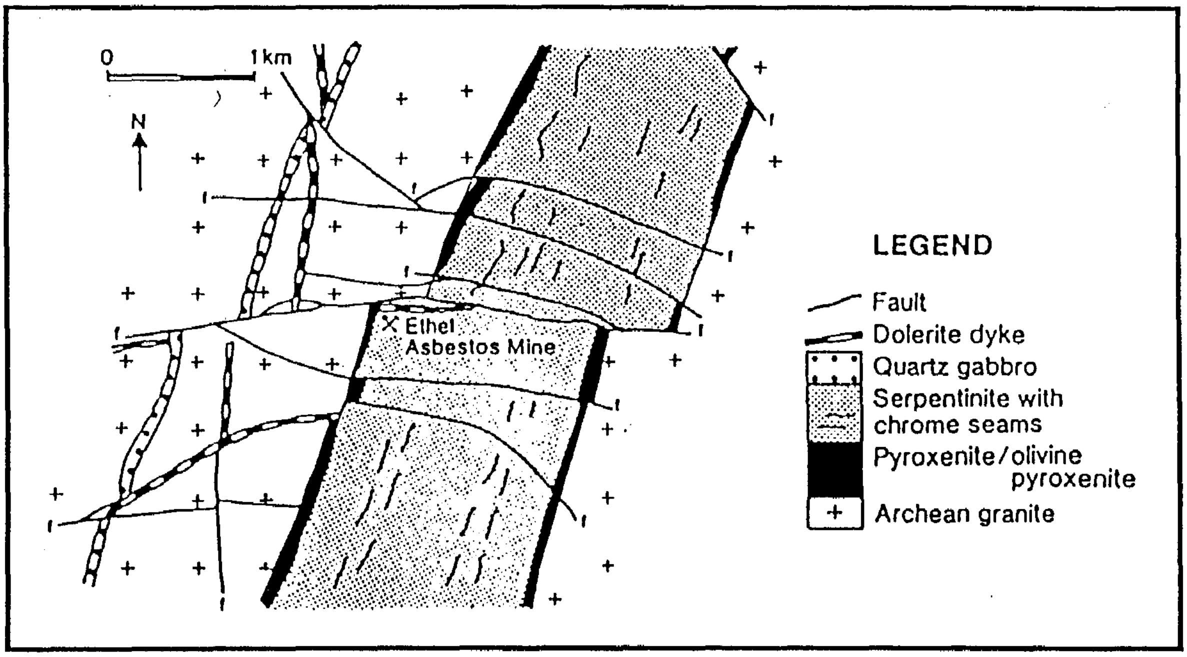

Figure 3.12 : Map of the (disused) Ethel chrysotile asbestos mine, Great Dyke, near Mutorashanga (from Annheusser, 1986)

CHAPTER 4 : GEOLOGY OF THE GREAT DYKE IN THE MUTORASHANGA AREA, DARWENDALE SUBCHAMBER.

4.1 : INTRODUCTION

The mapping project was undertaken during October and November, 1995. The mapped area is 30 km south of Mutorashanga and 65 km north-west of Harare, and consists of an area of approximately 38 km^2 (see figure 4.1). The Great Dyke is approximately 6 km wide in this locality, the dyke rocks forming the elevated topography of the Umvukwe Range. In the study area, and in the dyke in general, orthopyroxenite layers tend to form resistant ridges: the P3 orthopyroxenite dominates the axial section; away from the axis the P4, P5, and P6 layers form scarps, with serpentine ledges in between, as shown in plate 4.1. Into the Dunite Succession, the serpentinite flattens out to the level of the regional Post-African pediplain at the margin at an elevation of approximately 1400 metres (4590 feet). The western margins of the Great Dyke in this region are ~250 metres lower than the eastern side. Wilson and Prendergast (1987) consider this to be the result of the Great Dyke acting as a resistant feature during African erosion cycles; with the western margin representing a more juvenile erosional surface than the east.

The Umvukwe range in this area shows a well-developed summit planation at a height of approximately 1550 metres (5081 feet), as noted by Lister (1987). This planation is a remnant of the Cretaceous-early Tertiary African erosion surface and is seen in pyroxenite ridges towards the axis, and in silicified serpentinite hills nearer the margins. The Miocene Post-African erosion cycle is responsible for much of the erosion of the dyke in this area, and is particularly evident in the narrow, steep-sided valleys of the Mukwadzi river and Aireys Pass. Incision of the NW-trending valley to the south of the Aireys Pass shows similar features, but did not reach the level of the regional Post-African pediplain.

Wild (1965) completed a thorough study of the flora associated with the Great Dyke and noted that the restricted vegetation on serpentinite, mainly grasses of *Loudetia simplex* and species of *Andropon* and *Aristida*, was mainly due to the high Mg/Ca ratios, combined with relatively high

Ni and Cr content, of the serpentinite soils. Some succulents, such as *Euphorbia monteiri, E.memoralis,* and *Aloe ortholopha*, and a few geophytes, are also found in the serpentinite hills. Shrubs and trees are generally small and sparsely distributed. The pyroxenites contrast with the serpentinites in that they support significant additional woodland flora, mainly *Julbernardia globiflora* and *Brachystegia spiciformis* (Wild, op.cit). The contrasting vegetation associated with serpentinites and pyroxenites can be clearly seen in Plate 4.2.

The contact of the Great Dyke in the mapped area was very poorly exposed, and showed no distinct change in geomorphology. As the contact region was generally located in grassy farmland, no distinct vegetational change could be detected, and the spread of granitic sands within the farmland soils further obscured the contact.

Two dolerite dykes cross-cut the mapped area, trending at approximately 100°. The dykes are typically exposed as small rounded mounds 1 metre across, with an estimated width of 3 to 3.5 metres for the dykes at surface.

4.2 : MAP GENERATION

The fair-copy map presented in figure 4.2 was produced using Microimages TNT-MIPS™ (Map and Image Processing System) software. The field map and available aerial photographs of the area were both scanned in and enlarged to a scale of 1:18000 for ease of interpretation. Interpretation of the aerial photographs and comparison with the field map was enhanced by conversion of the photos into orthophotographs; this was done by georeferencing the aerial photos against the topographic map, merging the 3 photographs together, and then warping and resampling them to the base map projection and cell size. The fair-copy map was drawn as a CAD product directly into MIPS, and was then converted into a vector map, where all lines and polygons were assigned the relevant style attributes. The base geology layer was georeferenced from a scanned and georeferenced topographical map (Sheet: Kildonan 1730B_3). The contour lines have all been assigned height values during classification, thereby giving the map 3-dimensional rendering capabilities. Figure 4.1 gives locality names in the mapped area used in the following text.

Figure 4.1 : Location of the mapping area and locality names referred to in the text.

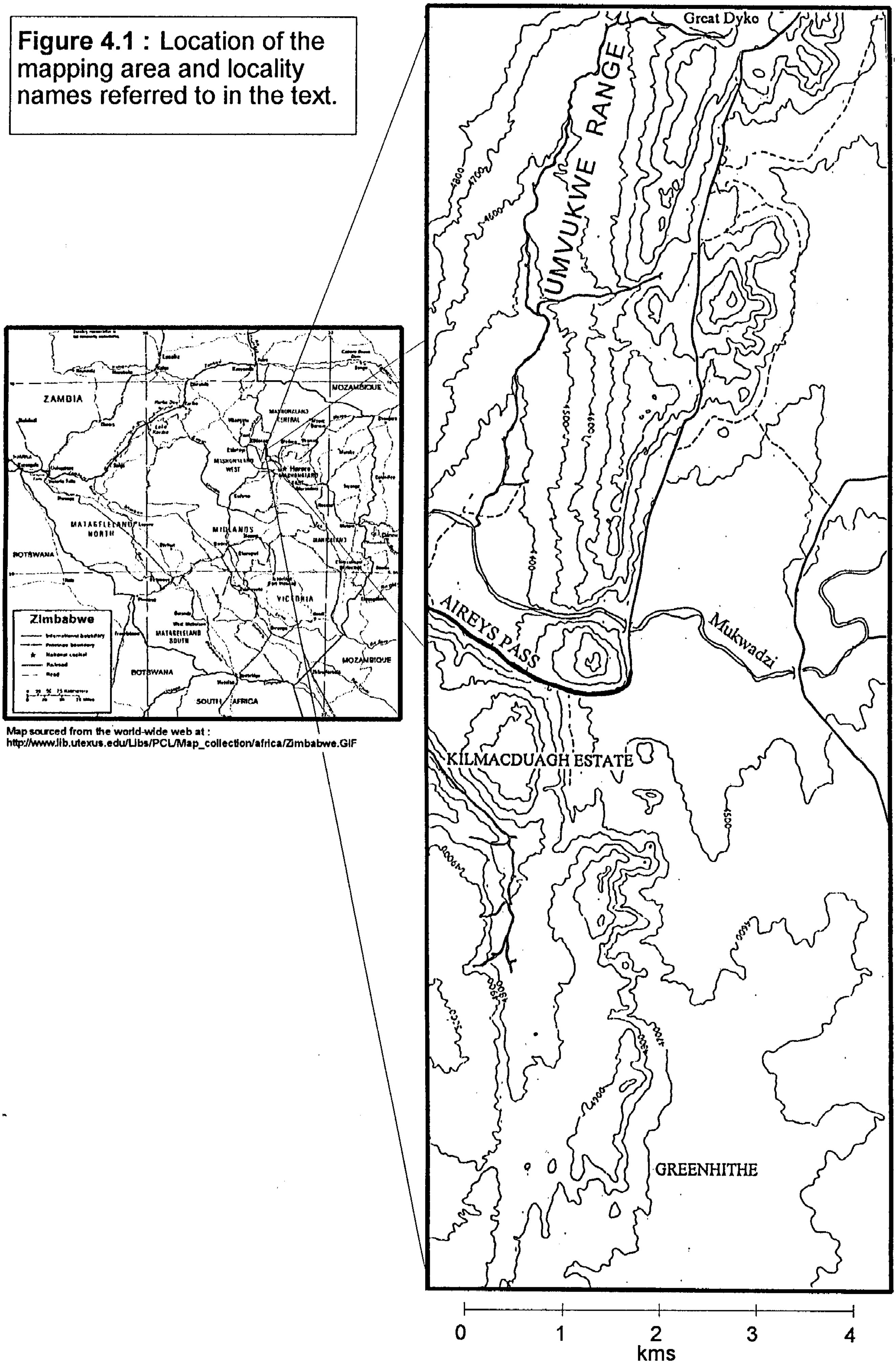

Map sourced from the world-wide web at : http://www.lib.utexus.edu/Libs/PCL/Map_collection/africa/Zimbabwe.GIF

Figure 4.2 : Geological map of the Great Dyke of Zimbabwe in the Aireys Pass area, Mutorashanga.

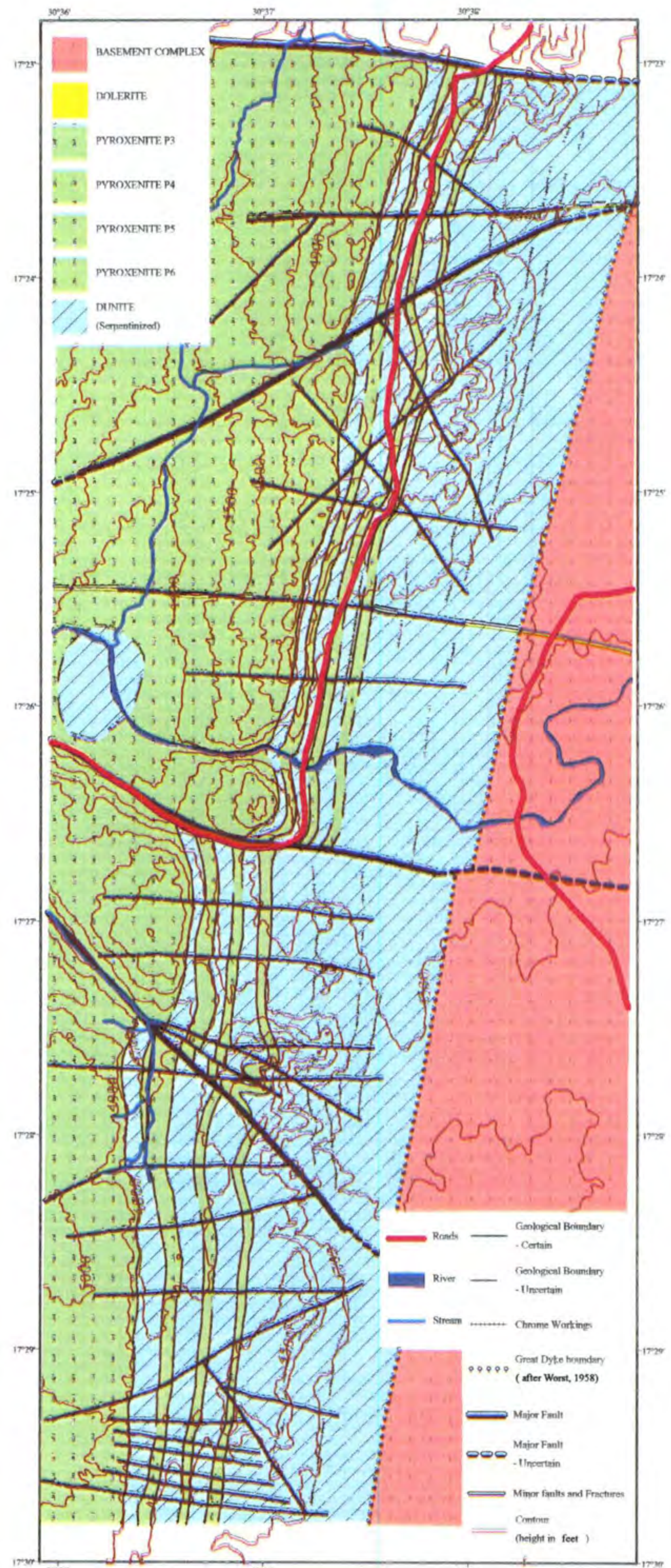

Plate 4.1 : View to the northern end of the mapped area from pyroxenite P6. Aireys Pass is in the middle distance. Serpentinized dunite of CU2 is preserved within the valley north of Aireys Pass in the left hand side of the photograph, and is flanked by pyroxenite P3, which forms prominent ridges clearly illustrating the synclinal structure of the Great Dyke. Note the trenches and waste dumps in chromitites C6 in the serpentinite hills on the right hand side of the photograph.

4.3 : STRATIGRAPHY

4.3.1 : Introduction

The mapped area contains rocks of the lower Pyroxenite Succession and the upper Dunite Succession. The highest stratigraphic unit preserved is a remnant of serpentinized dunite of CU2; the lower-most stratigraphic units are poorly exposed serpentinized dunites of CU9 to 11 at the Great Dyke margins.

Information of the local stratigraphy of the dyke was obtained through field observations and from borehole core-logging, particularly from the 400 m geotechnical borehole H10/4a, drilled whilst the field study was ongoing. A stratigraphic log of borehole H10/4a is presented in figure 4.3. The stratigraphy is frequently disturbed by faulting and dolerite dyke emplacement; in borehole H10/4a, the important chromitite layer, C5, had been tectonically removed.

4.3.2 : Borehole study

Borehole H10/4a intersected 400 metres of the lower Pyroxenite Succession from serpentinized dunite of CU6 through to harzburgite of CU4 at surface (figure 4.3). Within CU4 (78 m - surface) and CU5 (~216-78 m), the serpentinized dunite shows an overall upwards increase in orthopyroxene content and a textural progression from poikilitic harzburgite (see plate 4.3) through to granular harzburgite (see plate 4.4). Complete textural and mineralogical progression through to olivine pyroxenite and orthopyroxenite is seen in CU5. In contrast to these cyclic units, serpentinized dunite S6 has a sharp contact with the overlying P6 layer. As previously noted, the basal lithologies of CU5 have been disturbed by tectonism and dolerite dyke emplacement, the base of CU4, however, is relatively undisturbed, as shown by the presence of the "Seam 3" chromite serpentinite, which has a maximum chromite content approximately 50 cm from the sheared contact with the footwall P5 layer.

Figure 4.3 : Stratigraphic log of Great Dyke North borehole H10/4a

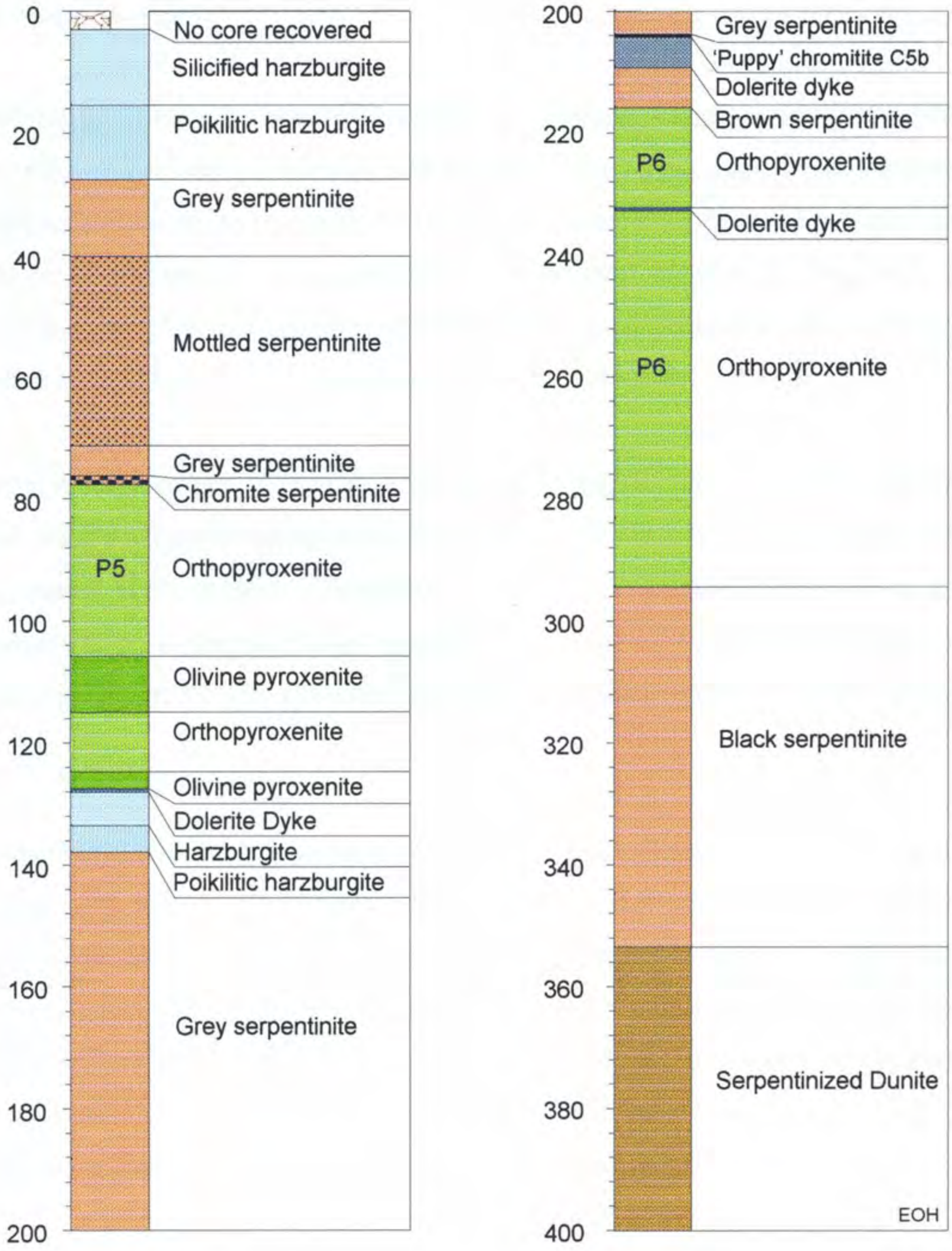

Although the overall pervasiveness of serpentinization decreases with depth, the local intensity is determined to a large extent by the degree of joint control. Between 300 and 400 m depth, the serpentinized dunite is dark green where there is a low joint control, with a more apparent crystallinity than the more heavily serpentinized dunite in regions of higher joint control, which is similar in appearance to the grey serpentinite closer to surface. Descriptions of the different styles of serpentinized dunite in borehole H10/4a are given in chapter 5.3 (see also plate 5.6).

4.3.3 : Mapped area

Serpentinites in the mapping area are always poorly exposed, forming sparsely vegetated rubbly ground with very low outcrop relief and a hard leached and silicified surface. Serpentinite of CU2 outcrops within the vlei to the north of Aireys Pass, where it is preserved in the synclinal axial zone of the Great Dyke on the downthrown (northern side) of the Aireys Pass Fault (see plate 4.1). In the centre of the S2 exposure, in/near-situ boulders of silicified poikilitic harzburgite with distinctive nodular light brown oikocrysts up to 2 cm across were observed.

The basal lithologies of CU3 and CU4 are chromite serpentinite. These are generally poorly exposed, and the heavy chromite content observed in surface soils is commonly the best indicator of the presence of the chromite serpentinite. Thicknesses are apparently variable, and chromite serpentinite of CU3 is generally thinner than that of CU4. The CU4 chromite serpentinite is locally referred to as "Seam 3", with good exposure for 10's of metres across strike and several metres across dip.

Gradational contacts from serpentinite to orthopyroxenite, through the range of intermediate lithologies, are locally well-developed by CU3, CU4, and CU5. Very distinctive poikilitic harzburgite containing varying proportions of olivine and orthopyroxene oikocrysts, generally ~1 cm across, occurs along the P4/S4 and P5/S5 contacts. The poikilitic harzburgite has a characteristic pitted appearance on weathered rock with positive relief exhibited by the oikocrysts, shown in plate 4.3. Where granular harzburgite is developed, the olivine is preferentially silicified, resulting in a negative relief of the orthopyroxen, shown in plate 4.4.

Plate 4.2 : View towards the southern end of the mapped area. Note the contrasting vegetation cover associated with pyroxenite (densely wooded), and serpentinite (grassland) layers.

Plate 4.3 : Surface and borehole samples of poikilitic harzburgite. 1 cm - wide orthopyroxene oikocrysts are more resistant to weathering than the serpentinized olivine, resulting in the distinctive 'nodular' weathered surface.

Plate 4.4 : Surface and borehole samples of granular harzburgite. The mesh-textured serpentinized olivine is preferentially silicified relative to orthopyroxene, resulting in the heavily pitted weathered surface.

Plate 4.5 : Surface samples of serpentinite associated with fault zones, showing (clockwise from top right): sheared magnesite lenses, chrysotile asbestos veins, and magnetite veins.

According to Wilson (1982), harzburgites are generally present as discontinuous layers towards the top of dunite layers. This was supported by the observed frequency and continuity of the harzburgite outcrops in the mapped area, although, particularly in the case of CU5, poikilitic harzburgite layers were apparently locally continuous for several hundred metres.

A chromite-rich poikilitic harzburgite occurs above chromitite C5 in some areas, consisting of orthopyroxene "mottles" approximately 3 cm across, and 5 cm apart, and containing abundant (~4 %) chain-textured chromite.

The P3 layer is by far the most conspicuous orthopyroxenite layer in the mapped area, forming the high ground in the axial region with substantial outcrop resulting from the near-complete erosion of the overlying CU2 dunite exposing the full lateral extent of the layer. Only the eastern limb of layers P4 to P6 is exposed in the mapped area. These orthopyroxenites show a general reduction in the areal extent of outcrop from P4 to P6, the P6 layer being relatively poorly exposed. The orthopyroxenites have a distinctive green colour, which is a feature of the high (~0.6%) chrome contents of the orthopyroxenes. Modal layering can sometimes be identified as a result of slightly differential weathering, and the orthopyroxenite is generally well-jointed.

The chromite seams in the Mutorashanga area are locally referred to using Worst's (1960) numbering system: therefore the C5 layer is called 'Seam 4', C6 and C7 are referred to as 'Seams 8 and 9' respectively, and so on. In this work, designation of chromitites is made according to cyclic unit number, as proposed by Wilson and Prendergast (1989). The occurrence of two previously unreported major chromitites in the Mutorashanga area was noted by Prendergast and Wilson (1989), the chromitites occur within cyclic units 8 and 10 and are named C8a and C10a, respectively. Neither of these chromitites were observed during the course of the current study.

In the Mutorashanga area, chromitites C5 to C10 have been extensively mined, with trenching along the seams on-going for the past 70 years. The trenching of chromitites is useful to mapping, as it reveals the near-surface location of chromitites that are otherwise very poorly exposed at surface. However, many of the trenches have not been worked for many years and exposures are generally poor. Waste dumps are a common feature immediately down-slope of worked trenches and adits, and generally provided the best source for chromitite sampling.

The 'Puppy Seam' occurs about 6 m above chromitite C5. This is a 3 cm thick, very fine-grained chromitite, which has a serpentinite hanging wall with disseminated chromite. 'Puppy Seam' is a local mining term, and it would be more appropriate to refer to this chromitite as C5b.

4.4 : STRUCTURE

4.4.1 : Internal structure

The layering in the area strikes in a north to north-northeast direction, and dips between 22° and 27° W/WNW. At Aireys Pass, the southward-plunging synclinal structure of the Great Dyke layering can be observed towards the south, where the serpentinite of CU2 (S2) has been removed by erosion (see plate 4.1). The mapped area essentially comprises the eastern half of the synclinal structure, with the western limit of the area broadly equivalent to the axis of the Great Dyke; therefore only the eastern limbs of the layers occur within the mapped area.

4.4.2 : Faults and fractures

The WNW-trending Aireys Pass Fault is very poorly exposed, due in part to the Aireys Pass road built directly on the fault (see figures 4.1 and 4.2), and due to the very soft nature of the fault material. The Aireys Pass Fault is a normal fault that is estimated to be downthrown to the north by at least 300 metres, resulting in S2 being preserved in the synclinal vlei to the north of Aireys Pass, and P3 forming an elevated axial region to the south. The effects of the fault were well seen in small adits on the southern slopes of the hill east of the S2 outcrop. Extensive tectonism of serpentinite was observed within these adits, with substantial development of talc and carbonate in highly sheared rocks, often locally strongly magnetic. Some of the tectonites were originally orthopyroxene-bearing, with visible bastite orthopyroxene cleavage planes.

The NW-trending Kilmacduagh Fault, developed to the south of the Aireys Pass Fault, has a well-developed, but generally poorly exposed, fault zone several metres wide. Within this zone, extensive silicification has occurred, and identification of different primary lithologies is difficult. NW-trending quartz veins of varying size, from 1 cm to over 1 m wide, are common within the fault zone, and are assumed to have developed subsequent to the main faulting event. Similar quartz vein development is associated with other fault and fracture zones in the area, particularly in the vicinity of the Great Dyke Fault at the northern limit of the mapped area. Re-activation of the fault zone was indicated by small-scale, parallel buckle folds observed in thin quartz veins. Larger quartz veins are commonly exposed as irregular rubbly outcrop of low relief, consisting of vuggy and net-textured quartz. Also associated with this fault zone is magnetite and cross-fibre asbestos veining up to 1 cm wide, shown in plate 4.5.

Broadly east - west trending parallel fractures are a common feature along the length of the dyke in the mapped area, particularly in the extreme south. These fractures are marked by poor outcrop of the main pyroxenite layers, and are often traceable within serpentinite where the fracture is represented by a narrow low-lying ridge of silicified serpentinite. These fractures generally show limited displacement, although some vertical movement may have occurred.

4.5 : SECONDARY/SURFACE PROCESSES

4.5.1 : Introduction

The pervasive surface - subsurface serpentinization of the dunites in the Great Dyke is an important feature, and the petrology and geochemistry of the serpentinized rocks are discussed in detail in chapters 5 and 7. Although the orthopyroxene-bearing rocks are generally far more resistant to serpentinization than dunite, intermediate lithologies, and sometimes orthopyroxenites, can be pervasively serpentinized. This is particularly evident where the rocks are heavily fractured and mature erosional surfaces are preserved. Surface orthopyroxenite can also become friable where extensively weathered.

4.5.2 : Silicification

Whilst partial silicification of surface serpentinites is ubiquitous, silicification is most pervasive on African erosion surfaces, and within the immediate vicinity of faults and fractures in lower topography outcrops. Isolated hills of silicified serpentinite are generally associated with a fracture / fault zone, where the preservation of older silicified erosion surfaces is facilitated by the more intense silicification associated with fractured rocks. Silicified serpentinite ridges associated with fractures are a common feature in the Post-African erosion surfaces, and generally form a break of slope, suggesting that silicification along the fractures formed a resistant feature during Post-African erosion.

Preferential silicification of serpentinite along pre-existing serpentine vein systems has resulted in the distinctive stockwork structure observed in saprolitic surface rocks associated with the Cretaceous African erosion surface, as shown in plate 4.6. The silicification of the surface rocks is associated with iron oxide and iron hydroxide alteration. Ferricrete is locally common, and is best developed in the vicinity of faults and in mature surfaces in the south of the mapped area.

4.5.3 : Secondary processes and Chromitites

Wilson and Prendergast (1987) noted that there is a general correlation between secondary processes and the friability of the chromitite ore, shown diagrammatically in figure 4. 4. Friable ore is predominantly found at depth, within highly serpentinized zones in the axis of the dyke. Hard and Lumpy ore is either re-crystallized and/or fine-grained mylonitized chromitite, or is coarse-grained annealed chromitite cemented by a selvedge of secondary silicate minerals. Although C5 is generally one of the least friable chromitites on account of the low intergrain silicate proportions and the presence of the P5 footwall, the wide variation in the nature of near-surface chromitite C5 within the mapped area is illustrated in plate 4.7.

The intense silicification of chromitite is shown in the left foreground of plate 4.7, and in plate 4.8, where polycrystalline quartz is seen to be associated with the brittle deformation of the chromite grains. Such secondary modification will obviously have a significant effect on SiO_2 and Cr_2O_3 contents of the chromite ore .

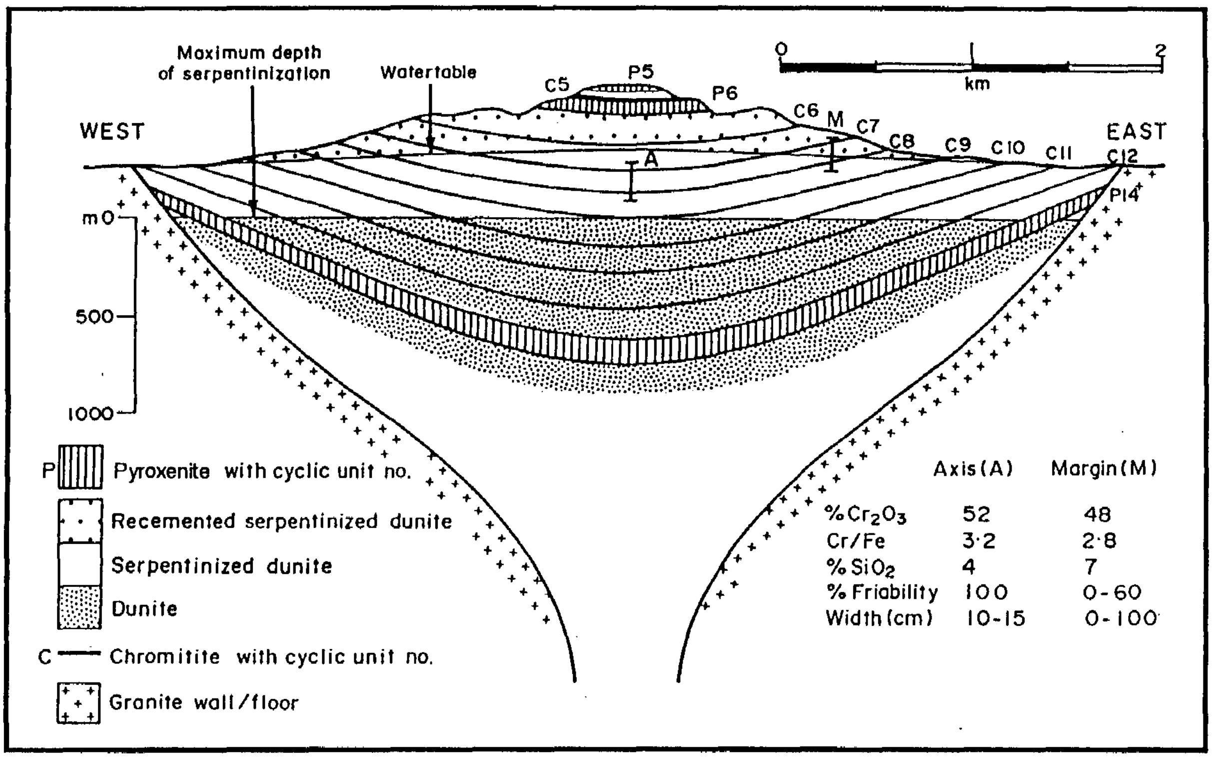

	Axis (A)	Margin (M)
$\%Cr_2O_3$	52	48
Cr/Fe	3·2	2·8
$\%SiO_2$	4	7
% Friability	100	0-60
Width (cm)	10-15	0-100

Figure 4.4 : The effects of secondary processes on characteristics and bulk ore grade of Lower Group Chromitites in the northern part of the Darwendale Subchamber. Note the horizontal zonation caused by serpentinization and subsequent groundwater movements. Transverse thrusting along chromitite-dunite contacts due to subsidence resulted in the strong variation in chromitite thickness near margins. Mean ore characteristics tabulated for chromitites C7 and C8. (After Prendergast and Wilson, 1989)

The relatively thin chromitites are susceptible to tectonism and extensive shearing. Tectonic pinch-outs and duplication were observed in the C5 chromitite in Great Dyke Mine Shaft no.2. Both footwall and hanging-wall contacts are commonly sheared, infilled by a range of material from magnesite to silicified magnesite to silica.

Eluvial chromite occurs in soils developed between pyroxenites P5 and P6 in the highly faulted serpentinite hills between the Aireys Pass and Kilmacduagh faults. The very friable chromite is sporadically mined by small-scale miners, and is apparently derived from extensive weathering of chromitite C5 where it was exposed at or near the African erosion surface.

Plate 4.6 : Stockwork structure in saprolitic serpentinite, associated with African erosion surfaces. Lens-cap included for scale..

Plate 4.7 : Surface samples of chromitite C5, showing the highly variable nature of the rock. Clockwise from top right: partially re-cemented 'hard and lumpy' ore, very friable ore, extensively silicified (opaline silica) and fractured chromitite, tectonized and re-cemented 'hard and lumpy' ore.

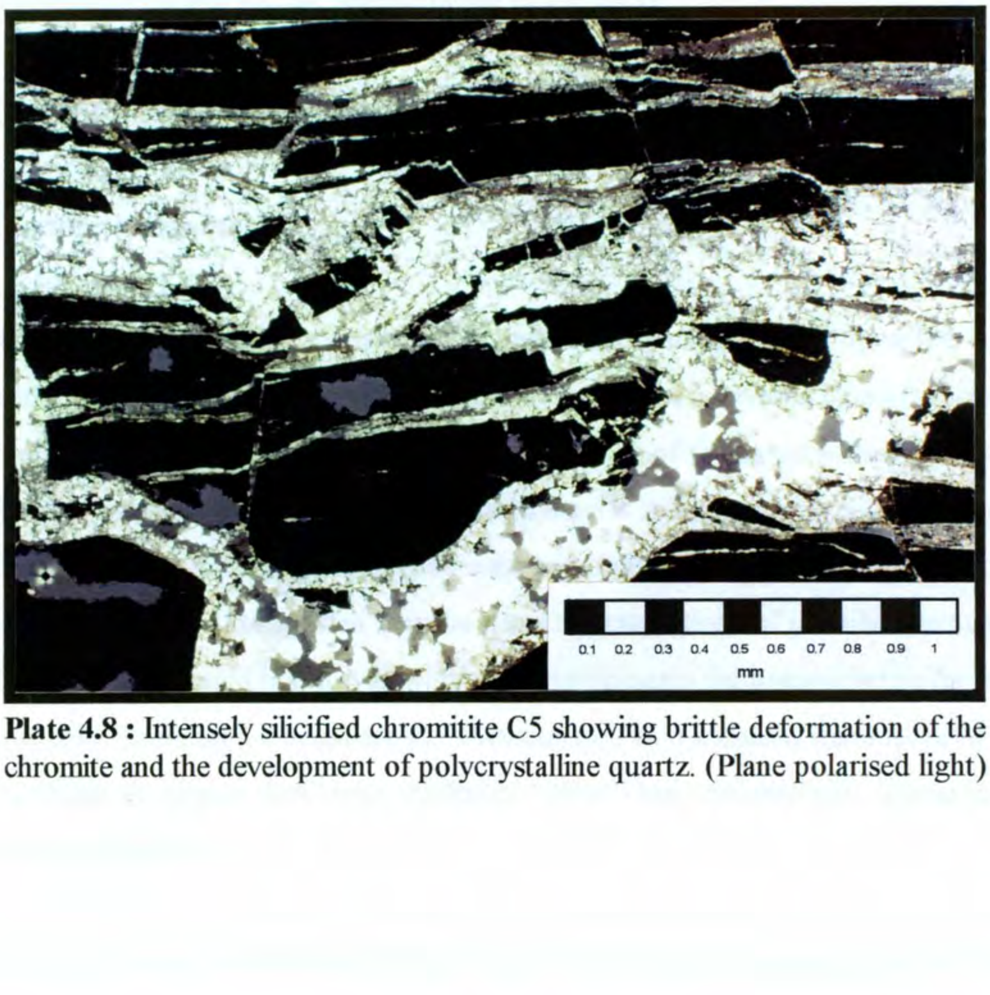

Plate 4.8 : Intensely silicified chromitite C5 showing brittle deformation of the chromite and the development of polycrystalline quartz. (Plane polarised light)

5 : PETROGRAPHY OF THE LOWER PYROXENITE SUCCESSION

5.1 : INTRODUCTION

The petrography of the lower Pyroxenite Succession is described and discussed in this chapter. In the course of the petrographical investigation approximately 80 thin sections were studied; these were cut from field samples and from selected levels of borehole H10/4a. A discussion of cumulus processes and textures, an overview of serpentine textures, and a discussion of annealing processes with particular reference to chromitites, are included in this chapter with an aim to clarify the description and aid the interpretation of the rocks.

5.2 : CUMULUS PROCESSES AND TEXTURES

5.2.1 : Cumulate terminology

Wager et al. (1960) proposed a system of cumulate terminology based upon the concept of gravity settling as the dominant process of crystal accumulation in layered igneous rocks. The *in situ* crystallization of cumulate rocks at or near the floor of the magma chamber is currently favoured as the dominant cumulus process, although there is still uncertainty as to the precise role of *in situ* crystallization, relative to crystal sedimentation processes (see chapter 8 for further discussion). Irvine (1982) suggested that the genetic connotations of cumulate terminology be largely discarded, but argued that it was worthwhile to maintain the nomenclature for essentially descriptive use. He defined a cumulate as "characterized by a cumulus framework of touching mineral crystals or grains that were evidently formed and concentrated primarily through fractional crystallization".

Cumulus crystals were described by Wager et al. (1960) as those crystals that had formed as primary precipitates from the main crystallizing body of magma. Intercumulus liquid referred to the interstitial spaces between cumulus crystals. The following descriptions are based upon the early work of Wager et al. (op.cit.) and subsequent recommendations of Irvine (1982):

1) Adcumulates are rocks that consist of essentially unzoned cumulus crystals, with very minor proportions of (0-7%, by volume) postcumulus material. Heteradcumulates are a subclass of adcumulates, in which unzoned cumulus crystals are poikilitically-subpoikilitically enclosed by unzoned oikocrysts. Hunter (1996) recommends the use of the term 'poikilitic adcumulate' to describe rocks with these cumulate textures.

2) Orthocumulates consist of cumulus phases and 7-25% additional interstitial phases formed by the crystallization of intercumulus liquid. Characteristic features of orthocumulates are the distinctive interstitial minerals, and the presence of zoned overgrowths on cumulus crystals, caused by crystallization from more evolved liquid compositions.

3) Mesocumulates are seen as rocks intermediate between adcumulates and orthocumulates defined as containing 25-50% postcumulus material.

Wilson (1992) suggested that it would be advantageous in studies of the Great Dyke to apply a modified cumulus terminology that has a genetic connotation. The relative proportion of orthocumulus and adcumulus components is used to define the cumulate type. The adcumulus component is essentially a primocryst, defined as that part of the cumulus crystal that grew in equilibrium with the crystallizing magma. The orthocumulus component represents material that grew from relatively evolved liquid in an essentially closed system. Orthocumulus overgrowth of a cumulus grain may obscure the adcumulus component; as a consequence of this, Wilson (1992) notes that observation of discrete postcumulus phases may not be an accurate indication of the proportion of trapped liquid in the cumulate.

5.2.2 : Cumulus processes and development of cumulus textures

An important cumulus process is that of adcumulus growth, by which cumulus crystals are enlarged by overgrowth from a melt of similar composition to that which formed the primocrysts. According to Wager et al. (1960), adcumulus growth of the cumulus crystals took place near the top of the crystal pile by isothermal diffusion-based interaction of intercumulus liquid with the overlying magma.

Irvine (1980) suggested a process of infiltration metasomatism and filter pressing to account for extensive adcumulus growth. This essentially involves the mechanical expulsion of intercumulus liquid upwards through the crystal pile in response to compaction and enlargement of cumulus phases. Adcumulus growth resulted from reaction of the cumulus crystals with the migrating solute. Morse (1986) showed that this was essentially an orthocumulus process, resulting in liquid entrapment, and would not produce true adcumulates.

Morse (1986) and Tait et al. (1984) proposed that convection within the magma chamber could provide a mechanism for enhancing the formation of adcumulate textures. During adcumulus growth, latent heat and light rejected solute is removed by the convecting magma from the top of the crystal mush. Compositional convection within the crystal pile could increase adcumulus growth by replenishing the intercumulus liquid with material from the overlying magma. This material would be compositionally similar to the melt from which the cumulus grains crystallized. Hunter (1996) noted that this process might lead to relatively rapid adcumulus growth at the top of the crystal pile, which would effectively inhibit compositional exchange between underlying material and the undepleted magma, resulting in orthocumulate development lower in the crystal pile through crystallization of the trapped liquid.

It is clear that the porosity and permeability of the crystal mush will be a fundamental control on the textural development of the cumulates. Adcumulus growth requires an open-system percolation of melt between the overlying magma and the cumulus crystals. Convection and densification and are considered to be the main processes involved in the formation of adcumulate textures (Morse, 1986; Hunter, 1996). Densification of the crystal pile essentially involves a reduction of porosity. This can be achieved through compaction, adcumulus growth, or by cementation.

Mechanical compaction is limited in its efficiency and is not likely to have been capable of producing adcumulate textures (Morse, 1986). Hunter (1996) emphasized the role of textural equilibration in the compaction process, whereby the solution and re-precipitation of material occurs in order to reduce the total energy of the system. This process can occur in solid-state, but will be most effective in the presence of a melt. The dominant mechanisms in improving compaction are diffusive creep and deformation creep. Figure 5.1 illustrates how the transfer of material from regions of high curvature, and therefore high surface energy, to regions of low curvature by diffusive creep results in the granular textures characteristic of adcumulus assemblages. A fully texturally-equilibrated rock will therefore have a constant mean grain boundary curvature (Hunter, 1996). Figure 5.2 shows how dislocation creep increases compaction of the crystal pile. Although dislocation creep itself does not necessarily reduce the energy of the grain topology, subsequent textural equilibration may take place. In addition to compaction processes, thermal annealing provides another form of textural equilibration. This process is discussed in detail, with particular reference to chromitites, in chapter 5.5.3.

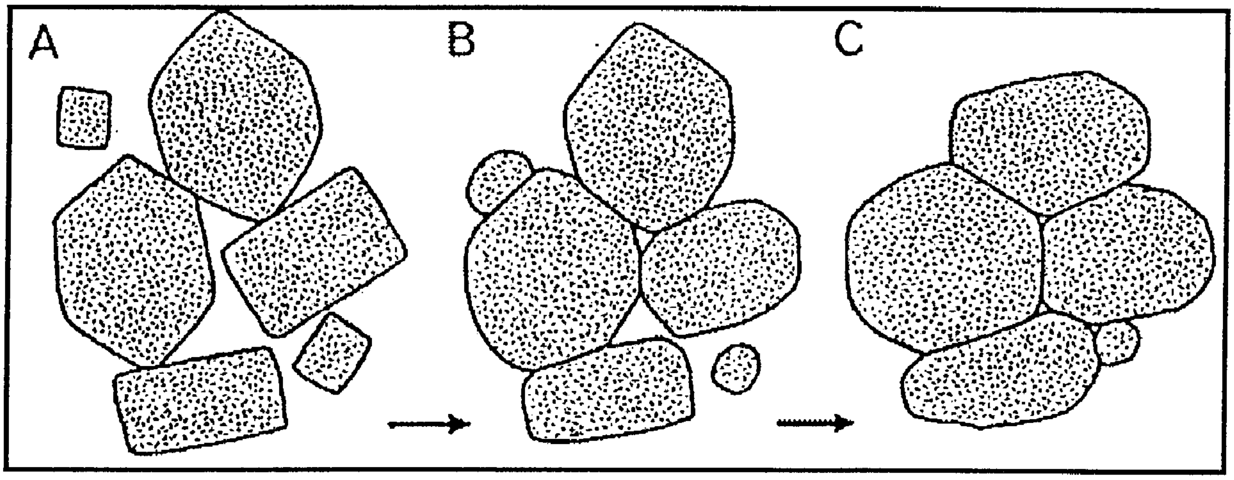

Figure 5.1 : Changes of grain shape produced by diffusive creep. Grain sizes change as a result of grain growth and/or Ostwald ripening. (After Hunter, 1996)

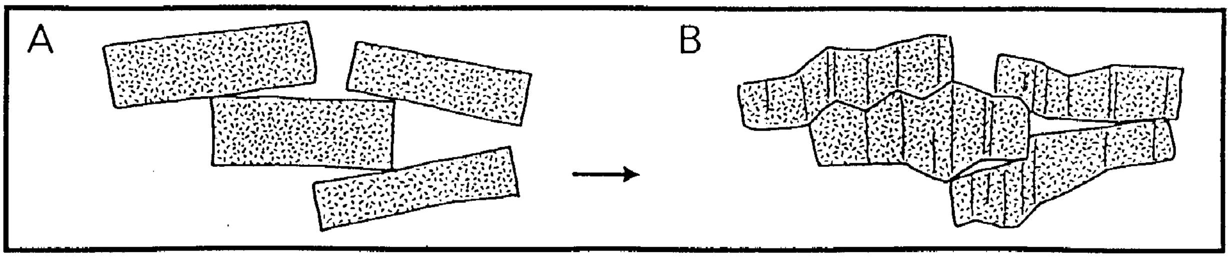

Figure 5.2 : Changes of grain shape produced by dislocation creep. Creep involves movement of dislocations both by glide and climb along slip systems. This mechanism does not result in equilibrated texture, although subsequent recovery will usually lead to local textural equilibrium. (After Hunter, 1996)

The topology of grains in cumulate rocks are therefore a feature of the extent of the textural equilibration in the rock. Where the volume fraction of cumulus grains is large, cumulus grains will share boundaries and the shape of the grains will be determined by the grain boundary geometry; hence the granular texture and polygonal mutual interference grain boundaries observed in strongly adcumulus assemblages.

Cementation of the cumulus crystals by the nucleation and growth of new poikilitic-subpoikilitic phases within the pore spaces will inhibit adcumulus growth. The nucleation and growth of these phases corresponds to an isotherm, termed the cementation front by Hunter (1996). The timing of the temperature interval prior to reaching the cementation front (ΔT_{ccm}) is therefore an important control on textural development. A long ΔT_{ccm} will allow extensive adcumulus growth and compaction, producing a well-densified adcumulate with granular textures. A short ΔT_{ccm} will produce a partly densified and cemented cumulate with poikilitic textures.

Wilson (1992) showed the effects of intrusion geometry on ΔT_{ccm}, illustrated in figure 5.3. At the margins of the Great Dyke, heat flow is relatively rapid and ΔT_{ccm} will therefore be short, producing the plagioclase and orthopyroxene oikocrysts of the marginal-facies P1 layer. At the axis, ΔT_{ccm} is long due to the low heat loss, resulting in the granular textures of the axial-facies P1 layer. Wilson (op.cit.) notes that the proportion of discrete postcumulus phases in both facies is broadly similar, but that in the axial facies they form as orthocumulus phases in a closed system, as opposed to the heteradcumulus oikocrysts formed in the margins.

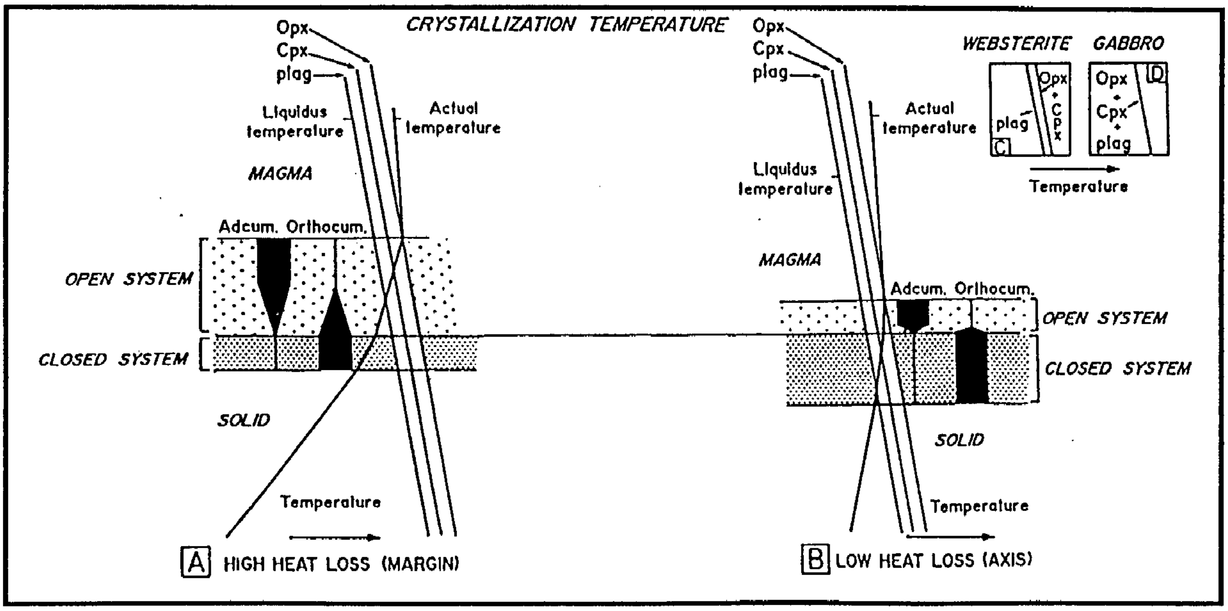

Figure 5.3 : The effects of intrusion geometry on the thermal conditions of axial and marginal zones during the formation of the cumulus sequence in the P1 layer. The relative proportion of adcumulus and orthocumulus components at any stage are shown by the solid blocks. See text for details. (After Wilson, 1992)

5.3 : SERPENTINITE / DUNITE

Dunites constitute approximately 70% of the Ultramafic Sequence within the Darwendale Subchamber (Wilson, 1982). However, along the length of the Great Dyke, the dunite is pervasively altered to serpentinite at surface, and serpentinization extends to varying depths, dependant largely upon the local topography of the dyke, position of the water table, and degree of joint control. In the Mutorashanga area, the dunite is serpentinized to varying degrees to a depth of over 300 metres, as evidenced by borehole H10/4a (see figure 4.3), in which the dunite is partially serpentinized to 400 metres.

The essentially complete serpentinization of the samples collected from the field and borehole complicates detailed mineralogical study on the original mineralogy of the rock, as many features are masked by alteration to pseudomorphic and non-pseudomorphic serpentine. Serpentinites in the Mutorashanga area show a wide variation in the degree of serpentinization, and related textural styles (see plate 5.6). The textural development of serpentinites is invariably complex, and therefore a brief review of serpentine textures is provided in the following section.

5.3.1 : Review of serpentine textures

Serpentine textures may be divided into three categories, each of which can relay a great deal of information about the serpentinization processes involved. *Pseudomorphic textures* form by the replacement of preexisting minerals but retain much of the morphological characteristics of the original mineral. However, the perfection of the morphology can range from excellent to barely distinguishable. *Non-pseudomorphic textures* are formed by the recrystallization of pseudomorphic serpentine textures; they may also form, albeit less frequently, by the direct serpentinization of preexisting minerals. *Vein textures* are generally formed at a late stage of the alteration process by crystallization of the serpentinizing fluids along fractures, shears and joint planes. It should be noted that the divisions among the three textural categories are gradational and identifying pseudomorphic textures with certainty when serpentinization is complete may often be difficult.

5.3.1.1 : *Pseudomorphic textures*

The characteristic mesh and hourglass textures of serpentine pseudomorphs after olivine represent 3-dimensional structures of polygonal cells that *en masse* appear as an irregular finely-chequered surface. The morphology of individual cells has been described by Wicks et al.(1977) and is shown in figure 5.4. Each cell consists of:

1) a **mesh centre**; the central zone of the cell, this may consist of relict olivine or serpentine (commonly lizardite 1T), the serpentine may be very fine-grained and isotropic.

2) the **mesh rim**, an outer zone where the apparent fibres of serpentine are aligned normal to the trace of the original fracture. This term is usually taken to include the outer zone of the two cells on either side of the central parting.

3) the **central parting** of the mesh rim; this marks the trace of the original fracture. The central parting commonly consists of either a simple parting, a string of magnetite grains or a narrow zone of isotropic/anisotropic serpentine. There may also be two partings present with an intermediate zone of serpentine in between. In **compound mesh rims** there are three partings, consisting of an *outer rim* next to the central parting and an *inner rim* adjacent to the mesh centre.

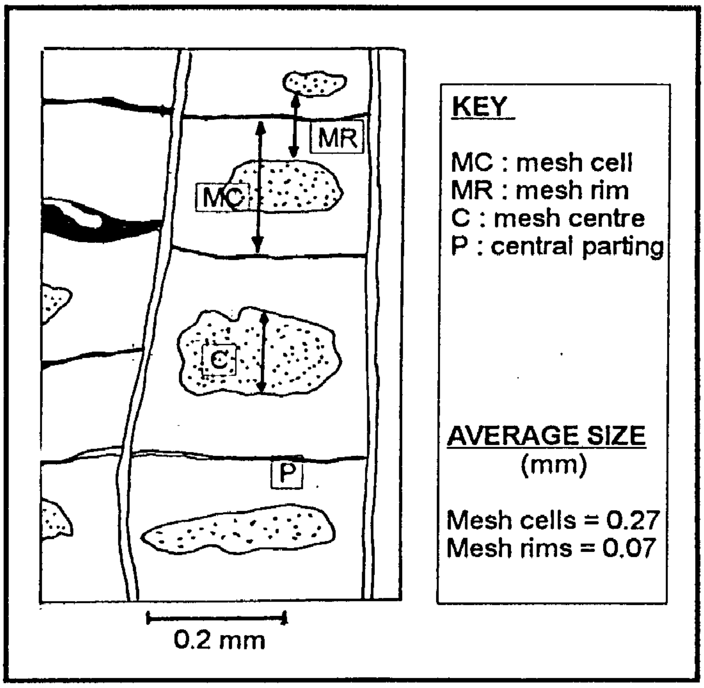

Figure 5.4 : Serpentine mesh texture morphology (modified after Wicks and Whittaker, 1977)

Hourglass textures are commonly mesh textures where the mesh centre has a characteristic hourglass morphology. *Pure* hourglass textures also occur, where the mesh rims form an hourglass morphology to the centre of the mesh cell and no mesh centre is present.

Serpentine in thin section may be characterized by the optical characteristics of the apparent fibres. Length fast apparent fibres are designated α-serpentine and length slow fibres' γ-serpentine. Table 5.1 is based on studies of the Cassiar serpentinite in British Columbia (Wicks and O'Hanley, 1988); these studies indicate that the identification of α- and γ- serpentine in relationship to the texture can provide a reasonably accurate guide to serpentine mineralogy. The mesh textures should be characterized by the optical orientation of the serpentine in the mesh rims, irrespective of that of the serpentine in the mesh centres. While γ-serpentine pseudomorphic textures after olivine may consist of either lizardite, chrysotile or antigorite, α-serpentine textures commonly consist of lizardite 1T ± brucite. Fine-grained magnetite and minor calcite are also present in the mesh structure.

Table 5.1: Serpentine textures and mineralogy (modified after Wicks and O'Hanley, 1988)

Texture	**Optical characteristics**	**Mineralogy**
	Pseudomorphic	
Mesh Rim	length-fast length-slow	lizardite chrysotile
Mesh centre, fine grained	isotropic	lizardite, antigorite, or chrysotile
Mesh centre, hourglass	length-fast length-slow	lizardite chrysotile or antigorite
Hourglass	length-fast	lizardite
	Non-pseudomorphic	
Transition	isotropic	lizardite, chrysotile, or antigorite
Interlocking	length-fast length-slow	lizardite antigorite, chrysotile, or lizardite
Interpenetrating	length-slow	antigorite, occasionally chrysotile or lizardite
Serrate veins	length-fast length-slow	lizardite antigorite

Bastites are defined by Wicks and Whittaker (1977) as " a serpentine pseudomorph after chain or sheet silicates", therefore although the term is commonly used to describe pseudomorphs after pyroxene, it may also be used to describe pseudomorphs after amphibole, talc, chlorite and phlogopite. In many cases, particularly when serpentinization is complete, it may not be possible differentiate between bastite types.

Orthopyroxenites are far more readily serpentinized than clinopyroxenites. Bastites after orthopyroxene are replaced by γ-serpentine, which parallels the (110) cleavage plane (Dungan, 1979): this commonly results in the serpentine appearing as smooth, featureless plates, although the bastites may also consist of apparent fibres. Slightly-patchy domainal bastites are common in the Great Dyke; these consist of zones of optically distinct serpentine not developed along fractures (Wicks and O'Hanley, 1988). Accessory minerals are rare, although brucite and magnetite may occur. Amphibole bastites are texturally very similar to pyroxene bastites, although mesh textures similar to pseudomorphs after olivine can occur. These amphibole mesh textures can be distinguished from olivine by the lack of a central parting in one set of mesh rims.

Serpentine pseudomorphs of talc, chlorite, and phlogopite are generally composed of lizardite 1*T*, although talc bastites may consist of an intimate admixture of lizardite and lesser brucite, and chlorite is generally replaced by antigorite. Where talc rims around orthopyroxene have been serpentinized, these may be easily mistaken for serpentine after orthopyroxene. Plagioclase feldspar may be replaced by hydrogrossular, thomsonite or serpentine during the serpentinization process (Wicks and Whittaker, 1977). Pseudomorphs after feldspar commonly have fine-grained interlocking textures, although they may also be featureless or have a very fine concentric banding.

5.3.1.2 : *Non-pseudomorphic textures*

There are essentially two types of non-pseudomorphic texture; *interpenetrating* and *interlocking*. The development of interpenetrating textures generally begins in pseudomorphic mesh centres, generally as elongate blades, flakes, or plates that interfere as recrystallization progresses, resulting in a tight interpenetrating fabric. Interpenetrating textures of antigorite form a very characteristic "flame texture". Interlocking textures consist of irregular, equant, occasionally spherulitic grains of serpentine that develop in isolated patches, merging with continued recrystallization. Unlike brucite associated with pseudomorphic textures, the brucite in these textures occurs as microscopically identifiable discreet anhedral grains.

5.3.1.3 : *Vein texture*

Three main types of veins result from late-stage serpentinization: asbestiform cross-fibre veins, asbestiform slip-fibre veins, and non-asbestiform veins. A fourth type, serrate veins, are the result of earlier recrystallization along hairline fractures and are generally identifiable by their serrated vein walls as opposed to the smooth walls of later veins.

Chrysotile asbestos cross-fibre veins are easily identified, with the fibres lying normal to the vein walls, although in larger veins the fibre orientation may be more complex, and a central parting may be present, frequently consisting of magnetite grains. Chrysotile asbestos slip-fibre veins are sheared veins in which the fibres tend to lie sub-parallel to the vein walls. Where highly sheared these slip-fibre veins have very well developed slickensides.

Chrysotile veins usually occupy large-scale fractures which cross-cut through both pseudomorphic and non-pseudomorphic textures. The vein mineralogy seems to be controlled by that of the wall rock serpentinites which suggests that the vein material is locally derived. The location and orientation of chrysotile asbestos veins are controlled by mechanical deformation. Cross-fibre veins generally occupy tension fractures and can therefore be used as kinematic indicators.

5.3.2 : Serpentinite of the study area

5.3.2.1 : *Mineralogy*

The serpentine minerals are generally colourless in plane polarized light (PPL), and low 1° grey to anomalous grey-blue under crossed polars (XPL). An apparently fibrous pale greenish-yellow sepentine is frequently intimately associated with the colourless variety, in XPL the colouration partially masks the low 1° interference colours. This yellow serpentine may represent a garnieritic serpentine with relatively high nickel content, formed as a result of near-surface weathering (Oliveira et al. 1992). Relict olivines are 'gin clear' in PPL and stands out well against the low relief serpentine minerals. In XPL the relict olivine exhibits variable interference colours from 3° blues and reds, through to low 1° yellows and light grey, depending upon the degree of alteration.

Chromite within the serpentine is a deep brick-red in PPL, and generally occurs as disseminated euhedral to subhedral grains approximately 2 mm across, as shown in plate 5.1. Chromite commonly constitutes 1-2% of the rock, and tends to form clusters on the margins and at triple point junctions of the serpentine pseudomorphs after olivine grains. Chromite is rarely seen to poikilitically enclose highly rounded olivine, as shown in plate 5.2. Where there is a fairly high proportion of chromite (>5%) in the rock, chain-textured chromite is a common feature. A well-developed example of chain textured chromite is the "Seam 3" chromite serpentinite shown in plate 5.3. Chromite is clustered at triple junctions, connecting with other concentrations via a chain of chromite along mutual grain boundaries of the original olivine grains.

The chromite is generally corroded, and is commonly bordered by a thin rim of serpentine ± talc. Magnetite generally forms a rim around corroded chromite grains, as seen in plate 5.4, and is best developed where serpentinization of the rock is complete. The original euhedral outline of the chromite grains is commonly delineated by isotropic serpentine. Partial alteration of chain-textured chromite to magnetite and serpentine is seen in plate 5.5.

Magnetite generally occurs as fine-grained crystals within central partings in mesh rims and within veins, which gives the rock a fairly strong response to magnetism. In some strongly serpentinized samples, magnetite forms lenticular aggregates over 1 mm across and 0.2 mm wide, surrounded by a thin rim of serpentine. The lenses cross-cut the mesh-textured serpentine, but show a general alignment with the main serpentinization trend. The textural character of magnetite has a significant effect on the appearance of a serpentinite, and is summarized in table 5.2.

Table 5.2: Magnetite distribution and rock colour

Serpentinization stage	Magnetite distribution	Rock colour
Early	Very fine, discreet grains throughout the serpentine.	Black or dark grey
Middle	Coarser grains, concentrates in mesh centres or central parting of mesh rims.	Pale grey or brown
Late	Migrates out of mesh cells into cross-cutting lenses and veinlets	Green, often a pale green.

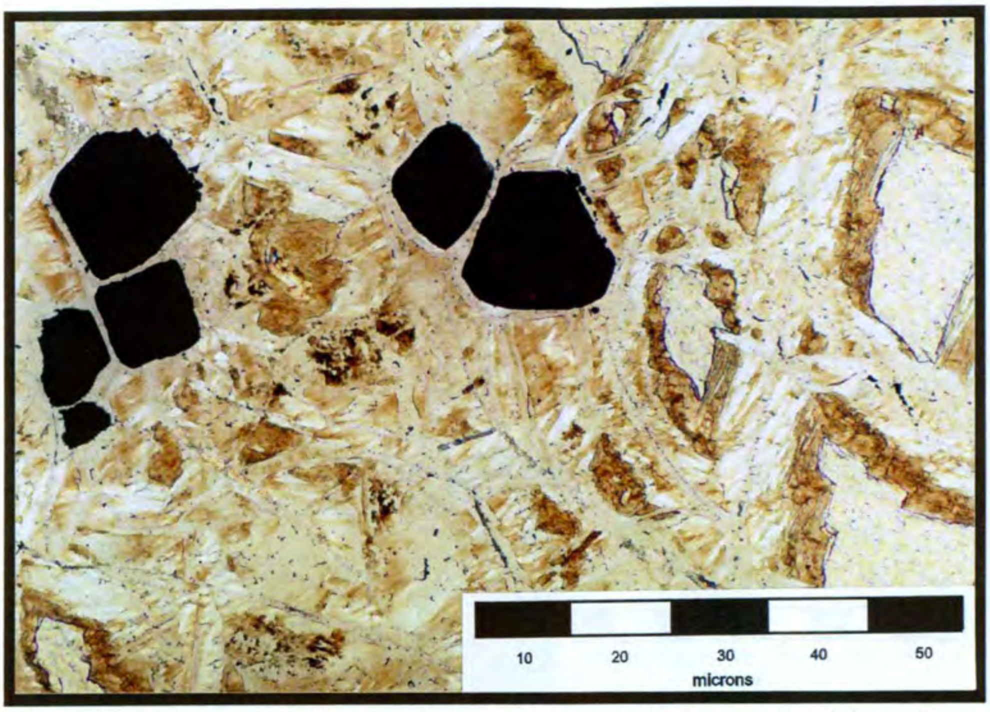

Plate 5.1 : Euhedral disseminated chromite grains in serpentinite. (Plane polarised light)

Plate 5.2 : Disseminated chromite grains enclosing olivine (serpentinized) in serpentinite. (Plane polarised light)

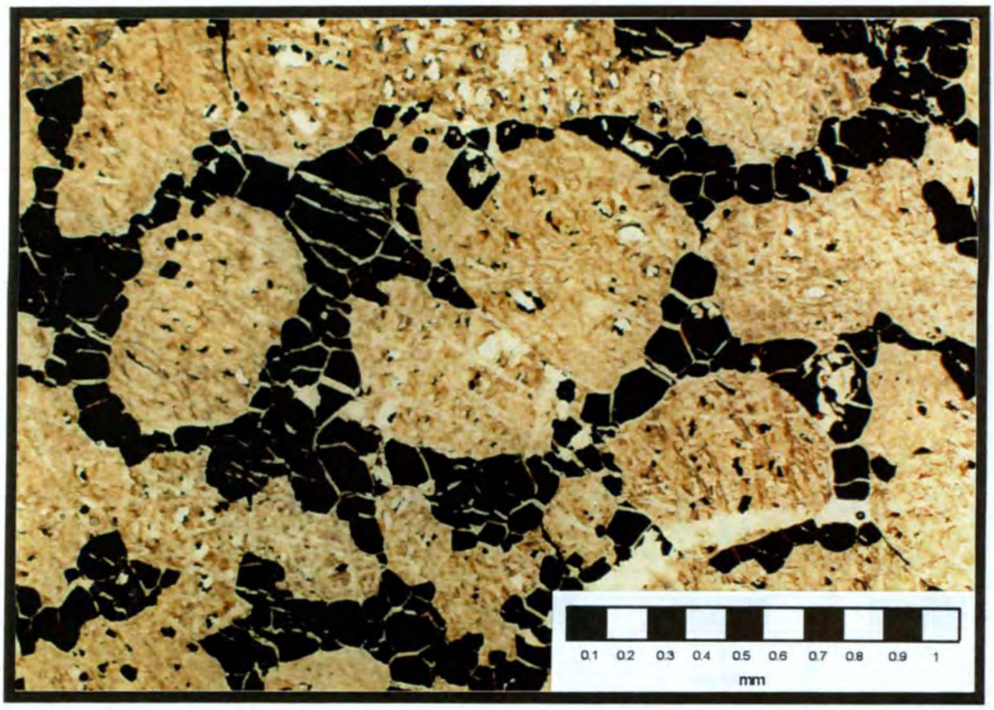

Plate 5.3 : Chain textured chromite from chromite serpentinite. (Plane polarised light)

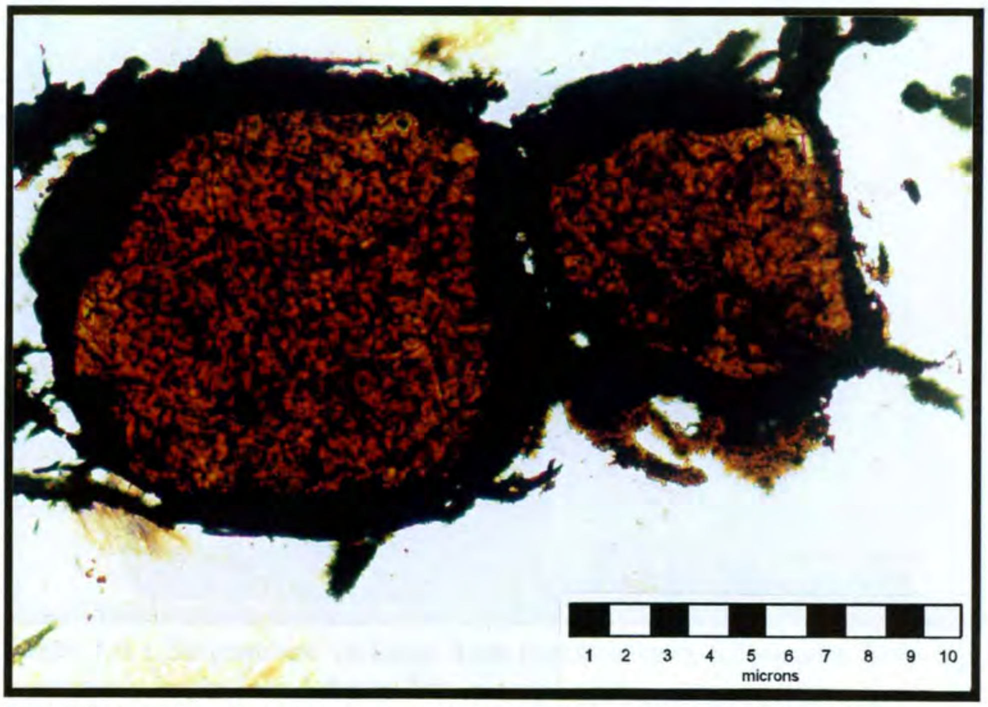

Plate 5.4 : Altered and corroded chromite rims. (Plane polarised light)

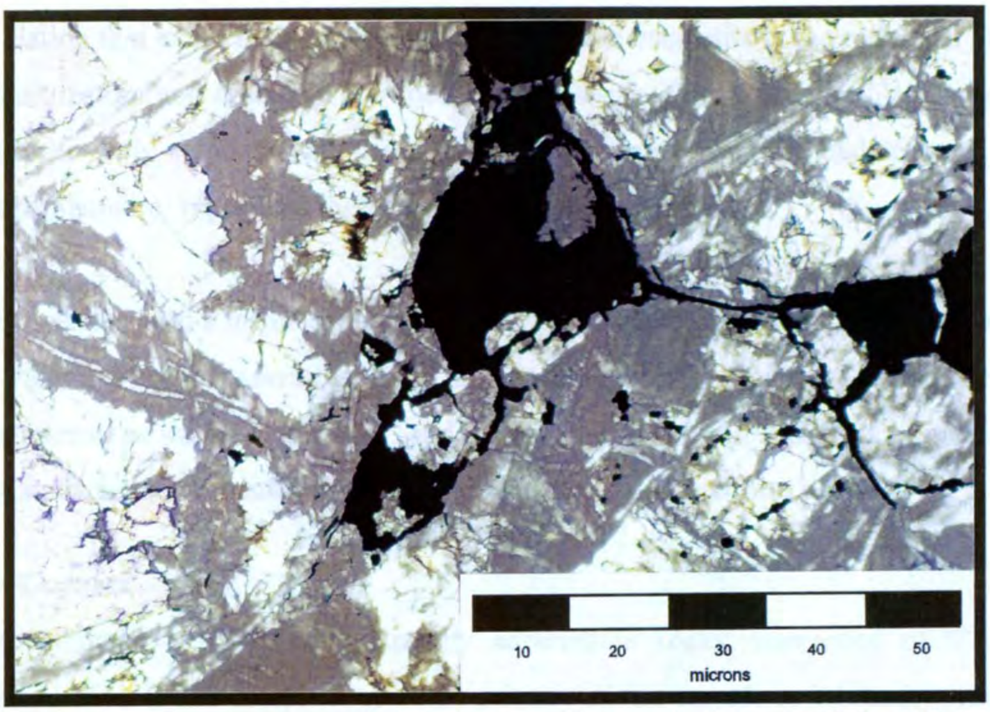

Plate 5.5 : Altered and corroded chain textured chromite in serpentinite. (Plane polarised light)

Plate 5.6 : Serpentinite varieties from borehole core. Clockwise from top: moderately serpentinized dunite, brown serpentinite, grey serpentinite, mottled serpentinite, black serpentinite. See text for discussion.

The correlation that exists between the distribution of the magnetite in the rock, and the degree of serpentinization and colour of the rock can be seen in plate 5.6. The 'black serpentinite' represents the early serpentinization stage, the 'grey serpentinite' the middle stage, and the 'mottled serpentinite' represents the late stage of serpentinization.

Talc ± magnesite is not a major component of the serpentinites, but it is a ubiquitous accessory mineral. Although talc occasionally occurs as very small discrete grains, it is commonly present as aggregations , as shown in plate 5.7, and in association with serpentine veins, particularly as cryptocrystalline material within the central parting of non-asbestiform veins.

5.3.2.2 : *Textures*

The serpentinites were originally strongly adcumulate rocks, composed of 97 to 99% serpentinized olivine. The morphology of the primary olivine cumulates is broadly preserved by the pseudomorphic textures. Outlines of the original grains are commonly delineated by chain-textured chromite and fine-grained magnetite along the primary grain boundary, differing degrees of serpentinization between grains, and the optical continuity of relict olivine in individual grains. Relicts of the original olivine are only preserved in the mesh centres of the well-developed pseudomorphic serpentine mesh textures shown in plate 5.8. The average grain size of the olivine pseudomorphs varies from 2-3 mm, and the proliferation of triple junctions amongst original grains, outlined by magnetite and chromite, are indicative of the granular textures of the cumulus assemblage.

Well-developed mesh-textured pseudomorphic serpentine characterises the majority of the serpentinites, although these textures are frequently modified by non-pseudomorphic interpenetrating and interlocking textures. The serpentine in the mesh cell surrounding the mesh centres frequently exhibits a 'herringbone' texture that reflects the distinctive serrated topology commonly shown by mesh centres, as seen in plate 5.8. It is postulated that the development of these textures is the result of dislocation creep in the relict olivine: either as a relict pre-serpentinization feature, or developed in response to stress produced by the increase in volume associated with the serpentinization process. Many mesh rims are compound and consist of an inner rim of γ- serpentine, such as the 'herringbone' serpentine, and an outer rim adjacent to the central parting commonly of α-serpentine. Within the mesh cell, a yellow-brown alteration rim is

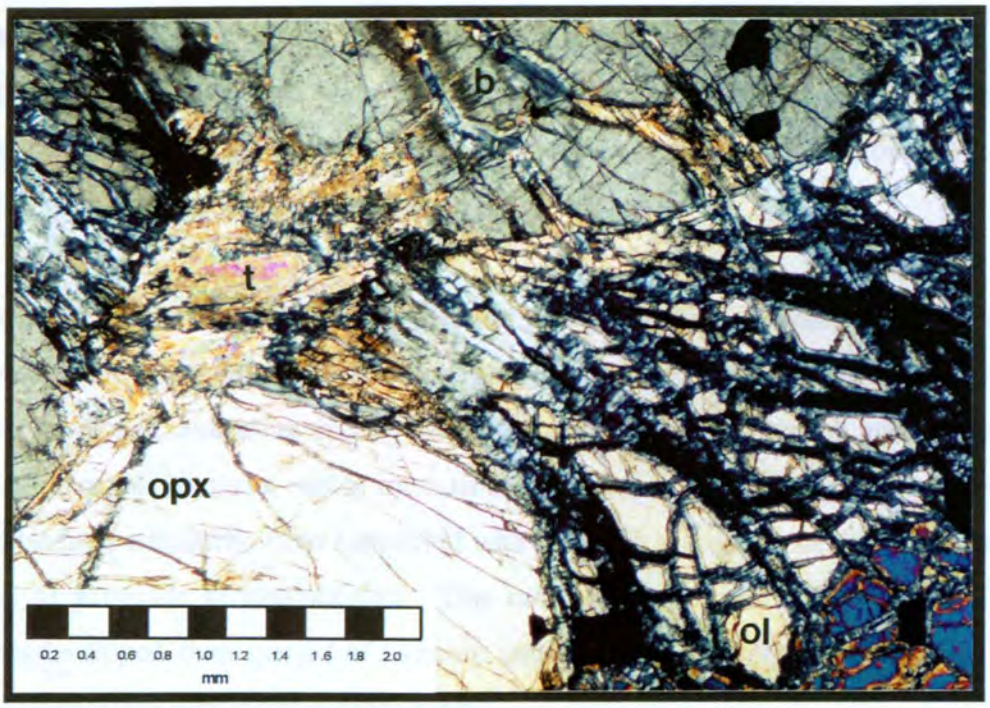

Plate 5.7 : Olivine pyroxenite showing development of talc (**t**) aggregates. Note bastite serpentinization (**b**) of large, rounded orthopyroxene (**opx**) grains, and serpentinized olivine (**ol**). (Crossed polars)

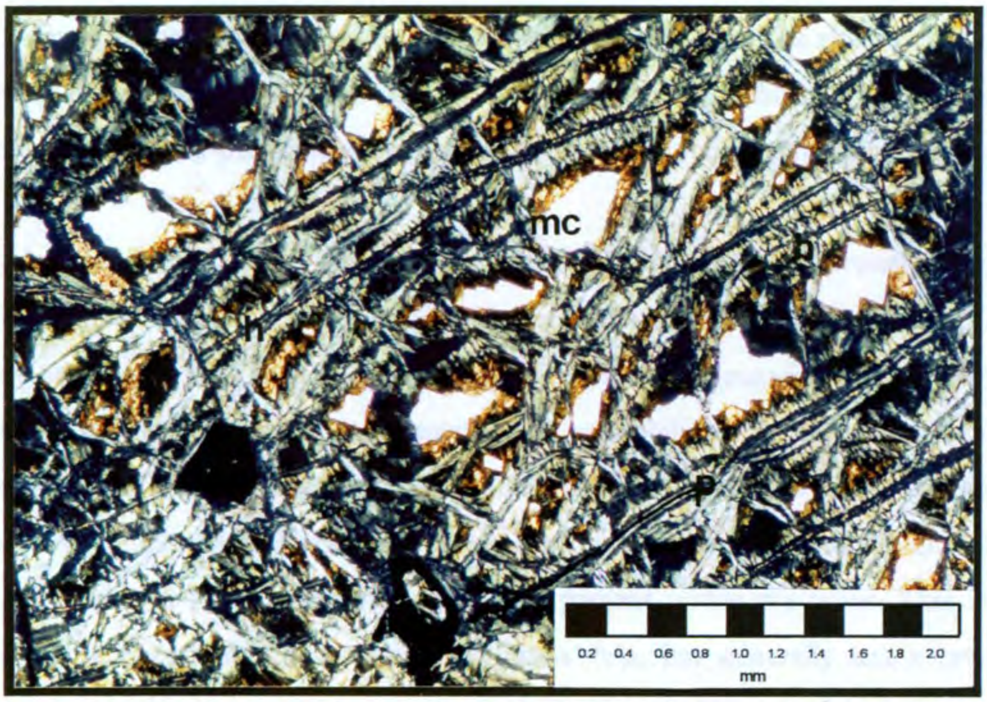

Plate 5.8 : Mesh textured serpentine with altered olivine mesh centres (**mc**). See text for discussion. Note 'herringbone' serpentine (**h**), and magnetite vein partings (**p**). (Plane polarised light)

commonly developed around the relict olivine, which is probably a result of the release of iron at the serpentinization front (see plate 5.1). Partings in mesh cells are well developed, and commonly bipartite, with a central parting of magnetite + serpentine, and an outer parting of α-serpentine with apparent cross-fibres normal to the vein walls.

Where serpentinization of the rock is complete, or nearly complete, all mesh centres are replaced by serpentine. The serpentine mesh centres are generally isotropic. Mesh textures in some samples are poorly developed, indicating that the serpentinite is transitional between pseudomorphic and non-pseudomorphic textures, within mesh rims, γ-serpentine frequently forms interpenetrative laths and blades, particularly when associated with isotropic serpentine mesh centres, suggesting a degree of prograde serpentinization. Thin cross-cutting serrate veins 0.1 mm across are sometimes developed: these consist of a serrate centre of isotropic serpentine bordered on either side by γ-serpentine with indistinct vein walls.

The purple-brown alteration of the 'brown serpentinite' (see plate 5.6) represents regions of cryptocrystalline aggregates of haematite, with indistinct non-pseudomorphic serpentine and fine-grained magnetite, magnesite (possibly altered to siderite) and talc. The altered bands are likely to represent ingress of post-serpentinization, late-stage oxidizing fluids. Between these areas, pseudomorphic and non-pseudomorphic textured serpentine occurs and magnesite is common.

A strong serpentinization fabric is prevalent in many samples. This fabric is broadly parallel to the dip of the primary layering, and is occasionally accentuated by fine light and dark lineations. These are seen under high magnification to be due to linear aggregations of very fine-grained magnetite. Chromite is strongly fractured and re-mobilized in the orientation of the serpentinization fabric. Multi-stage vein development is shown by large veins several millimetres wide that cross-cut the serpentinite. These consist mainly of cryptocrystalline granular serpentine that is pale green in PPL; opaline quartz is also present within the veins. Thin cross-fibre chrysotile sometimes forms a border to the main vein, but generally has a cross-cutting relationship, as do thin magnetite ± serpentine ± talc veins, as shown in plate 5.9.

Serpentinites near surface are commonly heavily silicified, which generally destroys many details of the pseudomorphic textures. However, where silicification is slight, mesh-textures are locally preserved but show a complex alteration of the mesh centres that generally exhibit the following zonation:

1) a core of isotropic serpentine.

2) an inner rim of clear-yellowish granular serpentine bordered by a reddy-brown haematitized zone

3) an outer rim of granular serpentine with localized areas of brown iron oxide concentration and some blebs of fine-grained magnetite.

The earthy aggregates of iron oxides associated with the mesh centres are sometimes extensively developed, occupying much of the mesh cell. The oxides were identified as haematite on the basis of the reddish brown colour and very high relief.

5.4 : PYROXENITES

The orthopyroxenites of the lower part of the Pyroxenite Succession are strongly adcumulate and contain more than 97% orthopyroxene. The orthopyroxenites are coarse-grained equigranular rocks with well-equilibrated granular texture and ubiquitous triple junctions. Average grain sizes are generally 2.5 to 3 mm, the exception being pyroxenite P6, which is of markedly coarser grain-size, averaging 4 mm across.

In PPL, the orthopyroxene is sometimes weakly pleochroic from colourless to pale green, but generally colourless. In XPL, the orthopyroxenes show 1° grey-yellow interference colours. Some orthopyroxene grains show fairly well-developed exsolution lamellae along 100, seen as very fine alternating light and dark striations. These lamellae are particularly common amongst the smaller grains. Evidence of dislocation creep is relatively common in some samples, the grain in the top right of plate 5.10 shows subgrain-wall development and slightly serrate (now equilibrated) grain boundaries.

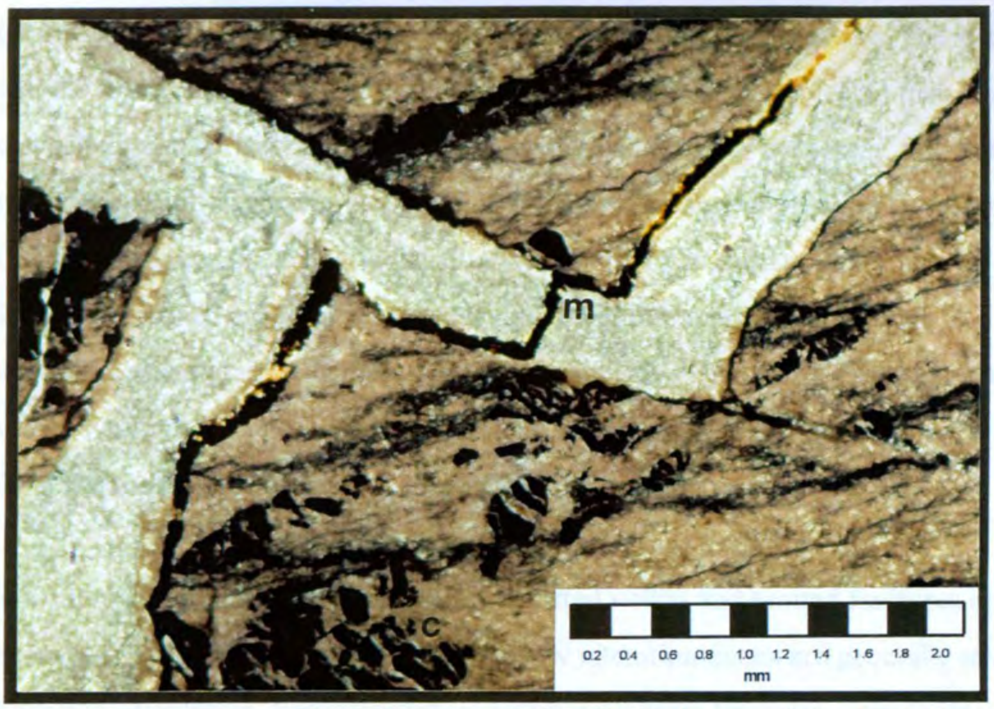

Plate 5.9 : Large serpentine veins cross-cutting silicified serpentinite. Note later cross-cutting magnetite vein (**m**), and highly fractured chromite (**c**). (Plane polarised light)

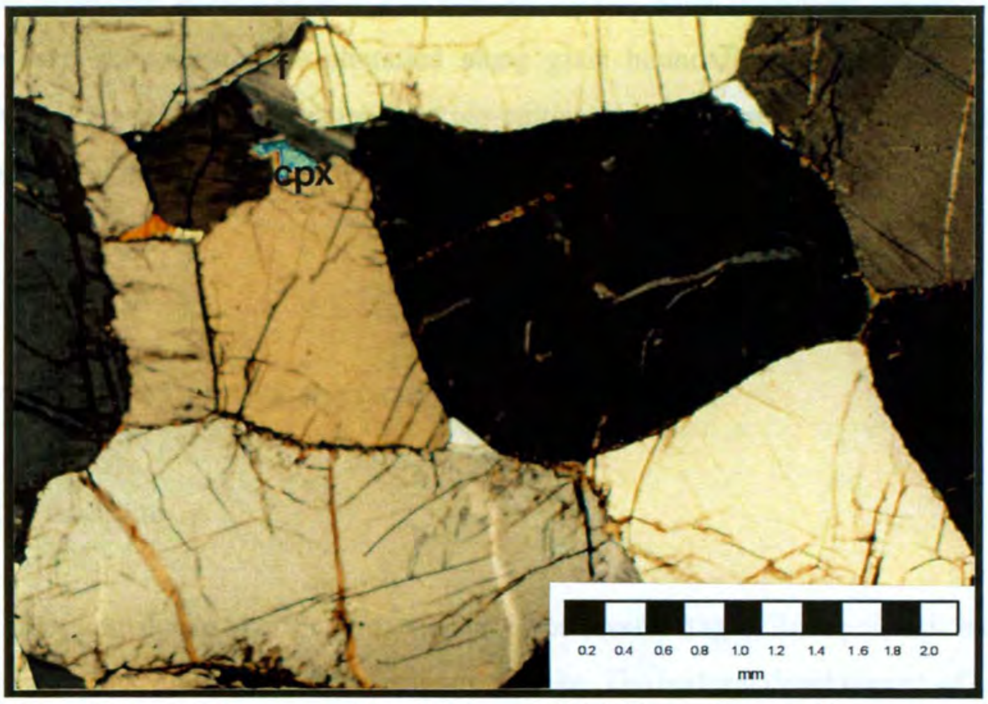

Plate 5.10 : Orthopyroxenite with interstitial feldspar (**f**) and clinopyroxene (**cpx**). See text for discussion. (Crossed polars)

The orthopyroxenites generally contain less than 1% interstitial plagioclase. The exception is pyroxenite P3, which contains slightly more post-cumulus plagioclase (1-2%) than layers P4 to P6. The plagioclase is variably altered and occurs as small, broadly triangular, interstitial grains less than 1 mm across, as shown in plate 5.10. Clinopyroxene and phlogopite are very minor interstitial components, occurring as small anhedral grains less than 1 mm across. A small proportion of fine-grained euhedral chromite is found within the orthopyroxenites. The chromite commonly occurs along grain boundaries, but is occasionally enclosed by orthopyroxene grains. Pyroxenite P5 was seen to contain slightly more chromite than the other pyroxenites, comprising up to 1% of the rock and disseminated throughout the orthopyroxenes.

Serpentinization of the orthopyroxenes is concentrated within and around fractures and diffuse alteration zones cross-cutting the zones. These narrow alteration zones are generally straight and show a preferred orientation. Serpentinization within intra-grain fractures extends into the grain along cleavage planes. When fractures are developed at high angles to the cleavage, the alteration develops along en echelon sigmoidal zones normal to the cleavage, with the alteration taking place along the cleavage plane. Grain boundaries are also corroded and serpentinized. Talc and opaque oxides are commonly associated with serpentinized zones. When tectonised, the rock is heavily fractured and shows extensive alteration along grain boundaries, where very fine-grained magnetite aggregations are common in cross-cutting veins of serpentine minerals and other alteration products.

5.5 : INTERMEDIATE LITHOLOGIES

5.5.1 : Introduction

The transition from dunite to orthopyroxenite involves several stages, from poikilitic harzburgite through granular harzburgite to olivine orthopyroxenite. The textural development of each stage is complex, and petrologic analysis is complicated further by the generally extensive serpentinization of the rocks.

5.5.2 : Poikilitic harzburgite

The distinctive poikilitic harzburgite in the area (see plate 4.3) consists of large optically-continuous orthopyroxenes, enclosing rounded olivine grains. The postcumulus orthopyroxene oikocrysts vary in size, from less than 5 mm to over 2 mm across. There is a general antipathetic relationship between the size of the oikocrysts and the frequency of their distribution. All the harzburgites in the study area exhibit fairly pervasive serpentinization. The most significant variation in the degree of serpentinization is shown by the orthopyroxenes, as olivines are invariably pervasively serpentinized.

Jackson (1961) showed that the replacement of olivine by peritectic reaction with the melt to produce orthopyroxene oikocrysts was a fundamental feature of poikilitic harzburgites. The textural development, and the reaction relationship between (now serpentinized) olivine and orthopyroxene is shown in plate 5.11. The orthopyroxene oikocryst encloses embayed and highly rounded olivine grains. Similar textures are observed in the boundaries of olivine grains bordering the oikocryst. Where not in contact with orthopyroxene, the olivine pseudomorphs generally show low-curvature mutual interference boundaries. An additional feature indicating the reaction relationship of olivine - orthopyroxene is illustrated in the middle of plate 5.11 by the interstitial appearance of the apices in the olivine pseudomorph.

The harzburgite shown in plate 5.11 has been pervasively serpentinized, the orthopyroxenes completely serpentinized to domainal bastite pseudomorphs. Boundaries between olivine and orthopyroxene pseudomorphs are commonly delineated by a thin rim of talc ± magnesite. In the most heavily altered poikilitic harzburgites, mesh textured serpentine after olivine is heavily altered to cryptocrystalline serpentine and silica. Cross-cutting corrosive veins of talc and magnesite after serpentine are observed, with cryptocrystalline silica replacing adjacent mesh textured serpentine.

5.5.3 : Granular harzburgite - olivine orthopyroxenite

The transition from poikilitic harzburgite to granular harzburgite is marked by a change of textural status of orthopyroxene from heteradcumulus to cumulus, with orthopyroxene present as discrete grains. The granular harzburgites are generally strongly adcumulate, with fairly well-equilibrated textures of low-curvature mutual-interference grain boundaries and triple-junctions developed in both olivine and orthopyroxene cumulates. However, mutual grain boundaries between the two phases are very complex and commonly exhibit reaction relationships. Olivine is generally interstitial to rounded, and frequently embayed orthopyroxene, although this is not always the case. Plate 12 shows a highly corroded and interstitial olivine in reaction relationship with the surrounding orthopyroxene; note the cumulus olivine grain in textural equilibrium with orthopyroxene in the bottom left of the photograph. Orthopyroxene grains tend to be slightly coarser (3 mm) than the original olivine grains (2 mm) which are delineated by fine-grained magnetite.

The textural transition to olivine orthopyroxenite is marked by the increasingly interstitial nature of the olivine grains, which eventually poikilitically enclose orthopyroxene. The relatively coarse orthopyroxene grains are rounded and frequently embayed. Wilson (1982) suggested that the corrosion of the pyroxene may take place by the reaction:

$$\underset{\text{pyroxene}}{MgSiO_3} = \underset{\text{olivine}}{MgSi_{0.5}O_2} + 0.5\ SiO_2$$

It has been suggested that this textural relationship of olivine and orthopyroxene is the result of metastable crystallization (Wilson, op.cit.), the downward percolation of primitive magma (Wilson and Prendergast, 1989), or by settling of orthopyroxene held in turbulent suspension into a basal magma layer crystallizing olivine (Eales and Cawthorn, 1996).

Plate 5.11 : Pervasively serpentinized poikilitic harzburgite showing large orthopyroxene oikocryst, now altered to bastite serpentine (**b**) and serpentinized olivine (**ol**). Overlay included to highlight olivine - orthopyroxene textural relationships: see text for textural discussion. Note small chromite grains enclosed by orthopyroxene in the lower left of the photomicrograph. (Crossed polars).

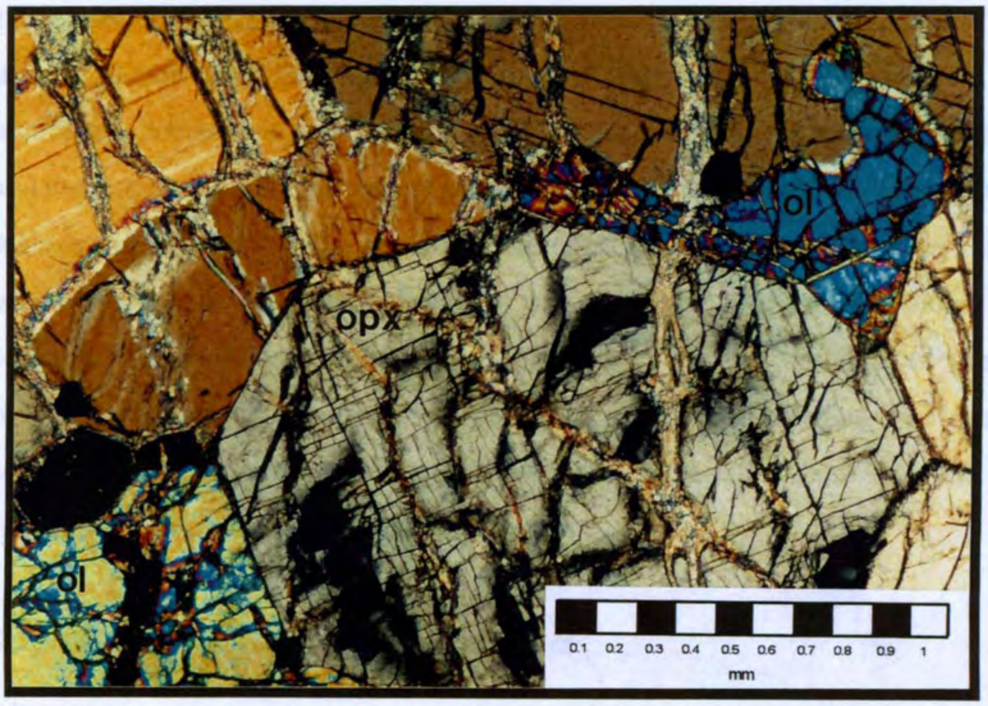

Plate 5.12 : Granular harzburgite showing textural equilibration of orthopyroxene grains (**opx**) and highly rounded olivine (**ol**). Note cross-cutting veins of serpentine + talc. See text for further discussion. (Crossed polars)

5.5.4 : Centimetre pyroxenite

An unusual 1 cm-wide orthopyroxenite, consisting of 97% orthopyroxene, occurs within a granular harzburgite developed beneath pyroxenite P4. This 'centimetre pyroxenite' was found at surface in the mapping area, and at 12.08 metres in borehole H10/4a, indicating at least some degree of continuity. The olivine-rich granular harzburgite, containing 20% bastite orthopyroxene, grades over the space of one millimetre into the orthopyroxenite, which then grades equally rapidly upwards back into the granular harzburgite. No significant differences were observed between the harzburgite above and below this layer. The origin of the 'centimetre pyroxenite' is unknown, but it seems likely to be the result of deviations from the olivine-orthopyroxene cotectic in response to a fluctuation in the crystallizing conditions within the magma chamber. The orthopyroxenes of the 'centimetre pyroxenite' are variously altered to bastite, with serpentinization generally strongest towards both contacts. The gradational nature of the transition from relatively featureless bastite to strongly domainal bastite textures can be seen in plate 5.13.

An interesting textural relationship was noted at the contact in one sample, shown in plate 13. This texture of mutual embayment of the olivine and orthopyroxene pseudomorphs is probably the product of reaction-relationship between the orthopyroxene and olivine. It is suggested that the textural development of this feature involved the replacement of cumulus olivine crystals by postcumulus overgrowth of the orthopyroxene. Unfortunately it is not known whether this feature is at the stratigraphically upper or lower contact of the 'centimetre pyroxenite'.It should be noted that the development of domainal bastite roughly coincides with the limit of the olivine-orthopyroxene reaction-replacement texture. The distinctive morphology of the mutual embayment may have been accentuated by dislocation creep, although there is no real evidence of this, perhaps due to obscuration by serpentinization.

5.5.5 : Serpentinization of intermediate lithologies

There appears to be a positive correlation between increasing olivine content and the degree of serpentinization, the more resistant orthopyroxenes presumably limiting ingress of serpentinizing fluids in the orthopyroxene-rich harzburgites. In olivine-rich granular harzburgites, the orthopyroxene is more pervasively altered to bastite pseudomorphs, and relict olivine mesh centres in serpentine are replaced by isotropic serpentine.

Pseudomorphic mesh-textured serpentine after olivine is consistently developed, with relict olivine generally well-preserved in mesh centres. There is a well-developed fabric within the serpentine, delineated by thin non-asbestiform veins, along which the orthopyroxenes are extensively fractured. Serpentinization of the orthopyroxene grains is concentrated along intra-grain fractures, and as a thin rim around grain boundaries. Serpentinization is frequently observed to extend into the orthopyroxene along the 100 plane, irrespective of the orientation of the fracture. In the upper middle of plate 5.7, serpentinization is seen to extend into the orthopyroxene approximately perpendicular to the serpentine-filled fracture.

Fine-grained magnetite development is well developed in vein partings within serpentine after olivine, but is infrequently associated with the orthopyroxene bastites. Talc is commonly developed within serpentine veins. Some talc aggregations occur, consisting of wispy laths showing perfect basal cleavage and high 3° interference colours. In plate 5.7, it can be seen that the talc alteration extends into the orthopyroxene and olivine grains. Cross-cutting talc-rich alteration zones several millimetres wide were frequently observed, in which pseudomorphic textures are partially destroyed, and mesh centres are replaced by isotropic serpentine. Orthopyroxenes are also affected by this zone, and exhibit extensive bastite development.

5.6 : CHROMITITES.

5.6.1 : Introduction

Layers C5 to C8 are essentially massive coarse-grained chromitites. Lower contacts are generally sharp, but upper boundaries commonly grade upwards through olivine chromitite to chromitiferous serpentinite. Chromitite C5 is the most economically important and complex of the chromitites within the studied succession, and petrological work concentrated on this chromitite.

The following description is an account of the textural and mineralogical features of the C5 layer and the immediate footwall and hanging wall to the chromitite.

5.6.2 : Chromitite C5

The P6 footwall orthopyroxenite to chromitite C5 contains 3-4% disseminated chromite towards the base of the C5 layer, and is strongly fractured and serpentinized along grain margins. Four different orthopyroxene- rich zones were identified within the 2 centimetres below chromitite C5, these are:

1) Orthopyroxenite of the P6 layer.
2) Weakly altered bastite after orthopyroxene (~4 mm thick).
3) Moderately altered bastite after orthopyroxene (~5 mm thick).
4) Heavily altered bastite after orthopyroxene (~4 mm thick).

As can be seen from plate 5.14, the base of the chromitite is quite irregular, and the thicknesses given are therefore approximations. The boundaries between the zones are gradual over 1-2 mm. The weakly-altered bastite zone consists of domainal bastite serpentine with abundant granular serpentine, talc, and magnesite occupying numerous fractures that extend into the underlying orthopyroxenite. Near the base of the bastite zone, haematitized iron oxides commonly occur as earthy aggregates associated with fractures. This zone grades into moderately altered bastite, wherein the bastite is pervasively altered to indistinct granular-fibrous talc, serpentine, magnetite and alteration products, cross-cut by veins of iron-rich silica parallel to the base of chromitite C5. Lenticular pods of bastite orthopyroxene are identifiable in this zone, but become rare in the heavily altered zone. Silica and iron alteration increases in the heavily altered zone; the talc and serpentine are apparently altered to clay-like minerals in this zone, and is seen to adsorb water when the rock is wetted.

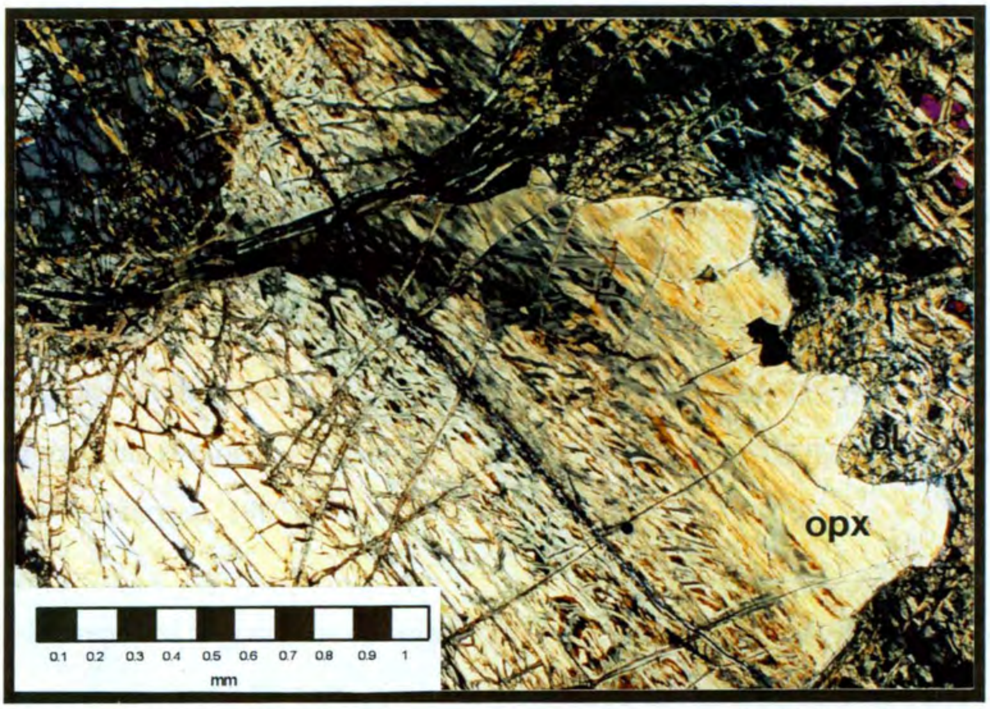

Plate 5.13 : Transition from the centimetre orthopyroxenite (left and centre) to granular harzburgite (top right). Note the mutual embayment of the contact between bastite orthopyroxene (**opx**) and olivine (**ol**). (Crossed polars)

Plate 5.14 : Footwall of chromitite C5. See text for discussion.

Chromite becomes strongly clustered and slightly coarser-grained (~0.4 mm) towards the top of the orthopyroxenite. At the base of the bastites, chromite becomes finer-grained (~0.2 mm) and weakly chain-textured. Chain-textured chromite persists through the bastite, although the textures are commonly disturbed by the intense serpentinization and alteration. Within the heavily altered zone, chromite abundance increases sharply towards the C5 layer and becomes more strongly chain-textured. Between the heavily altered zone and chromitite C5, shearing along the contact has resulted in the development of a 1 mm thick sliver of ferruginous silica that has a distinctive wispy texture. This shearing is a common feature of chromitite C5 in the Mutorashanga area (Wilson and Prendergast, 1987).

Wilson (1982) reported the common occurrence of a distinctive poikilitic harzburgite between the chromitite and the footwall P6 orthopyroxenite, described as representative of a zone of liquid entrapment. This is shown in figure 5.5, and is described as being generally a few millimetres thick in which optically continuous orthopyroxene encloses, and is enclosed by, selvedges of fine-grained chromite. The orthopyroxene is considered to have formed by reaction-replacement of primary olivine cumulates, indicated by the occurrence of relict and corroded olivines poikilitically enclosed by the orthopyroxene. A narrow concentration of fine-grained chromite occurs at the base of the zone, where it is draped over the underlying orthopyroxenite. It is suggested by the writer that the bastite zones observed at the base of chromitite C5 are representative of the poikilitic harzburgite described by Wilson (op.cit.), with many primary features, such as the relict olivine and the draped chromite at the base of the zone being obliterated by the pervasive serpentinization and subsequent alteration of the silicates.

Chromitite C5 is massive for most of its 10-20 cm thickness, consisting of densely interlocking polygonal chromite grains 1-3 mm across. This ‘hard & lumpy’ chromitite is characteristic of the C5 layer in the Mutorashanga area. No primary silicates occur between chromite grains, although thin selvedges of secondary serpentine and associated minerals are common; these are frequently replaced by cryptocrystalline silica. The chromitite is characteristically moderately fractured, probably due to expansion during the serpentinization process. Fractures are infilled by serpentine and/or cryptocrystalline silica.

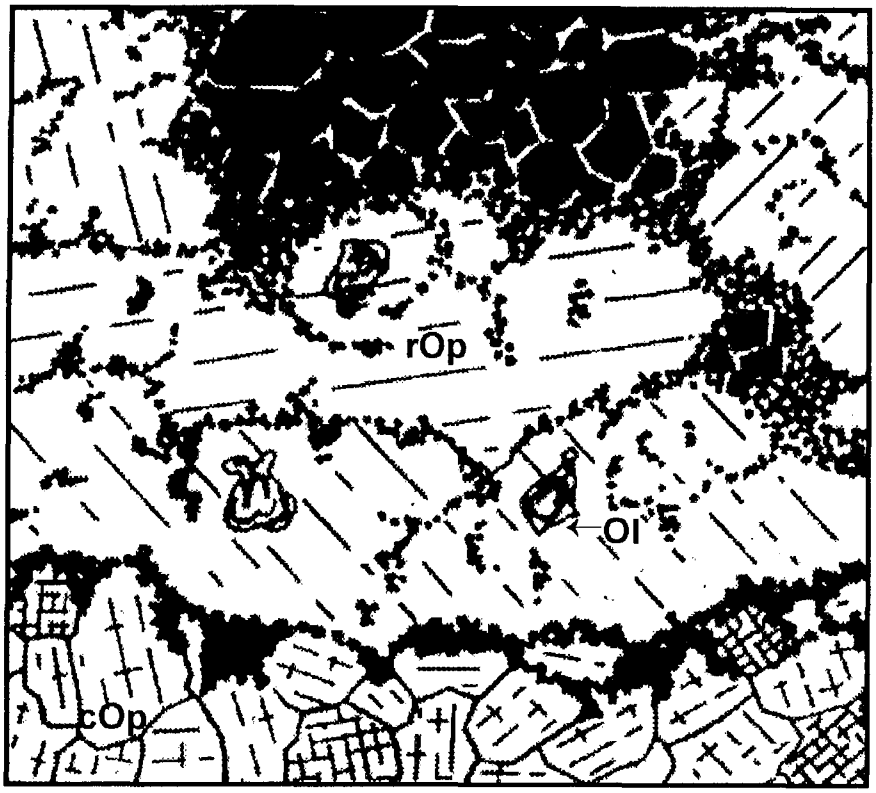

Figure 5.5 : Illustration of the interface between chromitite C5 and underlying pyroxenite P6 from the Mutorashanga area. Relict and corroded olivine (Ol) is enclosed by optically continuous reaction orthopyroxene (rOp), separated by layers of fine-grained chain-textured chromite. Outlines of original olivine crystals, of which only remnants remain, are marked by fine-grained chromite. Fine-grained chromite is also draped over cumulus orthopyroxene (cOp) of pyroxenite P6. (Modified after Wilson and Prendergast, 1987)

The massive chromitite passes upwards into a thin 'mottled chromitite' with common spherical inclusions of olivine within the chromite (see plate 5.15). The inclusions increase in size and abundance over a short distance, connecting up as the silicate component increases and giving way at the top of the chromitite to chain-textured chromite within serpentinite. Wilson and Prendergast (1987) report that a zone of reaction orthopyroxene development occurs immediately above chromitite C5 in the Mutorashanga area, within the axis, this can be up to a metre thick, although towards the axis the zone dies out. In the mapped area, this zone was not observed, and the chromitite was seen to grade upwards over a few millimetres into a serpentinized adcumulate dunite, containing approximately 5% disseminated chromite, decreasing to 2% away from chromitite C5. Limited development of reaction orthopyroxene (now serpentinized to pseudomorphic bastite) was observed near the top of the chromitite, however, as shown in plate 5.15: this was developed within the mottled chromitite, and partially enclosed highly rounded serpentinized olivine grains.

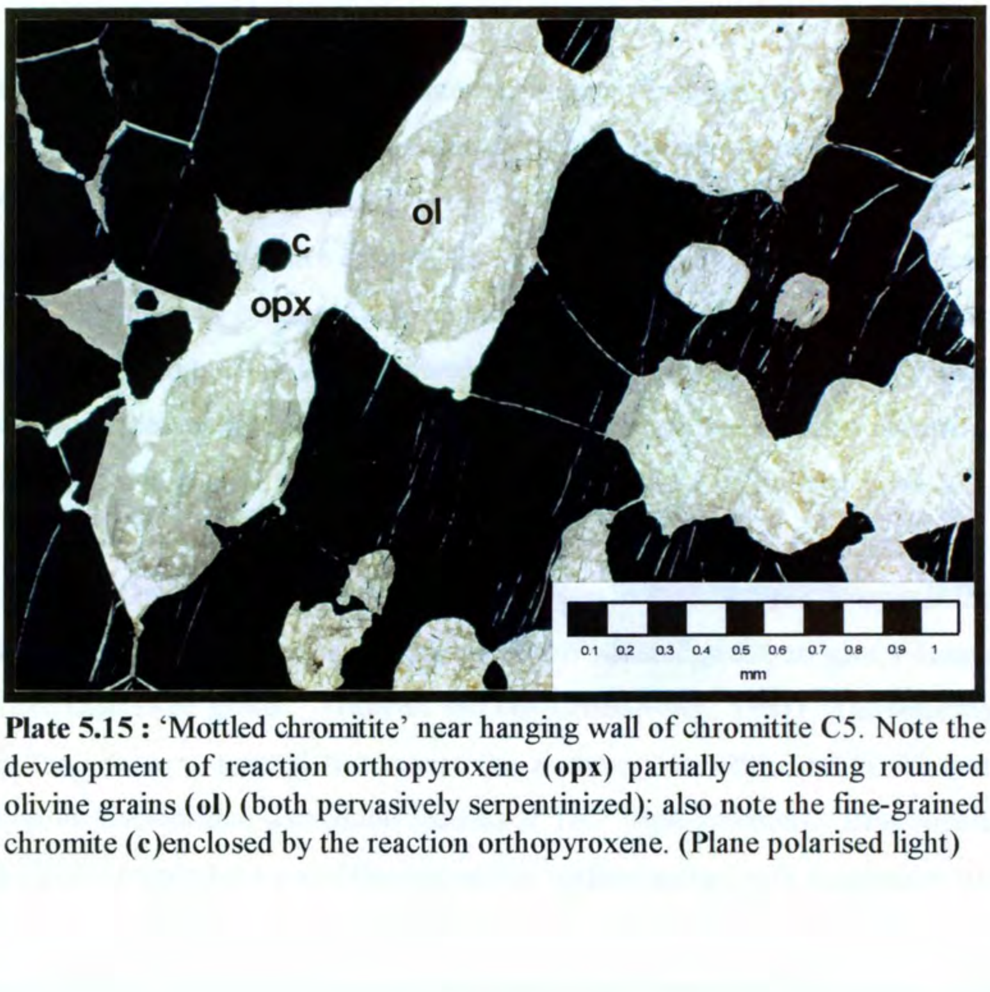

Plate 5.15 : 'Mottled chromitite' near hanging wall of chromitite C5. Note the development of reaction orthopyroxene (**opx**) partially enclosing rounded olivine grains (**ol**) (both pervasively serpentinized); also note the fine-grained chromite (**c**)enclosed by the reaction orthopyroxene. (Plane polarised light)

The "Puppy Seam", chromitite C5b, is a fairly persistent 3-5 cm thick layer that occurs 6-15 m above the C5 layer, the chromitite is termed C5b in this study, in accordance with the stratigraphic nomenclature suggested by Wilson and Prendergast (1989). In the mapped area, the chromitite is generally present as a fine-grained cataclastite. The chromitite is extensively micro-brecciated into angular fragments of widely varying grain size; grains are generally sub- 0.005 mm, although some clasts are up to 1 mm across. The chromite grains are hosted by an isotropic cryptocrystalline matrix.

5.6.3 : Post-cumulus enlargement of chromitites

The post-cumulus enlargement of chromites in massive chromitites is evidenced by the large anhedral grains in these environments, particularly those within the hard and lumpy ore that is characteristic of most of the LGC. Significant post-cumulus modification is also indicated by the observed porosities within massive chromitites: which is generally than 10%, significantly lower than the ~30-45% porosity calculated and experimentally determined for these rocks (Hulbert and von Gruenewaldt, 1985). Chain textured chromite also regularly shows evidence of enlargement. Within mottled chromite, the presence of considerably finer-grained euhedral chromite enclosed by silicates, shown in plate 5.15, also indicates two generations of chromite growth.

Within the Great Dyke, the most acceptable mechanism to explain these features is through the "annealing or sintering of fine-grained aggregates of strained grains to give a coarse-grained aggregate of unstrained grains." (Hulbert and von Gruenewaldt, 1985). The sintering process results in the coarse polygonal textures of the massive chromitites, when the system is in thermodynamic equilibrium, with grains meeting at 120° triple junctions. Grain boundaries will tend to be fairly straight because of the decrease in surface energy with decrease in curvature.

Small, semi-spherical, silicate inclusions within chromite have been described from several layered intrusions, including the Bushveld Complex (Hulbert and von Gruenewaldt, 1985) and Stillwater Complex (Jackson, 1966). The inclusions commonly consist of minerals that are not part of the cumulus assemblage at the stratigraphic level in which they occur, they are therefore considered to form as a result of the sintering process, as shown in figure 5.6. At the grain contacts high local

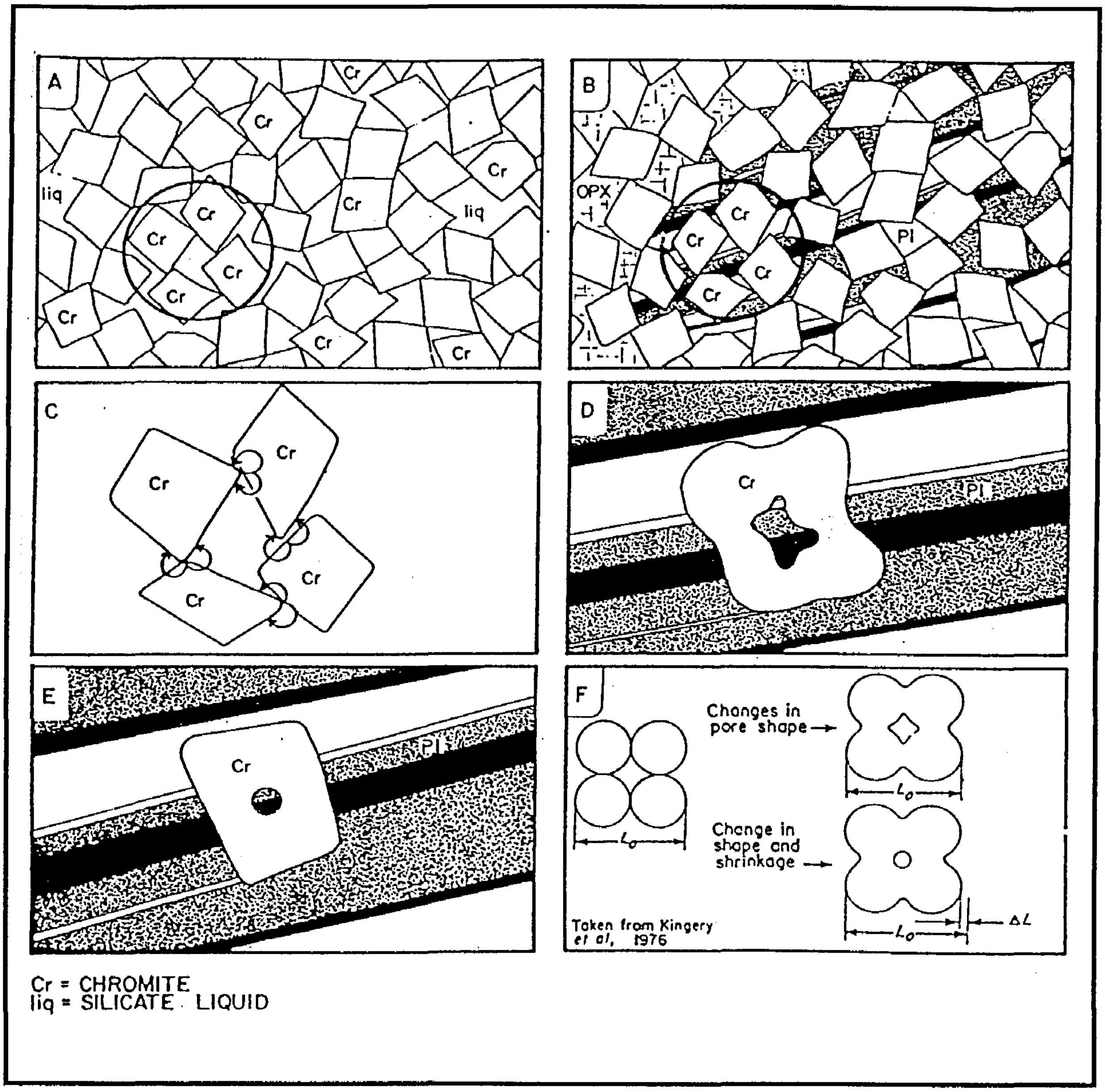

Figure 5.6 : Schematic representation of the sintering process as envisaged by Hulbert and von Gruenewaldt (1985) for the Bushveld chromitites: (A) accumulation of cumulus chromite crystals surrounded by intercumulus liquid; (B) crystallization of poikilitic plagioclase and orthopyroxene from intercumulus liquid; (C) high local stresses at grain contacts lead to plastic deformation and creep, thereby initiating sintering; (D) readjustment of grain boundaries to lower energy configurations leads to modification of the size and shape of the chromite grains, enclosing the pore space which becomes progressively smaller and more spherical (E) continued sintering results in smooth straight exterior grain boundaries and spherical internal boundaries with the inclusion, representing the form with the lowest surface energy. (F) illustrates the same principle for four spheres; L_0 refers to the original length, ΔL refers to the change in length. (After Hulbert and von Gruenewaldt, 1985)

stresses will lead to plastic deformation and creep, thereby initiating sintering (figure 5.6). The presence of a liquid phase enhances the sintering process as it facilitates effective packing and aids material transfer away from grain-contact areas towards grain boundaries of normal tensile stress. Pressure sintering due to pressure applied by the overlying crystal mush will lead to enhanced bulk diffusion and fluid flow, as well as improving packing. As the grain boundaries of the chromites are adjusted to a lower energy curvature, the pores containing the (initially) intercumulus silicate phase will become smaller and more spherical.

If the sintering process is allowed to proceed to completion, the inclusions will disappear completely, provided that material is allowed to diffuse out of the pore along a mutual grain boundary. The lack of abundant spheres in chromitites of the Great Dyke suggests that sintering progressed to a late stage, resulting in the development of hard and lumpy ore. Differing degrees of sintering may also account for some of the lateral variations in thickness and composition of chromitite layers.

5.7 : SUMMARY

The silicate rocks of the lower Pyroxenite Succession in the Mutorashanga area are predominantly monomineralic assemblages of olivine and orthopyroxene, with intermediate bi-minerallic rocks commonly developed between the dunite and orthopyroxenites of each cyclic unit. The monomineralic rocks are strongly adcumulate, commonly with less than 2% discrete postcumulus phases and generally exhibit well-developed granular textures. Common polygonal mutual interference boundaries are indicative of significant adcumulus growth in response to a long Δt_{ccm}.

The intermediate lithologies have complex textural relationships that are largely dependant on the relative modal proportions of cumulus olivine and orthopyroxene. The poikilitic harzburgites are partly densified cumulates that have had a short ΔT_{cem} and will therefore contain a significant postcumulus component, although the lack of zoning in the oikocrysts and cumulus grains indicates that cementation took place withinin an open system. Hunter (op.cit.) showed that there will be a tendency to produce cycles of granular and poikilitic textures when magmas are approaching 2-phase saturation, such as occurs in the Great Dyke, where granular textured dunite grades through poikilitic harzburgite to granular harzburgite and orthopyroxenite.

The C5 layer is generally a massive, coarse-grained chromitite that shows evidence of significant post-cumulus enlargement via annealing processes. With increasing proportions of silicates, there is a transition from massive chromitite, through 'mottled chromitite' and chain textured chromite, to disseminated chromite. Associated with this transition is a reduction in the degree of post-cumulus enlargement, and consequently grain-size of the chromite.

The olivine-rich rocks have been pervasively serpentinized, and generally exhibit well-developed pseudomorphic textures after olivine. Pseudomorphic textures are frequently modified to a small degree by re-crystallization to non-pseudomorphic textures, and thin cross-cutting veins of γ-serpentine are ubiquitous. Both γ- and α- serpentine was observed in the mesh textured serpentine, suggesting the presence of both chrysotile and lizardite. According to Wicks and Whittaker, 1977) lizardite is the most common serpentine mineral associated with pseudomorphic textures after olivine. The apparent dominance of chrysotile in these serpentinites may be the result of partial recrystallization of the original serpentine mineralogy.

CHAPTER 6 : GEOCHEMISTRY

6.1 : METHODS OF STUDY

6.1.1 : Electron microprobe

Mineral chemistry of chromite, orthopyroxene, and olivine from a total of 20 polished sections was determined using the electron microprobe (EM), representing 127 analysed points. The majority of the analyses were carried out at the Department of Geological Sciences, University of Cape Town. Analysis of sample GD28 (see 6.2.2) was carried out at the Laboratoire Minéralogie, Université Paul Sabatier, France. A 4-spectrometer Cameca Microbeam was used at both institutions.

6.1.1.1 : *The determination of ferrous and ferric iron from microprobe data*

Iron was determined as total ferrous oxide (FeO_T) using the electron microprobe. Total iron data for orthopyroxene and chromite was re-calculated into ferrous and ferric proportions using the Droop (1987) method for the calculation of Fe^{3+}. The calculation is very sensitive to analytical errors and several assumptions are made in the application of the method: iron is assumed to be the only element in the mineral with a variable oxidation state; the mineral is assumed to exhibit perfect stoichiometry. Nevertheless, it is considered by Droop (1987) to be an appropriate method for calculating Fe^{3+} proportions in spinels and pyroxenes, and provides a useful estimate of the relative proportions of ferrous and ferric iron. The application of the method to the microprobe analyses was as follows:

1) Calculate cationic proportions normalized to 32 oxygens from the reported oxide weight percentages.

2) If the observed cation total (S), is greater than the correct (stoichiometric) cation total (T), then calculate Fe^{3+} from the equation:

$$Fe^{3+} = 2X(1-T/S)$$

where X equals the correct number of oxygens. For spinels, T=24, and X=32; in pyroxenes, T=4, and X=6. If $S<T$, then all iron is left as Fe^{2+} in order to avoid negative calculations of Fe^{3+}.

3) Normalise the formula to T cations and check that calculated Fe^{3+}<total iron. If Fe^{3+}>total iron then all iron is set as Fe^{3+} in order to avoid negative calculations of Fe^{2+}.

4)The formula is written normalized to T cations, with Fe^{2+} as total iron minus calculated Fe^{3+}.

5) Re-calculate the oxide weight percentages as:

$$FeO = FeO_T * Fe^{2+}/(Fe^{3+} + Fe^{2+})$$

$$Fe_2O_3 = 1.1113 * FeO_T * Fe^{2+}/(Fe^{3+} + Fe^{2+}).$$

6.1.2 X-ray fluorescence spectrometry

All samples were analysed at the Department of Geology, Rhodes University, using a Phillips PW1410 X-Ray Fluorescence (XRF) spectrometer. A total of 10 samples were analysed from the current study, comprising four orthopyroxenites and six serpentinites. Major elements were determined in duplicate sets from fusion discs, and trace elements were determined from pressed-powder briquettes.

Iron is given in the ferric state where the data is presented with loss-on-ignition (LOI) included, on account of the oxidation of some Fe^{2+} to Fe^{3+} in the furnace (Ragland, 1989). Chromium and nickel were measured as trace elements in parts per million, but are presented as weight percent oxides in this study, in the light of their relative importance in these rocks.

6.2 : CHROMITE CHEMICAL COMPOSITIONS

Chromite chemistry can be a useful indicator of crystallization conditions and early magmatic evolution within the magma chamber of ultramafic-mafic bodies. The sensitivity of chromite as a petrogenetic indicator is essentially due to the relatively early formation of chromite cumulates and the low solubility of chromite in basaltic melts, which causes chromite crystallisation to have very little effect on the residual melt composition.

The chromite series are members of the spinel group of minerals, which also contain the magnetite and spinel series. The spinel group are oxide minerals with 32 oxygen anions and 24 cations arranged in a close-packed cubic framework (Deer et al., 1982). Eight of the cations occupy tetrahedral sites (X-sites) and the remaining 16 cations occupy octahedral sites (Y-sites), giving the general spinel formula:

$$XY_2O_4$$

The chromite series consists of a solid solution series with end-members chromite ($Fe^{2+}Cr_2O_4$) and magnesiochromite ($MgCr_2O_4$): pure end-members are rare, and unaltered chromites of the Great Dyke are ferroan magnesiochromites, with the formula:

$$(Mg,Fe^{2+})Cr_2O_4$$

Numerous elements can substitute the dominant cations, including Al, Ti, Fe^{3+}, Ni, Mn, and Zn. There is significant replacement of Cr by Al, and lesser Fe^{3+}, in the Y-sites of Great Dyke chromite.

An understanding of the controls on chromite composition is essential to the interpretation of chromite compositional data, and the interaction of primary and secondary controls on chromite compositions can be complex. It is therefore considered necessary to provide a comprehensive review of these factors in the following sections. The Y-site cation ratios, $Cr/(Cr+Al+Fe^{3+})$, $Al/(Cr+Al+Fe^{3+})$, and $Fe^{3+}/(Cr+Al+Fe^{3+})$ are subsequently referred to as Y_{Cr}, Y_{Al} and Y_{Fe} respectively. Similarly, X_{Fe} refers to $Fe^{2+}/(Fe^{2+}+Mg)$, and X_{Mg} refers to $Mg/(Mg+Fe^{2+})$.

6.2.1 : Primary controls on chromite composition

6.2.1.1 : *Degree of fractionation*

Cameron (1977) showed that with increasing fractionation, the Y_{Al} and Y_{Fe} ratios of chromite in chromitites increases, whereas Y_{Cr} decreases. Decreasing Y_{Cr} ratios are essentially a feature of gradually decreasing Cr^{3+} content in the melt with continued spinel crystallization. Ti has a significantly lower distribution coefficient than Cr, will become enriched in the melt relative to the solid phase during crystallization. As Ti is also virtually unaffected by fO_2, increasing Ti contents should therefore indicate increasing degrees of differentiation.

Within layered intrusions there is a commonly observed correspondence between chromite composition and the chromite concentration in the rock (Cameron, 1975; Hamlyn and Keays, 1979). In the Panton Sill, Western Australia, Hamlyn and Keays (op.cit.) identified a trend of increasing X_{Mg} and Y_{Al} with increasing chromite concentration, accompanied by a decrease in Y_{Cr} and Y_{Fe} ratios. These trends were attributed to differing solubilities of these elements within the crystallizing portion of the melt. Similarly, a small grain crystallizing from a limited reservoir of liquid would have a higher Cr content than a larger grain from the same volume of liquid, due to the low solubility of chromium in the liquid.

6.2.1.2 : *Oxygen fugacity*

Experiments on basaltic melts by Roeder and Reynolds (1991) show that the Fe^{2+}/Fe^{3+} ratio of a chromite is generally proportional to, but lower than, that of the coexisting melt. Increasing fO_2 should therefore lead to increasing $Fe^{3+}/(Fe^{2+}+Fe^{3+})$ ratios of crystallizing spinels. It is well documented that the X_{Mg} ratio of co-precipitating silicates rises with increasing fO_2 under isothermal conditions (Hamlyn and Keays, 1979; Hulbert and von Gruenewaldt, 1985; Wilson, 1982). It has also been shown that the X_{Mg} ratio decreases with decreasing temperature, probably reflecting depletion of Mg in the melt due to crystallization of Mg-rich silicates. At a fixed fO_2, the Cr_2O_3 content and the $Cr/(Fe^{2+}+Fe^{3+})$ ratio drop with decreasing temperature (Hill and Roeder, 1974). An increasing Y_{Fe} ratio coupled with a decreasing X_{Mg} ratio may indicate a drop in temperature at constant fO_2 conditions.

There are some discrepancies between the results of experimental data, which are frequently derived from simple systems and studies of spinel crystallization in natural basaltic melts. In basaltic melts, decreasing fO_2 within the range associated with these magmas is accompanied by an increase in X_{Mg} and Al content of the spinel (Hamlyn and Keays, 1979; Roeder and Reynolds, 1991), suggesting that chromitite crystallization should have occurred at lower values of fO_2 than chromite-poor layers.

6.2.1.3 : *Crystallization of co-existing phases*

Changes in melt composition due to crystallization of early silicate phases, mainly olivine, pyroxene, and plagioclase, is the most significant factor affecting chromite composition at liquidus temperatures. Removal of olivine will lead to an increase in X_{Fe} of chromite and the residual melt, but has little effect on chromite Cr/(Cr+Al) ratios. Orthopyroxene can incorporate a higher quantity of Al into its lattice than olivine, therefore chromite crystallizing in the presence of orthopyroxene will have a higher Cr/(Cr+Al) ratio than that with olivine. Similarly, the crystallization or resorption of plagioclase has a major effect on the Cr/(Cr+Al) of chromite as it causes significant variation in Al_2O_3 content of the melt (Roeder and Reynolds, 1991). Crystallization of clinopyroxene leads to decreasing Cr/(Cr+Al) in chromite, as clinopyroxene has a higher Cr/Al ratio than the coexisting melt. The crystallization of clinopyroxene is believed to be the main control on limiting chromite crystallization to the early stages of magmatic evolution (Irvine, 1967; Eales et al., 1980).

6.2.1.4 : *Pressure*

Experimental work by Roeder and Reynolds (1991) suggests that changes in pressure does not have a significant effect on the solubility of Cr in basaltic melts or on the Cr/(Cr+Al) ratio of coexisting chromite. Small changes in Cr/(Cr+Al) ratios in chromite with changing pressure are due to the pressure effects on the liquidus temperature, therefore decreasing temperature will only lead to a small decrease in Cr/(Cr+Al) ratios.

6.2.2 : Post-cumulus modification of chromites

Chromite disseminated within and between silicates will "continue to equilibrate at subsolidus temperatures with any interstitial melt that may be present, and with coexisting silicate phases" (Rollinson, 1995). The primary chromite chemistry is commonly masked by subsolidus reaction with associated silicates, and re-equilibration amongst adjacent chromite grains, due to the high cation diffusivity of chromite relative to silicates.

Chromite compositions from chromitite layers are therefore likely to be good indicators of liquidus compositions due to the lack of significant modification by sub-solidus processes, relative to chromites from silicate-rich environments, mainly as a result of the large mass/surface area ratio of seam chromite relative to silicate phases. However, factors such as the degree of postcumulus modification and varying proportions of cumulus silicates within chromitites must be considered. In the Great Dyke, the most magnesian and chrome-rich of the seam chromites are likely to give the best indication of liquidus composition (Rollinson, 1995).

6.2.2.1 : *Sub-solidus reaction with co-existing silicates*

Major changes in chromite composition due to subsolidus re-equilibration are essentially restricted to the re-distribution of magnesium and ferrous iron between chromite and the host silicates, due to therapidity of divalent cation diffusion relative to the trivalent cations. Trivalent cations are therefore more likely to preserve the original cation ratios of the parental liquid than divalent cation ratios. Subsolidus reequilibration between olivine and chromite, where olivine shows an appreciable increase in Mg near the olivine-chromite boundary, has been observed in a number of layered intrusions, including the Jimberlana Intrusion (Roeder and Campbell, 1985), Bushveld Complex (Cameron, 1975), and the Great Dyke (Wilson, 1982). In figure 6.1 the Mg content of olivine is shown to increase systematically, from a distance of approximately 60 microns, to the boundary with the chromite. Wilson, (op.cit) observed similar zoning at orthopyroxene-chromite grain boundaries, although the exchange of Mg and Fe was shown to be much lower than that between chromite and olivine. Rates of reaction during subsolidus re-equilibration are essentially controlled by diffusion rates, and are not particularly temperature-dependant. Chromites show a lack of compositional zoning which is a feature of the diffusion coefficients of chromite being 60-100 times faster than olivine (Scowen et al., 1991).

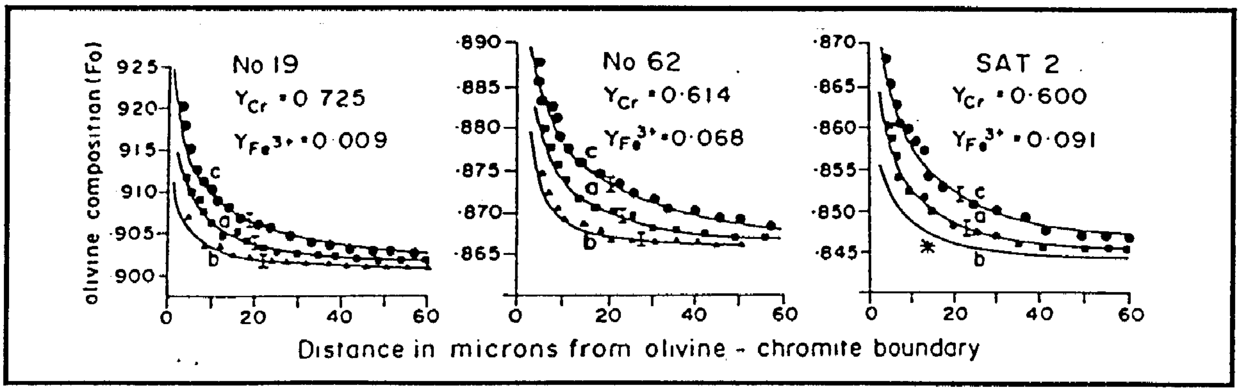

Figure 6.1 : Compositional profiles of olivine where in contact with enclosed chromite grains. Individual analytical points (error bars indicated) are shown for the three axial directions and curves represent the modelled diffusion profiles. The star indicates that suitable crystals for analysis in the *b* direction could not be found for SAT 2 (sample SAT 2 was from the Main Satellite). Sample No 19 was from CU8, No 62 was from CU2. (After Wilson, 1982)

6.2.2.2 : *Sub-solidus reaction with liquid*

Cameron (1977) showed that whilst chromite in chromitites were relatively homogeneous, disseminated chromite showed extensive variation. The complexity of chromite compositions and rock textures in these environments is cited as evidence of the extremely localized conditions within the intercumulus liquid; these complexities can obscure compositional variation related to the cumulus stage. Such reactions will obviously be dependent upon the availability of trapped liquid, and will therefore be highest in strongly orthocumulate rocks. In these assemblages, reaction will continue over a wide range of declining temperatures (Henderson, 1975).

Roeder and Campbell (1985) found that chromites in adcumulates have a narrow compositional range and high Cr and Al values, whereas orthocumulates contain chromites with a wide range of compositions. Total iron, Ti, and Fe^{3+}/Fe^{2+}ratios are found to increase from adcumulate to orthocumulate environments. In the Great Dyke, where development of adcumulates is extensive, Wilson (1982) demonstrated that significant reaction of chromites with intercumulus liquid is not common; although in some of the more orthocumulate harzburgites, where the chromite compositions are highly variable, reaction with liquid did occur. Wilson (1982) established that no compositional trend or grain size dependence is observed for chromites enclosed by postcumulus silicates. This lack of correlation is attributed to reaction with intercumulus liquid from locally variable environments.

Relatively high Ti and Fe values of chromites enclosed by olivine in contact with intercumulus material indicates that element exchange between chromite and intercumulus liquid is possible through olivine. In cumulates of the Jimberlana Intrusion, Roeder and Campbell (1985) observe that X_{Mg} ratios, and Al and Cr values, are higher in chromite enclosed in orthopyroxene as opposed to that in olivine. Orthopyroxene therefore appears to prevent the reaction of chromite with intercumulus liquid. In the few situations where chromites apparently enclosed in orthopyroxene have low Al and Cr values, Roeder and Campbell (op.cit) found evidence that the chromite was able to maintain that the direct contact with the liquid.

The most viable mechanism for Fe-Mg re-equilibration between chromite enclosed in olivine and the residual melt is considered to be via lattice inter-diffusion, rather than dislocation-based diffusion through microfractures and discontinuities. The exchange of elements such as Cr, Ti, Al, and Fe^{3+} between chromite and the melt, through olivine, is more problematic. Roeder and Campbell (1985) suggest that the low solubility for these elements in the olivine structure makes diffusion an unlikely mechanism, and that the chromite may have been able to maintain direct contact with the melt, via fractures in the olivine formed with decreasing temperature.

6.2.2.3 : *Post-cumulus overgrowth in chromitites*

The Grasvally (Bushveld Complex) and Great Dyke chromitites have the highest X_{Mg} ratios and Cr_2O_3 values of any layered intrusion. Hulbert and von Gruenewaldt (1985) propose that the X_{Mg} ratios are too high to be the product of primary factors alone, and suggest that this enrichment may be due to post-cumulus overgrowth by sintering. The *in situ* crystallization of abundant chromite in a semi-stagnant environment will lead to an increase in the X_{Mg} ratios of the residual melt. Interstitial liquid within the chromitite would therefore be enriched in Mg, as would the intercumulus liquid of the underlying silicate cumulate in order to maintain equilibrium. Re-equilibration of the silicate phases with this interstitial liquid would result in relatively high X_{Mg} ratios, as observed in the olivine cumulates below the Grasvally chromitites (Hulbert and von Gruenewaldt, 1985). The Mg-enriched liquid immediately above the cumulate pile would replenish the loss of Mg from the chromitite to the underlying material, allowing Mg-enrichment to be maintained in the intercumulus liquid for some time. Sintering in the presence of Mg-rich interstitial liquid could therefore persist until the overlying Mg-rich liquid was destroyed by convective overturn or double-diffusive convection.

6.2.3 : Chromite of this study

6.2.3.1 : *Seam and disseminated chromite*

The results of the chromite analyses are presented in table 6.1, these are averaged compositions compiled from a number of individual chromite analyses. Samples from each major chromitite seam from the mapped area were analysed, with additional analysis of a tectonised sample from chromitite C5 and the minor 'Puppy Seam' chromitite C5b. Chain-textured chromite from the 'Seam 3' chromite dunite (serpentinized), and disseminated chromite from dunite in CU6 were also analysed. The compositions of chrome spinels, and the cation ratios of the X- and Y- sites, from the chromitites of the study area are shown graphically in figure 6.2.

The most significant compositional variation between the chromitites is shown by the C6 layer relative to chromitites C7 and C5. The EM analysis of chromitite C6 produced the lowest total weight percent (wt%) oxide of the chromitites (see table 6.1), with an average individual point analysis total of 97.2 wt%. Consequently the calculation of the relative proportions of Fe^{3+} are probably inaccurate, and the quality of the C6 analysis in general should be treated with caution. The sample from which the analyses were made was strongly fractured with abundant gangue fracture filling (generally silica), and gave a relatively poor polish.

With the exception of the marked peak at chromitite C6, figure 6.2 shows a slight overall increase in chromium. Al decreases progressively from chromitites C8 towards C5. Mg and Fe^{3+} show a small increase from chromitites C8 to C7, and a small decrease from layers C5 to C5b. Fe^{2+} displays a perfect inverse relationship with Mg. Ni and Ti broadly correlate with Mg and Fe, respectively, although the effects of the sharp drop in Fe^{3+} are more subdued. It seems probable that the higher proportions of Cr, Ti, and Fe^{2+}, and lower Mg, Ni, and Fe^{3+}, shown by chromitite C6 cannot all be attributed to analytical error, and that a component of the observed variation represents genuine compositional features. This is also indicated by the fact that whilst Cr proportions are strongly affected by the very low Fe^{3+} ratio, Al shows only a slight decrease. Manganese proportions exhibit little variation between chromitites C8 and C6, but show a systematic increase upwards from the C6 layer.

The cationic X- and Y- site ratios shown in figure 6.2 reflect very similar trends to those shown by the cation proportions. It is observed that Y_{Cr} and Y_{Al} exhibit an inverse relationship that is only disturbed by the anomalously low Fe^{3+} proportions associated with chromitite C6, which results in a marked increase in Y_{Cr}. This indicates that Fe^{3+} preferentially substitutes for Cr in the chromite, rather than Al.

Figure 6.3 shows ratios of the major cations occupying the Y-site in chromite plotted against X_{Fe}. The Y_{Cr} versus X_{Fe} plot shows an overall positive correlation for most of the seam chromites, the exception being the highly micro-brecciated Puppy Seam (C5b), and the C6 layer. Chromitite C5b ratios are strongly clustered, suggesting equilibration of chromite compositions related to the intense tectonism of the chromitite. Y_{Al} shows a stronger clustering of points than Y_{Cr}, although there is an overall positive correlation with X_{Fe}. Y_{Fe} exhibits a strong negative correlation with X_{Fe}, with the exception of chromitite C6, which has a positive correlation with X_{Fe}, and chromitite C5b, which has clustered points showing only a slight negative correlation.

Table 6.1 :
Averaged electron microprobe analyses of chromite compositions

Rock-type	C8 chromitite	C7 chromitite	C6 chromitite	C5 chromitite	C5 chromitite	C5 (t)	C5b (t)	Ol.chromitite	dunite
Sample no.	GD1	GD5	GD60	GD13	GD28	GD39	GD9	GDC18	GD62
N	5	6	4	7	1	5	8	8	2
Weight percent oxide									
SiO2	0.03	0.04	0.04	0.03	0.073	0.05	0.03	0.05	0.07
TiO2	0.35	0.31	0.32	0.32	0.251	0.32	0.34	0.33	0.42
Al2O3	13.43	12.62	10.49	10.58	9.684	10.38	9.98	10.96	14.97
Cr2O3	55.95	55.95	58.99	56.54	59.623	59.48	57.56	54.97	52.97
Fe2O3	2.60	2.87	0.19	5.44	2.727	1.21	3.73	4.47	2.35
FeO	12.78	11.77	15.97	13.03	13.674	14.17	13.95	17.30	17.16
NiO	0.11	0.14	0.07	0.09	0.126	0.08	0.05	0.05	0.00
MnO	0.20	0.20	0.19	0.23	0.202	0.20	0.25	0.31	0.26
MgO	13.48	14.13	11.13	13.41	12.994	12.29	12.55	10.54	11.30
V205	nd	nd	nd	nd	0.173	nd	nd	nd	nd
Total	98.92	98.04	97.40	99.67	99.53	98.18	98.45	98.99	99.48
Cations per 32 oxygens									
Al	4.074	3.852	3.318	3.230	2.978	3.234	3.104	3.427	4.552
Cr	11.388	11.454	12.520	11.577	12.299	12.430	12.008	11.528	10.806
Fe3+	0.411	0.574	0.043	1.069	0.535	0.208	0.753	0.912	0.480
Ti	0.068	0.061	0.066	0.063	0.049	0.064	0.067	0.066	0.081
Mg	5.173	5.453	4.453	5.178	5.054	4.843	4.936	4.168	4.346
Fe2+	2.816	2.535	3.535	2.813	2.984	3.159	3.065	3.818	3.678
Ni	0.022	0.030	0.015	0.018	0.026	0.017	0.011	0.012	0.000
Mn	0.043	0.043	0.044	0.051	0.045	0.045	0.057	0.069	0.057
V	nd	nd	nd	nd	0.030	nd	nd	nd	nd
Fe2/(Fe2 + Mg)	0.353	0.317	0.443	0.352	0.371	0.395	0.383	0.478	0.458
Cr/(Cr+Al)	0.737	0.748	0.790	0.782	0.805	0.794	0.795	0.771	0.704
Cr/(Cr+Al+Fe3)	0.717	0.721	0.788	0.729	0.778	0.783	0.757	0.727	0.682
Ti/Cr	0.006	0.005	0.005	0.005	0.004	0.005	0.006	0.006	0.007
Fe3/(Fe2+Fe3)	0.127	0.185	0.012	0.275	0.152	0.062	0.197	0.193	0.115

N : number of analyses averaged
nd : not determined
t : tectonized

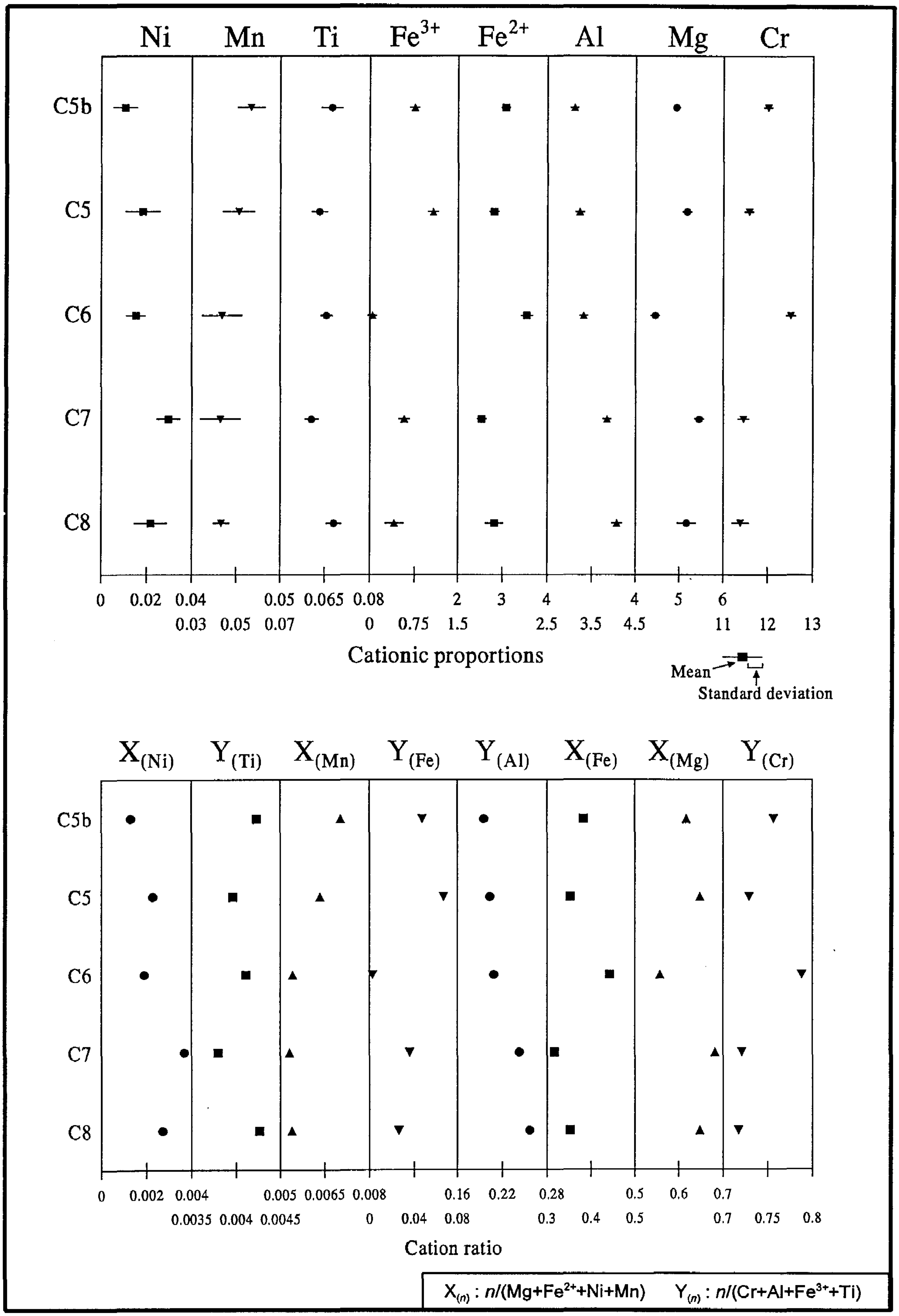

Figure 6.2 : Composition of chrome spinels from chromitite layers in the study area

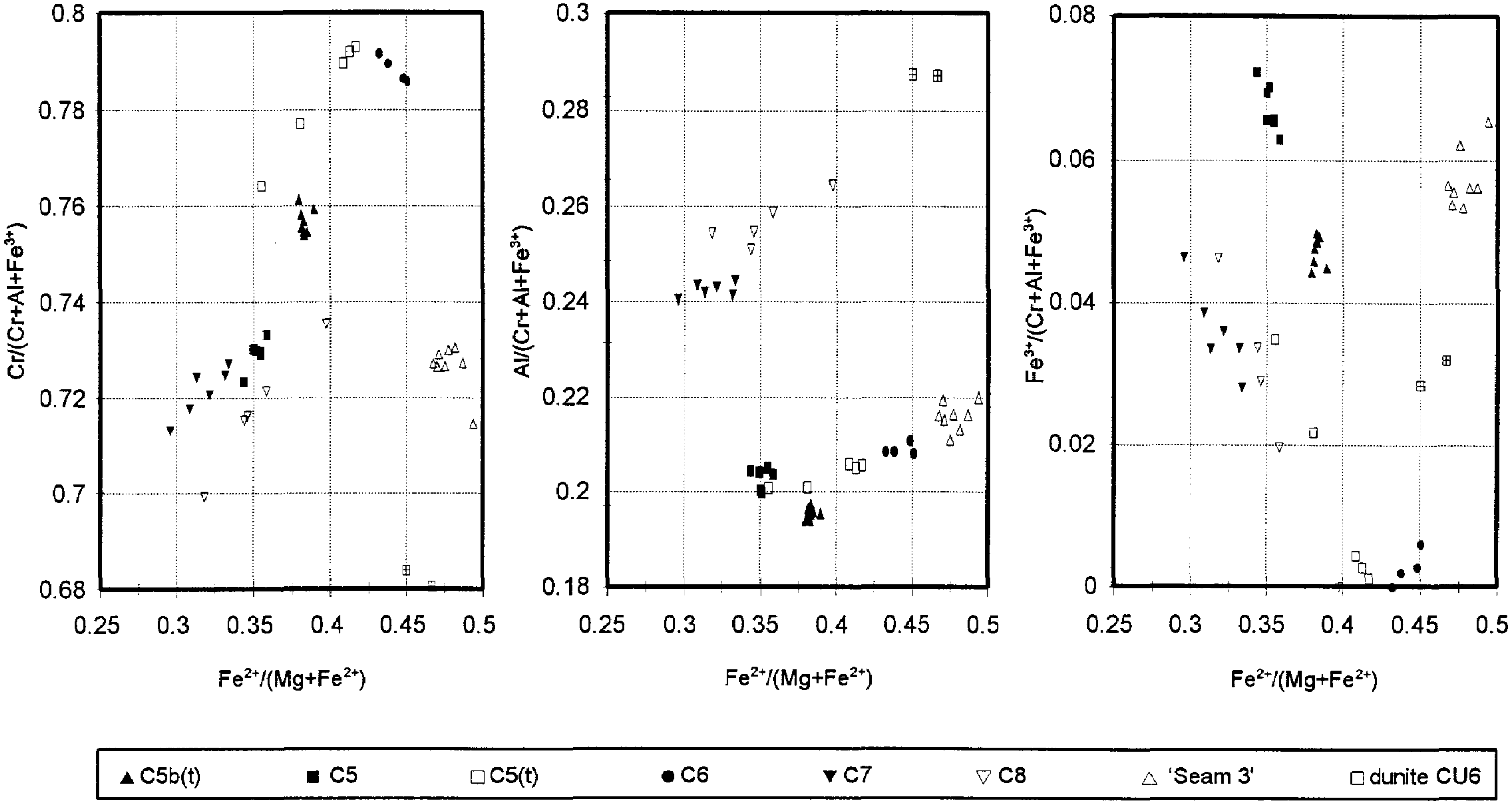

Figure 6.3 : Bivariate plots of chrome spinel Y-site cation ratios against Fe^{2+}/(Mg+Fe^{2+})

Figure 6.4 illustrates the X- and Y- site ratios for the main seam chromites in the Great Dyke, using the data of Wilson (1982) and the results of the present study. The data are in fairly good agreement, with the exception of chromitite C6, probably due to the erroneous Fe^{3+} value previously discussed. Y_{Al} and Y_{Fe} ratios of the C8 layer also show some disagreement with the data of Wilson (1982), indicating a greater relative proportion of Al in the sample from the present study.

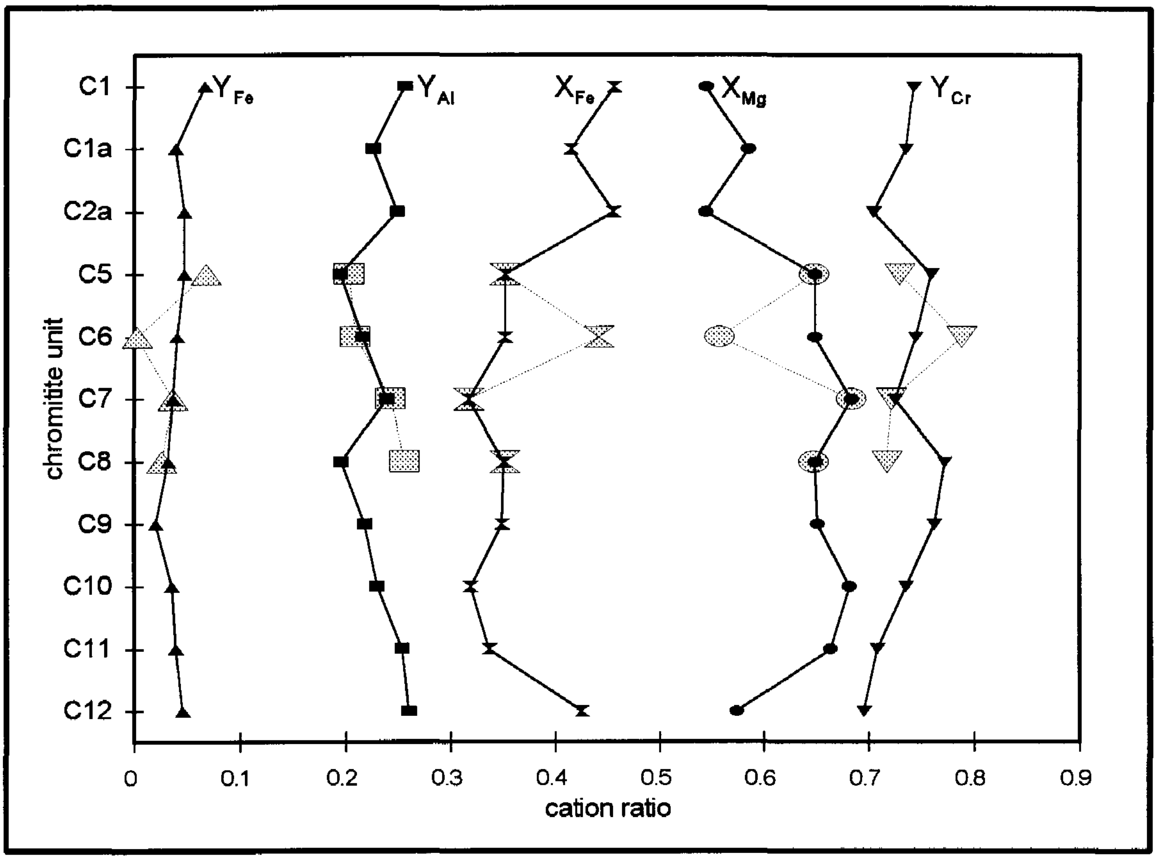

Figure 6.4 : X- and Y- site ratios for chromites of the Great Dyke chromitites. Solid symbols represent data from Wilson (1982), shaded symbols represent data from the present study.

Y_{Cr} ratios increase towards a maximum in chromitite C8, from C8 to C7 there is a sharp reversal of trend, followed by a gradual increase to chromitite C5. Y_{Al} displays a strong antipathetic relationship to Y_{Cr} . Y_{Fe} ratios gradually decrease from layers C12 to C9, subsequently showing a slight progressive increase to chromitite C5. X_{Fe} ratios display a similar trend to those shown by Y_{Cr}, excepting the marked decrease in X_{Fe} from chromitites C12 to C10. C12 is the lowermost chromitite of the Great Dyke, yet is compositionally similar to the uppermost chromitites of the ultramafic sequence (Wilson, 1982).

The Upper Group Chromitites contain a significantly higher proportion of ferrous iron than the lower chromitites, reflected in the X_{Fe} and X_{Mg} ratios in figure 6.4. Y_{Cr} ratios are comparable to lower ratios displayed by the Lower Group Chromitites, and the ratio increases from chromitites C2a to C1. Y_{Fe} ratios of C2a and C1a are similar to those shown by the upper LGC, but are notably higher in chromitite C1.

The chromites in association with silicates, i.e. those from the CU6 dunite and 'Seam 3' chromite dunite, show higher X_{Fe} ratios than chromite in massive chromitites (figure 6.3). The disseminated chromite from CU6 dunite has a higher proportion of Al_2O_3, and lower Cr_2O_3 (see table 6.1) than massive chromitite, reflected in the Y_{Al} and Y_{Cr} ratios. The chromites exhibit a less well-developed correlation of Y-ratios versus X_{Fe}, being more strongly clustered, but show similar trends to the C6 layer chromites, with a negative correlation of X_{Fe} with Y_{Cr} and positive correlation with Y_{Fe}.

6.2.3.2 : *C5 footwall chromite*

In an attempt to detail the changing magmatic conditions immediately preceding chromite crystallization, Hulbert and von Gruenewaldt (1985) undertook a detailed study of the compositional variation in the footwall of a chromitite in the Grasvally mine, Bushveld Complex. Their results indicated increasing temperature, coupled with increasing fO_2, towards the chromitite that was interpreted as the result of magma mixing, where a hotter, relatively primitive, liquid entered the system and mixed with the cooler, more evolved melt magma.

A similar study was undertaken on the C5 chromitite footwall to investigate whether such evidence regarding chromitite formation is apparent in the Great Dyke. EM analysis of chromites in the C5 footwall was conducted at intervals of 1-3 mm from a maximum of 26 mm below the chromitite. The results of the study are given in table 6.2, and the compositional variation of the chromitites with increasing height are shown in figure 6.5. Although the chromite compositions apparently reflect the changing (primary) lithologic conditions to some degree, the pervasive secondary alteration of the C5 footwall does not appear to have had a significant effect on the chromite.

Table 6.2 :

Individual electron microprobe analyses of chromite compositions approaching the base of C5

Sample no.	GD28a	GD28A	GD28c	GD28D	GD28d	GD28e	GD28f	GD28g	GD28h	GD28i	GD28j	GD28k	GD28l	GD28m
Height (mm)*	6	1	-0.5	-1.5	-4	-6	-7	-8	-11	-13	-17	-19.5	-21	-25.5
Weight percent oxide														
SiO2	0.07	0.00	0.00	0.01	0.02	0.02	0.01	0.04	0.07	0.03	0.00	0.09	0.11	0.02
TiO2	0.25	0.25	0.25	0.27	0.28	0.27	0.34	0.29	0.38	0.27	0.35	0.38	0.46	0.48
Al2O3	9.68	9.78	9.65	9.35	9.97	10.17	10.94	11.04	12.41	11.89	11.38	13.48	13.87	18.14
Cr2O3	59.62	58.99	59.76	60.08	59.94	59.24	57.44	57.94	55.96	57.08	56.81	54.20	53.89	49.07
Fe2O3	2.73	2.73	2.87	2.72	2.40	0.72	2.38	3.03	2.09	2.31	2.61	2.88	2.85	2.48
FeO	13.67	13.68	13.83	14.03	14.35	16.69	15.89	15.38	17.34	16.36	16.29	16.25	17.43	16.70
NiO	0.13	0.04	0.11	0.17	0.07	0.00	0.08	0.08	0.07	0.04	0.00	0.14	0.08	0.13
MnO	0.20	0.23	0.21	0.21	0.27	0.24	0.27	0.17	0.21	0.21	0.20	0.17	0.14	0.17
MgO	12.99	12.89	12.73	12.77	12.74	10.93	11.65	12.01	11.05	11.46	11.54	11.80	11.18	12.06
V2O5	0.17	0.17	0.02	0.18	0.17	0.17	0.24	0.09	0.19	0.11	0.14	0.22	0.09	0.20
ZnO	0.00	0.00	0.00	0.00	0.00	0.00	0.20	0.26	0.04	0.15	0.00	0.12	0.05	0.00
Total	99.53	98.76	99.44	99.79	100.19	98.43	99.42	100.33	99.80	99.91	99.33	99.73	100.15	99.45
Cations per 32 oxygens														
Al	2.978	3.027	2.974	2.874	3.046	3.190	3.377	3.375	3.812	3.646	3.511	4.105	4.220	5.415
Cr	12.299	12.246	12.353	12.394	12.292	12.472	11.899	11.878	11.531	11.742	11.762	11.074	11.000	9.830
Fe3+	0.535	0.539	0.564	0.534	0.468	0.144	0.470	0.590	0.411	0.452	0.515	0.560	0.553	0.472
Ti	0.049	0.050	0.049	0.052	0.054	0.053	0.066	0.056	0.074	0.053	0.069	0.075	0.090	0.092
Mg	5.054	5.045	4.962	4.969	4.925	4.340	4.550	4.644	4.293	4.446	4.506	4.547	4.302	4.557
Fe2+	2.984	3.005	3.024	3.061	3.113	3.716	3.482	3.335	3.779	3.560	3.568	3.513	3.763	3.538
Ni	0.026	0.008	0.022	0.037	0.015	0.000	0.016	0.018	0.014	0.008	0.000	0.030	0.017	0.026
Mn	0.045	0.050	0.047	0.047	0.058	0.055	0.060	0.038	0.046	0.046	0.043	0.036	0.031	0.036
V	0.030	0.029	0.003	0.031	0.028	0.029	0.041	0.015	0.033	0.018	0.024	0.037	0.016	0.033
Zn	0.000	0.000	0.000	0.000	0.000	0.000	0.039	0.050	0.007	0.029	0.000	0.023	0.009	0.000
Fe2/(Fe2 + Mg)	0.371	0.373	0.379	0.381	0.387	0.461	0.434	0.418	0.468	0.445	0.442	0.436	0.467	0.437
Cr/(Cr+Al)	0.805	0.802	0.806	0.812	0.801	0.796	0.779	0.779	0.752	0.763	0.770	0.730	0.723	0.645
Cr/(Cr+Al+Fe3)	0.778	0.774	0.777	0.784	0.778	0.789	0.756	0.750	0.732	0.741	0.745	0.704	0.697	0.625
Ti/Cr	0.004	0.004	0.004	0.004	0.004	0.004	0.006	0.005	0.006	0.005	0.006	0.007	0.008	0.009
Fe3/(Fe2+Fe3)	0.152	0.152	0.157	0.149	0.131	0.037	0.119	0.150	0.098	0.113	0.126	0.137	0.128	0.118

Height : height relative to the base of C5*

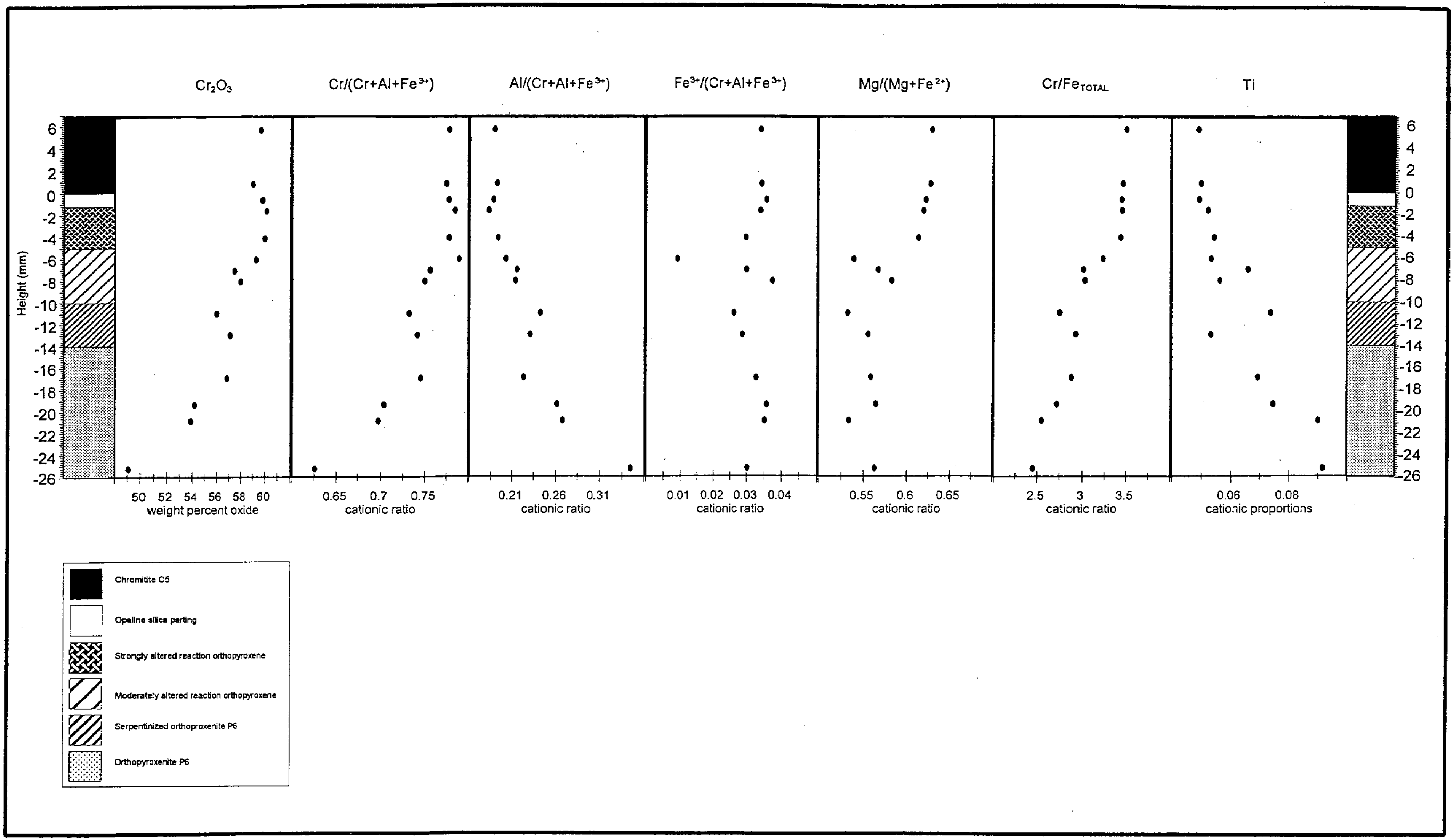

Figure 6 5 : Compositional variation of chrome spinels with increasing height within the footwall of chromitite C5

An overall progressive increase in Cr_2O_3, Y_{Cr}, and Cr/total iron towards the base of chromitite C5 is evident from figure 6.5. These increases are likely to be the result of increasing Cr content of the crystallizing melt, coupled with an increase in temperature, and are suggested to be due to progressive mixing of the residual melt with a fresh input of primary, Cr-rich magma. A strongly antithetic relationship is seen to exist between Y_{Cr} and Y_{Al}, and therefore the Cr/(Cr+Al) ratio would show a similar pattern to Y_{Cr}. The decrease in Y_{Cr} and corresponding increase in Y_{Al} near the top of pyroxenite P6 (-10 mm) is likely to be due to the crystallization of olivine causing more Al to be incorporated into the chromite lattice than during orthopyroxene-only crystallization.

Y_{Fe} ratios are generally relatively consistent, showing a slight increase with height. The obvious exception to this is the strong decrease at -6 mm. This analysis, point GD28e, can be seen in table 6.2 to have the lowest total oxide value and a significantly lower $Fe^{2+}/(Fe^{2+}+Fe^{3+})$ ratio than the average (0.13). This suggests that the calculation of Fe^{3+} for this point is erroneous, and therefore ratios affected by this data should be treated with caution. A sharp increase in Y_{Fe} is observed from -11 to -8 mm: this interval represents an important lithological change, and the changing conditions are also evidenced elsewhere in figure 6.5; therefore this is considered to be a valid increase. The trends shown in the Y_{Fe} ratios closely match those produced on a $Fe^{2+}/(Fe^{3+} + Fe^{2+})$ diagram.

The decrease of the $Mg/(Mg+Fe^{2+})$ ratio at the top of the P6 layer is probably due to the crystallization of magnesium-rich olivine. From this point upwards, however, the $Mg/(Mg+Fe^{2+})$ ratio exhibits a marked overall increase towards the chromitite. The given ratio at -6 mm should be treated with caution as previously noted. The increasing $Mg/(Mg+Fe^{2+})$ ratios, coupled with the decreasing Al_2O_3 content of chromite (reflected in the Y_{Al} ratio), may be the result of increasing fO_2 of the crystallizing magma, as suggested by Hulbert and von Gruenewaldt (1995).

Titanium shows an antithetic correlation with chromium, and indicates an overall decrease in the degree of differentiation, possibly in response to the continued mixing of residual magma with the more primitive magma input. From the footwall contact of chromitite C5, the Ti proportions appear to stabilize, suggesting that initial magma mixing had reached completion. A comparison with Ti values from GD13 (see table 6.1), a few centimetres below the hanging-wall contact of the C5 layer, indicates an increase upwards through the chromitite with progressive fractionation of the hybrid magma, also suggested by the decrease in Cr_2O_3 from GD28 to GD13. The sharp increase in Ti content near the top of pyroxenite P6, from -13 to -11 mm, may be a feature of the lower preference of Ti for olivine relative to orthopyroxene causing Ti to be preferentially incorporated into chromite.

Hulbert and von Gruenewaldt (1985) estimated that the systematic increase in the Cr/(Cr+Al) ratio, from 0.693 to 0.753, over a 12 mm interval from the footwall to the base of the chromitite indicated a 19°C increase in temperature. In this study, the Cr/(Cr+Al) ratio increases 0.752 to 0.802 over a similar interval (table 6.2), suggesting a temperature increase of an equivalent magnitude. Temperature increases are believed to lead to an increase in the fO_2 of the crystallizing magma, as crystallization temperatures normally parallel buffer curves (Hulbert and von Gruenewaldt, op.cit.). Increasing Cr_2O_3 resulting from mixing with a primitive Cr_2O_3-rich magma, coupled with an increase in fO_2, may drive the crystallizing liquid from the olivine-chromite cotectic into the chromite stability field, causing abundant chromite precipitation to form the chromitite layer.

Whilst determination of the extent of re-equilibration of chromites within the footwall silicates is beyond the scope of the present study, it is probable that chromite enclosed in reaction orthopyroxene, itself a product of reaction between olivine and liquid, should exhibit a fair degree of compositional modification. Further reaction of enclosed chromite with interstitial liquid would have been effectively halted by the development of orthopyroxene oikocrysts (Roeder and Campbell, 1985).

6.2.3.3 : *Core and rim chromite compositions*

A limited study of compositional variation between core and rim domains was made during the EM work. The results of these analyses are presented in figure 6.6; analyses GD28A and GD13 are of coarse-grained chromite from the C5 massive chromitite layer, GD28B is of a fine-grained chromite enclosed by orthopyroxene in pyroxenite P6. There is insufficient data to make conclusive observations and interpretation, but some general trends may be noted. Cr proportions for the three samples shows a slight increase towards the rim domains, with Al showing a strong antithetic relationship. Fe^{3+} exhibits a fairly consistent decrease from core to rim in all samples. Mg and Fe^{2+} display an antithetic relationship, Mg showing a slight increase towards the rim in GD28A and GD28B, but a slight decrease in GD13. Ni increases towards the rim in all cases. Mn and Ti show a marked decrease towards the rim in GD28B, but display varying trends in GD28B and GD13.

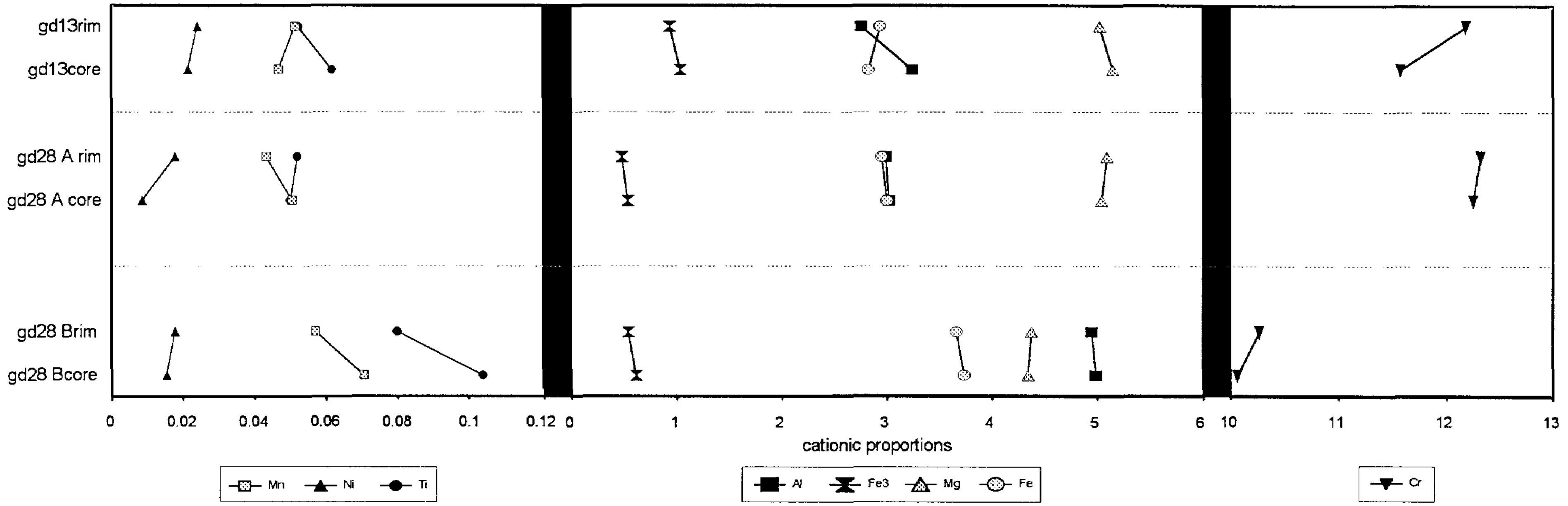

Oxide weight percent	gd28A core	gd28A rim	gd28B core	gd28B rim	gd13 core	gd13 rim
SiO_2	0.00	0.04	0.00	0.03	0.04	0.06
TiO_2	0.25	0.26	0.54	0.41	0.32	0.27
Al_2O_3	9.78	9.76	16.73	16.40	10.67	8.98
Cr_2O_3	58.99	59.75	50.21	50.64	56.53	58.81
Fe_2O_3	2.73	2.45	3.25	2.82	5.36	4.78
FeO	13.68	13.56	17.67	17.11	13.09	13.44
MnO	0.23	0.20	0.33	0.26	0.21	0.23
MgO	12.89	13.12	11.51	11.47	13.36	12.89
NiO	0.04	0.08	0.08	0.09	0.10	0.11
V_2O_5	0.17	0.19	0.23	0.15	nd	nd
ZnO	0.00	0.00	0.00	0.02	nd	nd
Total	98.76	99.43	100.55	99.40	99.67	99.57

nd : not determined

Cations to 32 oxygens	gd28A core	gd28A rim	gd28B core	gd28B rim	gd13 core	gd13 rim
Ti	0.050	0.052	0.103	0.080	0.062	0.052
Al	3.027	3.000	4.998	4.955	3.258	2.772
Cr	12.246	12.317	10.061	10.265	11.575	12.180
Fe^{3+}	0.539	0.481	0.619	0.543	1.044	0.943
Fe^{2+}	3.005	2.957	3.746	3.668	2.836	2.944
Mn	0.050	0.043	0.070	0.057	0.047	0.051
Mg	5.045	5.099	4.348	4.385	5.158	5.033
Ni	0.008	0.018	0.015	0.018	0.021	0.024
V	0.029	0.033	0.038	0.026	nd	nd
Zn	0.000	0.000	0.000	0.004	nd	nd
$Fe^{2+}(Fe^{2+}+Mg)$	0.373	0.367	0.463	0.455	0.355	0.369
Cr/(Cr+Al)	0.802	0.804	0.668	0.674	0.780	0.815

Figure 6.6 : Core and rim analyses of chrome spinel compositions

GD13 and GD28A : C5 chromitite

GD28B : C5 footwall P6 layer

6.3 : SILICATE CHEMICAL COMPOSITIONS

A limited study of orthopyroxene and olivine compositions was made, with the primary aim being an assessment of mineral compositional variation between cyclic units. The results of the EM analyses are given in table 6.3.

6.3.1 : Orthopyroxene

The pyroxene group consist of orthorhombic and monoclinic pyroxenes, respectively termed orthopyroxene and clinopyroxene. Clinopyroxenes only occur as minor interstitial postcumulus phases within the Ultramafic Sequence below CU1, and no analyses of clinopyroxene compositions were conducted in this study. Orthopyroxenes form a solid-solution series, occupying the base of the pyroxene group ternary system, $Mg_2Si_2O_6$ - $Ca_2Si_2O_6$ - $Fe_2Si_2O_6$, with less than 5% $Ca_2Si_2O_6$. The Mg-Fe series orthopyroxenes may also contain minor proportions of Al, Mn, Fe^{3+}, Ca, Ti, Cr, and Ni (Deer et al.,1982). In accordance with the 50% rule of Morimoto (1988), orthopyroxenes are classified with reference to the nearest end-member of the Mg-Fe series. Therefore, natural orthopyroxenes are either termed enstatite (En), with >50% $Mg_2Si_2O_6$, or Ferrosilite (Fs), with >50% $Fe_2Si_2O_6$. The pyroxenes of this study exhibit enstatite compositions between a high of $En_{87.9}$ and a low of $En_{85.7}$ for P5 and P3 layers, respectively (see table 6.3). The data suggest an overall decrease in En content upwards through the succession, as observed by Wilson (1982).

Figure 6.7A details the compositional variation of cumulus orthopyroxenes in the major orthopyroxenite layers of the study area. Ca and Al are present in similar proportions and show sympathetic variation, increasing from pyroxenites P6 to P5, decreasing to P4, then increasing again to pyroxenite P3. Similar, but more subtle trends are shown by Mg, Cr, and Ti. Fe^{2+} and Si display antithetic relationships to Ca, and Mg, respectively. Mn decreases from pyroxenites P6 to P5, followed by a gradual increase from pyroxenites P5 to P3. Na shows a progressive increase from pyroxenites P6 to P4, at which point there is a marked reversal of trend at the P3 layer. The X_{Mg} ratios shown by pyroxenite P5 (table 6.3) are consistently high, relative to the other pyroxenites.

Table 6.3 : Averaged electron microprobe analyses of orthopyroxene and olivine compositions

Sample no.	GD56a	GD57a	GDC21	GDC47	GD33i	GD33ii		GDC18	GDC12	GDC35	GD62
Rock-type	opxenite	opxenite	opxenite	opxenite	harzburgite	opxenite		Cr-dun(s)	s.dunite	s.dunite	s.dunite
Unit	P3	P4	P5	P6	P5	P5		S4	S4	S5	S6
N	6	7	11	7	2	4		2	6	6	10
SiO2	55.64	57.66	55.97	56.89	56.39	55.61	SiO2	37.19	40.08	39.87	40.17
TiO2	0.06	0.05	0.06	0.05	0.05	0.04	TiO2	0.00	0.01	0.01	0.01
Al2O3	1.18	0.99	1.11	0.94	0.84	0.79	Al2O3	0.02	0.01	0.01	0.01
Cr2O3	0.60	0.60	0.62	0.62	0.57	0.56	Cr2O3	0.01	0.02	0.01	0.02
Fe2O3	1.74	0.00	1.60	0.00	1.88	2.02	FeO*	7.56	11.50	12.33	9.08
FeO	6.46	7.89	5.83	7.74	5.36	5.34	NiO	0.20	0.28	0.30	0.33
MnO	0.19	0.17	0.15	0.17	0.17	0.17	MnO	0.09	0.16	0.19	0.12
MgO	32.68	32.51	33.31	32.49	33.98	33.45	MgO	46.32	47.93	47.17	49.24
CaO	1.16	0.97	1.07	0.94	0.87	0.89	CaO	0.12	0.06	0.06	0.07
Na2O	0.04	0.05	0.05	0.04	0.05	0.06	Na2O	nd	nd	nd	nd
Total	**99.74**	**100.90**	**99.78**	**99.88**	**100.16**	**98.93**	**Total**	**91.50**	**100.06**	**99.96**	**99.04**
			Cations per 6 oxygens						*Cations per 4 oxygens*		
Si	1.944	1.986	1.948	1.980	1.951	1.950	Si	0.991	0.992	0.991	0.993
Al	0.048	0.040	0.045	0.038	0.034	0.033	Al	0.001	0.000	0.000	0.000
Cr	0.017	0.016	0.017	0.017	0.016	0.015	Cr	0.000	0.000	0.000	0.000
Fe3+	0.046	0.000	0.042	0.000	0.049	0.053	Ti	0.000	0.000	0.000	0.000
Ti	0.002	0.001	0.001	0.001	0.001	0.001	Mg	1.840	1.768	1.749	1.815
Mg	1.702	1.670	1.728	1.686	1.753	1.749	Fe2+*	0.168	0.238	0.256	0.188
Fe2+	0.189	0.227	0.170	0.225	0.155	0.156	Ni	0.004	0.006	0.006	0.007
Mn	0.006	0.005	0.004	0.005	0.005	0.005	Mn	0.002	0.003	0.004	0.002
Ca	0.043	0.036	0.040	0.035	0.032	0.033	Ca	0.002	0.001	0.001	0.001
Na	0.002	0.003	0.003	0.003	0.003	0.004	Na	nd	nd	nd	nd
Xmg	90.01	88.01	91.05	88.21	91.87	91.79	Xmg	91.62	88.13	87.21	90.62
En	85.72	86.15	87.09	86.39	87.90	87.57	Fo	91.52	87.99	87.04	90.51
Fs	12.10	11.99	10.90	11.81	10.48	10.76	Fa	8.48	12.01	12.96	9.49
Wo	2.18	1.86	2.01	1.80	1.62	1.67					

s : serpentinized
N : number of analyses averaged.
nd : not determined.
FeO : all iron as FeO; Fe2+* : all iron as Fe2+*
Xmg : Mg/(Mg+Fe2+)

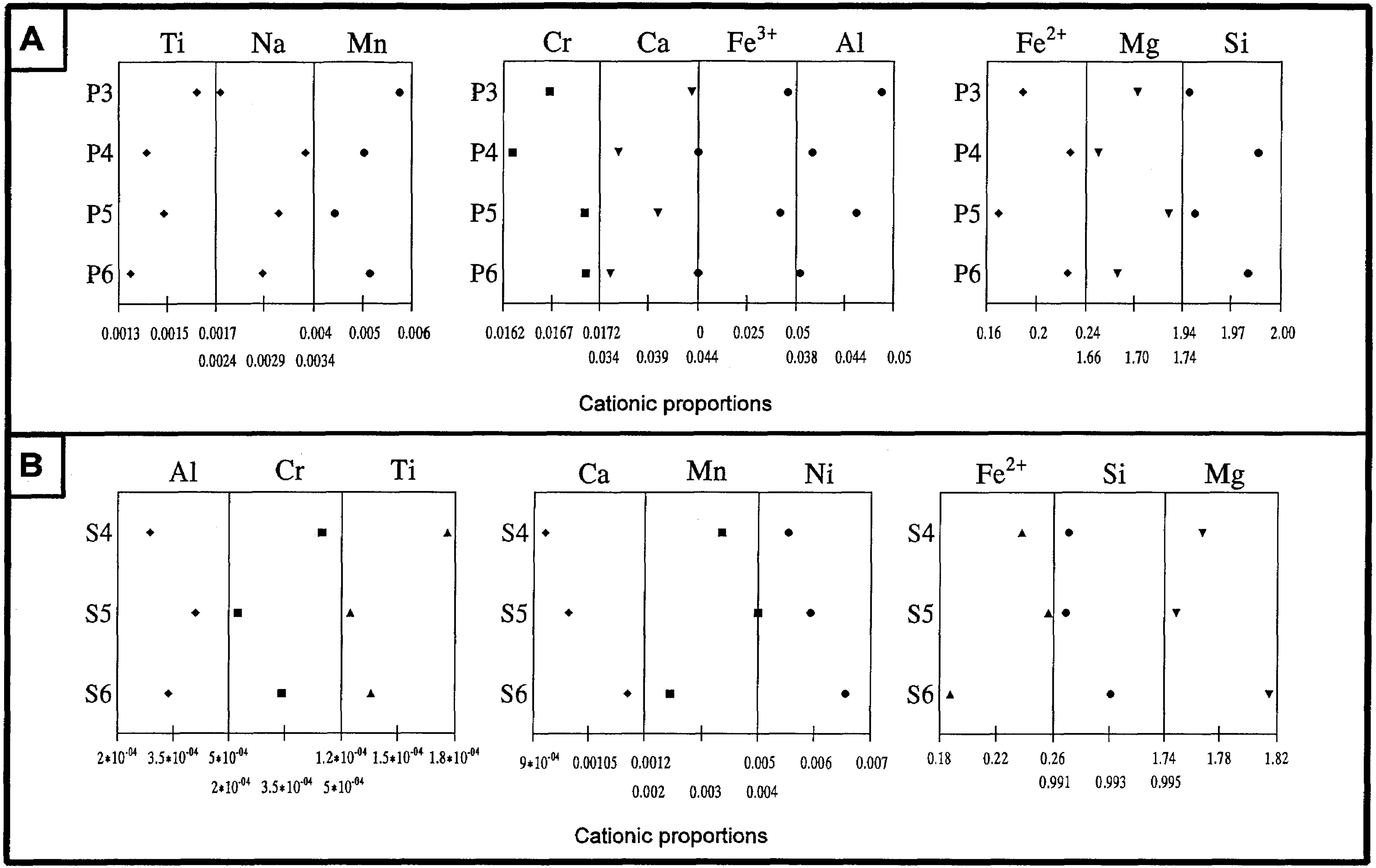

Figure 6.7 : Compositional variation of orthopyroxene (A) and olivine (B) between cyclic units..
Pn and *Sn* represent orthopyroxenite and serpentinite layers, respectively, of cyclic unit *n.*

It is important to note that Wilson (1982) identified significant variation of orthopyroxene compositions within layers P6 to P3, as shown in figure 6.8. Each layer displays an upwards decrease in X_{Mg} (and En values) towards the upper portions of the layer, at which point there is a marked reversal of trend, X_{Mg} increasing towards the top of the layer. The intra-layer compositional variation complicates the assessment of trends indicated by a small number of samples, such as in the current study. The compositional trends within units are attributed by Wilson (1982) to progressive differentiation of the crystallizing magma, followed by mixing with a new influx of primitive magma, marked by the reversal of trend near the top of the units.

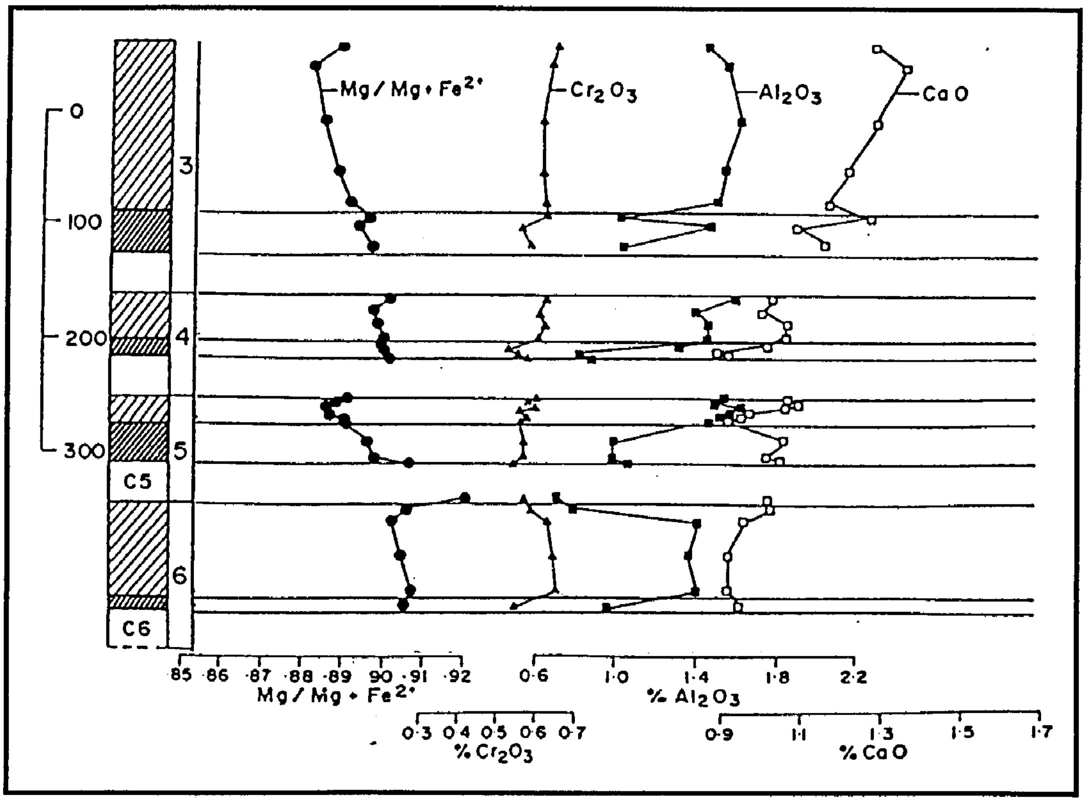

Figure 6.8 : Compositional variation of orthopyroxenes in the lower Pyroxenite Succession in the Darwendale Subchamber (modified after Wilson, 1982). Pyroxenites (open hatching) and olivine pyroxenites (closed hatching) are shown to scale thickness (scale bar in metres), but the dunites and harzburgites are not to scale.

Sample GD33 is an example of the 'centimetre pyroxenite' layer; GD33ii is from orthopyroxene within the 1 cm layer and GD33i is from orthopyroxene within the surrounding granular harzburgite. The compositional differences between pyroxene from the two environments within the sample are not significant, as shown in table 6.3. This indicates that the pyroxenes crystallized from the same batch of crystallizing magma, therefore indicating short-lived and rapid fluctuations in crystallizing conditions in the magma. This resulted in orthopyroxene-only crystallization to produce the centimetre pyroxenite, followed by a return to 'normal' crystallizing conditions along the olivine-orthopyroxene cotectic.

6.3.2 : Olivine

The results of the olivine analyses are given in table 6.3. Unfortunately, a lack of suitable relict olivine in the pervasively serpentinized and partially silicified surface samples of CU3 dunites prevented the analysis of olivine from this cyclic unit. Similarly, the analyses of GDC18, a chromite-dunite, produced poor totals, due to a combination of limited fresh olivine and the highly uneven polish resulting from the contrasting character of chromite and serpentine.

The olivine group are orthorhombic silicates consisting of discrete SiO_4 tetrahedra, joined by divalent cations. Olivines have a general formula: $(Mg, Fe^{2+})SiO_4$, and form a solid solution series between the magnesian end-member, forsterite (Fo), and ferroan end-member, fayalite (Fa). Ca, Mn, Ni, and Co may substitute for Mg and Fe^{2+}. Olivines of the Ultramafic Sequence of the Great Dyke have strongly forsteritic compositions, olivines of the study area have compositions between Fo_{87} and Fo_{92}, as shown in table 6.3.

Compositional variation shown by olivines from serpentinized dunites of CU6 to CU4 are illustrated in figure 6.7B. Very little variation is shown by Si and Mg. Proportions of total iron (as Fe^{2+}) are highest in serpentinite S5, decreasing to S4 and S6. Mn and Al show a similar variation trend to iron, and a broadly inverse relationship is displayed by Cr and Ti. Ni and Ca exhibit a systematic decrease from serpentinites S6 to S4.

6.4 : WHOLE-ROCK CHEMICAL COMPOSITIONS

6.4.1 : Introduction

Only a small number of samples were analysed for the purposes of this study, and are intended to give an approximate indication of compositional variation between cyclic units in the study area. The samples were chosen to be representative of the lithostratigraphic unit, and core samples were used where possible to mitigate the effects of surface alteration. A highly silicified surface sample, GD36 (see table 6.4), was analysed to determine the compositional variation in serpentinite as a result of intense surface silicification. The results of major and trace element analyses are presented in table 6.4; major element variation with unit height is graphically presented in figure 6.9 and trace element variation in figure 6.10.

6.4.2 : Orthopyroxenite

Four orthopyroxenite samples were analysed using XRF. These represented the major orthopyroxenite layers in the study area, P6 to P3. Table 6.5 presents these analyses re-calculated minus LOI and H_2O^-, and normalized to 100%. The close correlation of this data with the EM mineral compositions for the same layers underlines the essentially monomineralic nature of these rocks.

Table 6.5 : XRF analyses of orthopyroxenite compositions normalized to 100 %

Sample	GD56a	GD57	GDC21	GDC46
Unit	P3	P4	P5	P6
Weight % oxide				
SiO_2	56.28	56.63	56.59	56.75
TiO_2	0.08	0.06	0.07	0.06
Al_2O_3	1.43	1.01	1.27	1.03
Cr_2O_3	0.64	0.69	0.66	0.73
FeO*	7.91	7.47	7.30	7.36
NiO	0.08	0.13	0.09	0.09
MnO	0.18	0.17	0.16	0.17
MgO	31.90	32.81	32.54	32.69
CaO	1.34	0.96	1.18	1.00
Na_2O	0.14	0.06	0.13	0.10
K_2O	0.02	0.00	0.02	0.01

FeO : all iron as FeO*

Table 6.4 : X-ray fluorescence spectrometry analyses of major and trace element compositions

Sample	GD56b	GDC12	GD36	GDC38	GDC42	GDC53	GD56a	GD57	GDC21	GDC46
Type	s.dunite	s.dunite	s.dunite	s.dunite	s.dunite	s.dunite	opxenite	opxenite	opxenite	opxenite
Unit	S3	S4	silic.S5	S5	S5	S6	P3	P4	P5	P6
Weight percent oxide										
SiO_2	38.53	32.91	73.46	32.76	34.02	33.74	56.73	56.89	57.08	57.12
TiO_2	0.02	0.01	0.04	0.02	0.02	0.02	0.08	0.06	0.07	0.06
Al_2O_3	0.89	0.29	0.96	0.29	0.47	0.30	1.45	1.02	1.28	1.04
Fe_2O_3*	11.18	10.74	12.58	10.94	11.39	9.31	8.86	8.34	8.18	8.24
Cr_2O_3	0.51	0.84	0.71	0.67	0.94	0.51	0.65	0.70	0.67	0.74
NiO	0.27	0.23	0.30	0.32	0.24	0.25	0.08	0.13	0.09	0.09
MnO	0.13	0.13	0.17	0.15	0.16	0.12	0.18	0.17	0.16	0.17
MgO	35.13	39.62	1.88	38.78	36.52	40.47	32.16	32.96	32.82	32.91
CaO	0.02	0.05	0.06	0.01	0.34	0.11	1.35	0.97	1.19	1.01
Na_2O	0.02	0.02	0.00	0.02	0.02	0.03	0.14	0.06	0.13	0.11
K_2O	0.03	0.00	0.03	0.00	0.04	0.00	0.02	0.01	0.02	0.01
LOI	12.53	12.96	3.69	14.48	13.93	14.22	-0.22	-0.10	-0.12	-0.07
H20-	1.62	1.24	6.60	1.63	1.11	1.30	0.13	0.16	0.15	0.17
TOTAL	100.89	99.03	100.49	100.06	99.20	100.38	101.60	101.35	101.71	101.58
ppm										
Co	155	153	185	155	160	148	97	96	93	93
V	21	21	21	18	23	6	80	57	60	56
Cu	6	6	19	2	4	2	10	7	9	7
Zn	46	46	72	49	42	41	65	55	53	53
Sr	2	LLD	4	LLD	8	LLD	6	2	5	5
Rb	LLD	LLD	3	LLD	LLD	LLD	2	LLD	2	2

opxenite : orthopyroxenite
s. : serpentinized; silic. : silicified
Fe_2O_3 : all iron as Fe_2O_3
LOI : loss on ignition
LLD : analysis below lower limit of detection

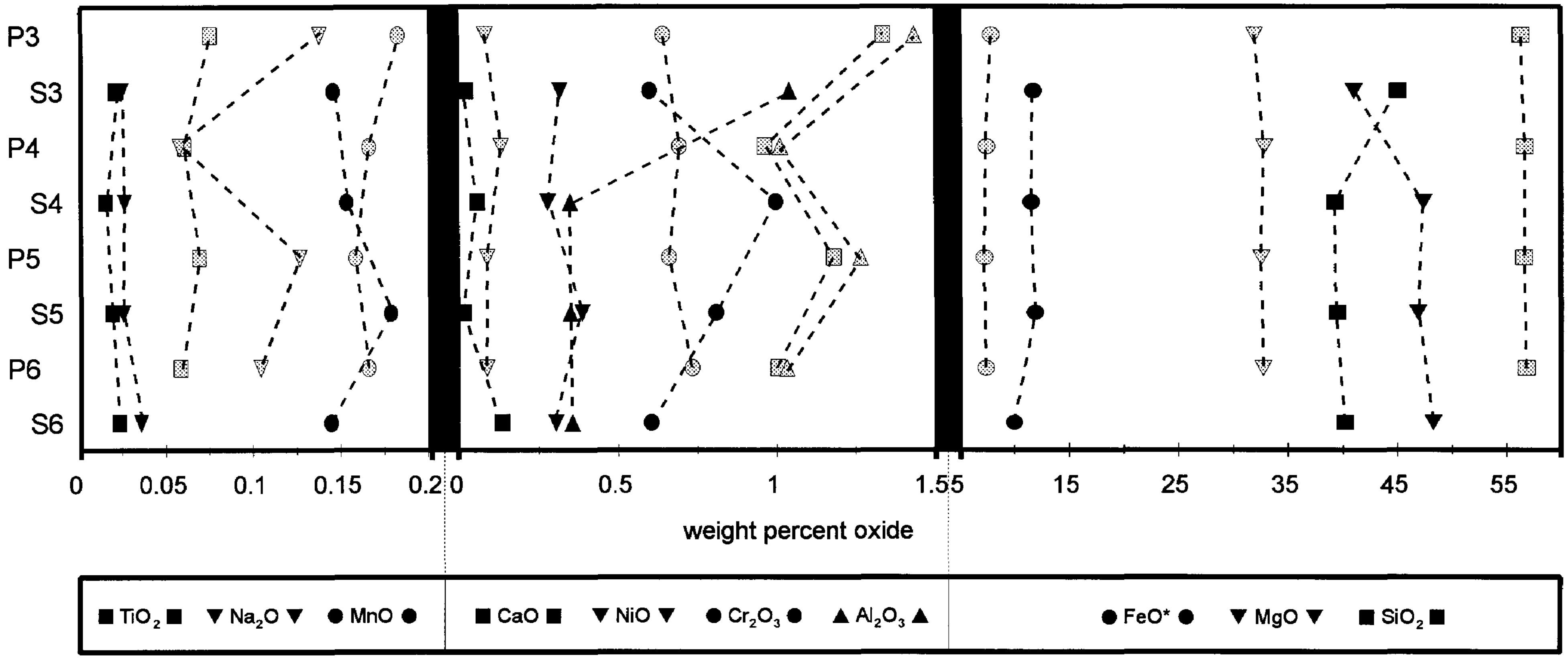

P*n* : Orthopyroxenite layer of Cyclic Unit *n* (denoted by shaded symbols)
S*n* : Serpentinize dunite layer of Cyclic Unit *n* (denoted by solid symols)

Figure 6.9 : Whole-rock compositional variation of the silicate rocks in the Ultramafic Sequence

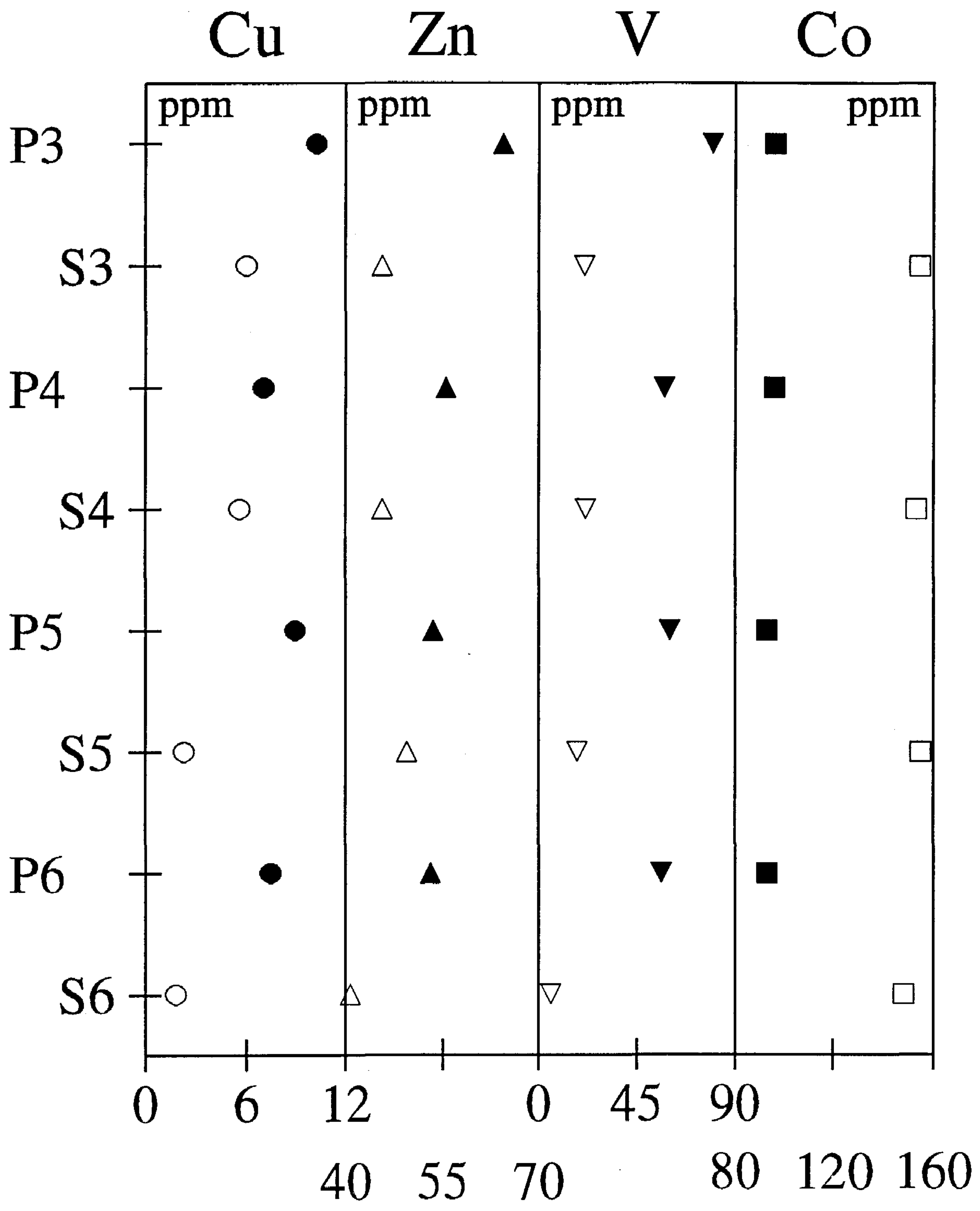

P*n* : Orthopyroxenite layer of Cyclic Unit *n* (denoted by shaded symbols)
S*n* : Serpentinized dunite layer of Cyclic Unit *n* (denoted by solid symols)

Figure 6.10 : Whole-rock trace element variation of the silicate rocks in the Ultramafic Sequence

Very little variation is shown by MgO, SiO_2, and FeO_T, although the analyses indicate a slight increase in FeO_T at the expense of MgO at pyroxenite P3. Significant and sympathetic variation is shown by Al_2O_3 and CaO (see figure 6.9), which show an overall upward increase from pyroxenites P6 to P3, although a reversal of trend is seen from P5 to P4, which has Al_2O_3 and CaO values similar to the P6 layer. TiO_2 and Na_2O show similar trends, but the decrease to pyroxenite P4 is less marked for TiO_2 and more extreme for Na_2O. Variation of Cr_2O_3 and NiO is subdued, but follows a broadly antithetic trend to Al_2O_3 and CaO. MnO decreases from pyroxenites P6 to P5 before gradually increasing to P3.

Trace element variation in the orthopyroxenites is shown in figure 6.10. Cu exhibits a similar trend to TiO_2, and Co shows little variation. Vanadium and Zinc are relatively constant from pyroxenites P6 to P4, but display a shift to higher values at the P3 layer.

6.4.3 : Serpentinized dunite

A total of 6 samples were analysed by XRF, the results of which are presented in table 6.4. The study included three samples from CU5; GDC38 was chosen as representative of the unit, GDC42 is an example of 'brown serpentinite', and GD36 is a heavily silicified sample, as previously noted.

Major element compositional variation of serpentinites is shown in figure 6.9 (with data normalized to 100%, minus LOI and H_2O^-). Compositional variation between serpentinites S6 and S4 is limited, with the exception of higher FeO_T, NiO, and MnO proportions in the S5 layer, and correspondingly lower MgO and CaO. MgO and FeO_T display a perfect inverse relationship between serpentinites S6 and S4. However, between S4 and S3 layers, proportions of MgO decrease dramatically, with a sympathetic increase shown by SiO_2, whilst FeO_T proportions remain essentially unchanged. This feature is most likely to be a result of the effects of partial silicification: the sample of serpentinite S3, GD56b, is a surface sample, whereas analyses of S4, 5, and 6 are from borehole core samples. This is also indicated by Al_2O_3 proportions which are relatively consistent below the S3 layer, but shows a three-fold increase from serpentinites S4 to S3.

Trace element variation between the serpentinites of CU6 to CU3 is illustrated in figure 6.10. An overall increase is indicated for the base metals with increasing height, serpentinite S5 showing the highest values for Zn and Co.

Table 6.6 is a comparison of volatile-free serpentinite whole-rock compositions with relict olivine compositions determined by EM analysis. The data highlight the essentially isochemical nature of the serpentinization process, with most weight oxide percentages being very similar. The high Cr_2O_3 and Al_2O_3 values from the whole-rock analyses are due to the presence of 1-2% free chromite.

Table 6.6 : Comparison of EM olivine data with LOI-free serpentinite XRF data, normalized to 100%

Sample	GDC12	GDC38	GDC53	GDC12	GDC35	GD62
Type	s.dunite	s.dunite	s.dunite	s.dunite	s.dunite	dunite
Unit	S4	S5	S6	S4	S5	S6
XRF data normalized to 100%				*EM data*		
SiO_2	39.29	39.54	40.20	40.08	39.87	40.17
TiO_2	0.02	0.02	0.02	0.01	0.01	0.01
Al_2O_3	0.35	0.35	0.35	0.01	0.01	0.01
Cr_2O_3	1.00	0.81	0.60	0.02	0.01	0.02
FeO*	11.53	11.88	9.98	11.50	12.33	9.08
NiO	0.28	0.39	0.30	0.28	0.30	0.33
MnO	0.15	0.18	0.14	0.16	0.19	0.12
MgO	47.30	46.80	48.22	47.93	47.17	49.24
CaO	0.06	0.01	0.13	0.06	0.06	0.07
Na_2O	0.03	0.03	0.04	nd	nd	nd
Total	100.00	100.00	100.00	100.06	99.96	99.04

FeO : all iron as FeO*

The effects of late-stage alteration are illustrated by a series of graphs shown in figure 6.11. The relatively unaltered serpentinites, GDC12, 38, and 53, display a well-developed clustering in most plots, the notable exceptions being CaO vs SiO_2, and Zn vs SiO_2. These samples are from increasing depth in borehole H10/4a, and the CaO and Zn trends are probably a feature of decreasingly pervasive serpentinization with increasing depth. GDC42 is an example of the 'brown' serpentinite described in chapter 4. The most obvious chemical indication of this

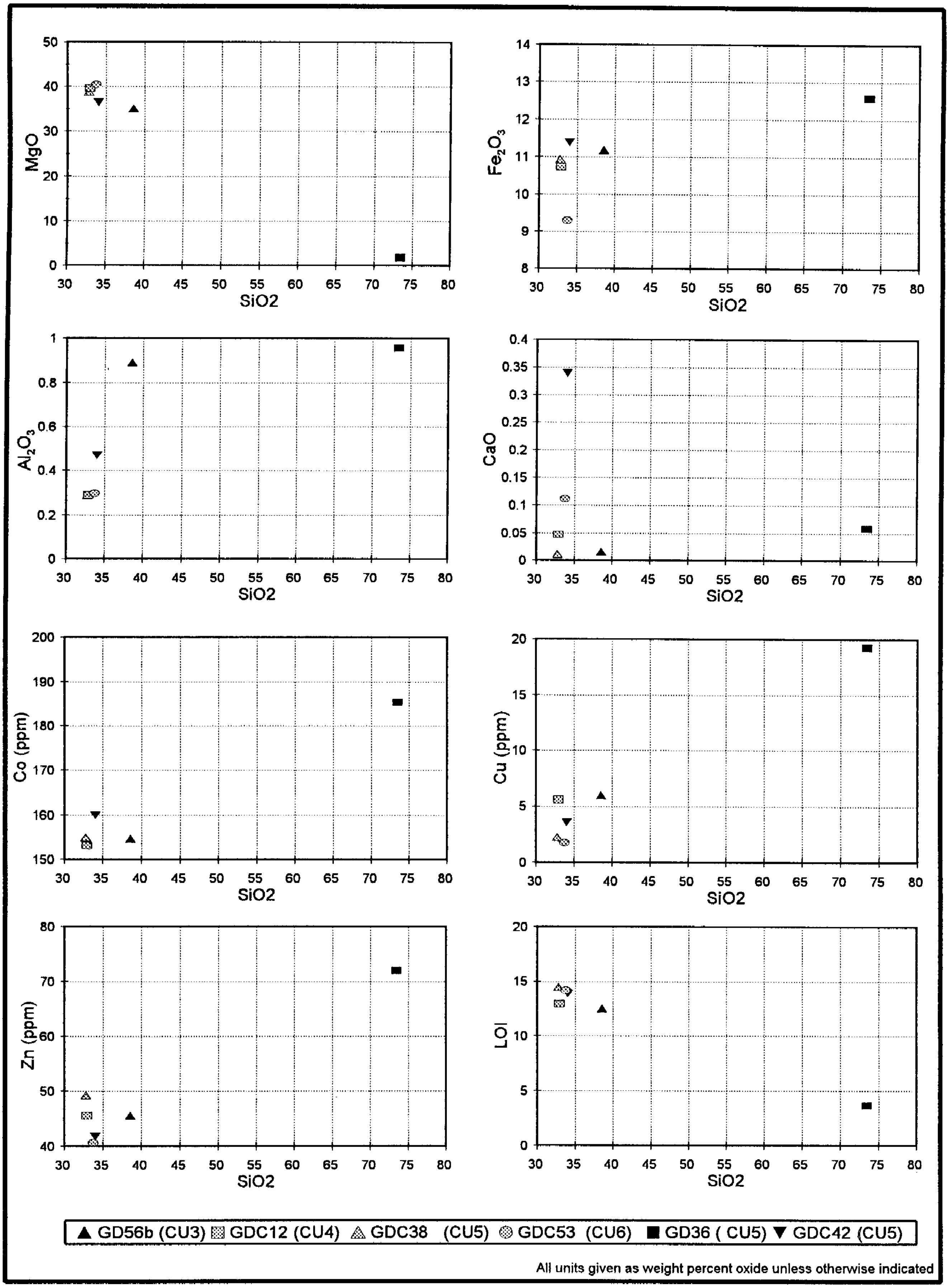

All units given as weight percent oxide unless otherwise indicated

Figure 6.11 : Bivariate plots against SiO_2 of serpentinite whole rock data.

GDC12, GDC38, and GDC53 are relatively unaltered serpentinites from borehole core; GDC42 is an example of 'brown serpentinite ' from borehole core; GD36 and GD56b are surface samples that are pervasively and partially silicified, respectively.

'brown' serpentinite described in chapter 4. The most obvious chemical indication of this alteration is shown by the significantly high CaO proportions, relative to unaltered serpentinites. This is probably a reflection of the occurrence of calcite as part of the extensive carbonate development noted in the rock, indicating that the alteration took place in the presence of carbonate-rich fluids. Small relative increases in Al_2O_3, Fe_2O_3, and Co are also shown by GDC42, accompanied by a small decrease in MgO.

Comparison of unaltered serpentinite with a pervasively silicified sample, GD36, and a relatively 'fresh' surface sample, GD56b, in figure 6.11, clearly illustrates the chemical effects of serpentinite silicification. Most trends indicate a linear progressive chemical variation with increasing silicification. Base metal trace elements are particularly sensitive to serpentinization, Co, Cu, and Zn showing a strong positive correlation with increasing SiO_2. A well-developed negative correlation with SiO_2 is shown by both MgO and LOI. Proportions of Al_2O_3 suggest a high degree of sensitivity to surface silicification, rapidly increasing with initial silicification (shown by GD56b), but remaining essentially unchanged by increasing silicification (shown by GD36). It should also be noted from table 6.4 that Sr was only measured above the lower limit of detection (LLD) in the altered serpentinites, being highest in GDC42, and Rb was measured only in the highly silicified GD36.

6.5 : SUMMARY

The results of EM studies of the chromite from chromitites C8 to C5 were in good overall agreement with previously published data, with the exception of unsatisfactory results from chromitite C6. The chromites show a fairly limited compositional range, with the most striking chemical features being the high chromium and magnesium contents. The high magnesium contents are partly the result of primary cumulus processes, reflecting the highly magnesian nature of the Great Dyke magma, but are also considered to be a reflection of postcumulus annealing processes. Disseminated chromite within dunite has a significantly higher X_{mg} ratios than seam chromites, and lower chromium values. The compositional differences between seam and disseminated chromites are due to several factors, including primary controls such as higher X_{mg}

of chromite crystallizing cotectically with olivine, and secondary controls such as sub-solidus re-equilibration and the relative importance of the sintering process.

Studies of chromite mineral chemistry approaching the base of the C5 chromitite indicate increasing temperature, Cr content, and possibly fO_2 conditions within the magma prior to chromite crystallization. This strongly suggests a mechanism of chromitite formation related to primitive magma input and subsequent magma mixing that will be discussed in detail in chapter 8.

The high magnesium nature of the Great Dyke rocks is also highlighted by the compositions of the silicate mineralogies. Orthopyroxenes have enstatitic compositions in the range En_{85} to En_{88} , and the olivines have forsteritic compositions from Fo_{87} to Fo_{92}.

Mineral and whole rock data are consistent with an overall fractionation trend, within the context of periodic reversals to more primitive compositions associated with the base of cyclic units, as proposed by Wilson (1982).

Serpentinite whole rock compositions highlighted the isochemical nature of the serpentinization process, and the chemical effects of the weathering profile, particularly the effects of surface silicification. The major chemical change during silicification was a removal of Mg and structural water from the serpentine minerals.

CHAPTER 7 : SERPENTINE MINERALOGY AND SERPENTINIZATION

7.1 : INTRODUCTION

This chapter deals with several aspects of serpentine mineralogy and the serpentinization process. Results of powder X-ray diffraction studies of serpentinite and chromitite are discussed with reference to serpentine and serpentinite mineralogy, and the possible alteration effects of serpentinization on chromite.

7.2 : SERPENTINE MINERALOGY

The classification of the serpentine minerals as lizardite, chrysotile, and antigorite, based on structural observations, was initially proposed by Whittaker and Zussman (1956), who were also the first to identify and name lizardite as a serpentine mineral. The classification scheme proposed by Whittaker and Zussman (op.cit.) incorporated a threefold division of chrysotile, as shown below:

- Serpentine
  - Chrysotile
    - Clinochrysotile
    - Orthochrysotile
    - Parachrysotile
  - Lizardite
  - Antigorite

The serpentine minerals are trioctahedral hydrous phyllosilicates based on differing 1:1 layer structures: all have a structural misfit problem resulting from the Mg-occupied octahedral sheets being laterally larger than the Si-occupied octahedral sheets (Wicks & O'Hanley, 1988). The main differences among the three minerals arise from their different solutions to this misfit problem. In Lizardite, the misfit is accommodated within the planar structure. Chrysotile has a cylindrical structure, in which the misfit is partly accommodated by the curvature of the layers. Chrysotile occurs in three structural sub-types: clinocrysotile is the most common type, where *a* is parallel to the cylindrical axis (Whittaker, 1956a); orthochrysotile has 180° rotations between layers

(Whittaker, 1956b); the rarest of these sub-types is parachrysotile, which has 180° rotations between layers, and where *b* is parallel to the cylindrical axis (Whittaker, 1956c). In antigorite, the misfit is accommodated within the curvature of the alternating-wave modulation of the structure.

The polymorphs lizardite and chrysotile are generally described with reference to the polytype of the mineral: for example, the most common lizardite polytype is Lizardite $1T$. The first number corresponds to the number of layers in the repeating unit along *z*, and the subsequent letters refer to the lattice symmetry (e.g. Trigonal = T, Or = Orthorhombic). The subscripts adjoining these letters are used to differentiate structures that have the same periodicity and symmetry (Bailey, 1988). In chrysotile, the first subscript, c, refers to the cylindrical structure and it is the second subscript that is used to differentiate similar structures.

The ideal serpentine mineral composition is $Mg_3Si_2O_5(OH)_4$. Antigorite is known to deviate from this, as it contains less Mg and OH, which is an effect of the alternating wave structure (O'Hanley et al.,1989). Because of the slightly different composition of antigorite, it cannot be considered a polymorph of lizardite and chrysotile. Aluminium substitutes for both Mg and Si in lizardite and forms a continuous reaction series that extends to amesite $(Al,Mg_2)(Si,Al)O_5(OH)_4$. Wicks and O'Hanley (1988) suggest that lizardite and chrysotile cannot be considered true polymorphs when lizardite contains more than 3.5 wt% Al_2O_3, and propose that lizardite may be classified as low- (1% Al_2O_3), intermediate- (1-3.5% Al_2O_3), and high-Al lizardite (>3.5% Al_2O_3). Pseudomorphic textures are usually composed of low Al-lizardite.

Serpentine minerals have a low preference for iron, and as most of the primary phases in ultramafic rocks contain significant amounts of iron, much of the excess iron goes into brucite and/or magnetite. Brucite often occurs as an intimate admixture with lizardite, rather than as discreet grains, and is therefore only rarely visible in thin section. Magnetite is the most common accessory mineral produced by the serpentinization of olivine. Very little magnetite is associated with pseudomorphs after pyroxene, however, although the Mg:Fe ratio is similar to that of olivine. This is due to the (Mg+Fe):O ratio being the same in enstatite and lizardite (Wicks & Whittaker, 1977).

Garnierite is a collective term for hydrous nickel silicates that belong to the serpentine and talc mineral groups (Springer, 1974). The garnierite serpentines form structural analogues of the magnesian serpentines, with the two main varieties, nepouite and pecoraite, being structurally related to lizardite and chrysotile, respectively (Bayliss, 1981).

7.3 : POWDER X-RAY DIFFRACTION STUDIES OF SERPENTINITES

7.3.1 : Introduction

The most convenient method of establishing the mineralogy of serpentine observed in thin section is analysis by powder X-ray diffraction (XRF). XRF studies of several serpentinite samples were undertaken, including analysis of vein and fracture-filling material. Analysis of one sample from chromitite C5 was completed in order to examine the mineralogy of intergrain silicates, and to investigate alteration of the chromite rims.

The interplanar spacing, *d*, was established from the 2θ wavelengths (of $K\alpha_1$ from a Cu X-ray tube) using the Fang and Bloss (1966) reference tables. Whole rock relative intensities (Int 100*) given in tables 7.1 and 7.2 are measured by peak height, relative to the maximum which is given a value of 100: between 100 and 20, percentages are rounded off to the nearest multiple of 5; between 20 and 0, they are rounded off to the nearest integer, in accordance to the system used by Berry (1974). Peaks referred to in the following text are given by the *d* values.

7.3.2 : Serpentinites

Table 7.1 presents a summary of the strongest diffractogram peaks for sample GDC12, a pervasively serpentinized dunite from 68 m depth in borehole H10/4a. The results indicate that the dominant serpentine polymorph is chrysotile $2Mc_1$, shown by very strong main peaks at 7.30 and 3.66. The wide spread of the chrysotile $2Mc_1$ peaks suggest that several polytypes of chrysotile and lizardite are present in lesser proportions. The relatively low intensity of the lizardite $1T$ main peak at 2.50 confirms the presence of lizardite and its relative subordinance to chrysotile. The other lizardite peaks are obscured by chrysotile, although their presence is suggested by the skew to the right hand side of the diffractogram (see 3.66 and 7.30 peaks in figure 7.1). A weak forsterite reflection is observed at 2.46, other forsterite peaks are masked by stronger reflections of other minerals (see table 7.1).

Table 7.1: Summary of XRD analysis of serpentinite sample GDC12

***d*-spacing**	**Int 100***	**Assigned to:**	***hkl***
7.75	100	$Mg(OH)_2$ .0.25(Ni, Fe) OOH	003
7.30	100	chrysotile2Mc$_1$ (+ lizardite 1*T* @ 7.40)	002
4.60	7	chrysotile2Mc$_1$ (+ lizardite 1*T* @ 4.60)	020
3.88	40	$Mg(OH)_2$ .0.25(Ni, Fe) OOH (+ forsterite @ 3.88	006
3.66	65	chrysotile2Mc$_1$ (+ lizardite 1*T* @ 3.67)	004
2.99	3	magnetite	220
2.77	3	forsterite	130
2.62	5	$Mg(OH)_2$ .0.25(Ni, Fe) OOH	012
2.52	10	magnetite + chromite (*hkl* of magnetite given)	311
2.50	14	lizardite 1*T* (+ forsterite @ 2.51)	201
2.46	7	forsterite olivine	112
2.33	5	$Mg(OH)_2$ .0.25(Ni, Fe) OOH	015
2.15	5	lizardite 1*T*	202

When bracketed, refers to presumed peaks (from Berry, 1974) masked by strong peaks of other minerals. Analysis was run from a 2Θ angle of 10-40 degrees.

An important result of the XRD analyses was the occurrence of very strong peaks representing *d*-spacings of 7.75 and 3.88, with subordinate peaks at 2.62 and 2.33 (table 7.1). The *d*-spacings and relative intensities of this mineral match the published XRD data of an un-named mineral with the formula $Mg(OH)_2$ .0.25(Ni, Fe) OOH (Berry, 1974). The single known report of this mineral was from the Cedar Hill serpentinite in Pennsylvania, USA, by Lapham (1965). The nickeliferous magnesium hydroxide was described as a yellow-green flaky powder, occurring in an intimate association with serpentine, brucite, and magnesite. The hydroxide was considered to be structurally similar to pyroaurite and brucite. No discernible brucite reflections were observed in the diffractograms, and it is suggested that the hydroxide may represent an analogue of brucite in these serpentinites.

Figure 7.1 : Comparison of selected diffractogram patterns from powder X-ray diffraction analysis of serpentinites .

Numbers in bold font correspond to average *d* values for the main peaks

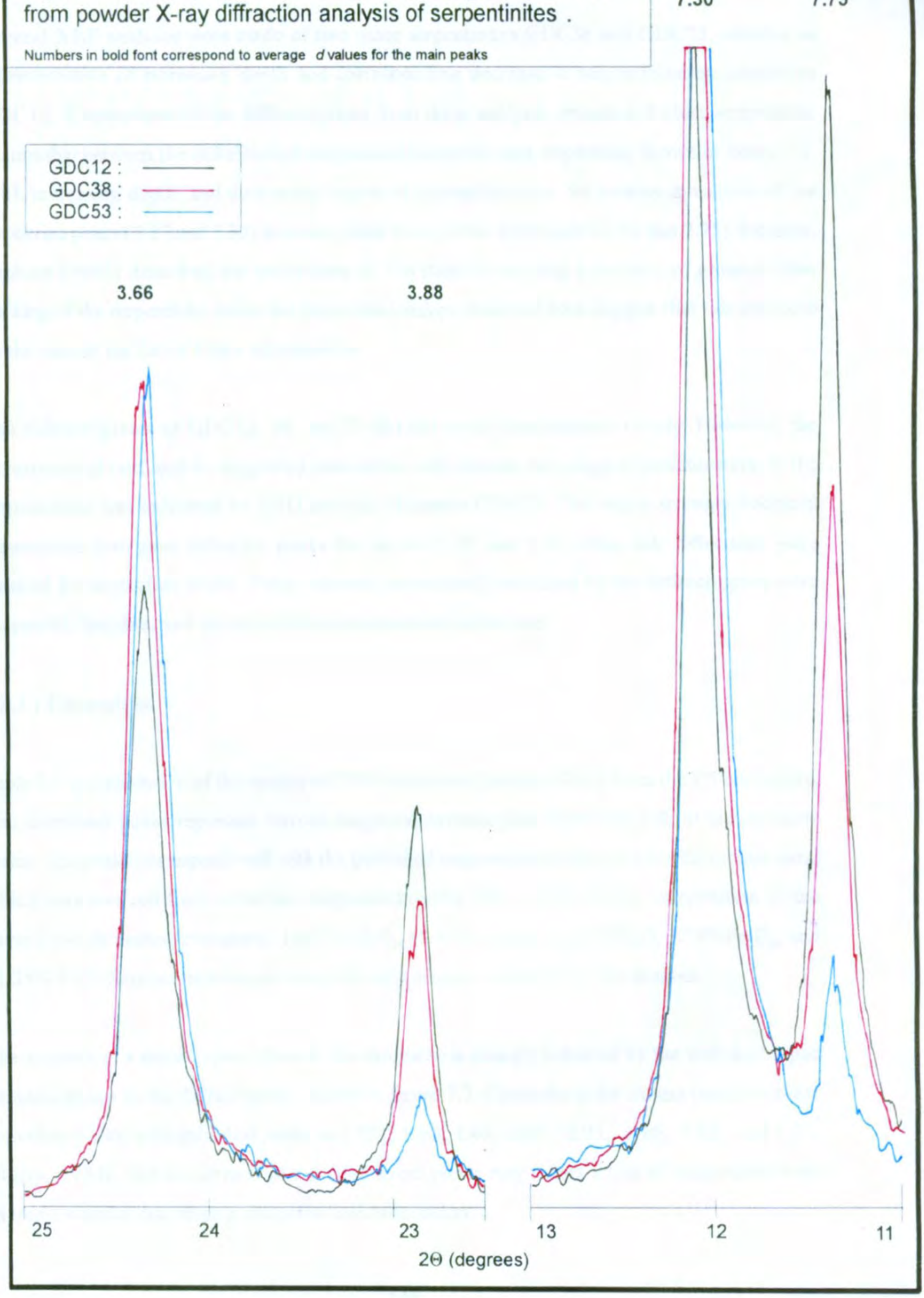

Several XRF analyses were made of two other serpentinites GDC38 and GDC53, selected as representative of increasing depth and corresponding decrease in serpentinization relative to GDC12. Comparison of the diffractograms from these analyses reveals a distinct antipathetic relationship between the nickeliferous magnesium hydroxide and serpentine, shown in figure 7.1. With increasing depth, and decreasing degree of serpentinization, the relative intensities of the serpentine peaks (3.67 and 7.30) increase, whilst those of the hydroxide (3.88 and 7.75) decrease. Lapham (1965) described the occurrence of this mineral as being a product of ground-water leaching of the serpentinite rocks; the depth-relationships observed here suggest that this may also be the case in the Great Dyke serpentinites.

The diffractograms of GDC12, 38, and 53 did not reveal the presence of talc. However, the occurrence of talc, and its suggested association with intense late-stage serpentinization, in the serpentinites was indicated by XRD analysis of sample GDC10. This was a strongly-fractured serpentinite that gave definitive peaks for talc at 9.35, and 3.11, other talc reflections were masked by serpentine peaks. Other minerals prominently indicated by the diffractogram were chrysotile, lizardite, and the nickeliferous magnesium hydroxide.

7.3.3 : Chromitite

Table 7.2 is a summary of the results of XRD analysis of sample GD13 from the C5 chromitite. The dominant peaks represent ferroan magnesiochromite that forms the bulk of the chromite grains. The peaks correspond well with the published magnesiochromite powder diffraction data, which was sourced from a ferroan magnesiochromite with a fairly similar composition to the Great Dyke chromites, containing: 14.03% Al_2O_3, 55.51% Cr_2O_3, 14.83%MgO, 3.79%Fe_2O_3, and 11.35% FeO. Serpentine minerals were the only silicates indicated by the analysis.

The presence of a second spinel phase in the chromitite is strongly indicated by the well-developed doublets shown by the diffractogram, shown in figure 7.2. Chromite is the closest match to these secondary peaks, with published peaks at 2.52_{10}, 1.60_9, 1.46_9, 2.07_7, 2.95_6, 1.10_6, 4.82_5, and 1.26_5 (Berry, 1974). The occurrence of a second spinel phase may reflect a loss of magnesium from altered chromite rims during alteration/serpentinization.

Figure 7.2 : Doublet peak patterns from powder X-ray diffraction analysis of C5 chromitite, sample number GD13

Numbers in bold font correspond to average *d* values for the dominant peak of each doublet

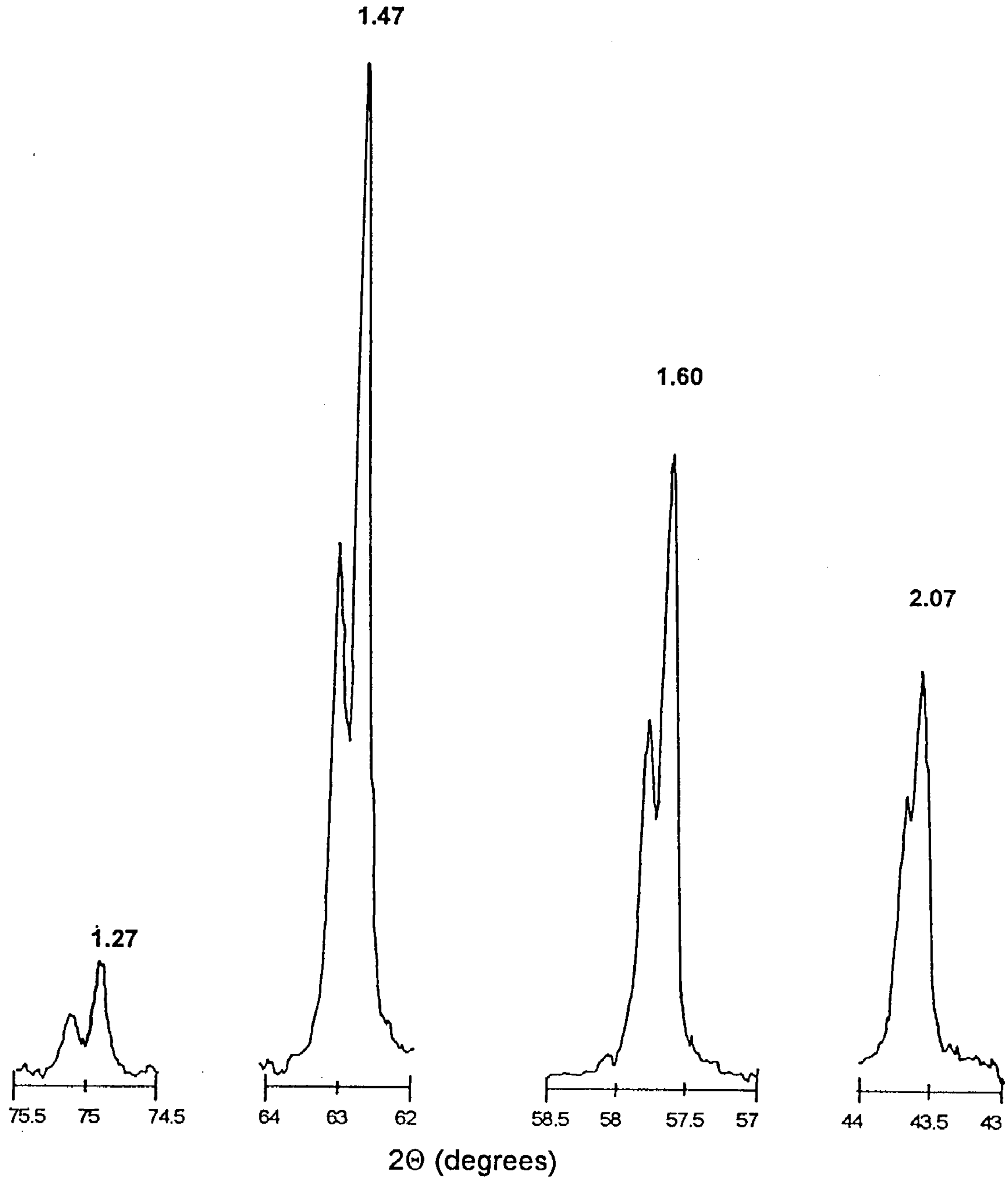

Table 7.2: Summary of XRD analysis of chromitite sample GD 13

d-spacing	Int 100*	Assigned to:	*hkl*
7.28	13	serpentine (*hkl* of chrysotile 2Mc$_1$ given)	002
4.79	35	magnesiochromite	111
3.64	8	serpentine (*hkl* of chrysotile 2Mc$_1$ given)	004
2.93	25	magnesiochromite	022
2.50	100	magnesiochromite	113
2.07	25	magnesiochromite	004
2.07	25	chromite	004
1.60	40	magnesiochromite	115
1.59	25	chrome spinel	115
1.47	65	magnesiochromite	044
1.46	40	chrome spinel	044
1.27	9	magnesiochromite	335
1.26	5	chrome spinel	335

Analysis was run from a 2Θ angle of 05-80 degrees.

7.4 : SERPENTINIZATION

7.4.1 : Introduction

The main alteration products of magnesian olivines are serpentine, brucite, magnetite, talc, and carbonates. During serpentinization of ultramafic rocks, the serpentinizing fluids are undersaturated with respect to forsterite and enstatite, and supersaturated with respect to serpentine and brucite. This situation results in rapid dissolution of anhydrous phases and slow precipitation of hydrous phases. The dissolution of grains initially takes place preferentially at grain margins and along dislocations and cleavages. Associated with the onset of serpentinization is the development of a grid-like framework of fractures surrounding olivine and pyroxene grains, the geometry of these fractures is consistent with a water-diffusion controlled process (Wicks & O'Hanley, 1988). Large-scale, continuous veins of lizardite represent conduits for the serpentinizing fluids which fed this fracture framework.

7.4.2 : Rock-volume change during serpentinization

Serpentinization causes an increase in volume of ~18% for 50% serpentinization; however, the overall linear expansion could be as little as ~2.7% if the expansion occurs equally in all three dimensions (Deer et al, 1982). Part of this expansion could be accommodated by fractures around partially altered olivines and possibly by shear faulting within the ultramafic body. In the Jimberlana intrusion of Western Australia (Campbell, 1975), a widening of fractures occurred close to surface due to unloading processes, this enabled a greater fluid flow and increased levels of alteration, thereby causing an increase in volume due to serpentinization. The volume change led to more microfracturing and therefore increased penetration of serpentinizing fluids, which resulted in the cumulates being 60% serpentinized within 100 m of the water table.

According to Beeson and Jackson (1969), textural relations and field evidence from the Stillwater Complex suggest approximately constant volume. Serpentinites from the area of their study showed no detectable brucite, and Beeson and Jackson (op.cit.) suggested that the formation of brucite during serpentinization may be an important factor influencing volume increase associated with serpentinization. Within the Great Dyke, the ubiquitous fracturing of the chromitites as an apparent response to the serpentinization process suggest a volume increase. Although no brucite was detected, the presence of a proposed nickeliferous analogue of brucite would be consistant with Beeson and Jackson's (op.cit.) observations.

7.4.3 : Reactions

In the absence of talc and amphiboles, the first serpentinization reaction is:

$$\underset{\text{forsterite}}{2Mg_2SiO_4} + \underset{\text{water}}{3H_2O} \rightleftharpoons \underset{\text{serpentine}}{Mg_3Si_2O_5(OH)_4} + \underset{\text{brucite}}{Mg(OH)_2}$$

this process consumes water and occurs at a reaction front that migrates through the ultramafic body as a kinematic wave as water percolates through the rock.

Except for the addition of water (+/- CO_2, SiO_2), the serpentinization process only involves minimal changes in rock composition (see chapter 6.4.3). The serpentine minerals are very sensitive to some solvents in the serpentinizing fluid: very little CO_2, for example, is required to stabilize a carbonate mineral. Significant amounts of CO_2 in the fluid will cause serpentine minerals to become unstable and be replaced by talc and carbonates possibly formed by the reaction:

$$\underset{\text{serpentine}}{2Mg_3Si_2O_5(OH)_4} + 3CO_2 \rightarrow \underset{\text{talc}}{Mg_3Si_4O_{10}(OH)_2} + \underset{\text{magnesite}}{3MgCO_3} + 3H_2O$$

The textural occurrence of talc and magnesite in the Great Dyke are consistant with late-stage CO_2-rich serpentinising fluids.

Relative to unaltered ultramafic rocks, serpentinites are commonly enriched in chlorine, boron, and possibly fluorine (Sanford, 1981). Halides are preferentially partitioned into the serpentinizing fluids, so where there is excess water they will tend to remain in solution, hence the greatest enrichment will be in partially altered rock where water availability was restricted. Maximum enrichment of these elements is in fine-grained serpentine adjacent to relict olivine grains, whereas in veins, where serpentinization took place in excess water, the serpentine is poor in halides.

Chlorine can exist in partially serpentinized rocks as a submicroscopic solid phase with the composition $Fe_2(OH)Cl$. This hydroxychloride is only stable at the reaction front, where the consumption of hydrogen in the serpentinization process causes alkaline conditions, as shown by the reaction:

$$4(Mg_{0.75}Fe_{0.25})SiO_4 + 5H_2O + HCl \rightarrow 2Mg_3Si_2O_5(OH)_4 + Fe_2(OH)_3Cl$$

As fresh solutions (which will be generally acid or neutral) replace those modified by the serpentinization process, the hydroxychloride will be dissolved, thereby providing a mechanism for the removal of any excess iron not taken up by magnetite and brucite.

Experimental investigations by Martin & Fyfe (1970) have shown that the rate of conversion of forsterite to serpentine increases as the water availability increases, with a maximum hydration rate (at pressures of ~1 to 3 kb) between 250 and 350°C. Three stages of conversion rates were identified:

1) an initial period, during which the nuclei of the hydration product are forming.
2) an accelerated period, during which there is both nucleation and growth.
3) the growth period, in which no more nucleation takes place.

7.4.4 : Temperature of formation

Phase relations indicate that chrysotile is the low pressure, low temperature serpentine mineral, lizardite is the high pressure, low temperature mineral and antigorite is the high pressure, high temperature mineral. The higher equilibrium temperatures of antigorite make it the most stable of the serpentine minerals; although at low pressures aluminous lizardite may be stable above the upper thermal stability limit of antigorite (Caruso & Chernosky, 1979). Figure 7.3 shows the relative stabilities of chrysotile, lizardite and antigorite; derived from experimental data by Caruso & Chernosky (op.cit.) and others.

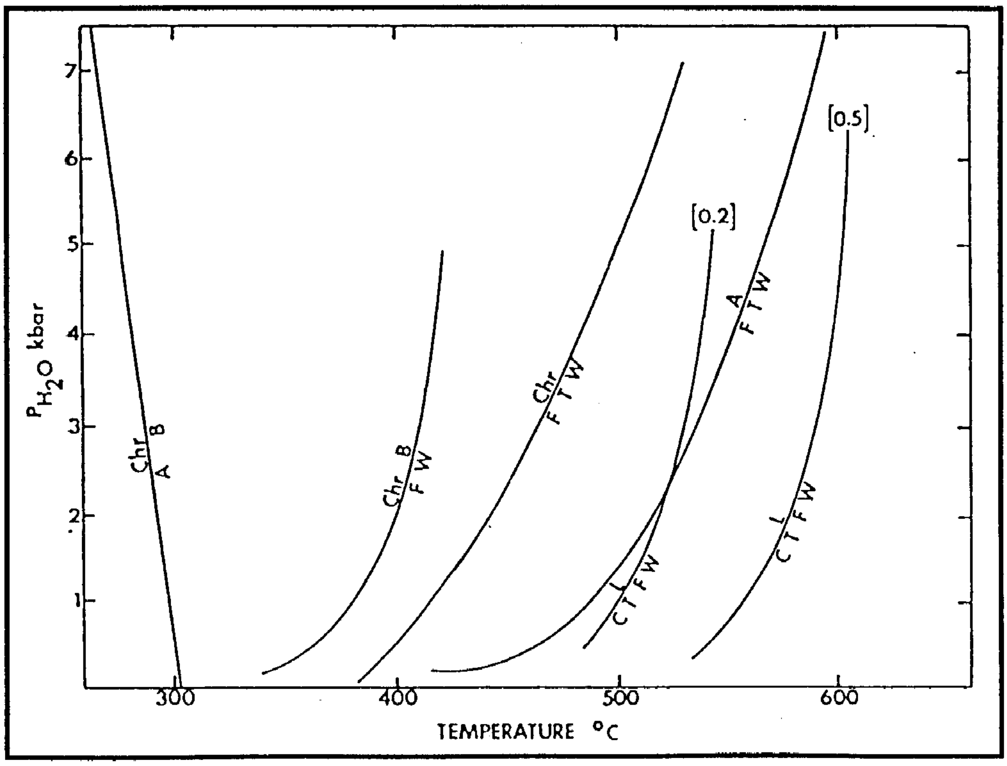

Figure 7.3 : P-T diagram illustrating relative stabilities of chrysotile (Chr), lizardite (L), and antigorite (A). [0.2]and {0.5] refers to lizardite synthesized with 3.7 and 9.25 wt% Al_2O_3, respectively. Other abbreviations: B, brucite; F, forsterite; W, water; C, clinochlore; T, talc. (After Caruso and Chemosky, 1979)

At pressures of 2 kb the equilibrium temperature of the reaction

forsterite + water ⇋ serpentine + brucite

occurs at 380 °C (Johannes, 1968). The effect of iron on the reaction forsterite → serpentine + brucite is indicated by figure 7.4 ,which shows a 15 °C shift to lower temperatures on the reaction phase diagram, relative to pure forsterite, for olivine of composition Fo_{93} (Deer et al.,1982)

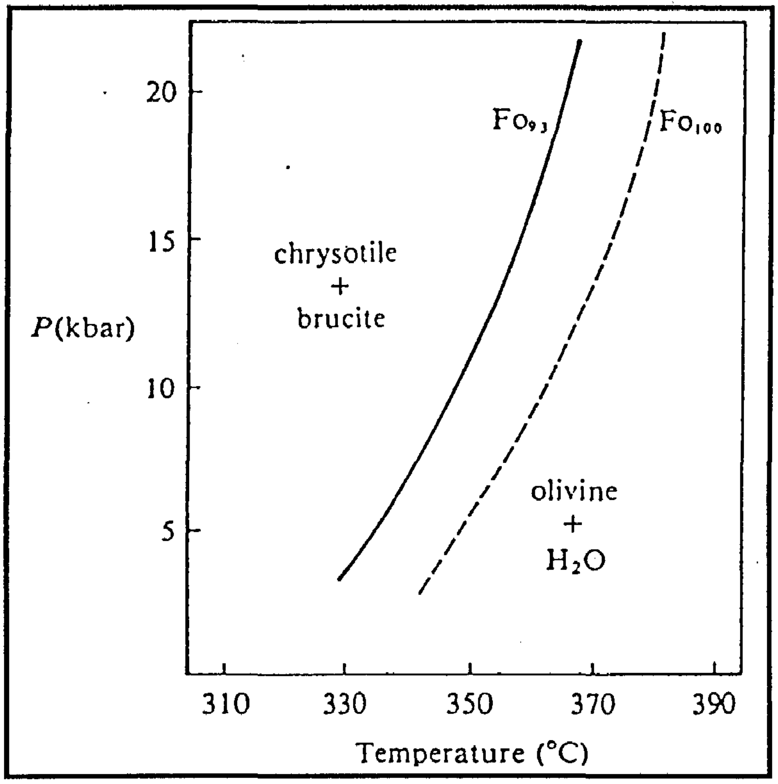

Figure 7.4 : Reaction curves for Fo_{93} and Fo_{100} (after Deer et al., 1982).

Serpentinization often occurs at relatively low temperatures and often in broadly constant temperature regimes, therefore the rate-limiting factor of the serpentinization process will be the availability of water, rather than temperature. In continental rocks lizardite and chrysotile tend to form within the temperature range 85 to 115 °C, with antigorite forming at higher temperatures between 220 and 460°C (Wenner & Taylor, 1971). These temperatures are consistent with formation of lizardite and chrysotile by groundwater, connate water and brines, and antigorite formation by deeper, metamorphic waters.

A low temperature of serpentinization is supported by studies of the composition of surface waters in ultramafic rocks. Surface waters from unaltered ultramafic rocks contain Mg^{2+} and HCO_3^- as the predominant cation and anion; in partially serpentinized rocks, Ca^{2+} and $(OH)^-$ are the predominant ions which make the waters undersaturated with respect to forsterite. Therefore there is Gibbs free energy potential to dissolve forsterite (Deer et al., 1982).

7.4.5 : Role of water

For the pervasive serpentinization of a rock body to take place, a significant amount of water (~13 wt%) is required for the hydration reactions involved in the serpentinization process. At the likely depths of serpentinization (between 2 and 7 km), hydraulically-driven fluid flow would allow access of large quantities of water to the rock body.

In retrograde metamorphism, conditions are often such that water pressure, $P(H_2O)$, is less than the total/rock pressure, P_t. This is achieved in several ways: H_2O in the fluid may be diluted by other volatiles or by dissolved solids, if H_2O exists solely as absorbed molecules on the surface of mineral grains with no fluid phase present, or if the total/rock pressure exceeds $P(H_2O)$.

The properties of ultramafic rocks are favourable for creating conditions of $P(H_2O) < P_t$: at the onset of serpentinization there is limited trapped fluid, so initial hydration reactions continue only until all trapped H_2O is consumed; the rocks generally have low permeability, so H_2O from pore fluid or grain boundaries can be consumed faster than H_2O can diffuse into the rock so that serpentinization is controlled by the rate of diffusion and availability of water. The hydration reactions of serpentinization in retrograde conditions also provide a constant sink for H_2O, thereby keeping $P(H_2O)$ low. The local variations in $P(H_2O)$ conditions during retrograde metamorphism enables assemblages of mutually incompatible phases to coexist, such as relict olivine and pyroxene occurring with serpentine minerals, brucite and amphiboles (Sanford, 1981).

7.4.6 : Serpentinization models

Changes in serpentine mineralogy and texture can result from three factors:

1) a change in fluid composition.
2) a change in fluid pressure.
3) a change in temperature.

Wicks and O'Hanley (1988) refined the chemographic model of Wicks & Whittaker (1977) due to the lack of appreciable influence on mineralogy exerted by penetrative deformation. Both models are outlined in table 7.3.

Table 7.3. Classification of serpentinization (modified after Wicks & O'Hanley, 1988).

Wicks & O'Hanley (1988)	**Wicks & Whittaker (1977)***				
Regime	Type	Temperature	Textures	Antigorite*	Foliation**
A	1	decreasing	pseudomorphic	yes	no
	2	decreasing	non-pseudomorphic	yes	yes
B	3	decreasing	pseudomorphic	no	no
	4	decreasing	non-pseudomorphic	no	yes
C	5	increasing	transitional	no	no
	6	increasing	non-pseudomorphic	no	yes
D	7	increasing	non-pseudomorphic to transitional	yes	no
	8	increasing	non-pseudomorphic	yes	yes

*Antigorite: nucleation (yes) or absence (no)

** Foliation: presence (yes) or absence (no) of shearing.

Serpentine mineral transitions are solely dependant on P(H_2O) and temperature, therefore each of the regimes has a specific location in P-T space. Regimes A & B occur under retrograde metamorphic conditions, with falling or constant temperature, whereas Regimes C & D occur during prograde metamorphism. A brief summary of the regimes is given below, with an emphasis on regimes B and C, which are considered to be the most relevant to the serpentinization of the Great Dyke rocks:

A) Serpentinization begins in at the highest possible temperature to form antigorite. Regime A is not a common situation, because during retrograde metamorphism, where the conditions generally result in a lowered P(H_2O), olivine will commonly hydrate to lizardite and/or chrysotile.

B) This is the common situation in retrograde conditions. Serpentinization takes place at lower temperatures, where the alteration is initiated by a free-fluid phase or by conditions created by the presence of intergranular water. The initial serpentinization is thought to take place rapidly and simultaneously at a reaction front, producing the randomly oriented and fine grained serpentine such as that observed in mesh centres and along the grain boundaries of remnant pre-existing minerals (Cressey, 1979). Remnant olivine fragments in mesh centres indicate that the serpentinization front was halted at some point, probably due to cooling or a lack of water. Following the initial serpentinization stage, recrystallization causes development of the coarsely crystalline and well orientated serpentine observed in mesh rims. If the recrystallization episode was short lived then it would be expected that the mesh rims would be narrow and mesh centres large; complete recrystallization may result in the development of pure hourglass textures (Cressey, op.cit.), where no 'initial' serpentine mesh centres are present. Regime B produces pseudomorphic textures of lizardite ± brucite; where there is penetrative deformation, the result is an assemblage of chrysotile ± lizardite ± brucite with foliated non-pseudomorphic textures and veins. When highly sheared, "fish-scale" serpentine is produced, this is slickenside material that is slippery to the touch.

C) This regime occurs when serpentinization is complete and water pressure rises, leading to recrystallization of pseudomorphic lizardite ± brucite to produce non-pseudomorphic (generally interlocking) textures with chrysotile as the matrix phase (±lizardite ± brucite). Where Regime C occurs under deformative conditions, foliated non-pseudomorphic textures and veins occur, with a similar assemblage to that produced under static conditions; although occasionally spherulitic interlocking textures of multi-layer lizardite ± brucite are formed. Chrysotile asbestos deposits are often formed during serpentinization of Regime C type.

D) Rising temperatures lead to the recrystallization of pre-existing assemblages, producing non-pseudomorphic textures of antigorite ± brucite, although under static conditions crudely pseudomorphic textures can occur. With increasing temperature, dehydration reactions lead to formation of forsterite from antigorite.

7.5 : DISCUSSION

The extensive serpentinization of the olivine-rich rocks in the Mutorashanga area is developed to a depth of up to and over 300 m, as evidenced by borehole H10/4a. Textural and mineralogical studies of the serpentinites in the study area are suggestive of low temperature retrograde serpentinization of Regime B conditions (Wicks and O'Hanley, 1988) with a degree of post- main serpentinization to a chrysotile-dominant assemblage with partial recrystallization of pseudomorphic textures to non-pseudomorphic textures associated with serpentinization under Regime C conditions.

The serpentinization of dunites has been an essentially isochemical hydration reaction, with additional geochemical modification of serpentinites being the result of weathering phenomena and late-stage alteration. The silicification of serpentinites is closely associated with the Cretaceous African erosion surface, and silicified saprolitic serpentinites were regularly observed to retain the initial serpentinite textures. Serpentinization was therefore developed prior to the development of the mature African surface, and was most likely initiated with early uplift and erosion associated with the onset of the African event.

The presence of a nickeliferous magnesium hydroxide as an important phase within surface / near-surface serpentinites as revealed by XRD is notable. The depth relations of this mineral with serpentine strongly indicate that the relative proportions of the hydroxide decrease with increasing depth from surface and decreasing degrees of serpentinization. It is suggested that the nickeliferous magnesium hydroxide, considered to be an analogue of brucite in these rocks, forms as increasingly pervasive alteration of olivine leads to an excess of magnesium and nickel that is not taken up by the serpentine minerals.

It should be noted that the XRD peaks of the nickeliferous varieties of serpentine exhibit similar peaks in diffractograms to lizardite and chrysotile, and a certain proportion of the serpentine from the higher levels of the weathering profile may indeed be garnieritic, as suggested by the 'yellowish' serpentine in chapter 5, and as noted from highly weathered serpentine by Slatter (1979). Nickel enrichment is most likely to be developed in the saprolitic serpentinite developed on the hills associated with the African erosion surface. The best developed nickel laterite deposits are likely to be developed in the serpentinite hills between the Aireys Pass and Kilmacduagh Fault (see chapter 4), the highly fractured rocks associated with the Kilmacduagh Fault in this area being particularly favourable to downward leaching (see Golightly, 1981). A more detailed study of the leached profile would be required to fully characterise the nickel laterite deposits and the overall effects of surface processes on the serpentinized Great Dyke rocks.

CHAPTER 8 : EVOLUTION OF THE GREAT DYKE

8.1 : COMPOSITION OF THE GREAT DYKE MAGMA

The initial composition of the Great Dyke magma has been the source of much debate. Maufe et al. (1919) noted the high magnesium content of the Dyke and suggested that the parent magma would have been "probably of norite composition, that is, a basic magma rather than an ultrabasic one". Hughes (1976) concluded that the parental magma would have been broadly equivalent to a high magnesian basalt. The lack of a definite chill phase means that estimates of the Great Dyke parental magma have had to be derived by indirect methods, namely by calculation from cyclic unit bulk compositions (Bichan, 1970), or by comparison with genetically-related chill phases (Robertson and van Breemen, 1970; Wilson, 1982). To date, the best equivalent to the initial Great Dyke magma is provided by the East Dyke chill phase (Wilson, op.cit.), described in chapter 3.2. Textural evidence indicates that the crystallization sequence of this olivine basalt is:

Chromite → olivine → orthopyroxene → clinopyroxene→ plagioclase (represented by felsic groundmass)

(Wilson and Prendergast, 1989). The initial liquid composition predicted by analysis of the East Dyke chill phase and phase diagrams of the modelled liquid line of descent by Wilson (1982) are given in figure 8.1. It can be seen from the phase diagrams that the East Dyke chill phase fits well with the observed features of CU1, particularly the short-lived crystallization of websterite at the top of the P1 layer.

The magnesian nature of the Great Dyke magma is demonstrated by the strongly magnesian compositions of silicate rocks, and the chromites, of the present study: olivines showed a range of forsteritic compositions from Fo_{87} to Fo_{92} and orthopyroxene compositions ranged from En_{86} to En_{88}. Chromite compositions are exceptionally Mg-rich relative to most other layered intrusions, this is partly a reflection of the parental magma compositions; however, postcumulus processes in the presence of an Mg-rich reactant are believed to have been important in achieving the observed high-magnesium compositions.

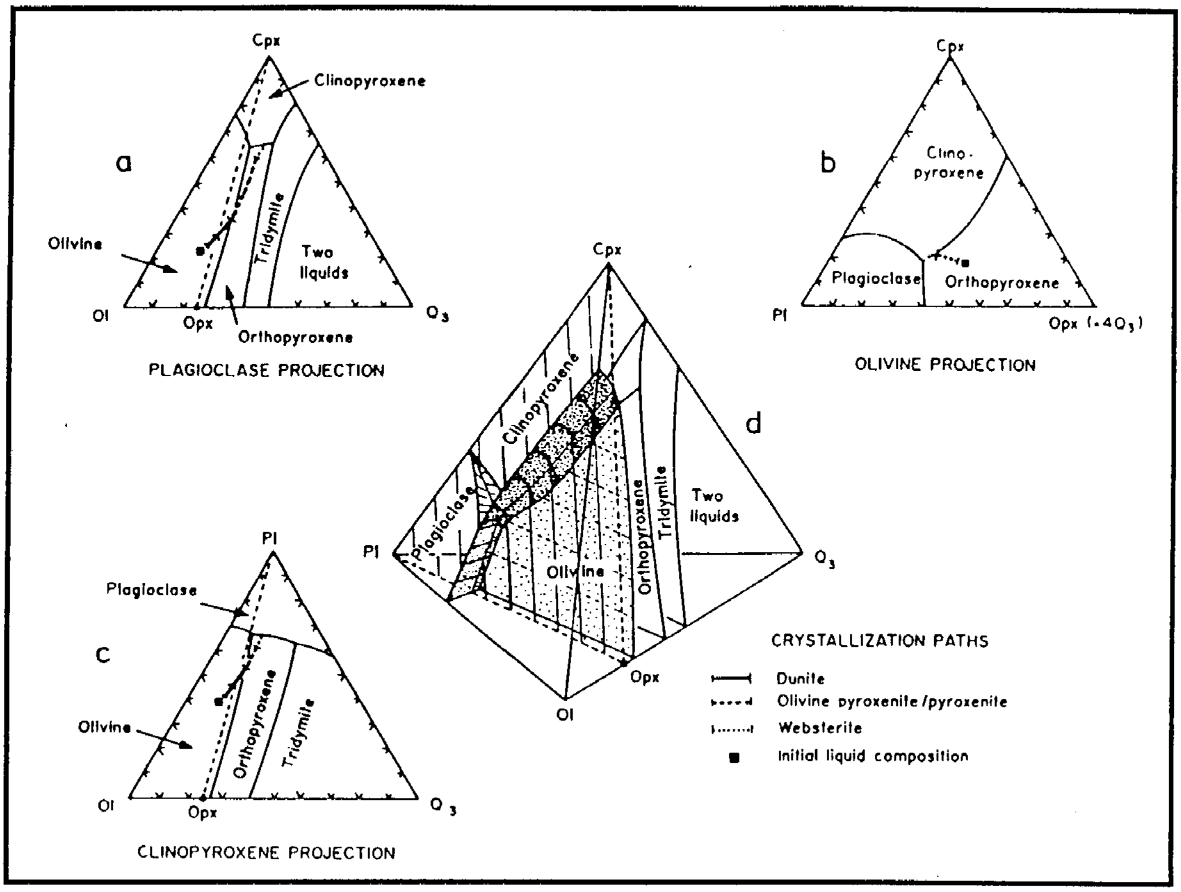

Figure 8.1 : Modelled evolutionary path of the Great Dyke magma using the East Dyke Chill phase as representative of the initial magma composition. The modelled liquid paths correspond to the different mineral assemblages crystallizing to give the Ultramafic Sequence (dunite, pyroxenite, and websterite). (After Wilson, 1996)

8.2 : EVOLUTION OF THE GREAT DYKE MAGMA CHAMBER

8.2.1 : Magmatic processes in the formation of the Ultramafic Sequence

Lightfoot (1926) considered that the Great Dyke lithologies were "almost certainly derived by differentiation, probably gravitative, from a parent magma". Worst (1960) and Bichan (1969) ascribed the macro- layering to separate injections of magma, intruded only after near-solidification of the previous cyclic unit. Worst (op.cit.) considered that the layering of the Dunite Succession and subsequent Pyroxenite Succession were formed as differentiates from chrome-rich magma of dunitic and pyroxenitic composition, respectively. Such a process is now discounted, mainly because of the untenable magma bulk compositions that are invoked.

Hughes (1970) considered the possibilities of both convective overturn and injection of primary magma, concluding that the dominant process was density-driven convective overturn as a result of gravitational settling, with a possible influx of primary magma at the level of CU2 (Hughes' Unit 9).

The relative role of gravity settling has been the subject of intense debate since Campbell (1978) and McBirney and Noyes (1979) argued that field relations and the non-Newtonian behaviour of crystallizing magma precludes gravitational segregation as the main process of differentiation, suggesting instead a mechanism of *in-situ* crystallization. Crystallization occurs near the crystal-liquid interface, with the crystallizing phase governed by the relative rates of chemical and thermal diffusion, and with considerable control on crystal layering by convection and diffusion between liquid layers within a density-stratified magma chamber. Of considerable importance to the relative roles of *in situ* crystallization and gravity settling is the nature of convective systems within the magma chambers (Huppert and Sparks,1980; Marsh, 1988; Martin, 1990; Sparks et al., 1993). It is now believed that whilst *in situ* crystallization is the dominant process, gravitational settling may still be an important factor in the formation of igneous layering.

The concept of replenishment of the magma chamber by periodic injection of fresh primary magma that is compositionally primitive, relative to the evolved residual magma, has been applied to a number of layered intrusions, including Muscox (Irvine, 1977), the Bushveld Complex(Eales et al., 1988), and Munni Munni Complex (Barnes and Hoatson, 1994). The macro-rhythmic layering of the Ultramafic Sequence in the Great Dyke is also considered to have been an open-system process of primary magma injection and slow mixing with the resident magma, followed by a period of 'normal' fractionation that is terminated by a new magma input (Wilson, 1982; Prendergast, 1987; Wilson, 1996). However, the required regularity of repeated magma injection and the relatively constant volume of the inputs, coupled with mass-balance problems, are difficult to explain and some researchers question the validity of the model, suggesting instead some form of closed system processes (Brandeis, 1992; Naslund and McBirney, 1996).
Orthopyroxene trends in the Great Dyke have been shown by Wilson (1982) to display a shift to less evolved compositions at the base of each cyclic unit (see figure 6.8) and are considered to be representative of periods of magma influx. The dynamics of primitive magma input mixing with

an evolved magma crystallizing orthopyroxene will differ from that of mixing with a less evolved magma crystallizing olivine, as the physico-chemical differences between the two magmas will be less marked. This may explain why chemical reversals at the top of cyclic units are located at the lithological contact in the Dunite Succession, yet are located some distance below the contact in the Pyroxenite Succession.

Orthopyroxenes in the Pyroxenite Succession display an overall progression to more evolved compositions, as shown in figure 8.2 : similar trends have been observed in the olivines of the Dunite Succession and are interpreted as indications of fractionation of the primary magma source, resulting in successively more evolved magma injections (Wilson, 1982, Wilson and Prendergast, 1989).

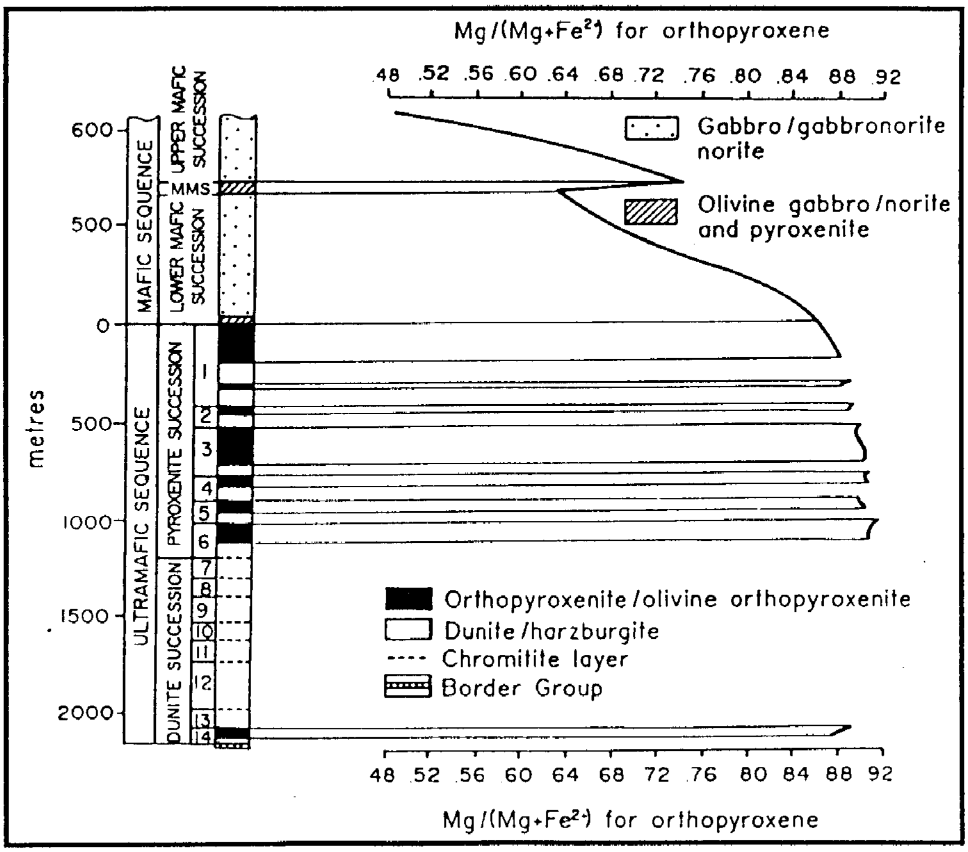

Figure 8.2 : Variation of orthopyroxene Mg/(Mg + Fe^{2+}) ratios through the Mafic and Ultramafic Sequences. Limited fractionation in the Ultramafic sequence contrasts with the rapid fractionation trend shown by the Mafic Sequence. Note the major reversal in the Middle Mafic Succession (MMS). (After Wilson, 1996)

8.2.2 : Genesis of chromitite layers

The occurrence of chromitite layers at the base of cyclic units is a phenomenon that is common to many large layered intrusions, notably the Great Dyke, Stillwater, Muscox, and Bushveld intrusions (Jackson, 1970). Prior to the mid-1970's gravity settling was a fundamental feature of models of chromitite formation. Worst (1960) and Bichan (1969) proposed that olivine and chromite crystallized simultaneously from the magma and formed a basal layer to the cyclic units on account of it's higher density.

The formation of chromitite as a result of *in situ* crystallization requires either a shift in magma composition, or a shift in the position of the olivine-chromite phase boundary, in order for the magma composition to be in the chromite primary phase volume.

Increased oxygen fugacity could lead to an expansion of the chromite liquidus field (Ulmer, 1969), although there is some doubt as to whether such fluctuations in fO_2 could take place on the chamber-wide scale required for chromitite formation (Eales and Cawthorn, 1996). Oxygen fugacity fluctuations in the magma may result from a number of factors:

1) assimilation of volatile-rich country rocks
2) loss of gases by diffusion or expulsion through volcanic vents
3) temperature fluctuations
4) magma convection
5) fractionation of oxide-rich phases

Cameron (1980) suggested that changes in total pressure may cause the shifting of the chromite field, as a result of tectonism or magma influx. Lipin (1993) proposed that chromitite formation in the Stillwater Complex resulted from overpressure caused by rising and expanding CO_2. The CO_2 was derived from degassing of a new magma input in an open-system magma chamber.

Magma mixing is considered by Wilson (1982) to be the primary cause of chromitite formation in the Great Dyke. Irvine (1977) proposed a model whereby magma mixing of evolved and primitive magmas may lead to the shifting of the magma composition into the chromite liquidus field, resulting in the crystallization of chromitites (figure 8.3). For such a model to be viable, it is essential that the mixing of the new magma with the evolved magma takes place at an early stage, and is thus dependant upon the fluid dynamics of the magma influx. Campbell and Turner (1986) predicted that a primitive magma could enter the magma chamber as a fountain if it was injected in a turbulent state, and as such would be expected to achieve a degree of mixing with the evolved magma.

Alternatively, Lipin (1993) argued that turbulent injection is not a realistic prospect and concluded that the primitive magma would enter the magma chamber as an "ooze", and would subsequently spread out at the base of the liquid column. Magma mixing would not take place until the new magma fractionated to a similar composition as the resident magma, this would occur where orthopyroxene was on the liquidus and is suggested as an explanation of the thick pyroxenites observed in cyclic units of the Stillwater Complex. Presumably in the Dunite Succession of the Great Dyke, mixing would take place earlier, with olivine ± orthopyroxene on the liquidus of both magmas.

Magma mixing is the preferred model for the Great Dyke as applied to this study. Whilst valid criticisms of the model remain, it is believed that periodic influx of primitive magma and subsequent mixing with the evolved magma, resulting in a hybrid melt portion, is the most complete and satisfactory explanation for both the chromitites and cyclic unit development. The results of the current study of footwall chromites of the C5 layer strongly support this contention, displaying an apparent comprehensive reversal to primitive compositions towards the chromitite, with compositions indicative of increasing temperature, coupled with a concomitant increasing fO_2. In accordance with Wilson (1982), the mixing of new and residual magmas are considered to have resulted in replenished Cr content of the melt, which, accompanied by an increase in fO_2 led to chromitite precipitation, following the model of Irvine (1977). It is accepted that interpretation of geochemical data from chromites must be treated with some caution due to the difficulty in estimating the effects of subsolidus processes on chromite compositions, discussed in chapter 6.2. However, it is believed that, although some postcumulus compositional modification of the chromite has taken place, dependant upon micro-environments, the overall compositional trends shown in figure 6.5 are indicative of the primary processes within the magma chamber immediately preceding chromitite formation.

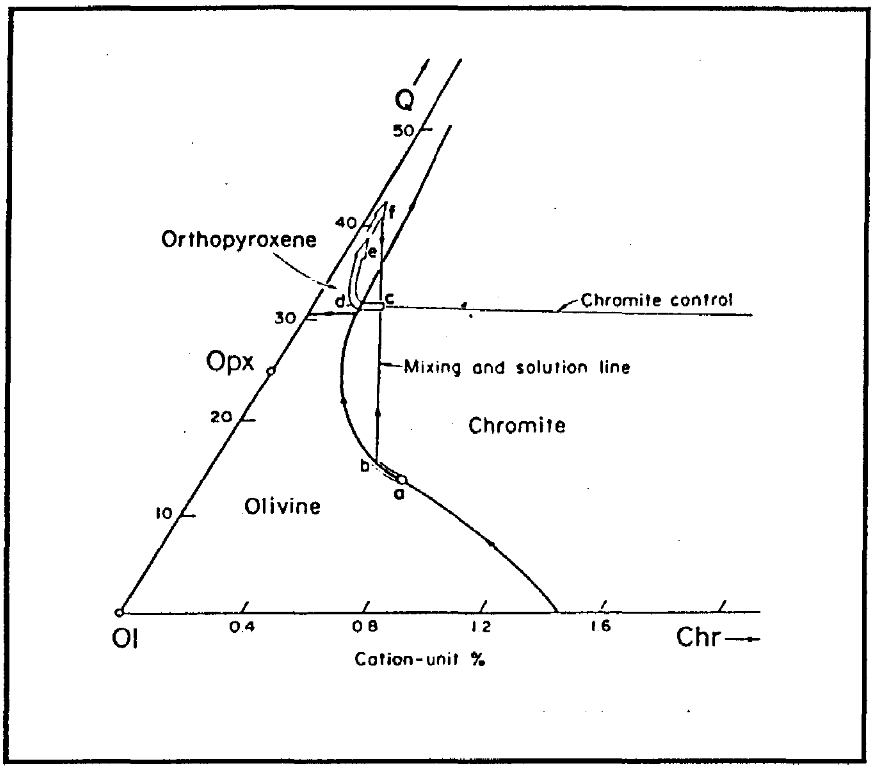

Figure 8.3 : Magma mixing model of Irvine (1977). Mixing of differentiated magma of composition *f* with a primitive magma at *b* results in hybrid magma towards a bulk composition *c* that will crystallize chromite only until the composition returns to the olivine-chromite cotectic. A basal peridotite could be formed if a primitive magma of composition *a* differentiated to *b* along the olivine-chromite cotectic prior to mixing. If , as in the case of the Dunite Succession, the differentiated magma was on the olivine-chromite cotectic, mixing could still result in chromite-only crystallization assuming sufficient compositional differences existed between the differentiated and primitive magmas. (After Irvine, 1977)

Analyses of chromite compositions from chromitite layers in this study are in broad agreement with the data of Wilson (1982). Variation between individual layers can be ascribed to the effects of varying volume and momentum of magma input, coupled with postcumulus processes. From the middle of the lower group chromitites there is an overall upward trend of iron enrichment that is in agreement with the evolving compositions of the primary magma inputs indicated by silicate chemical trends. Upper group chromitites exhibit compositions generally more evolved than the lower group, but detailed compositional variation is a less reliable indicator of primary factors due to the less massive nature of the chromitites, and hence greater postcumulus modification. A reversal of the normal fractionation trend is shown by the increasingly primitive compositions of lower group chromitites from C12 to C8, and is also known from silicate compositional trends (Wilson, 1982). This is suggested by Wilson (1996) to be the result of the same magma layer in a liquid-stratified magma chamber being in contact with successively higher levels of the sloping chamber floor.

8.2.3 : Cyclic Unit 1 and the Mafic Sequence

Cyclic Unit 1 formed as a result of the final major new magma pulse of the Ultramafic sequence. The complexity of the P1 pyroxenite, relative to pyroxenites of earlier cyclic units, is a reflection of the changing conditions of the Great Dyke magma chamber at that stratigraphic level. The continued fractionation of the crystallizing magma during P1 formation is considered to have lead to the segregation of an immiscible sulphide melt (Wilson and Tredoux, 1990; Prendergast, 1990; Coghill and Wilson, 1993); although it has been suggested that the sulphides of the MSZ were formed by melt segregation due to a combination of fractionation and magma mixing processes (Wilson et al., 1989). Murahwi (1995) suggested that a reversal of iron-enrichment trends in orthopyroxene at the top of the MSZ indicates that sulphide formation was halted by a repeated magma input. Sulphide liquation occurred at the base of a double-diffusive layering system, extracting PGE and chalcophile metals from the overlying convective magma in the order of the apparent affinity of the metals for incorporation into the sulphide melt (Coghill and Wilson, op.cit.).

The initial PGE mineralization was therefore the result of wholly orthomagmatic processes. Low chlorine contents in apatite and biotite also argue against significant PGE transport by hydromagmatic fluids (Prendergast, 1990). However, formation of the low-T PGM minerals and local re-mobilization of the mineralization was the result of hydromagmatic processes associated with the observed hydrosilicate alteration. This alteration assemblage is considered by Coghill and Wilson (1993) to be caused by a reactive acidic fluid released during the crystallization of the late-stage assemblage of the P1 layer.

The lack of a major magma influx during P1 crystallization resulted in continued fractionation with formation of the Main Websterite Layer, and ultimately in the mafic rocks of the LMU.

However, Wilson and Chaumba (1997) noted that the presence of olivine in the basal zone of the LMU, after a considerable break in olivine crystallization in the P1 layer, implies that an injection of a more differentiated magma at the top of the Ultramafic Sequence cannot be ruled out. This plagioclase-saturated magma may have been injected from a fractionating magma chamber at depth (figure 8.4).

The LMU represents a period of notably uniform fractionation trends, as shown in figure 8.2, indicative of fractional crystallization in a closed system. The magma chamber is considered by Wilson and Chaumba (1997) to become relatively narrower upwards through the succession of the LMU. A further magma injection at the base of the MMU is suggested by a reversal of the orthopyroxene fractionation trend (see figure 8.2).

8.2.4 : A model for the evolution of the Great Dyke

Modelling of the liquid line of descent by Wilson (1982) indicated that the observed compositional reversals would require the input of a considerable amount of magma, suggesting an 'open' magma chamber that may have been a feeder to surface volcanism. Wilson and Prendergast (1989) proposed the following model for the evolution of the Great Dyke, also shown diagrammatically in figure 8.4:

1) Magma was emplaced through a feeder dyke system, which possibly included deep seated magma chambers, as indicated by gravimetric modelling (see figure 3.4).

2) Expansion of the magma chamber in response to magma input took place by elevation of the roof, and by subsidence of the floor, which may have been a fundamental factor in the development of the transverse synclinal layering structure.

3) Extensive stoping of roof rocks, evidenced by the large xenoliths preserved in the UMU near Darwendale, would probably have produced a silicic buoyant magma that was subsequently erupted.

4)The greater volume of the North Chamber compared to the South Chamber suggests that emplacement took place from the north and progressed southwards.

5) Subchambers that were initially separated by floor irregularities became physically linked late in the development of the Ultramafic Sequence, culminating in the linking of the North and South Subchambers at Lalapanzi at the level of CU1. Subsequent development of the Dyke was as a single continuous chamber, with the probable exception of the Mvuradona Chamber in the extreme north.

The significant transverse variations across the magma chamber are essentially a result of the high heat flux and heat gradient caused by the narrow transverse structure of the Dyke and the angular relationships of the sloping chamber floor and stratified magma. Convection within the magma chamber, and the dynamics of new magma input and mixing processes, would have been markedly different between axial and marginal regions. Increased cooling rates may have a fundamental impact on the relative importance of crystal settling versus *in situ* crystallization, and the efficiency of processes such as double diffusive convection. The effects of the narrow transverse shape on PGE-mineralization is emphasized by the overall similarities with the Jimberlana and Munni Munni layered intrusions in Australia (Wilson and Tredoux, 1990).

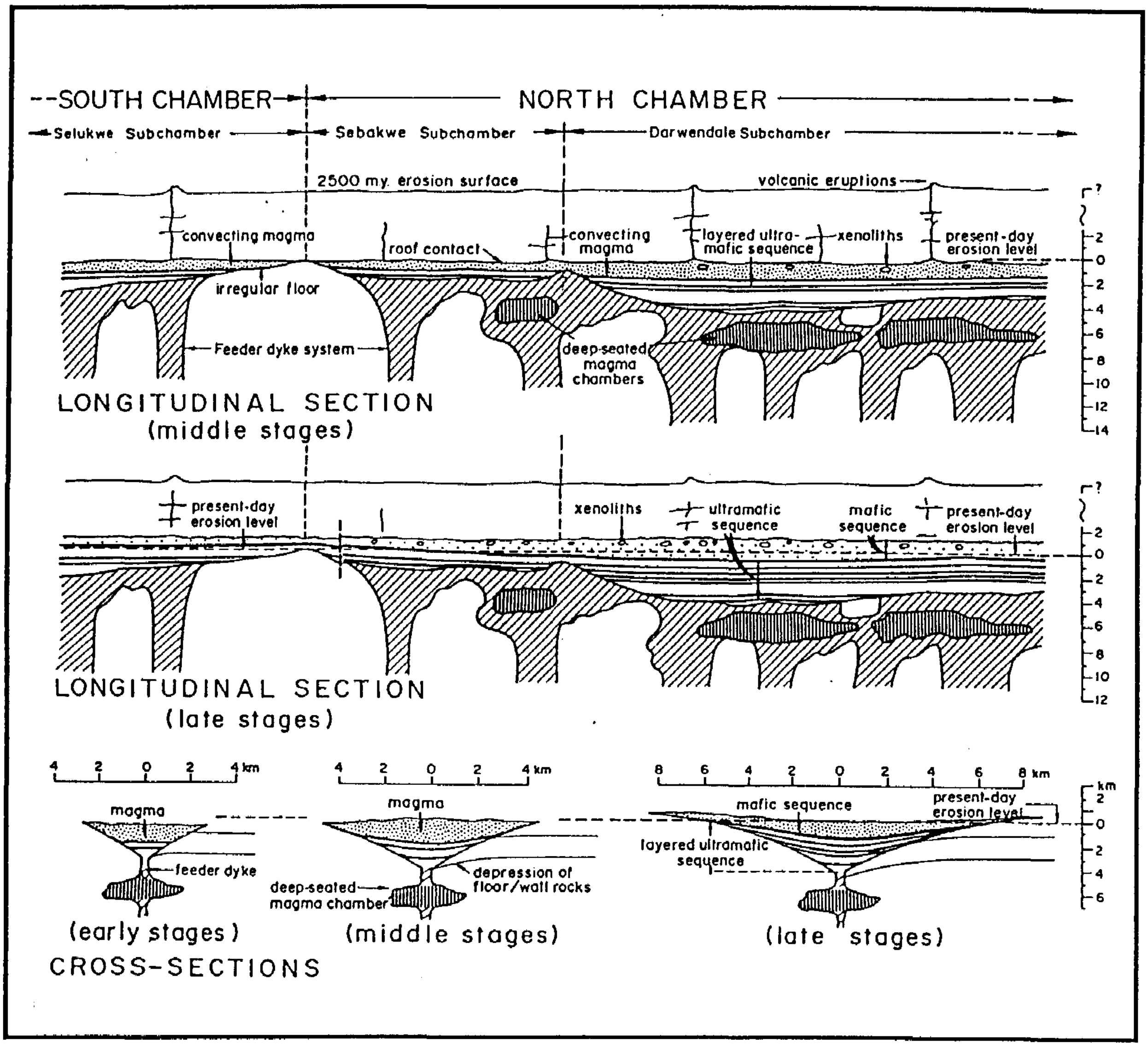

Figure 8.4 : Diagrammatic longitudinal section of part of the Great Dyke showing the sequence of emplacement and crystallization. Chambers, which were fed through a series of dykes and deep seated magma chambers, had irregular floors with barriers separating different compartments. As the chambers filled, barriers were breached and individual compartments coalesced. The postulated sill-like extensions of the Mafic Sequence is also shown. (After Wilson and Prendergast, 1989)

REFERENCES

Annheusser, C.R. (1986) The geological setting of chrysotile asbestos deposits in Southern Africa. *In*: Anhaeusser, C.R. and Maske, S. (Eds.), *Mineral Deposits of Southern Africa*, vol. I, Geol. Soc. S. Afr., Johannesburg, 359-375

Bailey, S.W. (1988) Polytypism of 1:1 layer silicates. *Rev.in Mineralogy.*, **19**, 9-27

Bartholomew, D.S. (1990) *Base metal and industrial mineral deposits of Zimbabwe*. Min. Res. Series no.22. Zim.Geol. Surv.,Harare. 154pp

Barnes, S. J. and Hoatson, D.M. (1994) The Munni-Munni Complex, W. Australia: Stratigraphy, structure and petrogenesis. *J. Petrol.*, **35**, 715-51

Barton, J.M. and Key, R.M. (1984) The tectonic development of the Limpopo Mobile Belt and the evolution of the Archaean cratons of southern Africa. *In* Kröner, A. (Ed.) *Precambrian Tectonics*. Elsevier, Amsterdam. 185-212

Bayliss, P. (1981) Unit cell data of serpentine group minerals. *Miner. Mag.*, **44**, 153-156

Beeson, M.H.. and Jackson, E.D. (1969) Chemical composition of altered chromites from the Stillwater Complex, Montana. *Am. Miner.*, **54**, 1084-1100

Berry, L.G. (Ed.) (1974) *Selected Powder Diffraction Data for Minerals*. Joint Committee on Powder Diffraction Standards.833pp

Bichan, H. R. (1969) Origin of chromite seams in the Hartley Complex of the Great Dyke, Rhodesia. *In* Wilson, H.D. B. (Ed.) *Magmatic Ore Deposits. Econ. Geol. Monogr.* **4**, 95-113

Bichan, R. (1970) The evolution and structural setting of the Great Dyke, Rhodesia. *In* Clifford, T.N. and Gass, I.G. (Eds) *African Magmatism and Tectonics*. Oliver and Boyd, Edinburgh. 55-71

Bliss, N.W.and Stidolph, P.A. (1969) A review of the Rhodesian Basement Complex. *Spec. Publ. geol. Soc. S. Afr.* **2**, 305-334

Brandeis, G. (1992) Constraints on the formation of cyclic units in ultramafic zones of large basaltic chambers. *Contrib. Miner. Petrol.*, **122**, 312-328

Cahen, L. and Snelling, N.J. (1984) *The Geochronology and Evolution of Africa.* Clarendon Press, Oxford. 512pp

Cameron, E. N. (1975) Postcumulus and subsolidus equilibration of chromite and coexisting silicates in the eastern Bushveld Complex. *Geochim. Cosmochim. Acta,* **39**, 1021-1033

Cameron, E. N. (1977) Chromite in the central sector of the eastern Bushveld Complex, South Africa. *Am. Miner.*, **62**, 1082-1096

Cameron, E. N. (1980) Evolution of the Lower Critical Zone, central sector, eastern Bushveld Complex, and its chromite deposits. *Econ. Geol.*, **75**, 845-871

Campbell, I.H. (1975) Direct evidence of present-day serpentinization in the Jimberlana intrusion, Western Australia. *Geol. Mag.*, **112**, 77-80

Campbell, I. H. (1978) Some problems with the cumulus theory. *Lithos,* **11**, 311-23

Campbell, I. H. and Turner, J. S. (1986) The influence of viscosity on fountains in magma chambers. *J. Petrol.*, 7, 1-30

Campbell, S.D.G., Oesterlen, P.M., Blenkinsop, T.G., Pitfield, P.E.J. and Munyanyiwa, H. (1992) A provisional 1:2500000 scale tectonic map and the tectonic evolution of Zimbabwe. *Annals Zim. Geol. Surv.*, **16**, 31-50

Caruso, L.J. and Chernosky, J.V. JR. (1979) The stability of lizardite. *Can. Miner.*, **17**, 757-769

Chaumba, J.C. (1995) *The Petrology and Petrogenesis of the Websterite Layer and the Mafic Sequence of the Darwendale Subchamber, Great Dyke, Zimbabwe.* M.Sc Thesis (unubl.). Univ. Natal

Coghill, B.M. and Wilson, A.H. (1993) Platinum Group minerals in the Sebakwe Subchamber, Great Dyke, Zimbabwe: implications for PGE collection mechanisms and post formational redistribution. *Miner. Mag.*, **57**, 613-634

Coward, M.P., James, P.R., and Wright, L. (1976) Northern margin of the Limpopo mobile belt, southern Africa. *Geol. Soc. Am. Bull.*, **87**, 601-611

Coward, M.P. and Daly, M.C. (1984) Crustal lineaments and shear zones in Africa: their relationship to plate movements. *Precamb. Res.*, **24**, 27-45

Cressey, B.A. (1979) Electron microscopy of serpentinite textures. *Can. Miner.*, **17**, 741-756

Deer, W.A., Howie, R.A., and Zussman, J. (1982) *Rock Forming Minerals - 2nd ed., Volume 1A: Orthosilicates.* Longman, London and New York., 919 pp

Dungan, M.A. (1979) Bastite pseudomorphs after orthopyroxene, clinopyroxene and tremolite. *Can. Miner.*, **17**, 729-740

Droop, G.T.R. (1987) Fe^{3+} in silicates and oxides. *Miner. Mag.*, **51**, 431-435

Eales, H.V., Reynolds, I.M., and Gouws, D.A. (1980) The spinel-group minerals of the central Karoo tholeiitic province. *Trans. Geol. Soc. S. Afr.*, **83**, 243-253

Eales, H.V., Field, M., De Klerk, W.J. and Scoon, R.N. (1988). Regional trends of chemical variations and thermal erosion in the western Bushveld Complex. *Miner. Mag.*, **52**, 63-79.

Eales, H.V. and Cawthorn, R.G. (1996) The Bushveld Complex. *In* Cawthorn, R.G. (Ed) *Layered Intrusions.* Elsevier Science, Amsterdam., 181-229

Fang, J.H. and Bloss, F.D. (1966) *X-ray Diffraction Tables.* Southern Illinois Univ. Press, Illinois.

Golightly, J.P. (1981) Nickeliferous laterite deposits. *Econ. Geol. 75th Anniv.Vol.*, 710-735

Hamilton J. (1977) Isotope and trace element studies of the Great Dyke and Bushveld mafic phase and their relation to early Proterozoic magma genesis in southern Africa. *J. Petrol.*, **18**, 24-52

Hamlyn, P. R. and Keays, R. R. (1979) Origin of Chromite compositional variation in the Panton Sill, Western Australia. *Contrib. Miner. Petrol.*, **69**, 75-82

Harger, H.S. (1934) An early Transvaal geological map by Carl Mauch. *Trans. Geol. Soc. S.Afr.* **37**, 1-4

Henderson, P. (1975) Reactions trends shown by chrome-spinels of the Rhum layered intrusion. *Geochim. et Cosmochim. Acta.*, **39**, 1035-1044

Hess, H.H. (1950) Vertical mineral variation in the Great Dyke of Southern Rhodesia.*Trans. Geol. Soc. S. Afr.*, **53**, 159-168

Hill, R. and Roeder, P. (1974) The crystallization of spinel from bassaltic liquid as a funcition of oxygen fugacity. *J. Geology,* **82**, 709-729

Hughes, C. J. (1970) Major rhythmic layering in the ultramafic rocks of the Great Dyke of Rhodesia, with particular reference to the Sebakwe area. *Spec. Publ. geol. Soc. S. Afr.* **1**., 594-609

Hughes, C.J. (1976) Parental magma of the Great Dyke of Rhodesia- voluminous late Archaean high magmetism basalt. *Trans. Geol. Soc. S. Afr.*, **79**, 179-82

Hulbert, L. J. and von Gruenewaldt, G. (1985) Textural and compositional features of Chromite in the lower and critical zones of the Bushveld Complex, south of Potgietersrus. *Econ. Geol.*, **80**, 872- 895

Hunter, D.R. and Pretorius, D.A. (1981) Structural framework (of Southern Africa). *In* Hunter, D.R. (Ed.) *Precambrian of the Southern Hemisphere*. Elsevier Science, Amsterdam., 397-422

Hunter, D.R. and Reid, D.L. (1987) Mafic Dyke Swarms in Southern Africa. *In* Halls, H.C. and Fahrig, W.F. (Eds.) *Mafic Dyke Swarms*, Spec. Pap. geol. Ass. Can. **34**, 445-456

Hunter, R.H. (1996) Texture development in cumulate rocks. *In* Cawthorn, R.G. (Ed) *Layered Intrusions*. Elsevier Science, Amsterdam., 77-101

Huppert, H.E. & Sparks, R.S.J. (1980) The fluid dynamics of a basaltic magma chamber replenished by influx of hot, dense ultrabasic magma. *Contrib. Miner. Petrol.*, **75**, 279 - 289.

Irvine, T. N. (1967) Chromian spinel as a petrogenetic indicator. Part 2, Petrological applications. *Canadian Jour. Earth Sci.*, **4**, 71-103

Irvine, T. N. (1977) Origin of chromitite layers in the Muskox Intrusion and other stratiform intrusions; a new interpretation. *Geology*, **5**, 273-277

Irvine, T. N. (1982) Terminology for layered intrusions. *J.Petrol.*, **23**, 127-62

Irvine, T. N. (1980) Magmatic density currents and cumulus processes. *Am. Journ. Sci.*, **280**, 1-58

Jackson, E.D. (1961) Primary textures and mineral associations in the ultramafic zone of the Stillwater complex, Montana. *U.S. Geol. Survey. Prof. Paper.*, **358**, 1-106

Jackson, E. D. (1966) Liquid immiscibility in chromite seam formation. *Econ. Geol.*, **61**, 777-780

Jackson, E. D.(1970) The cyclic unit in layered intrusions - a comparison of repetitive stratigraphy in the ultramafic parts of the Stillwater, Muscox, Great Dyke and Bushveld complexes. *Spec. Publ. Geol. Soc. S.Afr.* **1**. 391-424

Johannes, W. (1968) Experimental investigation of the reaction forsterite + $H_2O \rightleftharpoons$ serpentine + brucite. *Contrib. Miner. Petrol.*, **19**, 309-315

Jones, D.L. Robertson, I.D. M. and McFadden, P. L. (1975) A palaeomagnetic study of the Precambrian dyke swarms associated with the Great Dyke of Rhodesia., *Trans. Geol. Soc. S.Afr.*, **78**, 57-65

Katz, M.B. (1976) Early Precambrian granulite-greenstones, transform mobile belts and ridge-rifts on early crust? *In* Windley, B.F.(Ed.) *The Early History of the Earth*. Wiley, London. 147-155

Kamber, B.S., Kramers, J.D., Napier, R., Cliff, R.A. and Rollinson, H.R. (1995) the Triangle Shear Zone, Zimbabwe, revisited: new data document and important event at 2.0 Ga in the Limpopo Belt. *Precam. Res.*, **70**, 191-213

Keep, F.E. (1930) The geology of the chromite and asbestos deposits of the Umvukwe Range, Lomagundi and Mazoe Districts. *Geol. Surv Sth. Rhod. Bull.* **16**, 105pp

Lapham, D.M. (1965) A new nickeliferous magnesium hydroxide from Lancaster County, Pennsylvania. *Am. Miner.* **50**, 1708-1716

Lee, C.A. (1996) A review of mineralization in the Bushveld Complex and some other layered mafic intrusions. *In* Cawthorn, R.G. (Ed) *Layered Intrusions*. Elsevier Science, Amsterdam., 103-145

Lightfoot, B.A. (1926) Platinum in Southern Rhodesia. *Geol. Surv Sth. Rhod. Short. Rep.* **19**, 13pp

Lightfoot, B.A. (1927) Traverses along the Great Dyke of Southern Rhodesia. *Geol. Surv Sth. Rhod. Short. Rep.* **21**, 8pp

Lightfoot, B.A. (1940) The Great Dyke of Southern Rhodesia. Presidential Address, *Proc.Geol. Soc S. Afr.* XLIII, 27-46

Lister, L. A. (1987) The erosion surfaces of Zimbabwe.*Bull. Geol. Surv. Zim.* no.90, 163p

Lipin, B. R. (1993) Pressure increases, the formation of chromite seams, and the development of the ultra-mafic series in the Stillwater Complex, Montana. *J. Petrology.*, **34**, 955-976

Marsh, B.D. (1988) Crystal capture, sorting, and retention in convecting magmas. *Geol. Soc. Am. Bull.* **100**, 1720-1737

Martin, B. and Fyfe, W.S. (1970) Some experimental and theoretical observations of hydration reactions with particular reference to serpentinization. *Chem. Geol.*, **6**, 185-202

Martin, D. (1990) Crystal settling and *in situ* crystallization in aqueous solutions and magma chambers. *Earth. Planet. Sci. Lett.* **96**, 336-348

Maufe, H.B.(1921) Report of the Director, Geological Survey, 1920. *Geol. Surv Sth. Rhod.*, Salisbury. 5p

Maufe, H.B, Lightfoot, B.A. and Zealley, A. E. V. (1919) The geology of the Selukwe Mineral Belt *Geol. Surv Sth. Rhod. Bull.* **3**, 96pp

McBirney, A.R. and Noyes, R.M. (1979). Crystallization and layering of the Skaergaard Intrusion. *Jour. Petrology.*, **20**, 487-554

McGregor, A.M. (1951) Some milestones in the Precambrian of Southern Rhodesia. *Trans. Geol. Soc. S. Afr.*, **54**, 27-71

Morimoto, N. (1988) Nomenclature of pyroxenes. *Miner. Mag.*, **52**, 535-550

Morse, S.A. (1986) Convection in aid of cumulus growth. *J.Petrology*, **27**, 1183-1214

Murahwi, C.Z. (1995) *The Geology of the Unki Platinum-Base Metal Deposit, Selukwe Subchamber, Zimbabwe.* M.Sc thesis (unpubl.), Rhodes University.

Mushayendebvu, M. F. (1995) Magnetic modelling of the Umvimeela Dyke and East Dykes: evidence for regional tilting of the Zimbabwe craton adjacent to the Limpopo Belt. *Journ. Appl. Sci. Sth. Africa.* **1**, 47-58

Mushayendebvu, M. F. Jones, D. L. and Briden, J.C. (1994) A palaeomagnetic study of the Umvimeela Dyke, Zimbabwe: evidence for a Mesozoic overprint. *Precam. Res.*, **69**, 268-280

Mutemererwa, A. (1996) Survey of the World Chromium Market. *Zim. Inst. Min. Res.,Ann. Rep.* **159**, 59-61

Naslund, H.R. and McBirney, A.R. (1996) Mechanisms of formation of igneous layering. *In* Cawthorn, R.G. (Ed) *Layered Intrusions*. Elsevier Science, Amsterdam., 7-43

O'Hanley, D.S., Chernosky, J.V., JR., and Wicks, F.J. (1989) The stability of Lizardite and Chrysotile. *Can. Miner.*, **27**, 483-483

Oliveira, S.M., Trescases, J.J., and Melfi, A.J. (1992) Lateritic nickel deposits of Brazil. *Mineralium Deposita*, **27**, 137-146

Podmore, F. (1970) The shape of the Great Dyke as revealed by gravity surveying. *Spec. Publ. geol. Soc. S. Afr.* **1**, 610-20

Podmore, F. and Wilson, A.H. (1987) A Reappraisal of the structure, geology and emplacement of the Great Dyke of Zimbabwe. *In* Halls, H.C. and Fahrig, W.F. (Eds.) *Mafic Dyke Swarms*, Spec. Pap. geol. Ass. Can. **34**, 317-330

Prendergast, M.D. (1987) The chromite ore field of the Great Dyke, Zimbabwe. *In* Stowe, C.W. (Ed.) *Evolution of Chromite Ore Fields*. Van Nostrand Reinhold, New York, 89-108.

Prendergast, M. D. (1988) The geology and economic potential of the PGE-rich Main Sulphide Zone of the Great Dyke, Zimbabwe. *In* Prichard H.M. et. al. (Eds.) *Geo-Platinum 87*. Barking, Essex: Elsevier Applied Science, 281-302

Prendergast, M.D. and Keays, R.R. (1989). Controls of platinum-group element mineralization and the origin of the PGE-rich Main Sulphide Zone in the Wedza Sub chamber of the Great Dyke of Zimbabwe: implications for the genesis of, and exploration for, stratiform PGE mineralization in layered intrusions. *In*: Prendergast, M.D. and Jones, M.J. (Eds), *Magmatic Sulphides-The Zimbabwe Volume*. Inst. Min. Metall., 43-70

Prendergast, M.D. and Wilson A.H. (1989). The Great Dyke of Zimbabwe-II: mineralization and mineral deposits. *In*: Prendergast, M.D. and Jones, M.J. (Eds.), *Magmatic Sulphides-The Zimbabwe Volume*. Inst. Min. Metall., 21-42

Prendergast, M.D. (1990) Platinum -group minerals and hyrosilicate 'alteration' in the Wedza-Mimosa platinum deposit, Great Dyke, Zimbabwe - genetic and metallurgical implications. *Trans. Inst. Min. Metall.* **99(B)**, B91-105

Prendergast, M.D. (1991) The Wedza-Mimosa platinum deposit, Great Dyke, Zimbabwe: layering and stratiform PGE mineralization in a narrow mafic magma. *Geol. Mag.* **128**, 235-249

Ragland, P.C. (1989) *Basic Analytical Petrology*. Oxford Univ. Press., New York-Oxford. 369pp

Robertson, I.D.M. and van Breemen O. (1970) The southern satellites of the Great Dyke, Rhodesia. *Spec. Publ. geol Soc. S. Afr.* **1**, 821-44

Robertson, I.D.M. (1973) The geology of the country around Mount Towla, Gwanda District. *Bull. Geol. Surv. Sth. Rhod.* **68**, 166 p

Robertson, I.D.M. and du Toit, M.C. (1981) The Limpopo Belt. *In* Hunter, D.R. (Ed.) *Precambrian of the Southern Hemisphere*. Elsevier Sci. Publ. Comp., Amsterdam., 641-670

Roeder, P. L. and Campbell, I. H. (1985) The effect of postcumulus reactions on composition of chrome-spinels from the Jimberlana Intrusion. *J. Petrol.*, **26**, 763-86

Roeder, P. L. and Reynolds, I. (1991) Crystallization of chromite and chromite solubility in basaltic melts. *J. Petrol.* **32**, 909-934

Rollinson, H.R. (1995) The relationship between chromite composition and the tectonic setting of Archaean ultramafic rocks. *In* Blenkinsop, T.G., and Tromp, P.L. (Eds.). *Sub-Saharan Economic Geology*. Geol. Soc. Zim. Spec. Publ. no.3., 7-23

Rollinson, H.R.and Blenkinsop, T.G. (1995) The magmatic, metamorphic and tectonic evolution of the Northern Marginal Zone of the Limpopo Belt in Zimbabwe. *Journ. Geol. Soc.* London. **152**, 65-75

Sanford, R.F. (1981) Mineralogical and chemical effects of hydration reactions and applications to serpentinization. *Am. Miner.*, **66**, 290-297

Scowen, P.A.H., Roeder, P.L., and Helz, R.T. (1991) Re-equilibration of chromite within Kilauea Iki lava lake, Hawaii. *Contrib. Miner. Petrol.*, **107**, 8-20

Slatter, D.de L. (1979) Production of ferrochromium nickel alloys and stainless steels by direct smelting of oxide ores in Zimbabwe-Rhodesia. *Trans. Inst. Min. Metall.*, **88**, C209-C214

Smith, A.M. and Slatter, D.de L. (1978) The friability of chromium ore in a mine on the Great Dyke. *Zim. Inst. Min. Res.,Ann. Rep.* **26**, 62-67

Snowden, P.A. (1984) Non-diapiric batholiths in the north of the Zimbabwe Shield. *In* Kröner, A. and Greiling, R. (Eds.) *Precambrian Tectonics Illustrated.* Elsevier, Amsterdam. 161-183

Sparks, R.S.J., Huppert, H.E., Koyaguchi, T., Hallworth, M.A. (1993) Origin of modal and rhythmic igneous layering by sedimentation in a convecting magma chamber. *Nature*. **361**, 246-249

Springer, G. (1974) Compositional and structural variations in garnierites. *Can. Miner.* **12**, 381-388

Stowe, C. W. (1980) Wrench tectonics in the Archaean Rhodesian craton. *Trans. Geol. Soc. S. Afr.* **83**, 193-205

Tait, S.R., Sparks, R.S.J.,and Huppert, H.E. (1984) The role of compositional convection in the formation of adcumulus growth. *Lithos.* **17**, 139-146

Treloar, P.J., Coward, M.P., and Harris, N.B.W. (1992) Himalayan-Tibetan analogies for the evolution of the Zimbabwe craton and Limpopo Belt. *Precamb. Res.*, **55**, 571-587

Treloar, P.J. and Blenkinsop, T.G. (1995) Archaean deformation patterns in Zimbabwe: true indicators of Tibetan-style extension or not? *In* Coward, P.P. and Ries, A.C. (Eds.) *Early Precambrian Processes.* Geol. Soc. (London) Spec. Publ. 95., 87-108

Ulmer, G. C. (1969) Experimental investigations of chromite spinels. *In* Wilson, H. D. B. (ed.) *Magmatic ore deposits. Econ. Geol. Monogr.* **4**, 114-31

Wager, L.R., Brown, G.M., and Wadsworth, W.J. (1960), Types of igneous cumulates. *J. Petrol.*, **1**,73-85

Wagner, P.A.and Mellor, E.T. (1925a) On platinum-bearing hortonolite-dunite of the Lydenburg District. *Trans. Geol. Soc. S.Afr.* **28**, 1-18

Wagner, P.A. (1925b) Notes on the Platinum deposits of the Bushveld Igneous Complex. *Trans. Geol. Soc. S.Afr.* **28**, 83-134

Weiss, O. (1940) Gravimetric and Earth-magnetic measurements on the Great Dyke of Southern Rhodesia. *Trans. Geol. Soc. S. Afr.* **43**, 143-152

Wenner, D.B. and Taylor, H.P. (1974) Temperatures of serpentinization of ultramafic rocks based on O^{18}/O^{16} fractionation between coexisting serpentine and magnetite. *Contrib. Miner. Petrol.*, **32**, 165-185

Wicks, F.J. and Whittaker, E.J.W. (1977) Serpentine textures and serpentinization. *Can. Miner.*, **15**, 459-488

Wicks, F.J., Whittaker, E.J.W., and Zussman, J. (1977) An idealized model for serpentinization after olivine. *Can. Miner.*, **15**, 446-458

Wicks, F.J. and O'Hanley, D.S. (1988) Serpentine minerals: structures and petrology. *Rev.in Mineralogy.*, **19**, 91-167

Whittaker, E.J.W. (1956a) The structure of chrysotile II. Clinochrysotile. *Acta Cryst.*, **9**, 855-862

Whittaker, E.J.W. (1956b) The structure of chrysotile III. Orthochrysotile. *Acta Cryst.*, **9**, 862-864

Whittaker, E.J.W. (1956c) The structure of chrysotile IV. Parachrysotile. *Acta Cryst.*, **9**, 865-867

Whittaker, E.J.W. and Zussman, J. (1956) The characterization of serpentine minerals by X-ray diffraction. *Miner. Mag.*, **31**, 107-126

Wild, H. (1965) The flora of the Great Dyke of Southern Rhodesia with special reference to the Serpentine soils. *Kirkia*, **5**, 49-86

Wilson, A.H. and Wilson, J.F. (1981) The Great `Dyke'. *In* Hunter, D.R. (Ed.) *Precambrian of the Southern Hemisphere.*Elsevier, Amsterdam, etc., 572-578

Wilson, A.H. (1982) The geology of the Great 'Dyke', Zimbabwe: the ultramafic rocks. *J. Petrol.*, 23, 240-292

Wilson, A.H. and Prendergast, M.D. (1987) The Great Dyke of Zimbabwe-an overview. *In* Campbell, A.(Ed) *Guidebook for the 5th Magmatic Sulphides Field Conference*, Geological Society of Zimbabwe, Harare., 23-55

Wilson A.H. and Prendergast, M.D. (1988) The Great Dyke of Zimbabwe-I : tectonic setting, stratigraphy, petrology, structure, emplacement and crystallization. *In*: Prendergast, M.D. and Jones, M.J. (Eds), *Magmatic Sulphides - The Zimbabwe Volume*. Inst. Min. Metall., 1-20

Wilson, A.H., Naldrett, A. J., and Tredoux, M. (1989) Distribution and controls of platinum group element and base element mineralization in the Darwendale Subchamber of the Great Dyke, Zimbabwe. *Geology*, **17**, 649-652

Wilson, A.H. and Tredoux, M. (1990) Lateral and vertical distribution of platinum group element and petrogenetic controls on sulphide mineralization in the P1 pyroxenite layer of the Darwendale Subchamber of the Great Dyke, Zimbabwe. *Econ. Geol*, **85**, 556-584.

Wilson, A.H. (1992) The geology of the Great Dyke, Zimbabwe: crystallization, layering and cumulate formation in the P1 pyroxenite of Cyclic Unit 1 of the Darwendale Subchamber. *J. Petrol.*, **33**, 611-663

Wilson, A.H. (1996) The Great Dyke of Zimbabwe. *In* Cawthorn, R.G. (Ed) *Layered Intrusions*. Elsevier Science, Amsterdam., 365-402

Wilson, A.H.and Chaumba, J.B. (1997) Closed system fractionation in a large magma chamber: mineral compositions of the websterite layer and lower mafic succession of the Great Dyke, Zimbabwe. *Miner. Mag.* **61**, 153-173

Wilson, J.F. (1968) The geology of the country around Mashaba. *Bull. Geol. Surv. Sth. Rhod.* no. **62**, 239pp

Wilson, J.F., Bickle, M.J., Hawkesworth, C.J., Martin, A., Nisbet, E.G. and Orpen, J.L. (1978) Granite-greenstone terrains of the Rhodesian Archaean craton. *Nature*, **271**, 23-27

Wilson, J.F. (1981) The granitic-gneiss greenstone shield of Zimbabwe. *In* Hunter, D.R. (Ed.) *Precambrian of the Southern Hemisphere*. Elsevier Sci. Publ. Comp., Amsterdam., 454-488

Wilson, J.F. Jones, D.L. and Kramers, J.D. (1987) Mafic dyke swarms in Zimbabwe. *In* Halls H.C. and Fahrig W.F. (Eds.) *Mafic Dyke Swarms.. Spec. Pap. geol. Ass. Can.* **34**, 433-444

Wilson, J.F. (1990) A craton and its cracks: some of the behaviour of the Zimbabwe block from the late Archaean to the Mesozoic in response to horizontal movements, and the significance of some of its mafic dyke fracture patterns. *Journ. Afr. Earth. Sci.* **10**, 483-450

Wilson, J.F. and Nutt, T.H.C. (1990) The nature and occurrence of mineralization in the early Precambrian crust of Zimbabwe. *In* Naqvi, S.M. (Ed.) *Precambrian Continental Crust and its Economic Resources*. Elsevier Sci. Publ. Comp., Amsterdam., 555-592

Wilson, J.F., Nesbitt, R.W.,Fanning, C.M. (1995) Zircon geochronology of Archaean felsic sequences in the Zimbabwe Craton: A revision of greenstone stratigraphy and a model for crustal growth. *In* Coward, P.P. and Ries, A.C. (Eds.) *Early Precambrian Processes*. Geol. Soc. (London) Spec. Publ. 95., 109-126

Worst, B.G. (1956) The geology of the country between Belingwe and West Nicholson. *Bull. Geol. Surv. Sth. Rhod.* **43**, 218 pp

Worst, B.G. (1958) The differentiation and structure of the Great Dyke of Southern Rhodesia. *Trans. Geol. Soc. S. Afr.*, **61**, 283-358

Worst, B.G. (1960) The Great Dyke of Southern Rhodesia. *Bull. Geol. Surv. Sth. Rhod.* **47**, 234 pp

Zealley, A. E. V. (1912) District including Selukwe commonage and the country east and south of it. *In* Maufe, H.B. *Report of the Director, Geol. Surv., 1911. Geol. Surv Sth. Rhod.*, Salisbury. 7-21

APPENDIX A:

Borehole depth and sample numbers from borehole H10/4a

Sample # (GDC)	Depth (metres)	Description	Sample # (GDC)	Depth (metres)	Description
1	7.45 - 7.60	Harzburgite	28	132.00 - 132.26	Olivine pyroxenite
2	12.07 - 12.18	Harzburgite	29	133.05 - 133.28	Harzburgite
3	16.30 - 16.43	Harzburgite	30	136.33 - 136.48	Serpentinite
4	35.74 - 35.95	Serpentinite	31	142.26 - 142.45	Serpentinite
5	47.44 - 47.68	Serpentinite	32	145.41 - 145.64	Serpentinite
6	48.40 - 48.63	Serpentinite	33	148.49 - 148.63	Serpentinite
7	49.68 - 49.87	Serpentinite	34	151.34 - 151.57	Serpentinite
8	54.32 - 54.50	Serpentinite	35	154.34 - 154.57	Serpentinite
9	57.05 - 57.30	Serpentinite	36	187.88 - 188.08	Serpentinite
10	60.51 - 60.77	Serpentinite	37	190.85 - 190.99	Serpentinite
11	64.46 - 64.68	Serpentinite	38	193.59 - 193.84	Serpentinite
12	67.68 - 67.90	Serpentinite	39	196.83 - 197.00	Serpentinite
13	69.60 - 69.84	Serpentinite	40	199.61 - 199.81	Serpentinite
14	70.88 - 71.05	Serpentinite	41	201.07 - 201.19	Serpentinite
15	73.64 - 73.80	Serpentinite	42	212.25 - 212.52	Serpentinite
16	74.36 - 74.58	Serpentinite	43	214.31 - 214.55	Serpentinite
17	76.40 - 76.63	Chromite serpentinite	44	215.41 - 215.68	Serpentinite
18	77.05 - 77.30	Chromite serpentinite	45	220.36 - 220.51	Bronzitite
19	78.11 - 78.30	Bronzitite	46	221.17 - 221.49	Bronzitite
20	79.49 - 79.61	Bronzitite	47	223.95 - 224.18	Bronzitite
21	82.72 - 82.97	Bronzitite	48	244.65 - 245.11	Bronzitite
22	83.35 - 83.55	Bronzitite	49	295.37 - 295.56	Serpentinite
23	95.80 - 96.00	Bronzitite	50	299.30 - 299.54	Serpentinite
24	96.48 - 96.67	Bronzitite	51	309.01 - 309.22	Serpentinite
25	102.50 - 102.67	Bronzitite	52	312.35 - 312.58	Serpentinite
26	125.26 - 125.44	Olivine pyroxenite	53	327.70 - 327.88	Serpentinite
27	127.12 - 127.26	Olivine pyroxenite	GD62	400.00 - 400.10	Dunite

APPENDIX B : SAMPLE NUMBERS AND LOCALITIES OF PLATES

Plate 4.1 :		View from point 1 (see appendix C)
Plate 4.2 :		View from point 2 (see appendix C)
Plate 4.3 :	Surface and borehole samples of poikilitic harzburgite.	GDC3 and GD30
Plate 4.4 :	Surface and borehole samples of granular harzburgite.	GDC28 and GD34
Plate 4.5 :	Surface samples of serpentinite associated with fault zones.	GD55
Plate 4.6 :	Stockwork structure in saprolitic serpentinite.	taken at point 2 (see appendix C)
Plate 4.7 :	Surface samples of chromitite C5.	GD24, GD38, GD39
Plate 4.8 :	Intensely silicified chromitite C5.	GD39
Plate 5.1 :	Euhedral disseminated chromite grains in serpentinite.	GD62
Plate 5.2 :	Disseminated chromite grains enclosing olivine (serpentinized) in serpentinite.	GDC16
Plate 5.3 :	Chain textured chromite from chromite serpentinite.	GD3
Plate 5.4 :	Altered and corroded chromite rims.	GDC12
Plate 5.5 :	Altered and corroded chain textured chromite in serpentinite.	GDC12
Plate 5.6 :	Serpentinite varieties from borehole core.	GDC6, GDC16, GDC42, GDC49, GDC53
Plate 5.7 :	Olivine pyroxenite showing development of talc aggregates.	GD21
Plate 5.8 :	Mesh textured serpentine with altered olivine mesh centres.	GD62
Plate 5.9 :	Large serpentine veins cross-cutting silicified serpentinite.	GDC41
Plate 5.10 :	Orthopyroxenite with interstitial feldspar and clinopyroxene.	GD56a
Plate 5.11 :	Pervasively serpentinized poikilitic harzburgite.	GDC32
Plate 5.12 :	Granular harzburgite showing textural equilibration of orthopyroxene grains and highly rounded olivine.	GDC27
Plate 5.13 :	Transition from the centimetre orthopyroxenite to granular harzburgite.	GDC2
Plate 5.14 :	Footwall of chromitite C5.	GD28
Plate 5.15 :	'Mottled chromitite' near hanging wall of chromitite C5.	GD13

NB: Localities of samples with a GD prefix are shown in Appendix C. Samples with a GDC prefix are from borehole H10/4a: sample depth in borehole is given in Appendix A.

APPENDIX C:
Map of photograph and referenced sample localities

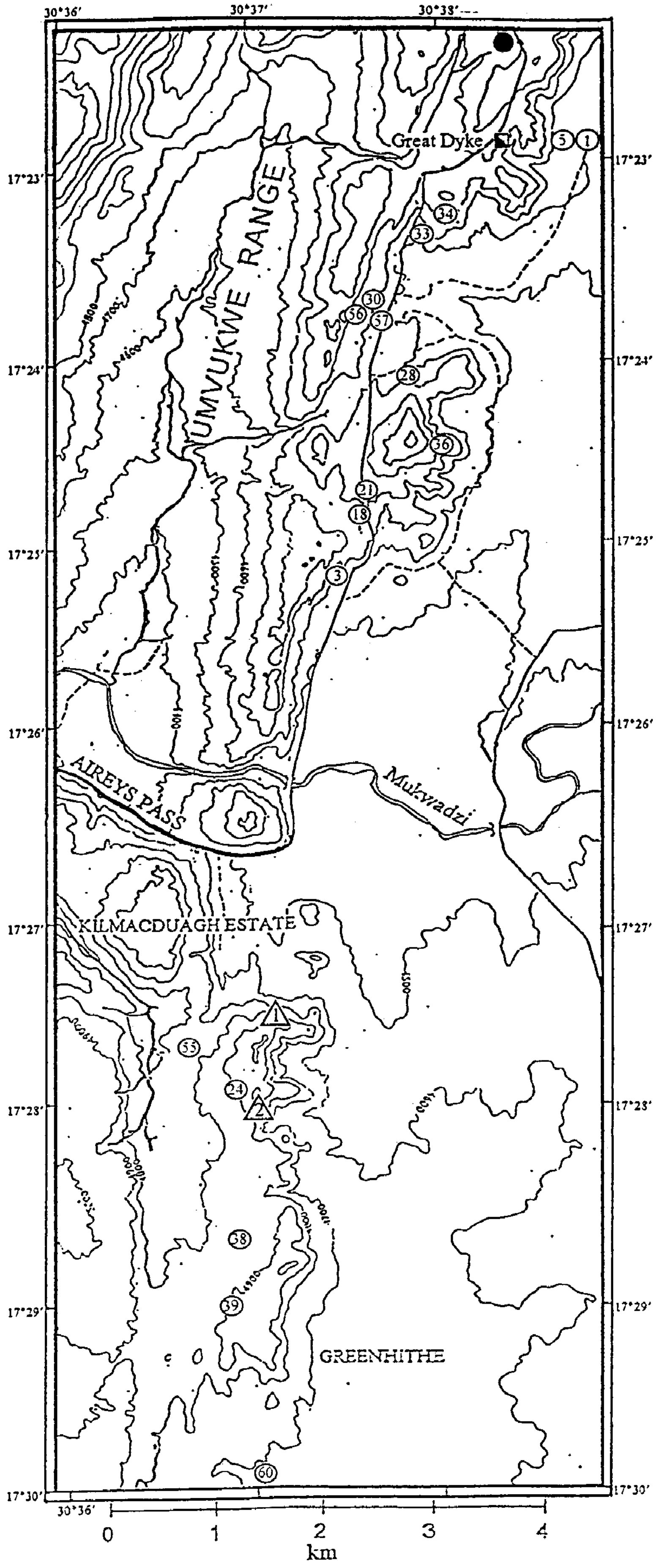

KEY:

◪ . Great Dyke Mine (samples GD9 and GD13 are from this locality)

(#). . GD- prefix sample number

● . . Borehole H10/4a (GDC-prefixed sample numbers and GD62)

△ . . . . photograph point

Appendix D : Individual electron microprobe analyses of chromite compositions

Sample no.	gdc18	gdc18	gdc18	gdc18	gdc18	gdc18	gdc18	gdc18	gd9	gd9	gd9	gd9	gd9	gd9	gd9	gd9
Rock-type	Olivine chromitite (serpentinized)								C5 "Puppy" seam							
SiO2	0.04	0.04	0.06	0.07	0.05	0.02	0.06	0.08	0.06	0.06	0.03	0.02	0.03	0.02	0.04	0.02
TiO2	0.34	0.33	0.34	0.36	0.33	0.29	0.33	0.31	0.36	0.37	0.33	0.33	0.35	0.34	0.33	0.31
Al2O3	10.75	10.93	10.99	11.13	11.01	10.72	10.94	11.22	9.93	10.06	10.00	9.96	9.93	9.96	9.96	10.06
Cr2O3	54.93	54.77	55.14	54.92	55.38	55.03	55.25	54.34	58.06	57.58	57.53	57.54	57.70	57.21	57.63	57.28
Fe2O3	4.37	4.38	4.39	4.15	4.17	4.91	4.32	5.08	3.44	3.72	3.94	3.63	3.86	3.90	3.51	3.84
FeO	17.32	17.52	16.99	17.06	17.32	17.11	17.09	17.95	13.91	13.95	13.94	13.84	13.96	13.95	14.16	13.86
NiO	0.04	0.01	0.06	0.00	0.05	0.10	0.05	0.07	0.00	0.07	0.05	0.04	0.05	0.03	0.02	0.08
MnO	0.29	0.33	0.28	0.34	0.29	0.30	0.30	0.35	0.29	0.26	0.26	0.20	0.22	0.25	0.26	0.29
MgO	10.42	10.32	10.78	10.71	10.59	10.57	10.69	10.24	12.67	12.62	12.57	12.58	12.60	12.48	12.39	12.49
Total	98.50	98.64	99.04	98.75	99.19	99.06	99.03	99.65	98.72	98.70	98.64	98.15	98.71	98.12	98.30	98.23
Cations per 32 oxygens																
Al	3.3817	3.4323	3.4294	3.4811	3.4346	3.3526	3.415	3.4925	3.0789	3.118	3.1028	3.1055	3.0809	3.1086	3.104	3.1346
Cr	11.588	11.541	11.537	11.521	11.585	11.543	11.571	11.345	12.076	11.978	11.978	12.032	12.006	11.974	12.051	11.971
Fe3+	0.8922	0.8933	0.8978	0.8537	0.8486	0.9888	0.8833	1.0385	0.7034	0.7565	0.7906	0.7298	0.7733	0.7833	0.714	0.7712
Ti	0.069	0.0669	0.0677	0.0719	0.0657	0.0579	0.0651	0.0619	0.0706	0.0739	0.0644	0.0663	0.07	0.0671	0.0654	0.0617
Mg	4.144	4.1002	4.2545	4.235	4.1759	4.1823	4.222	4.0331	4.9683	4.9501	4.9354	4.9584	4.9446	4.9241	4.8857	4.9221
Fe2+	3.8525	3.8904	3.7373	3.7603	3.8147	3.7878	3.7634	3.9354	3.0384	3.0506	3.0598	3.0544	3.064	3.0809	3.1175	3.0563
Ni	0.0076	0.0016	0.0125	0	0.0111	0.0215	0.0114	0.0157	0	0.0154	0.0108	0.0081	0.0113	0.007	0.0043	0.0173
Mn	0.0648	0.0746	0.0634	0.0766	0.064	0.0664	0.0684	0.0777	0.0639	0.0578	0.0585	0.0454	0.0501	0.055	0.0579	0.0659
Fe2/(Fe2 + Mg)	0.482	0.487	0.468	0.470	0.477	0.475	0.471	0.494	0.379	0.381	0.383	0.381	0.383	0.385	0.390	0.383
Cr/(Cr+Al)	0.774	0.771	0.771	0.768	0.771	0.775	0.772	0.765	0.797	0.793	0.794	0.795	0.796	0.794	0.795	0.792
Cr/(Cr+Al+Fe3)	0.731	0.727	0.727	0.727	0.730	0.727	0.729	0.715	0.762	0.756	0.755	0.758	0.757	0.755	0.759	0.754
Ti/Cr	0.006	0.006	0.006	0.006	0.006	0.005	0.006	0.005	0.006	0.006	0.005	0.006	0.006	0.006	0.005	0.005

Appendix D : Individual electron microprobe analyses of chromite compositions

Sample no.	gd13	gd13	gd13	gd13	gd13	gd13	gd13	gd13	gd39	gd39	gd39	gd39	gd39	gd62	gd62
Rock-type	C5 chromitite						core	rim	C5 chromitite (tectonised)					s.dunite	
SiO2	0.01	0.02	0.03	0.01	0.03	0.04	0.04	0.06	0.06	0.04	0.02	0.05	0.08	0.07	0.07
TiO2	0.32	0.31	0.33	0.31	0.33	0.36	0.32	0.27	0.33	0.30	0.33	0.32	0.33	0.40	0.43
Al2O3	10.64	10.74	10.54	10.36	10.37	10.65	10.67	8.98	10.48	10.37	10.30	10.33	10.41	15.00	14.94
Cr2O3	56.44	56.66	56.21	56.42	56.38	57.13	56.53	58.81	59.94	59.69	59.32	58.60	59.84	52.96	52.98
Fe2O3	5.29	5.91	5.25	5.68	5.57	5.08	5.28	4.68	0.26	0.16	1.71	2.72	0.00	2.50	2.20
FeO	13.08	12.85	12.90	12.93	12.92	13.37	13.16	13.53	14.85	14.88	13.89	13.06	15.12	17.48	16.83
NiO	0.05	0.09	0.03	0.13	0.06	0.14	0.10	0.11	0.07	0.09	0.07	0.09	0.09		
MnO	0.29	0.21	0.20	0.24	0.28	0.22	0.21	0.23	0.26	0.18	0.21	0.19	0.16	0.28	0.24
MgO	13.32	13.73	13.41	13.36	13.40	13.36	13.36	12.89	11.99	11.82	12.65	13.21	11.78	11.14	11.46
Total	99.44	100.52	98.91	99.44	99.34	100.34	99.67	99.56	98.24	97.53	98.49	98.57	97.80	99.83	99.14
Cations per 32 oxygens															
Al	3.25341	3.24461	3.24013	3.17335	3.1784	3.2326	2.77198	3.25774	3.26742	3.25878	3.19061	3.18876	3.26459	4.55281	4.55166
Cr	11.583	11.4875	11.5894	11.5902	11.5907	11.6314	12.1804	11.5754	12.5303	12.5768	12.3324	12.1326	12.5832	10.7834	10.8287
Fe3+	1.03726	1.14756	1.04156	1.11454	1.10105	0.99852	0.94319	1.04378	0.07093	0.04407	0.34574	0.55445	0.02075	0.5087	0.45101
Ti	0.06316	0.06015	0.06444	0.06097	0.06492	0.06875	0.0522	0.06155	0.06567	0.06017	0.06564	0.06209	0.06572	0.07753	0.08432
Mg	5.15483	5.24699	5.2111	5.17529	5.19258	5.12695	5.03269	5.15761	4.72742	4.6962	4.95777	5.15715	4.67022	4.27627	4.41638
Fe2+	2.83471	2.74855	2.80162	2.80678	2.79787	2.86566	2.94424	2.83585	3.26526	3.30324	3.04734	2.84319	3.34151	3.7407	3.61506
Ni	0.01089	0.0189	0.00694	0.02696	0.01192	0.02838	0.02402	0.02135	0.01516	0.01964	0.0148	0.0185	0.01851	0	0
Mn	0.06273	0.04571	0.04477	0.05194	0.06255	0.04777	0.05125	0.04673	0.05784	0.0411	0.04572	0.04325	0.03549	0.06055	0.05288
Fe2/(Fe2 + Mg)	0.355	0.344	0.350	0.352	0.350	0.359	0.369	0.355	0.409	0.413	0.381	0.355	0.417	0.467	0.450
Cr/(Cr+Al)	0.781	0.780	0.782	0.785	0.785	0.783	0.815	0.780	0.793	0.794	0.794	0.792	0.794	0.703	0.704
Cr/(Cr+Al+Fe3)	0.730	0.723	0.730	0.730	0.730	0.733	0.766	0.729	0.790	0.792	0.777	0.764	0.793	0.681	0.684
Ti/Cr	0.005	0.005	0.006	0.005	0.006	0.006	0.004	0.005	0.005	0.005	0.005	0.005	0.005	0.007	0.008

Appendix D : Individual electron microprobe analyses of chromite compositions

Sample no.	**gd60**	**gd60**	**gd60**	**gd60**	**gd5**	**gd5**	**gd5**	**gd5**	**gd5**	**gd5**	**gd1**	**gd1**	**gd1**	**gd1**	**gd1**
Rock-type	C6 chromitite				C7 chromitite						C8 chromitite				
SiO2	0.05	0.05	0.06	0.01	0.13	0.02	0.04	0.01	0.01	0.04	0.02	0.03	0.04	0.03	0.03
TiO2	0.33	0.33	0.31	0.34	0.29	0.32	0.32	0.32	0.30	0.32	0.33	0.36	0.36	0.35	0.37
Al2O3	10.46	10.43	10.57	10.50	12.51	12.66	12.60	12.59	12.71	12.67	13.31	13.33	13.41	13.70	13.39
Cr2O3	59.02	58.72	58.78	59.44	56.00	55.92	56.21	55.62	55.84	56.14	55.75	56.59	54.97	56.81	55.65
Fe2O3	0.07	0.39	0.12	0.00	2.50	2.90	2.67	3.79	3.15	2.20	2.34	2.75	3.76	0.00	1.55
FeO	15.69	16.15	16.06	15.32	12.41	11.88	11.62	11.00	11.40	12.33	12.88	13.04	11.97	14.48	13.24
NiO	0.10	0.05	0.05	0.08	0.17	0.14	0.13	0.10	0.16	0.15	0.06	0.10	0.16	0.07	0.13
MnO	0.21	0.21	0.23	0.13	0.11	0.23	0.22	0.18	0.23	0.19	0.21	0.19	0.21	0.21	0.17
MgO	11.23	10.98	11.01	11.29	13.79	14.03	14.22	14.68	14.32	13.73	13.62	13.89	14.31	12.32	13.25
Total	97.15	97.30	97.19	97.10	97.92	98.11	98.04	98.28	98.12	97.78	98.51	100.27	99.20	97.97	97.77
Cations per 32 oxygens															
Al	3.308	3.302	3.346	3.318	3.835	3.861	3.843	3.819	3.869	3.883	4.044	3.983	4.035	4.207	4.103
Cr	12.526	12.470	12.485	12.598	11.514	11.443	11.499	11.321	11.402	11.543	11.367	11.346	11.093	11.701	11.442
Fe3+	0.032	0.097	0.045		0.536	0.572	0.533	0.737	0.615	0.447	0.462	0.535	0.735		0.312
Ti	0.067	0.066	0.062	0.068	0.057	0.062	0.062	0.061	0.057	0.063	0.064	0.068	0.068	0.069	0.071
Mg	4.494	4.397	4.411	4.510	5.345	5.415	5.485	5.636	5.513	5.324	5.235	5.252	5.446	4.785	5.138
Fe2+	3.505	3.611	3.588	3.435	2.652	2.565	2.501	2.367	2.460	2.666	2.770	2.754	2.543	3.154	2.870
Ni	0.021	0.011	0.011	0.018	0.036	0.030	0.027	0.020	0.033	0.032	0.013	0.021	0.032	0.015	0.027
Mn	0.047	0.047	0.052	0.028	0.025	0.051	0.049	0.038	0.051	0.042	0.046	0.040	0.046	0.046	0.038
Fe2/(Fe2 + Mg)	0.438	0.451	0.449	0.432	0.332	0.321	0.313	0.296	0.309	0.334	0.346	0.344	0.318	0.397	0.358
Cr/(Cr+Al)	0.791	0.791	0.789	0.792	0.750	0.748	0.750	0.748	0.747	0.748	0.738	0.740	0.733	0.736	0.736
Cr/(Cr+Al+Fe3)	0.789	0.786	0.786	0.792	0.725	0.721	0.724	0.713	0.718	0.727	0.716	0.715	0.699	0.736	0.722
Ti/Cr	0.005	0.005	0.005	0.005	0.005	0.005	0.005	0.005	0.005	0.005	0.006	0.006	0.006	0.006	0.006